D 2018

U.PORTO
FEUP FACULDADE DE ENGENHARIA
UNIVERSIDADE DO PORTO

COMPUTATIONAL ANALYSIS OF PURELY-ELASTIC FLOW INSTABILITIES AND TRANSITION TO ELASTIC TURBULENCE IN MICROSCALE FLOWS OF VISCOELASTIC FLUIDS

FILIPE ANTÓNIO NOGUEIRA DA CRUZ

DOCTORAL THESIS SUBMITTED TO THE
FACULDADE DE ENGENHARIA DA UNIVERSIDADE DO PORTO
IN CHEMICAL AND BIOLOGICAL ENGINEERING

European Research Council

Established by the European Commission

(Grant Agreement n. 307499)

Computational analysis of purely-elastic flow instabilities and transition to elastic turbulence in microscale flows of viscoelastic fluids

Candidate: Filipe António Nogueira da Cruz, MEng

Advisor: Manuel António Moreira Alves, PhD, Associate Professor

A doctoral thesis submitted to the *Faculdade de Engenharia da Universidade do Porto* in partial fulfilment of the requirements for the degree of Doctor in Chemical and Biological Engineering.

Porto, January 2018

Abstract

The main purpose of this thesis is the computational investigation of purely, or nearly purely, elastic flow instabilities in cross-slot geometries.

Stationary flow instabilities are investigated in a two-dimensional, planar cross-slot geometry, for the upper-convected Maxwell, Oldroyd-B and simplified linearized Phan-Thien–Tanner constitutive models. Flows become asymmetry while steady above a given Deborah number, and then time-dependent with further increases in flow rate. The values of several characteristic parameters are calculated via Richardson extrapolation of results obtained using three systematically refined meshes and a new benchmark flow is proposed.

Stationary flow instabilities are further analyzed in a three-dimensional cross-slot geometry, with aspect ratio, defined as the depth-to-width ratio, ranging from 0.01 to 9, or infinity in the two-dimensional limit, for the upper-convected Maxwell and simplified linearized Phan-Thien–Tanner constitutive models. The aspect ratio is identified as the controlling parameter, determining if the increasing flow rate leads to the formation of a stationary asymmetry followed by time-dependent flow, for channel depth larger than width, or if the onset of the latter occurs directly from the base stable flow, when the depth is smaller than the channel width. The bifurcation mechanism is shown to be similar to a buckling instability, by which fluid is redirected via paths of least resistance, resulting in the emergence of peripheral stagnation points, above and below the central stagnation point. The intake of matter at the center via the inlet axis is thus reduced, being compensated by fluid flowing through low resistance corridors along the central vertical axis, above and below the central point.

Time-dependent flow instabilities are investigated in a specialized cross-slot geometry, numerically optimized to produce a wide region of homogeneous extensional flow along the central slot, for the Finitely Extensible Nonlinear Elastic constitutive model with Chilcott-Rallison (FENE-CR) closure. A family of predominantly elastic instabilities is uncovered, resulting from the interaction of stationary asymmetric and time-dependent flow transitions, which, with varying degrees of relative amplitude, leads to the emergence of five distinct instability regimes, categorized by the respective ratio of elastic to inertial forces. A detailed characterization of each instability regime is

provided, as well as spectral analysis of velocity fluctuations. The birefringence strand, understood as the band of highly stretched polymer molecules along the outflow axis of a cross-slot or other extensional flow, is periodically or aperiodically broken in three of the five regimes. The loss of strand integrity correlates with the onset of chaotic flow, with a locally turbulent character above certain flow rate thresholds.

A preliminary investigation on the transition to elastic turbulence in a standard planar cross-slot is presented, for the flow of Oldroyd-B and FENE-CR fluids. Various stages of the transition are discussed, up to and including elastic turbulence, as demonstrated by several characteristic properties, mainly the spectral decay of velocity fluctuations and the ejection of excessive elastic stresses concentrated in the boundary layers along the walls of the outlet channels.

Keywords: Finite Volume Method, Cross-Slot Flows, Viscoelastic Fluids, Flow Instability, Microscale Flows, Bifurcations, Elastic Turbulence.

Resumo

O objetivo principal desta tese é a investigação computacional de instabilidades puramente, ou quase puramente, elásticas em geometrias de canais cruzados.

As instabilidades estacionárias do escoamento são investigadas em geometrias de canais cruzados bidimensionais, para os seguintes modelos constitutivos: convectivo superior de Maxwell; Oldroyd-B; Phan-Thien–Tanner simplificado e linearizado. Os escoamentos tornam-se assimétricos, mas estacionários, acima de um determinado valor do número de Deborah, e posteriormente variáveis no tempo com aumentos sucessivos do caudal. Os valores de vários parâmetros característicos são calculados pela técnica da extrapolação de Richardson, a partir de resultados obtidos em três malhas sistematicamente refinadas, propondo-se um novo escoamento de referência.

A análise das instabilidades estacionárias do escoamento é aprofundada em geometrias de canais cruzados tridimensionais, com razão de forma, definida como o quociente entre a profundidade e a largura, entre 0.01 e 9, ou infinito no limite bidimensional, para os modelos constitutivos convectivo superior de Maxwell e de Phan-Thien–Tanner simplificado e linearizado. A razão de forma é identificada como sendo o parâmetro que determina se o aumento progressivo do caudal conduz à formação de uma assimetria estacionária seguida de escoamento transiente, para profundidade do canal superior à largura, ou se o surgimento do escoamento variável no tempo ocorre diretamente a partir do estado basal, para profundidade inferior à largura do canal. É demonstrado que o mecanismo de bifurcação se assemelha à encurvadura de uma coluna, mediante a qual o fluido é redirecionado por trajetos de menor resistência, resultando no aparecimento de pontos de estagnação periféricos, acima e abaixo do ponto de estagnação central. Consequentemente, a admissão de fluido no centro do canal cruzado sofre uma redução pela via dos ramais de entrada, sendo a conservação da massa assegurada pelo escoamento ao longo dos trajetos de menor resistência localizados ao longo do eixo central vertical, através do qual flui matéria redirecionada pelos pontos de estagnação periféricos para o ponto de estagnação central.

As instabilidades transientes do escoamento são investigadas numa geometria de canais cruzados numericamente otimizada com vista à obtenção de uma região alargada de extensão homogénea na vizinhança do centro do canal cruzado, para o modelo

constitutivo Finitamente Extensível Não-linear Elástico com fecho de Chilcott-Rallison (FENE-CR). É descoberta uma família de instabilidades predominantemente elásticas, as quais resultam da interação das transições assimétrica estacionária e transiente, donde, mediante diferentes níveis de amplitude relativa, surgem cinco regimes de instabilidade, classificados de acordo com o respetivo quociente entre forças elásticas e forças inerciais. É apresentada uma caracterização detalhada de cada instabilidade, bem como a respetiva análise espetral da componente desviante da velocidade. A banda de birrefringência, correspondente à banda de cadeias poliméricas fortemente esticadas ao longo do eixo dos ramais de saída do canal cruzado, é periodicamente ou aperiodicamente quebrada em três dos cinco regimes. A perda de integridade por parte da banda de birrefringência correlaciona-se com o surgimento de um escoamento caótico, com caráter localmente turbulento, para caudais acima de um determinado limiar.

A transição para o regime de turbulência elástica é investigada de forma preliminar numa geometria de canais cruzados padrão, para os modelos constitutivos Oldroyd-B e FENE-CR. São demonstradas múltiplas etapas da transição para o regime turbulento, mediante o cálculo do espetro de potência da componente desviante da velocidade, bem como pela ejeção de tensões elásticas concentradas na camada limite ao longo dos ramais de saída.

Palavras-chave: Método dos Volumes Finitos, Escoamento em Canais Cruzados, Fluidos Viscoelásticos, Instabilidades do Escoamento, Escoamentos à Microescala, Bifurcações, Turbulência Elástica.

Acknowledgements

A sincere thank you to my advisor, Prof. Dr. Manuel Alves, for his assistance.

I'd like to acknowledge the contributions made by my co-authors, Profs. Drs. Fernando Pinho, Paulo Oliveira, Robert Poole and Alexandre Afonso. I'd also like to acknowledge the individuals who introduced me to some of the elements of experimental rheology, Drs. Simon Haward and Pierre Ballesta. I'd further like to acknowledge the assistance I've received from Dr. Renato Sousa, concerning some aspects of computational rheology. Additionally, I'd like to acknowledge the positive atmosphere maintained during the monthly group meetings of the Microfluidics and Complex Fluid Flows division of CEFT, and the laughs and sometimes serious conversations I shared with my office mates. Lastly, I'd like to acknowledge the work of anonymous referees and of my opponents for the examination of this thesis.

I had the unique opportunity to participate in several research projects as an undergraduate and Master's student. These experiences have also shaped my character as a researcher, and I would therefore like to acknowledge, in no particular order, Drs. Cristina Barrias, Keila Fonseca, Benny Palmqvist, Magnus Wiman, Falk Harnisch and Profs. Gunnar Lidén and Cristian Picioreanu.

A special acknowledgement to family and friends, in particular my mother and my sister.

This thesis was funded by the European Research Council under the European Union's Seventh Framework Programme (ERC grant agreement Nº 307499).

Acronyms and Abbreviations

1D	One-Dimensional
2D	Two-Dimensional
3D	Three-Dimensional
AR	Aspect Ratio
CBC	Convection Boundedness Criterion
CDS	Central Differencing Scheme
CFD	Computational Fluid Dynamics
CPU	Central Processing Unit
CUBISTA	Convergent and Universally Bounded Interpolation Scheme for the Treatment of Advection
DNA	Deoxyribonucleic acid
DOF	Degrees of Freedom
ENO	Essentially Non-Oscillatory scheme
ET	Elastic Turbulence
EVSS	Elastic Viscous Split Stress
FENE	Finitely Extensible Nonlinear Elastic constitutive model
FENE-CR	FENE model with Chilcott-Rallison closure
FENE-P	FENE model with Peterlin closure
GNF	Generalized Newtonian Fluid
HRS	High Resolution Scheme
HWNP	High Weissenberg Number Problem
LCR	Log-Conformation Representation
LUDS	Linear Upwind Differencing Scheme
NC	Number of Cells
NVD	Normalized Variable Diagram
NVSF	Normalized Variable and Space Formulation

ODE	Ordinary Differential Equation
OSCER	Optimized Shape Cross-slot Extensional Rheometer
PTT	Phan-Thien–Tanner constitutive model
PDMS	Poly(dimethylsiloxane)
PSD	Power Spectral Density
QUICK	Quadratic Upstream Interpolation for Convective Kinematics
RCC	Radius of Curvature of Corners
SIMPLE	Semi-Implicit Method for Pressure Linked Equations algorithm
SIMPLEC	SIMPLE-Consistent algorithm
sPTT	simplified Phan-Thien–Tanner constitutive model
SUPG	Streamline Upwind Petrov-Galerkin finite element method
TV	Total Variation
TVD	Total Variation Diminishing
UCM	Upper-Convected Maxwell constitutive model
UDS	Upwind Differencing Scheme
WENO	Weighted Essentially Non-Oscillatory scheme

Table of Contents

1 Thesis Outline

The present thesis is an account of several systematic computational investigations on the dynamics of purely or nearly purely elastic instabilities in cross-slot flows, with a progressively greater degree of complexity. Context is provided by four opening chapters, including this outline.

Chap. 2: Introduction offers a conceptual overview of relevant topics within Rheology, followed by a focused discussion on differential constitutive equations. Chap. 3: Literature Review is subdivided into three major sections. Sections 3.1: Computational Fluid Dynamics (CFD) and 3.2: Computational Rheology discuss the two most important hurdles to the successful simulation of viscoelastic flows, respectively the numerical treatment of advective terms and the High-Weissenberg Number Problem, and conclude with an exposition of the two key methods used throughout this thesis, again respectively the Convergent and Universally Bounded Interpolation Scheme for the Treatment of Advection (CUBISTA) and the Log-Conformation Representation (LCR). The revision of methodology is then followed by a revision of phenomenology, given in section 3.3: Purely Elastic Instabilities, covering aspects of dynamical systems theory, stationary instabilities, time-dependent instabilities and elastic turbulence. Whenever possible, the survey of literature is centered on cross-slot flows. Chap. 4: Finite Volume Method provides a detailed description of the numerical method used in the subsequent chapters.

The thesis then enters a section dedicated to the presentation and discussion of numerical results. Chap. 5: The Planar Cross-Slot as a Benchmark Problem, offers an analysis of stationary asymmetries in two-dimensional (2D) creeping cross-slot flows. The chapter is constructed as a benchmark proposal, with an exhaustive compilation of parameters that may be of assistance to other researchers, with the purpose of incentivizing the use of the cross-slot geometry. Chap. 6: Stationary Instabilities in Cross-Slots with Different Aspect Ratio, reframes the discussion concerning purely elastic stationary instabilities via an analysis of three-dimensional (3D) cross-slots, i.e. with finite depth, for a very wide range of aspect ratios, defined as the ratio of depth-to-width. The aspect ratio is found to be the controlling parameter that determines if a stationary asymmetry forms as the flow rate increases, for depth>width, or if the flow transitions

directly to a time-dependent state, for depth<width. Additionally, the reduction in energy dissipation that had previously been suggested as a physical justification for the formation of asymmetries is reevaluated. In 3D cross-slots, stationary asymmetries are accompanied by the emergence of peripheral stagnation points, located along the central vertical axis, above and below the main stagnation point at the center of the geometry. The peripheral stagnation points redirect matter towards the center, implying, by mass conservation, a reduction in the intake of matter along the inlet axis therein. Visually, the streamlines of the inlet flow appear to bend around the central stagnation point, an observation that is consistent with a type of buckling instability. One final observation concerns the destabilizing effect of the corners around the slot, which motivated a change in geometry for the following chapter. Chap. 7: Time-Dependent Instabilities in an Optimized Cross-Slot Device, documents the investigation of nearly purely elastic instabilities in the Optimized Shape Cross-slot Extensional Rheometer, or OSCER device. This is a variant of the standard planar cross-slot numerically optimized to produce a homogeneous extensional field along a wide region in the central slot. The corners of the deformed geometry are greatly receded from their ordinary position, forming pockets that allow for the recirculation of fluid. This optimized cross-slot facilitates the investigation of instabilities of a purely extensional nature. The resulting time-dependent flow patterns clearly demonstrate the superposition of asymmetries with periodic flow, in a non-trivial manner. Five distinct regimes of instability are identified in this chapter, each of them delimited by the elasticity of the fluid, and the corresponding description is complemented primarily via the examination of power spectra of the velocity fluctuations. A correlation emerges between the integrity of the birefringence strand, i.e. the band of highly stretched polymer molecules along the outlet axis of a cross-slot, and the stability of the flow. Simulations in which the strand is broken, either periodically or aperiodically, invariably show a faster spectral decay than expected for elastic turbulence, measured as the slope of the aforementioned power spectra. Chap. 8: Time-Dependent Instabilities in a Standard Planar Cross-Slot offers a preliminary investigation on the emergence of elastic turbulence in a planar cross-slot. The transition to turbulence is demonstrated primarily via the analysis of the spectral decay of velocity fluctuations and also through the observation of the ejection of excessive elastic stresses concentrated in the boundary layers along the walls of the outlet channels.

Following the self-explanatory Chap. 9: Conclusions and Future Work, an appendix is included describing the implementation and validation of a fifth order accurate method for the numerical treatment of advective terms in the governing equations, a Weighted Essentially Non-Oscillatory (WENO) scheme. By itself, this scheme does not improve the overall performance of the in-house viscoelastic flow solver, and hence was not used in the main body of the thesis.

2 Introduction

2.1 Fluid Mechanics

Fluid mechanics is the domain of science concerned with the motion of liquids and gases and associated phenomena, such as aerodynamics and hydrodynamics, ocean circulation and climate science, lubrication and heat exchange, to name just a few. The field is transversal to most other disciplines within the natural sciences and ubiquitous in engineering applications. On a fundamental level, the motion of fluids is the result of the transfer of momentum to and between molecules. The typical length scale of flows is much larger than the size of molecules, and thus fluids are described as a continuous medium, the so-called continuum hypothesis. The resistance of fluids to deformation is termed viscosity. In gases, viscosity is primarily a result of molecular diffusion [1], and is often considered negligible. This approximation, termed inviscid flow, was first formalized by Euler, along with the systematization of many of the conventions in fluid mechanics [2-4], including the consolidation of the continuum hypothesis. In liquids, viscosity is several orders of magnitude larger and is attributed to the friction between relatively cramped molecules as they rearrange when a pressure gradient or shearing stress is applied to the liquid. This internal friction tends to be larger amongst larger molecules, hence oils tend to be significantly more viscous than water. However, viscosity is also affected by other molecular interactions. For example, the viscosity of water is higher than that of acetone, despite the larger molecular size of the latter. For many fluids, the rate of deformation is linearly proportional to the applied shear stress, as originally hypothesized by Newton in section IX of the second book of his *Principia* [5]. The proportionality constant later came to be known as viscosity, or more specifically, shear viscosity, and fluids that behave according to Newton's assertion are known as Newtonian fluids.

Fluid mechanics is concerned with the motion of fluids. Wind moves from hot, high pressure areas of the atmosphere to colder depressions, equalizing temperature differences. This type of flow is termed pressure driven, and in man-made setups is

usually accomplished using pumps. Flow may also be shear driven, for example, by dragging the movable wall of a container holding fluid. Shear driven flow is made possible by the adhesion of fluids to solid surfaces, a phenomenon which has come to be known as the no-slip boundary condition. In a review of contemporary literature, Stokes [6] summarized the evidence for the then controversial assertion. In particular, he mentions an experiment performed by Coulomb, in which a metallic disk suspended by an axis normal to its plane was made to slowly oscillate in water. Even when lubricated with grease, or if the grease was covered in powdered sandstone, the resistance to the motion of the disk was not altered. Stokes concluded that the water close to the disk is carried along with it, and more specifically, that, "in consequence of capillary attraction", a thin film of fluid adheres to the surface of the disk, such that any friction between the disk and the surrounding fluid in reality occurs between the thin film and the bulk of the fluid, and therefore is only affected by viscosity.

2.2 Rheology

Water is the principal example of a Newtonian liquid. Many other liquids exist in a gradient somewhere between the ideal behaviors of an elastic solid and a viscous fluid. Rheology is the domain of knowledge dedicated to the study of flow and deformation, and by convention rheologists primarily study industrially relevant materials that have both elastic and viscous properties [7]. The foundations of Rheology therefore lie in the behavior of idealized materials. Beginning in classical antiquity with the subject of Euclidean geometry, at first the study of mechanics was primarily concerned with rigid solids. Hooke extended the scope of the field to include elastic solids with his linear spring law [8], and Pascal is credited with the initial conceptualization of an inviscid fluid [9], although, as mentioned earlier, this would later be formalized by Euler, with preceding contributions by Huygens and Bernoulli [10]. Newton's law of viscosity was incorporated in the general theory of fluid motion by the work of Navier and Stokes [11]. The first investigation concerning viscoelastic materials is attributed to Weber [12] for his work on the extensional properties of silk threads, which led to the concepts of stress relaxation and relaxation time. Maxwell [13] proposed the first model of linear viscoelasticity, applicable for small deformations, which would later be generalized for large deformations by Oldroyd [14] and is since known as the upper-convected Maxwell

model. Rheology would remain in an embryonic state until the advent of the plastics industry. The increased interest in the deformation of polymeric materials led to the founding of The (North-American) Society of Rheology on April 29, 1929 [7].

2.3 Flow Classification

Flows are frequently classified as one of two main types, shear or extensional, although in practical settings there is often some degree of overlap between the two. Prototypical examples of the two types of flow are shown in Figure 2.1. In a shear flow, adjacent layers of fluid move past each other along the direction of shearing, whereas in an extensional flow, fluid particles move away from each other along the direction of extension and towards each other in the normal direction.

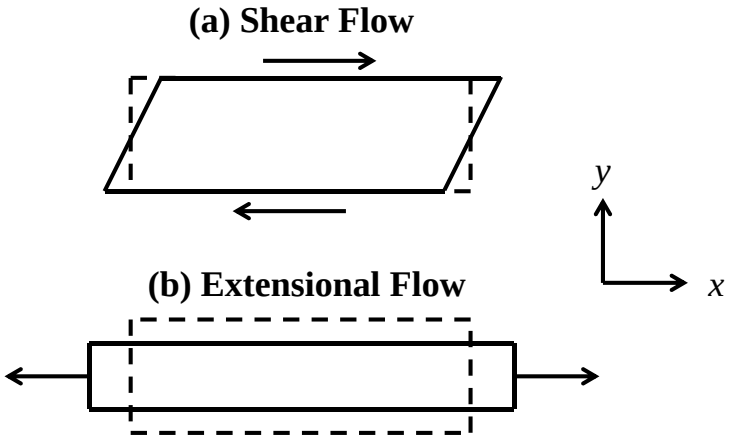

Figure 2.1 – Primary types of flow in Rheology. Dashed lines indicate the initial state, and continuous lines the deformed state.

The classical example of shear flow, Couette flow, occurs when fluid trapped between two parallel, horizontal plates, separated by a distance H, is dragged by the unidirectional motion of the upper plate, with velocity U. With the bottom plate remaining motionless, a linear velocity profile develops along the $y-$direction, normal to the plates,

$$u_x(y) = \frac{y}{H}U, \tag{2.1}$$

where $u_x(y)$ is the velocity profile. Therefore, the rate at which the fluid deforms is constant,

$$\dot{\gamma} = \frac{\mathrm{d}u_x}{\mathrm{d}y} = \frac{U}{H}, \tag{2.2}$$

where $\dot{\gamma}$ is the shear rate. Conversely, the fluid will offer some resistance to the motion imposed by the upper plate. For a Newtonian fluid, this resistance is proportional to the shear rate,

$$\sigma = \mu\dot{\gamma}, \tag{2.3}$$

where σ is the shear stress and the proportionality constant μ is the shear viscosity, with SI units Pa.s. More generally, the shear viscosity is denoted as η, although this nomenclature is usually reserved for non-Newtonian fluids, i.e. fluids with variable shear viscosity.

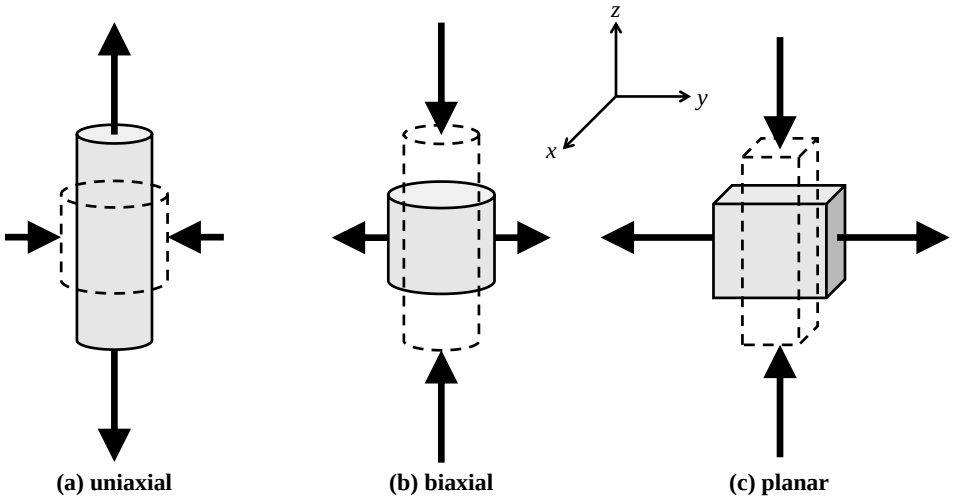

Figure 2.2 – Classification of extensional flows. Dashed lines indicate the initial state, and continuous lines the deformed state.

For extensional flows, it is customary to subdivide their classification into three categories, depicted in Figure 2.2: uniaxial extension, when a sample experiences

extension along one direction and compression along two directions; biaxial extension, when a sample is extended along two directions and experiences compression along one direction; and planar extension, if the sample is stretched in one direction and compressed also along a single direction. Importantly, the sample does not have to be simultaneously extended and compressed by external forces. For example, a liquid rod will spontaneously thin if stretched, as dictated by mass conservation principles. For each of the idealized extensional flows depicted in Figure 2.2, the velocity field assumes the following form,

$$\text{uniaxial extension}: \left(u_x, u_y, u_z\right) = \left(-\frac{1}{2}\dot{\varepsilon}x, -\frac{1}{2}\dot{\varepsilon}y, \dot{\varepsilon}z\right), \tag{2.4}$$

$$\text{biaxial extension}: \left(u_x, u_y, u_z\right) = \left(\frac{1}{2}\dot{\varepsilon}x, \frac{1}{2}\dot{\varepsilon}y, -\dot{\varepsilon}z\right), \tag{2.5}$$

$$\text{planar extension}: \left(u_x, u_y, u_z\right) = \left(0, \dot{\varepsilon}y, -\dot{\varepsilon}z\right), \tag{2.6}$$

where $\left(u_x, u_y, u_z\right)$ are the components of the velocity field along Cartesian directions $\left(x, y, z\right)$ respectively, and $\dot{\varepsilon}$ is the extension rate, commonly also referred to as strain rate, although technically the terminology also applies to the shear rate $\dot{\gamma}$, and its use can engender confusion without contextualization. As in shear flow, the sample will resist deformation, and this resistance is expressed in a similar manner,

$$\sigma_E = \eta_E \dot{\varepsilon}, \tag{2.7}$$

where σ_E is the extensional normal stress and η_E is the extensional viscosity.

For Newtonian fluids, it is possible to deduce the ratio between extensional and shear viscosities. However, this ratio depends on the type of extensional flow, namely [15],

$$\mathrm{Tr} = \frac{\eta_{E,uniaxial}}{\mu} = 3, \tag{2.8}$$

$$\frac{\eta_{E,biaxial}}{\mu} = 6, \tag{2.9}$$

$$\frac{\eta_{E,planar}}{\mu} = 4. \tag{2.10}$$

The symbols η_B and η_P may also be used to represent biaxial and planar extensional viscosity, respectively. The ratio of viscosities for the specific case of uniaxial extension is also termed Trouton ratio, Tr, named after Frederick T. Trouton, who first deduced the ratio between the "coefficient of viscous traction", which is now termed (uniaxial) extensional viscosity, and shear viscosity [16]. Informally, Tr may also denote the ratio of viscosities for biaxial and planar extension.

2.4 Generalized Newtonian Fluids

A Newtonian fluid is an inelastic fluid with constant shear viscosity, usually denoted as μ. More generally, the shear viscosity may depend on the shear rate,

$$\sigma = \eta(\dot{\gamma})\dot{\gamma}, \tag{2.11}$$

where η denotes the (non-Newtonian) shear viscosity. The classification of these fluids depends on whether the shear viscosity tends to increase or decrease with shear rate. Shear-thinning or pseudoplastic fluids have lower viscosity at higher shear rates. A salad dressing containing a small amount of xanthan gum will thin when it is squeezed through a bottleneck, as the polymer molecules align with the direction of flow, only to thicken almost immediately as it sets on the salad [17]. The polymer chains of xanthan gum are rigid and, in low concentrations, primarily interact with each other via hydrogen bonds [18], forming a network that is easily disturbed by external forcing and that quickly

recovers coherence once the forcing is removed. Shear-thickening or dilatant fluids have higher viscosities at higher shear rates. A well-known example of dilatancy are cornstarch suspensions in water, commonly used in popular science demonstrations. Most shear-thickening fluids are concentrated suspensions and the phenomenon is generally attributed to shear induced flocculation (see Chap. 15.9 in Ref. [19]), although the mechanistic details are still the subject of debate. For instance, in Ref. [20] cornstarch suspensions are shown to possess a small yield stress, followed by shear-banding induced liquefaction at low shear rates. Shear-thickening only occurs when the whole material flows.

A variety of empirical models have been developed for $\eta(\dot{\gamma})$, mostly intended to model shear-thinning behavior, which is a far more common property than dilatancy. The curve depicted in Figure 2.3 was created using the Cross model [21],

$$\frac{\eta(\dot{\gamma})-\eta_\infty}{\eta_0-\eta_\infty}=\frac{1}{1+\alpha\dot{\gamma}^n}, \tag{2.12}$$

where η_0 is the zero-shear-rate viscosity, η_∞ is the viscosity for very high shear rates, α is a constant with SI units s^n and n indicates the degree of thinning, with $n=0$ for Newtonian fluids and $0<n<1$ for shear-thinning fluids.

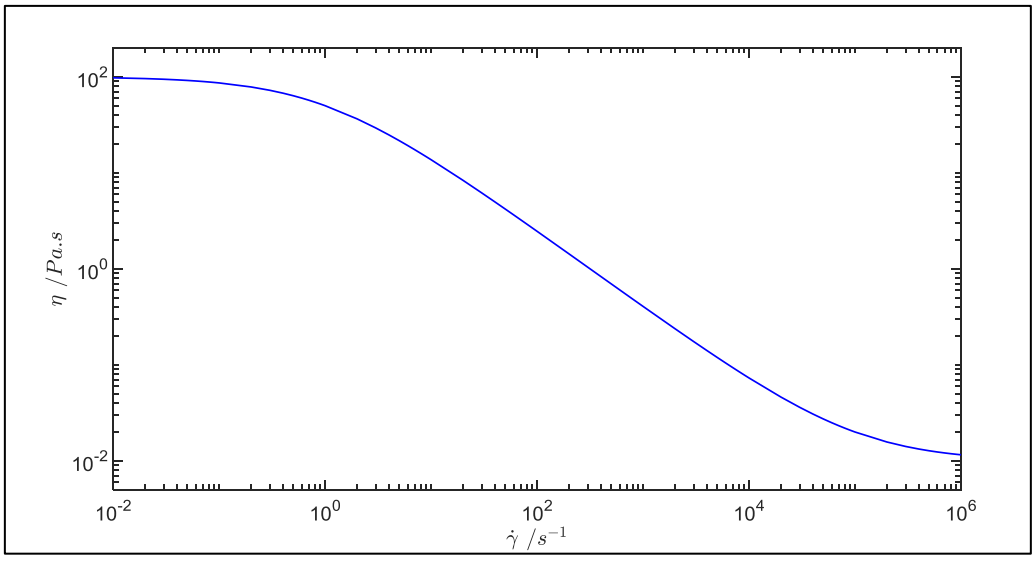

Figure 2.3 – Example of viscosity as a function of shear rate for a shear-thinning fluid, constructed with the Cross model, with: $\eta_0=100$ Pa.s, $\eta_\infty=0.01$ Pa.s, $\alpha=1$ s^{-1}, $n=0.8$.

The Cross model is arguably the simplest empirical model capable of fitting the entirety of a shear-thinning viscosity curve. Various other empirical models have been developed. One example is the power-law or Ostwald-de Waele model [22],[23],

$$\eta(\dot{\gamma}) = k\dot{\gamma}^{n-1}, \tag{2.13}$$

where k is the flow consistency index with SI units $\mathrm{Pa.s}^n$ and n is the dimensionless flow behavior index, with $n=1$ for Newtonian fluids and $0<n<1$ for various degrees of shear-thinning behavior. This model is only useful in situations where the shear rate is high and $\eta \gg \eta_\infty$, such that η_∞ is negligible. If the value of η_∞ is of practical importance, the Sisko model [24] is a suitable improvement,

$$\eta(\dot{\gamma}) = k\dot{\gamma}^{n-1} + \eta_\infty. \tag{2.14}$$

The power-law, Sisko and Cross models where developed in chronological order, and would be followed by further improvements, such as the Carreau model [25] and its generalization, the Carreau-Yasuda model [26],

$$\frac{\eta(\dot{\gamma}) - \eta_\infty}{\eta_0 - \eta_\infty} = \frac{1}{\left[1+(\Lambda\dot{\gamma})^a\right]^{-(n-1)/a}}, \tag{2.15}$$

where Λ determines the shear rate at the onset of thinning, $(n-1)$ is a power-law slope and a adjusts the smoothness of the transition between the low shear rate regime where viscosity remains at approximately η_0 and the power-law regime. One might be tempted to assume that, by simply changing the sign of the exponent n, the aforementioned models would suitably describe the behavior of a shear-thickening fluid. In reality, shear-thickening is a much more complex process, and often thickening fluids exhibit thinning

behavior at very low or very high shear rates [27], therefore requiring a piecewise approximation for $\eta(\dot{\gamma})$.

2.5 Structured Liquids

Broadly speaking, fluids with at least some solid-like properties generally possess an internal structure, be it in the form of a polymer network or colloidal suspension. In addition to viscoelasticity, which is the primary subject of this thesis, two other phenomena common in so-called structured liquids are briefly mentioned.

Some fluids only flow above a certain threshold in applied shear stress, such as for example butter or paint. These fluids are commonly designated as viscoplastic fluids [28] and their main characteristic is a finite yield stress. Most yield stress fluids can be accurately modelled using the Herschel-Bulkley equation [29],

$$\sigma = \sigma_0 + k\dot{\gamma}^n, \tag{2.16}$$

where σ is the shear stress, σ_0 is the yield stress and k and n are analogous to the same variables in the power-law model of shear-thinning behavior. Also commonly used is the Bingham equation [30], which can be thought of as a simplified version of the Herschel-Bulkley model with $n=1$. Historically, the existence of a finite yield stress has been called into question with the advent of precision controlled-stress rheometers [31]. Early measurements appeared to indicate the existence of a high, yet finite viscosity prior to yielding. However, further improvements in instrumentation suggest that the pre-yielding flow is complicated by unsteady, secondary flows [32].

Another phenomenon associated with structured liquids is thixotropy. Upon the application of a constant shear stress, the viscosity of these fluids gradually decreases over time. If the stress is removed, the fluid will recover its original properties, commonly over a period of several hours. Yogurt is a thixotropic fluid [33] as are many other colloidal suspensions [34]. The properties of these fluids arise as a result of a network formed by the suspended phase, mediated by noncovalent interactions. When disturbed

by an external forcing the structure disintegrates, causing the material to liquefy, only to slowly return to an ordered state if allowed to rest. The main difference between thixotropy and pseudoplasticity is the amount of time required for restructuring, which is almost none for the latter type of fluid.

2.6 Linear Viscoelasticity

The notion of a structured liquid is useful in understanding linear viscoelasticity. A hydrogel, such as for example an ionically cross-linked alginate solution [35], is simultaneously elastic and viscous. For low amplitude strains and low frequency strain rates, the two components of the hydrogel response may be modelled separately,

$$\text{elasticity}\left(\text{spring}\right): \sigma = G\gamma\,, \tag{2.17}$$

$$\text{viscosity}\left(\text{dashpot}\right): \sigma = \eta\dot{\gamma}\,, \tag{2.18}$$

where G is the elastic modulus and γ is the strain. Here, dashpot refers to a piston moving through a very viscous Newtonian fluid. These two fundamental elements can then be used in the construction of mechanical analogues. Two basic configurations are shown in Figure 2.4, namely the Maxwell model composed of a spring and dashpot in series and the Kelvin-Voigt model with the same elements in a parallel arrangement (see Chap. 13 in Ref. [19]).

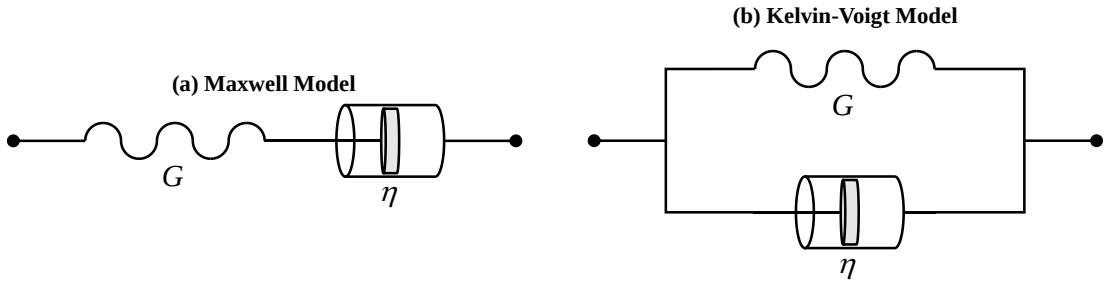

Figure 2.4 – Mechanical analogues of linear viscoelasticity models. The elastic modulus G denotes a spring and the viscosity η denotes a dashpot.

For the Maxwell model, the total strain γ is the sum of the individual spring and dashpot strains, $\gamma = \gamma_{spring} + \gamma_{dashpot}$, therefore $\dot{\gamma} = \dot{\gamma}_{spring} + \dot{\gamma}_{dashpot}$, where $\dot{\gamma} = \mathrm{d}\gamma/\mathrm{d}t$, and thus,

$$\sigma + \lambda\dot{\sigma} = \eta\dot{\gamma}, \tag{2.19}$$

where $\dot{\sigma} = \mathrm{d}\sigma/\mathrm{d}t$ and $\lambda = \eta/G$ is the relaxation time. Alternatively, for the Kelvin-Voigt model, the total stress σ is the sum of the individual spring and dashpot stresses, and consequently,

$$\frac{1}{G}\sigma = \gamma + \lambda\dot{\gamma}, \qquad \text{or} \qquad \sigma = G\gamma + \eta\dot{\gamma}\,. \tag{2.20}$$

The different element configurations result in different theoretical responses. For instance, in a creep test, in which a sample at rest is subjected to a constant stress σ_{probe} and the resulting strain is monitored, a Maxwell material would initially comply with an elastic response, $\gamma_{spring} = \sigma_{probe}/G$, followed by further viscous deformation, $\gamma_{dashpot} = \left(\sigma_{probe}/\eta\right)t$. Therefore a Maxwell material behaves as an elastic solid on small time scales and as a viscous liquid on large time scales. On the other hand, a Kelvin-Voigt material would initially comply with a viscous response, $\gamma = \left(\sigma_{probe}/\eta\right)t$, and eventually reach an asymptotic deformation limit, $\gamma = \sigma_{probe}/G$, or in other words, a Kelvin-Voigt material behaves as a liquid for $t \ll \lambda$ and as a solid for $t \gg \lambda$.

Using springs and dashpots, various mechanical analogues of arbitrary complexity can be constructed to fit the properties of a sample. For example, the standard linear solid or Zener model [36] is comprised of a Maxwell element in a parallel configuration with a second spring, the Jeffreys model [37] is also composed of a Maxwell element in a parallel arrangement with a second dashpot, or the Burgers model [38] which is derived by assembling a Maxwell element and a Kelvin-Voigt element in a serial configuration. The number of elements in a given mechanical analogue may be extended indefinitely in

order to account for e.g. the distribution of polymeric molecular weights in a hydrogel, which in turn is responsible for a distribution of relaxation times, as proposed by Wiechert [39].

Creep tests, especially those of a compressive/extensional nature, are often used to measure the properties of predominantly solid samples, such as steel beams or rigid polymer rods. For samples with a more liquid character, oscillatory assays are commonly used (see Chap. 13 in Ref. [19]). These can be performed in e.g. a plate-and-plate shear rheometer by having the upper plate alternate smoothly between clockwise and counterclockwise rotation. This applied sinusoidal shear strain, $\gamma(t)=\gamma_0\sin(wt)$, where $w=2\pi f$ is the angular frequency, generates a sinusoidal shear stress response, $\sigma(t)=\sigma_0\sin(wt+\delta)$, where δ is a phase lag. Given that for a spring the stress is proportional to the strain, thus $\sigma_{spring}\propto\sin(wt)$, and that for a dashpot the stress is proportional to the strain rate, therefore $\sigma_{dashpot}\propto\cos(wt)$, the output of the assay can be decomposed in two components, one in phase with $\gamma(t)$ and another which is out of phase by $\pi/2$. Rearranging $\gamma(t)$ and $\sigma(t)$,

$$\frac{\sigma(t)}{\gamma_0}=G'(w)\sin(wt)+G''(w)\cos(wt), \tag{2.21}$$

$$G'(w)=\frac{\sigma_0}{\gamma_0}\cos(\delta), \tag{2.22}$$

$$G''(w)=\frac{\sigma_0}{\gamma_0}\sin(\delta), \tag{2.23}$$

where $G'(w)$ is the storage modulus, representative of elastic restoration and $G''(w)$ is the loss modulus, which indicates viscous dissipation. The oscillatory response of a Maxwell material is shown in Figure 2.5. In creep testing, this type of material is primarily elastic for $t\ll\lambda$ and viscous for $t\gg\lambda$. Conversely, as one would expect, $G''(w)>>G'(w)$ at low frequencies and the opposite is true for high frequencies.

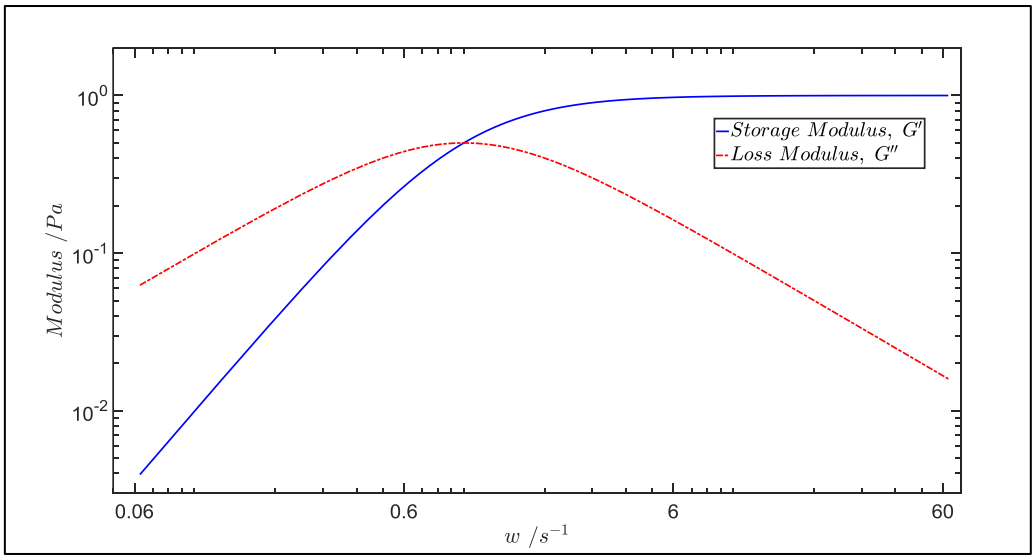

Figure 2.5 – Behavior of a Maxwell material in an oscillatory test, with $G = 1$ Pa, $\eta = 1$ Pa.s. $w = 2\pi f$ is the angular frequency.

2.7 Nonlinear Viscoelasticity

For certain liquids, especially polymer solutions or melts, the application of high amplitude strains or high frequency strain rates generates a set of emergent phenomena that cannot be readily explained by linear viscoelasticity models. Some of the more iconic examples are: (1) the Weissenberg or rod-climbing effect, when a viscoelastic fluid climbs along the surface of a partially immersed, rotating vertical rod; (2) the tubeless syphon or Fano flow, when the syphoning motion of a fluid is maintained in the absence of a bounding tube; (3) extrudate swell, often accompanied by extrudate instabilities, when a viscoelastic fluid is pushed through the outlet of a container, causing the stream to swell upon exiting the orifice. These and other viscoelastic flows are documented in the photographic album compiled by Boger and Walters [40]. Critical to the analysis of these phenomena is the notion of material functions. One of these functions, the shear viscosity $\eta(\dot{\gamma})$, has already been discussed. Two other functions are now introduced, the normal stress coefficients,

$$\Psi_1(\dot{\gamma}) = \frac{N_1}{\dot{\gamma}^2} = \frac{\sigma_{xx} - \sigma_{yy}}{\dot{\gamma}^2}, \tag{2.24}$$

$$\Psi_2(\dot{\gamma}) = \frac{N_2}{\dot{\gamma}^2} = \frac{\sigma_{yy} - \sigma_{zz}}{\dot{\gamma}^2}, \tag{2.25}$$

where $\Psi_1(\dot{\gamma})$ and $\Psi_2(\dot{\gamma})$ are respectively the first and second normal stress coefficients, N_1 and N_2 are respectively the first and second normal stress differences, and σ_{xx}, σ_{yy} and σ_{zz} are the normal stress components of the stress tensor $\boldsymbol{\sigma}$. By convention, the x-axis is normally chosen as the main direction of flow. Together with $\eta(\dot{\gamma})$, the normal stress coefficients completely characterize steady state, simple shear flows, and in much the same manner as viscosity, for polymer solutions or melts $\Psi_1(\dot{\gamma})$ and $\Psi_2(\dot{\gamma})$ are frequently shear-thinning.

Viscoelastic fluids assayed in a shear rheometer will typically exert some measurable normal force on the upper and lower plates (or upper cone), attempting to push them apart, as a result of the hoop stress that develops during the radial shearing of viscoelastic liquids. This same hoop stress also explains the rod-climbing effect, and is in both cases an azimuthal stress, that is, normal to both the axial and radial directions. Crucially, the hoop stress pulls the fluid inwards, and as a result of mass conservation, an incompressible viscoelastic fluid under radial shearing tends to contract in the radial direction and expand in the axial direction. Although driven by different mechanisms, this type of deformation is similar to that experienced by a sample in uniaxial extension: axial extension and radial compression. Intuitively, the hoop stress and associated phenomena demonstrate how, for non-linear viscoelastic flows, elasticity and viscosity effects can no longer be modelled independently.

2.7.1 Conservation Equations

Before proceeding with a discussion on the constitutive modelling of nonlinear viscoelasticity, it is convenient to review the conservation laws relevant for isothermal

flows, which are presented here in differential form [41]. The conservation of mass is prescribed by the continuity equation. For an incompressible flow,

$$\nabla \cdot \mathbf{u} = 0, \tag{2.26}$$

where $\mathbf{u}$ is the velocity field. This formulation is a simplification of the general case, $\partial\rho/\partial t + \nabla \cdot (\rho \mathbf{u}) = 0$, since incompressibility implies a constant volumetric mass density ρ. The conservation of linear momentum is prescribed by the Cauchy equations. Again, for an incompressible flow,

$$\rho\left(\frac{\partial \mathbf{u}}{\partial t} + \mathbf{u} \cdot \nabla \mathbf{u}\right) = -\nabla p + \nabla \cdot \boldsymbol{\sigma}, \tag{2.27}$$

where p is the pressure and $\boldsymbol{\sigma}$ is the extra stress tensor. When $\boldsymbol{\sigma}$ is specified through a constitutive relation, eqs. 2.27 lead to the Navier-Stokes equations.

Between the two conservation equations, a total of ten variables are related. Therefore, an additional six equations are required in order to solve the system, either by analytical or computational means. To this end, the purpose of constitutive modelling is the formulation of the extra stress tensor $\boldsymbol{\sigma}$.

2.7.2 Differential Constitutive Models

Broadly speaking, a constitutive equation is an expression relating two physical quantities, typically of a kinetic nature, that models the response of a material to an external stimulus. Within the context of Rheology, constitutive equations relate stress and strain-rate, and for the purposes of this thesis, differential constitutive models are the primary focus of attention. When modelling a polymer solution, it is common practice to segregate the properties of the solvent from those of the dissolved polymer. The overall form of this class of models is then,

$$\boldsymbol{\sigma} = \eta_s\left(\dot{\gamma}\right)\dot{\boldsymbol{\gamma}} + \boldsymbol{\tau}, \tag{2.28}$$

where $\dot{\boldsymbol{\gamma}}$ is the rate-of-strain tensor, $\boldsymbol{\tau}$ is the polymeric extra stress tensor, which is reserved for the stresses attributable to the polymeric component of the solution, and $\eta_s\left(\dot{\gamma}\right)$ is the solvent shear viscosity, which is often Newtonian. The scalar strain rate $\dot{\gamma} = \sqrt{\frac{1}{2}\left(\dot{\boldsymbol{\gamma}} : \dot{\boldsymbol{\gamma}}^{\dagger}\right)}$ is defined as the magnitude of the strain rate tensor $\dot{\boldsymbol{\gamma}} = \nabla\mathbf{u} + \left(\nabla\mathbf{u}\right)^{\dagger}$ [41]. Since $\dot{\boldsymbol{\gamma}}$ is symmetric, the scalar product $\dot{\boldsymbol{\gamma}} : \dot{\boldsymbol{\gamma}}^{\dagger}$ is equal to the second invariant of the rate-of-strain tensor, $II\left(\dot{\boldsymbol{\gamma}}\right) = \mathrm{tr}\left(\dot{\boldsymbol{\gamma}}^2\right)$, and the definition of the scalar strain rate $\dot{\gamma}$ is often given using this invariant.

One approach employed in the derivation of constitutive equations for the polymeric extra stress $\boldsymbol{\tau}$ is to rewrite linear viscoelasticity models in a convected frame of reference, as originally envisioned by Hencky [42]. This is accomplished by substituting the first time derivative of the variables related in the constitutive equation, namely stress and, when applicable, strain-rate, by the upper-convected time derivative proposed by Oldroyd [14],

$$\overset{\nabla}{\mathbf{T}} = \frac{\mathrm{D}\mathbf{T}}{\mathrm{D}t} - \mathbf{T}\cdot\nabla\mathbf{u} - \left(\nabla\mathbf{u}\right)^{\dagger}\cdot\mathbf{T}, \tag{2.29}$$

where $\mathbf{T}$ is a generic tensor, and the operator $\mathrm{D}/\mathrm{D}t$ is the material derivative,

$$\frac{\mathrm{D}\mathbf{T}}{\mathrm{D}t} = \frac{\partial\mathbf{T}}{\partial t} + \nabla\cdot\mathbf{u}\mathbf{T}, \tag{2.30}$$

Since $\nabla\cdot\mathbf{u}\mathbf{T}=\mathbf{u}\cdot\nabla\mathbf{T}+\left(\nabla\cdot\mathbf{u}\right)\mathbf{T}$, sources concerned only with incompressible flows often write the material derivative in the simplified form, $\mathrm{D}\mathbf{T}/\mathrm{D}t = \partial\mathbf{T}/\partial t + \mathbf{u}\cdot\nabla\mathbf{T}$. Rewriting the Maxwell model in tensor notation and substituting the time derivative of the stress $\dot{\sigma}$

by the upper-convected time derivative of the polymeric extra stress tensor $\overset{\nabla}{\boldsymbol{\tau}}$ results in the upper-convected Maxwell (UCM) model [14],

$$\text{UCM}: \begin{cases} \boldsymbol{\sigma} = \boldsymbol{\tau} \\ \boldsymbol{\tau} + \lambda\left(\dfrac{\partial \boldsymbol{\tau}}{\partial t} + \nabla \cdot \mathbf{u}\boldsymbol{\tau}\right) = \eta\left(\nabla\mathbf{u} + \left(\nabla\mathbf{u}\right)^{\dagger}\right) + \lambda\left(\boldsymbol{\tau}\cdot\nabla\mathbf{u} + \left(\nabla\mathbf{u}\right)^{\dagger}\cdot\boldsymbol{\tau}\right) \end{cases}, \tag{2.31}$$

where η is the (constant) shear viscosity, derived from the viscosity of the dashpot analogue in the linear version of the model. Importantly, since the mechanical analogue contains only one dashpot, the UCM model implicitly assumes that the solvent has negligible viscosity, or more accurately, that only the largest shear viscosity is relevant, which typically is derived from a polymer solute. This issue may be circumvented by converting a different linear model, namely the Jeffreys model [37], which, as mentioned earlier, is composed of a Maxwell element in a parallel arrangement with a second dashpot,

$$\sigma + \lambda\dot{\sigma} = \eta_0\left(\dot{\gamma} + \lambda\beta\ddot{\gamma}\right), \tag{2.32}$$

where $\ddot{\gamma} = \mathrm{d}\dot{\gamma}/\mathrm{d}t$, $\eta_0 = \eta_s + \eta_p$ is the sum of the viscosities of both analogue dashpots, or alternatively the sum of the solvent and polymer contributions, respectively, to the shear viscosity, $\beta = \eta_s/\eta_0$ is the solvent viscosity ratio, and the product $\lambda\beta = \lambda_r$ is the retardation time (λ_r or sometimes λ_2 is the preferred notation for sources dealing primarily with linear viscoelasticity). Since the total stress for a mechanical analogue with parallel elements is the sum of stresses in each branch, the Jeffreys model can alternatively be written as,

$$\begin{cases} \text{Total stress}: \sigma = \sigma_s + \sigma_p \\ \text{Parallel dashpot}: \sigma_s = \eta_s \dot{\gamma} \\ \text{Maxwell element}: \sigma_p + \lambda \dot{\sigma}_p = \eta_p \dot{\gamma} \end{cases}, \tag{2.33}$$

which, for the purposes of this text, is a more suitable form for conversion into a nonlinear model. Substituting $\dot{\sigma}_p$ by $\overset{\nabla}{\boldsymbol{\tau}}$ and rewriting the equations in tensor notation results in the Oldroyd-B model [14], also known as the upper-convected Jeffreys model,

$$\text{Oldroyd-B}: \begin{cases} \boldsymbol{\sigma} = \eta_s \dot{\boldsymbol{\gamma}} + \boldsymbol{\tau} \\ \boldsymbol{\tau} + \lambda \overset{\nabla}{\boldsymbol{\tau}} = \eta_p \dot{\boldsymbol{\gamma}} \end{cases}. \tag{2.34}$$

Another limitation of the UCM and Oldroyd-B models is the lack of shear-thinning, which is especially problematic considering that reasonably concentrated polymer solutions satisfy the condition of negligible solvent viscosity, not to mention polymer melts. One possible solution is the White-Metzner model [43],

$$\text{White-Metzner}: \begin{cases} \boldsymbol{\sigma} = \boldsymbol{\tau} \\ \boldsymbol{\tau} + \lambda\left(\dot{\gamma}\right) \overset{\nabla}{\boldsymbol{\tau}} = \eta\left(\dot{\gamma}\right) \dot{\boldsymbol{\gamma}} \end{cases}, \tag{2.35}$$

where $\lambda\left(\dot{\gamma}\right) = \eta\left(\dot{\gamma}\right)/G$. This empirical model incorporates the notion of shear rate dependent viscosity into the UCM framework. Consequently, the relaxation time is now also a function of $II\left(\dot{\boldsymbol{\gamma}}\right)$. The zero-shear-rate relaxation time is referred to as λ_0 and the effective relaxation time for a given set of flow conditions is commonly represented as λ_{eff}. The inclusion of tensor invariants can be used in different ways. For instance, the Phan-Thien–Tanner (PTT) model [44],[45],[46], which was derived from a Lodge-

Yamamoto network theory of polymeric liquids (see Chap. 20 in Ref. [47]), incorporates the first invariant of the polymeric extra stress tensor, $I(\boldsymbol{\tau}) = \mathrm{tr}(\boldsymbol{\tau})$,

$$\text{PTT}: \quad \begin{cases} \boldsymbol{\sigma} = \eta_s \dot{\boldsymbol{\gamma}} + \boldsymbol{\tau} \\ \mathrm{Y}\left(I(\boldsymbol{\tau})\right)\boldsymbol{\tau} + \lambda \overset{\triangledown}{\boldsymbol{\tau}} + \frac{1}{2}\xi\lambda\left(\dot{\boldsymbol{\gamma}}\cdot\boldsymbol{\tau} + \boldsymbol{\tau}\cdot\dot{\boldsymbol{\gamma}}\right) = \eta_p \dot{\boldsymbol{\gamma}} \end{cases}. \tag{2.36}$$

The slip constant ξ defines the slip tensor $\frac{1}{2}\xi\dot{\boldsymbol{\gamma}}$, and indicates to what extent junctions in the polymer network are advected by the embedded fluid: for $\xi = 0$, the junctions are transported by the velocity field $\mathbf{u}$ as though they were isolated particles; for $0 < \xi < 2$, the junctions offer progressively more resistance to advection; and for $\xi = 2$, the junctions are stationary. For clarity, in polymer solutions or melts, these junctions correspond to entanglements between polymer chains, whereas in macromolecular solids, junctions are chemical crosslinks between adjacent, large molecules. Thus, assigning $\xi = 0$ implies a polymeric solution that is essentially free of entanglements, and can therefore be thought of as dilute. This variant of the model is termed simplified PTT, or sPTT, and is the preferred formulation in this thesis. Concerning the incorporation of $I(\boldsymbol{\tau})$ in the model,

$$\mathrm{Y}\left(\mathrm{tr}(\boldsymbol{\tau})\right) = \exp\left(\frac{\lambda\varepsilon}{\eta_p}\mathrm{tr}(\boldsymbol{\tau})\right) \approx 1 + \frac{\lambda\varepsilon}{\eta_p}\mathrm{tr}(\boldsymbol{\tau}), \tag{2.37}$$

where ε is a parameter inversely proportional to the maximum extensional viscosity. The two forms given for $\mathrm{Y}\left(\mathrm{tr}(\boldsymbol{\tau})\right)$ correspond, respectively, to the exponential and linearized PTT models, and the linear form can be obtained by a truncated Taylor expansion of the exponential form about $\mathrm{tr}(\boldsymbol{\tau}) = 0$. Phan-Thien discusses the two formulations [45] and illustrates how the linear form produces a constant maximum plateau in extensional viscosity, for sufficiently high elongation rates, whereas the exponential form has a local

maximum η_E followed by a decrease for higher deformation rates. Since the PTT model is based on a balance between the creation and destruction of junctions in polymer networks, the exponential form is consistent with the experimental behavior of polymer melts, which above a certain extension rate, experience a net loss of entanglements. On the other hand, the extensional viscosity of a dilute polymer solution is expected to plateau for sufficiently vigorous extension, since, considering the near absence of junctions to begin with, the only source of normal stresses is the extension of individual molecular chains.

2.7.3 Critical Appraisal of Constitutive Models

The constitutive models reviewed so far have various attributes that render them, to a certain extent, unphysical or otherwise unsuitable for the simulation of real fluids. Three different concerns are addressed.

First, the unbounded steady-state extensional viscosity. The UCM and Oldroyd-B models yield divergent η_E for Weissenberg number $\mathrm{Wi} = \lambda\dot{\varepsilon} \geq 1/2$ (see e.g. Table 7.3-2 in Ref. [41]), where $\dot{\varepsilon}$ is the extension rate, not to be confused with the PTT model parameter ε. Although the potential for infinite η_E is less of a concern in predominantly shear flows, and can even be considered a desirable trait when testing the robustness of a numerical method, it is preferably avoided when attempting to simulate the extensional behavior of real fluids. The White-Metzner model also suffers from similar limitations, although the exact value of $\dot{\varepsilon}$ that yields divergent η_E varies according to the shape of the $\eta(\dot{\gamma})$ and consequently $\lambda(\dot{\gamma})$ functions. The PTT model is a substantial improvement in this department, considering that $\max(\eta_E) \propto 1/\varepsilon$.

Second, the absence of a solvent viscosity contribution in the UCM and White-Metzner models, which is particularly problematic concerning dilute polymer solutions, such as Boger fluids [48]. These fluids are prepared by adding small amounts of a long-chained polymer to a Newtonian solvent, and their main characteristic is a constant or near constant shear viscosity η_0. The solvent viscosity ratio β tends to be relatively high, $\beta \approx 1$, and η_s cannot be neglected. Alternatively, the Oldroyd-B model is often used to

describe Boger fluids, yet this class of fluids is not representative of the general behavior of polymeric liquids, which are overwhelmingly shear-thinning. Again, the PTT model remedies this problem, since, considering the simplified variant of the model,

$$\begin{cases} \eta_{p,eff} = \eta_p \big/ \mathrm{Y}\left(I\left(\boldsymbol{\tau}\right)\right) \\ \lambda_{eff} = \lambda \big/ \mathrm{Y}\left(I\left(\boldsymbol{\tau}\right)\right) \end{cases}. \tag{2.38}$$

Third, the linearization of the PTT model. It would appear that this model satisfies all of the listed requirements. The characteristics of a dilute polymer solution are best represent by its simplified, linearized formulation. However, since the linear form of $\mathrm{Y}\left(I\left(\boldsymbol{\tau}\right)\right)$ can be obtained by Taylor expansion of the exponential form about $\mathrm{tr}\left(\boldsymbol{\tau}\right)=0$ and truncation of second-order and higher terms, this should in principle restrict the validity of the linearization to small $\mathrm{tr}\left(\boldsymbol{\tau}\right)$, as pointed out by Bird and Wiest [49], and thus reduce the usefulness of the model in simulations of strong extensional flows.

Although the UCM, Oldroyd-B and PTT models were initially used in this thesis, their various inherent limitations eventually led to a shift towards Finitely Extensible Nonlinear Elastic (FENE) dumbbell models.

2.7.4 Finitely Extensible Nonlinear Elastic (FENE) Dumbbell Models

FENE dumbbell models yield differential constitutive equations capable of reproducing the solvent viscosity contribution, the finite extensibility of real polymers and, if desired, shear-thinning behavior. The derivation of FENE models would require a foray into kinetic theory, a branch of statistical mechanics, and therefore falls outside the scope of this thesis. For the interested reader, an introduction to kinetic theory, in so far as it relates to Rheology, is given in Part IV of Ref. [47]. There are, however, certain elements of the derivation that are of practical significance to a rheologist, which are addressed here.

An elastic dumbbell is composed by two beads connected by a spring, as shown in Figure 2.6. Four types of forces may act upon the beads. First, a hydrodynamic drag force, which can be approximated using Stokes' law and is proportional to the difference

between the velocity of each bead and that of the surrounding solvent. Second, a Brownian force, as a result of the thermal agitation of the fluid. Third, an external force, be it gravitational, electromagnetic or of some other kind. Fourth, an intramolecular force, which describes how the elasticity of the spring attempts to return the two beads it connects to their equilibrium positions. Once expressions for the four forces are deduced and the mass of the beads is assumed negligible, Newton's second law of motion yields a balance of forces, which can be converted into an expression for the polymeric extra stress tensor using the procedure first outlined by Kramers [50],[51].

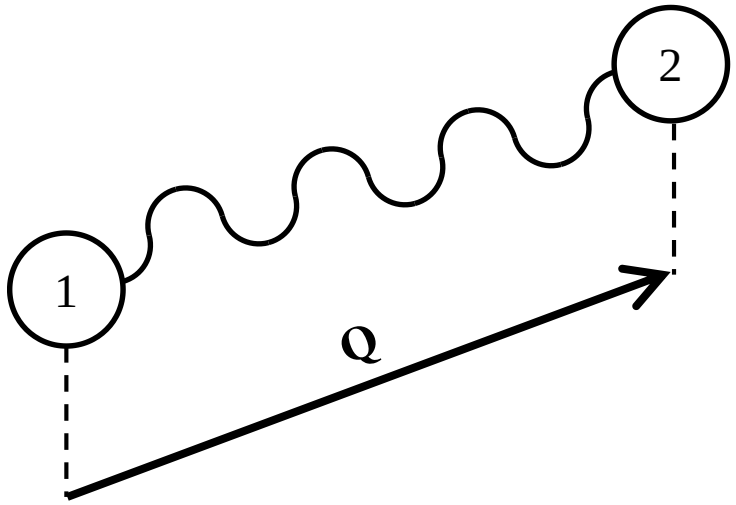

Figure 2.6 – Elastic dumbbell. Two beads, 1 and 2, are connected by a spring. The orientation and length of the dumbbell is defined be the connector vector $\mathbf{Q}$.

The form of the intramolecular force is of particular importance to this discussion. For a Hookean spring,

$$\mathbf{F}^{(c)} = H\mathbf{Q}, \tag{2.39}$$

where $\mathbf{F}^{(c)}$ is the restorative force exerted by the spring, H is a spring constant and $\mathbf{Q}$ is the connector vector, defined as $\mathbf{Q} = \mathbf{r}_2 - \mathbf{r}_1$, where $\mathbf{r}_1$ and $\mathbf{r}_2$ are the positions of each bead (see Figure 2.6). A Hookean spring can extend indefinitely, given the linear relation between force and connector length, and the derivation of a constitutive equation from a suspension of Hookean dumbbells yields the Oldroyd-B model. Another type of spring behavior is prescribed by Warner's force law [52],

$$\mathbf{F}^{(c)} = \frac{H\mathbf{Q}}{1-\left(Q/Q_0\right)^2}, \quad \left(Q < Q_0\right), \tag{2.40}$$

where $Q = \|\mathbf{Q}\|$ is the connector length and Q_0 is the corresponding maximum length. A comparison between Hooke and Warner spring laws is shown in Figure 2.7. For low extensions, say $Q/Q_0 < 0.2$, Warner springs are linear, however the restorative force diverges as the connector length approaches Q_0, effectively halting further stretching. The derivation of a constitutive equation from a suspension of Warner dumbbells yields the FENE family of models.

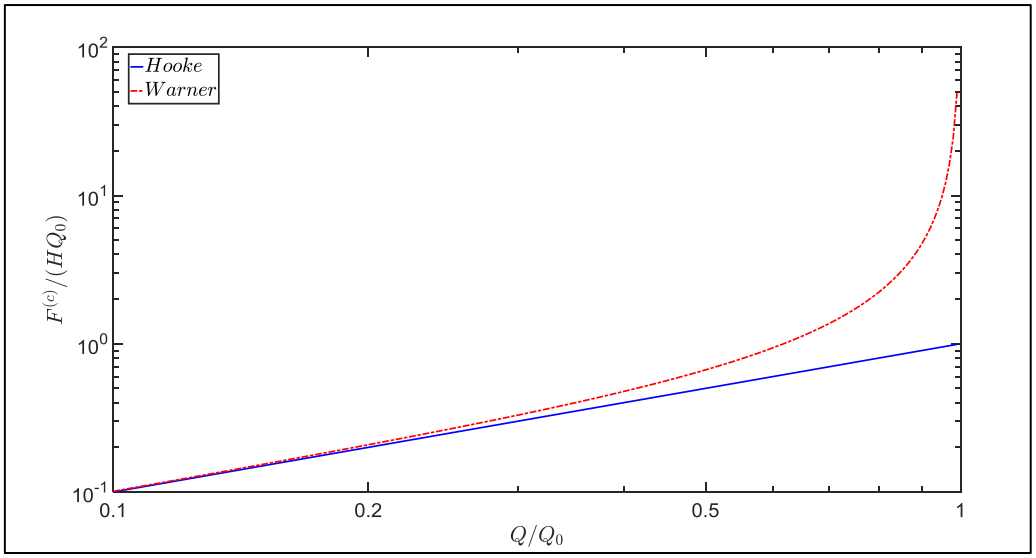

Figure 2.7 – Comparison of Hooke and Warner spring laws.

Although Kramer's procedure is sufficient for the derivation of the Oldroyd-B model from a suspension of linear elastic dumbbells, the closure of FENE models requires additional assumptions. One approach is to substitute the squared dimensionless connector length in the Warner force law by its average, $\left(Q/Q_0\right)^2 \approx \left\langle \left(Q/Q_0\right)^2 \right\rangle$, relative to the distribution of dumbbell configurations for a given instantaneous local flow field [53]. This approach is commonly named pre-averaging. The resulting constitutive equation is given elsewhere in a form more familiar to fluid dynamicists [54],

$$\text{FENE}-\text{P}:$$

$$\begin{cases} \boldsymbol{\sigma} = \eta_s \dot{\boldsymbol{\gamma}} + \boldsymbol{\tau} \\ \boldsymbol{\tau} + \lambda \dfrac{\mathrm{D}}{\mathrm{D}t}\left(\dfrac{\boldsymbol{\tau}}{g}\right) = \dfrac{\alpha \eta_p}{g}\dot{\boldsymbol{\gamma}} + \dfrac{\lambda}{g}\left(\boldsymbol{\tau}\cdot\nabla\mathbf{u} + \left(\nabla\mathbf{u}\right)^{\dagger}\cdot\boldsymbol{\tau}\right) - \mathbf{I}\dfrac{\mathrm{D}}{\mathrm{D}t}\left(\dfrac{\alpha\eta_p}{g}\right) \\ \alpha = \dfrac{L^2}{L^2-3} \\ g = \dfrac{L^2 + \dfrac{\lambda}{\alpha\eta_p}\mathrm{tr}\left(\boldsymbol{\tau}\right)}{L^2-3} \end{cases}, \qquad (2.41)$$

where L^2 is the maximum extensibility, sometimes defined as $b = L^2 - 5$, and α and g are auxiliary variables. The resulting model is referred to as FENE-P, since the pre-averaging closure approximation was originally devised by Peterlin [55]. For large polymer chains, i.e. $L^2 \gg 3$, an additional simplification is often employed, namely $\alpha \approx 1$.

The FENE-P model satisfies all the requirements outlined earlier. However, when studying viscoelastic flows, it is often useful to isolate the effects of elasticity and shear-thinning viscosity, including in this thesis, hence why Boger fluids are so common in the rheological literature [56]. To this end, Chilcott and Rallison [57] proposed an empirical modification to the FENE-P model, by assigning $\eta_p / g \approx \eta_p$, and the resulting model bears their initials and is shown here with $\alpha \approx 1$,

$$\text{FENE}-\text{CR}:$$

$$\begin{cases} \boldsymbol{\sigma} = \eta_s \dot{\boldsymbol{\gamma}} + \boldsymbol{\tau} \\ \boldsymbol{\tau} + \lambda \dfrac{\mathrm{D}}{\mathrm{D}t}\left(\dfrac{\boldsymbol{\tau}}{g}\right) = \eta_p\dot{\boldsymbol{\gamma}} + \dfrac{\lambda}{g}\left(\boldsymbol{\tau}\cdot\nabla\mathbf{u} + \left(\nabla\mathbf{u}\right)^{\dagger}\cdot\boldsymbol{\tau}\right). \\ g = \dfrac{L^2 + \dfrac{\lambda}{\eta_p}\mathrm{tr}\left(\boldsymbol{\tau}\right)}{L^2-3} \end{cases} \qquad (2.42)$$

The FENE-CR model is often written in conformation tensor notation, which not coincidentally is the form in which the model was first presented [57],

FENE-CR in conformation tensor notation

$$\begin{cases} \overset{\nabla}{\mathbf{A}} = -\dfrac{g}{\lambda}\left(\mathbf{A}-\mathbf{I}\right) \\ g = \dfrac{L^2}{L^2 - \mathrm{tr}\left(\mathbf{A}\right)} \end{cases}, \tag{2.43}$$

where $\mathbf{A}$ is the conformation tensor, and is related with the polymeric extra stress tensor as follows,

$$\boldsymbol{\tau} = \frac{\eta_p}{\lambda/g}\left(\mathbf{A}-\mathbf{I}\right). \tag{2.44}$$

The auxiliary variable g retains the same value for either polymeric extra stress or conformation formulations. The conformation tensor is especially useful as a direct measure of extension, since $\mathrm{tr}\left(\mathbf{A}\right)/L^2$ has the same meaning as the ratio Q/Q_0 in Warner's force law. Although very useful, the FENE-CR model is, as noted by Bird and Wiest [49], devoid of molecular significance. Most notably, despite a constant shear viscosity, the relaxation time is variable, $\lambda_{eff} = \lambda/g$, which is the approximate behavior of real Boger fluids.

Many other constitutive models have been proposed, many of which are covered in the reviews and textbooks by Bird and co-authors, mainly in Refs. [41],[47],[49]. For a more recent discussion on the state of constitutive modelling, see Ref. [58].

2.8 References

[1] J.C. Maxwell, The Bakerian Lecture: On the Viscosity or Internal Friction of Air and Other Gases, Philos. Trans. R. Soc. London. 156 (1866) 249–268.

doi:10.1098/rstl.1866.0013.

[2] L. Euler, Principes Generaux de l'Etat d'Equilibre des Fluides, Mémoires l'Académie Des Sci. Berlin. 11 (1757) 217–273.

[3] L. Euler, Principes Generaux du Mouvement des Fluides, Mémoires l'Académie Des Sci. Berlin. 11 (1757) 274–315.

[4] L. Euler, Continuation des Recherches sur la Theorie du Mouvement des Fluides, Mémoires l'Académie Des Sci. Berlin. 11 (1757) 316–361.

[5] I. Newton, Philosophiæ Naturalis Principia Mathematica, Benjamin Motte, London, 1687.

[6] G.G. Stokes, Report on Recent Researches on Hydrodynamics, in: Math. Phys. Pap. vol.1, Cambridge University Press, Cambridge, 1847: pp. 157–187. doi:10.1017/CBO9780511702242.011.

[7] D. Doraiswamy, The origins of rheology: a short historical excursion, Rheol. Bull. 71 (2002) 1–9.

[8] R. Hooke, Lectures, De Potentia Restitutiva, or of Spring, Explaining the Power of Springing Bodies, Jonh Martyn, London, 1678.

[9] B. Pascal, Traitez de l'Equilibre des Liqueurs, et de la Pesanteur de la Masse de l'Air, Guillaume Desprez, Paris, 1663.

[10] D. Bernoulli, Hydrodynamica, sive de Viribus et Motibus Fluidorum Commentarii, Joh. Henr. Deckeri, Strasbourg, 1738.

[11] G.G. Stokes, On the Theories of the Internal Friction of Fluids in Motion, and of the Equilibrium and Motion of Elastic Solids, in: Math. Phys. Pap. vol.1, Cambridge University Press, Cambridge, 1845: pp. 75–129. doi:10.1017/CBO9780511702242.005.

[12] W. Weber, Ueber die Elasticität der Seidenfäden, Ann. Der Phys. Und Chemie. 110 (1835) 247–257. doi:10.1002/andp.18351100204.

[13] J.C. Maxwell, On the Dynamical Theory of Gases, Philos. Trans. R. Soc. London. 157 (1867) 49–88. doi:10.1098/rstl.1867.0004.

[14] J.G. Oldroyd, On the Formulation of Rheological Equations of State, Proc. R. Soc. A Math. Phys. Eng. Sci. 200 (1950) 523–541. doi:10.1098/rspa.1950.0035.

[15] C.J.S. Petrie, Extensional viscosity: A critical discussion, J. Non-Newt. Fluid Mech. 137 (2006) 15–23. doi:10.1016/j.jnnfm.2006.01.011.

[16] F.T. Trouton, On the Coefficient of Viscous Traction and Its Relation to that of Viscosity, Proc. R. Soc. A Math. Phys. Eng. Sci. 77 (1906) 426–440. doi:10.1098/rspa.1906.0038.

[17] B. Katzbauer, Properties and applications of xanthan gum, Polym. Degrad. Stab. 59 (1998) 81–84. doi:10.1016/S0141-3910(97)00180-8.

[18] G. Cuvelier, B. Launay, Concentration regimes in xanthan gum solutions deduced from flow and viscoelastic properties, Carbohydr. Polym. 6 (1986) 321–333. doi:10.1016/0144-8617(86)90023-8.

[19] H.A. Barnes, A Handbook of Elementary Rheology, The University of Wales Institute of Non-Newtonian Fluid Mechanics, Aberystwyth, 2000.

[20] A. Fall, N. Huang, F. Bertrand, G. Ovarlez, D. Bonn, Shear Thickening of Cornstarch Suspensions as a Reentrant Jamming Transition, Phys. Rev. Lett. 100 (2008) 18301. doi:10.1103/PhysRevLett.100.018301.

[21] M.M. Cross, Rheology of non-Newtonian fluids: A new flow equation for pseudoplastic systems, J. Colloid Sci. 20 (1965) 417–437. doi:10.1016/0095-8522(65)90022-X.

[22] A. de Waele, Viscometry and plastometry, Oil Color Chem Assoc J. 6 (1923) 33–88.

[23] W. Ostwald, Ueber die Geschwindigkeitsfunktion der Viskosität disperser Systeme. I, Kolloid-Zeitschrift. 36 (1925) 99–117. doi:10.1007/BF01431449.

[24] A.W. Sisko, The Flow of Lubricating Greases, Ind. Eng. Chem. 50 (1958) 1789–1792. doi:10.1021/ie50588a042.

[25] P.J. Carreau, Rheological Equations from Molecular Network Theories, Trans. Soc. Rheol. 16 (1972) 99–127. doi:10.1122/1.549276.

[26] K. Yasuda, R.C. Armstrong, R.E. Cohen, Shear flow properties of concentrated solutions of linear and star branched polystyrenes, Rheol. Acta. 20 (1981) 163–178. doi:10.1007/BF01513059.

[27] F.J. Galindo-Rosales, F.J. Rubio-Hernández, A. Sevilla, An apparent viscosity

function for shear thickening fluids, J. Non-Newt. Fluid Mech. 166 (2011) 321–325. doi:10.1016/j.jnnfm.2011.01.001.

[28] N.J. Balmforth, I.A. Frigaard, G. Ovarlez, Yielding to Stress: Recent Developments in Viscoplastic Fluid Mechanics, Annu. Rev. Fluid Mech. 46 (2014) 121–146. doi:10.1146/annurev-fluid-010313-141424.

[29] W.H. Herschel, R. Bulkley, Konsistenzmessungen von Gummi-Benzollösungen, Kolloid-Zeitschrift. 39 (1926) 291–300. doi:10.1007/BF01432034.

[30] E.C. Bingham, Fluidity and Plasticity, McGraw-Hill, New York, 1922.

[31] H.A. Barnes, The yield stress—a review or "παντα ρει"—everything flows?, J. Non-Newt. Fluid Mech. 81 (1999) 133–178. doi:10.1016/S0377-0257(98)00094-9.

[32] D. Bonn, M.M. Denn, L. Berthier, T. Divoux, S. Manneville, Yield stress materials in soft condensed matter, Rev. Mod. Phys. 89 (2017) 35005. doi:10.1103/RevModPhys.89.035005.

[33] T. Benezech, J.F. Maingonnat, Characterization of the rheological properties of yoghurt—A review, J. Food Eng. 21 (1994) 447–472. doi:10.1016/0260-8774(94)90066-3.

[34] H.A. Barnes, Thixotropy—a review, J. Non-Newt. Fluid Mech. 70 (1997) 1–33. doi:10.1016/S0377-0257(97)00004-9.

[35] K.B. Fonseca, F.R.R. Maia, F.A. Cruz, D. Andrade, M.A. Juliano, P.L. Granja, et al., Enzymatic, physicochemical and biological properties of MMP-sensitive alginate hydrogels, Soft Matter. 9 (2013) 3283. doi:10.1039/c3sm27560d.

[36] C. Zener, Elasticity and Anelasticity of Metals, University of Chicago Press, Chicago, 1948.

[37] H. Jeffreys, The Earth: Its Origin, History and Physical Constitution, Cambridge University Press, Cambridge, 1924.

[38] F. Mainardi, G. Spada, Creep, relaxation and viscosity properties for basic fractional models in rheology, Eur. Phys. J. Spec. Top. 193 (2011) 133–160. doi:10.1140/epjst/e2011-01387-1.

[39] E. Wiechert, Gesetze der elastischen Nachwirkung für constante Temperatur,

Ann. Phys. 286 (1893) 546–570. doi:10.1002/andp.18932861110.

[40] D.V. Boger, K. Walters, Rheological Phenomena in Focus, Elsevier, Amsterdam, 1993.

[41] R.B. Bird, R.C. Armstrong, O. Hassager, Dynamics of Polymeric Liquids, Vol. 1 - Fluids Mechanics, 2nd ed., Jonh Wiley & Sons, New York, 1987.

[42] H. Hencky, Die Bewegungsgleichungen beim nichtstationären Fließen plastischer Massen, Zeitschrift Für Angew. Math. Und Mech. 5 (1925) 144–146.

[43] J.L. White, A.B. Metzner, Development of constitutive equations for polymeric melts and solutions, J. Appl. Polym. Sci. 7 (1963) 1867–1889. doi:10.1002/app.1963.070070524.

[44] N.P. Thien, R.I. Tanner, A new constitutive equation derived from network theory, J. Non-Newt. Fluid Mech. 2 (1977) 353–365. doi:10.1016/0377-0257(77)80021-9.

[45] N. Phan-Thien, A Nonlinear Network Viscoelastic Model, J. Rheol. 22 (1978) 259–283. doi:10.1122/1.549481.

[46] R.I. Tanner, Some useful constitutive models with a kinematic slip hypothesis, J. Non-Newt. Fluid Mech. 5 (1979) 103–112. doi:10.1016/0377-0257(79)85006-5.

[47] R.B. Bird, C.F. Curtiss, R.C. Armstrong, O. Hassager, Dynamics of Polymeric Liquids, Vol. 2 - Kinetic Theory, 2nd ed., Jonh Wiley & Sons, New York, 1987.

[48] D.V. Boger, A highly elastic constant-viscosity fluid, J. Non-Newt. Fluid Mech. 3 (1977) 87–91. doi:10.1016/0377-0257(77)80014-1.

[49] R.B. Bird, J.M. Wiest, Constitutive Equations for Polymeric Liquids, Annu. Rev. Fluid Mech. 27 (1995) 169–193. doi:10.1146/annurev.fl.27.010195.001125.

[50] H. Kramers, Het gedrag van macromoleculen in een stroomende vloeistof, Physica. 11 (1944) 1–19. doi:10.1016/S0031-8914(44)80015-5.

[51] H.A. Kramers, The Behavior of Macromolecules in Inhomogeneous Flow, J. Chem. Phys. 14 (1946) 415–424. doi:10.1063/1.1724163.

[52] H.R. Warner, Kinetic Theory and Rheology of Dilute Suspensions of Finitely Extendible Dumbbells, Ind. Eng. Chem. Fundam. 11 (1972) 379–387. doi:10.1021/i160043a017.

[53] R.B. Bird, P.J. Dotson, N.L. Johnson, Polymer solution rheology based on a finitely extensible bead—spring chain model, J. Non-Newt. Fluid Mech. 7 (1980) 213–235. doi:10.1016/0377-0257(80)85007-5.

[54] P.J. Oliveira, Reduced-stress method for efficient computation of time-dependent viscoelastic flow with stress equations of FENE-P type, J. Non-Newt. Fluid Mech. 248 (2017) 74–91. doi:10.1016/j.jnnfm.2017.09.001.

[55] A. Peterlin, Hydrodynamics of macromolecules in a velocity field with longitudinal gradient, J. Polym. Sci. Part B Polym. Lett. 4 (1966) 287–291. doi:10.1002/pol.1966.110040411.

[56] D.F. James, Boger Fluids, Annu. Rev. Fluid Mech. 41 (2009) 129–142. doi:10.1146/annurev.fluid.010908.165125.

[57] M. Chilcott, J. Rallison, Creeping flow of dilute polymer solutions past cylinders and spheres, J. Non-Newt. Fluid Mech. 29 (1988) 381–432. doi:10.1016/0377-0257(88)85062-6.

[58] R.G. Larson, P.S. Desai, Modeling the Rheology of Polymer Melts and Solutions, Annu. Rev. Fluid Mech. 47 (2015) 47–65. doi:10.1146/annurev-fluid-010814-014612.

3 Literature Review

3.1 Computational Fluid Dynamics (CFD)

The solid-fluid dichotomy, blurred by Rheology, also has ramifications in the computational simulation of physical phenomena. For example, the transient diffusion of scalar quantities in a solid is governed by a differential equation such as the heat equation. In its simplest form,

$$\frac{\partial \phi}{\partial t} = \Gamma \nabla^2 \phi \tag{3.1}$$

where ϕ is a scalar and Γ is a diffusivity. More generally, Γ may not be constant, in which case the left hand side of eq. 3.1 would be $\nabla \cdot (\Gamma \nabla \phi)$, and an additional source term q_ϕ may also be present. Nevertheless, this formulation is only applicable to diffusion through a stationary medium, i.e. an idealized rigid solid. On the other hand, the transport of scalar quantities in a flow is also dependent on the underlying fluid motion, leading to the following generic transport equation (see e.g. Chap. 1 in Ref. [1] for a derivation),

$$\frac{\partial (\rho \phi)}{\partial t} + \nabla \cdot (\rho \phi \mathbf{u}) = \nabla \cdot (\rho \Gamma \nabla \phi) + q_\phi , \tag{3.2}$$

where ρ is the density of the fluid and $\mathbf{u}$ is the velocity field. Critically, a new type of transport is introduced by the term $\nabla \cdot (\rho \phi \mathbf{u})$, denominated convection or advection. If incompressibility is assumed, as is the case throughout this thesis, then $\nabla \cdot (\rho \phi \mathbf{u}) = \rho \mathbf{u} \cdot \nabla \phi$.

CFD is one of the parent disciplines of Computational Rheology, and as such the difficulties generated by advection, and the corresponding countermeasures, feature

preeminently in the specialized literature. Arguably, the treatment of advection is more significant in Computational Rheology, since, in addition to the advective terms of the Navier-Stokes equations, $\rho\mathbf{u}\cdot\nabla\mathbf{u}$, differential constitutive equations also express the advection of the polymeric extra stress tensor $\boldsymbol{\tau}$, e.g. for an Oldroyd-B fluid, $\lambda\mathbf{u}\cdot\nabla\boldsymbol{\tau}$, where λ is the relaxation time, thereby contributing to the High Weissenberg Number Problem, discussed in section 3.2.

3.1.1 Treatment of Advection

Recasting the generic transport equation (3.2) in integral form and applying the divergence theorem (see e.g. Chap. 1 in Ref. [1]),

$$\underbrace{\frac{\partial}{\partial t}\int_V \rho\phi \,\mathrm{d}V}_{\text{Transient term}} + \underbrace{\int_S \rho\phi\mathbf{u}\cdot\mathbf{n}\,\mathrm{d}S}_{\text{Advection}} = \underbrace{\int_S \rho\Gamma\nabla\phi\cdot\mathbf{n}\,\mathrm{d}S}_{\text{Diffusion}} + \underbrace{\int_V q_\phi \,\mathrm{d}V}_{\text{Source term}} \tag{3.3}$$

where V is a control volume with boundary S. This formulation, which ensures the conservation of physical quantities, forms the basis of the finite volume (FV) discretization.

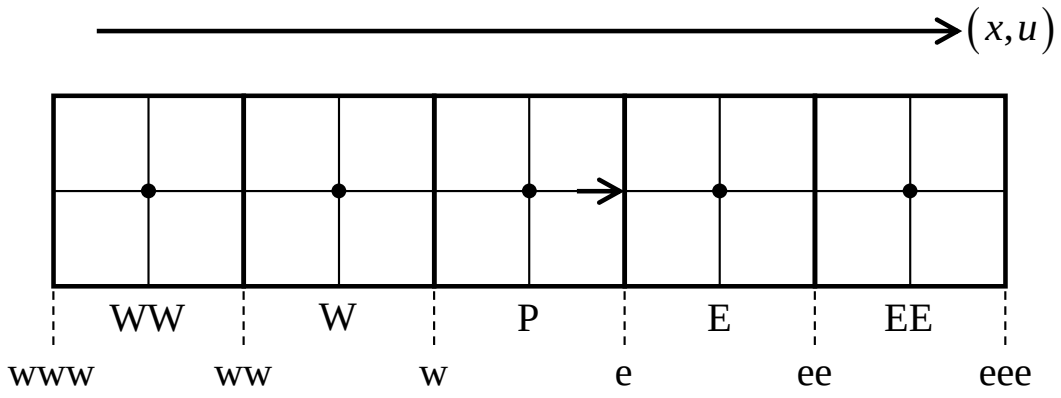

Figure 3.1 – Illustrative finite volume discretization. Uppercase letters designate cells and the respective centers, whereas lowercase letters refer to faces and the respective centers. Velocity u is assumed positive.

A one-dimensional (1D) orthogonal mesh is shown in Figure 3.1. The value of ϕ at the center of cell C is denoted as ϕ_C and, with second-order accuracy, is also the

average of ϕ within the corresponding cell. Accordingly, the value of ϕ at the center of face f is denoted as ϕ_{f} and, with second-order accuracy, is also the average of ϕ within the corresponding face. Considering only the influence of advection along the x-axis, and further noting that $u > 0$, the discrete rate of change of ϕ in cell P is given by,

$$\rho \frac{\Delta \phi_{\mathrm{P}}}{\Delta t} V_{\mathrm{P}} = \rho \mathbf{u}_{\mathrm{w}} \cdot \mathbf{n}_{\mathrm{w}} S_{\mathrm{w}} \phi_{\mathrm{w}} - \rho \mathbf{u}_{\mathrm{e}} \cdot \mathbf{n}_{\mathrm{e}} S_{\mathrm{e}} \phi_{\mathrm{e}} = F_{\mathrm{w}} \phi_{\mathrm{w}} - F_{\mathrm{e}} \phi_{\mathrm{e}}, \tag{3.4}$$

where $\mathbf{n}_{\mathrm{f}}$ is the unit vector normal to the surface S_{f}, and $F_{\mathrm{f}} = \rho \mathbf{u}_{\mathrm{f}} \cdot \mathbf{n}_{\mathrm{f}} S_{\mathrm{f}}$ is the mass flux across the same surface. The various strategies devised for the treatment of advection consist of different ways to approximate the face center values ϕ_{f} using cell center values ϕ_{C}. By convention, interpolation schemes are presented for ϕ_{e}. Furthermore, the Péclet number Pe is often used to quantify the influence of advection relative to diffusion, as a ratio of transport rates,

$$\mathrm{Pe} = \frac{u}{\Gamma / \delta x}, \tag{3.5}$$

where δx is a characteristic length, usually defined as a cell width, and the diffusivity Γ has the same units as the kinematic viscosity $\nu = \eta / \rho$, where η is the dynamic viscosity (see Chap. 5 in Ref. [2]).

By default, interpolations utilize central differencing schemes (CDS). For a second-order approximation,

$$\phi_{\mathrm{e}} = \frac{x_{\mathrm{e}} - x_{\mathrm{E}}}{x_{\mathrm{P}} - x_{\mathrm{E}}} \phi_{\mathrm{P}} + \frac{x_{\mathrm{e}} - x_{\mathrm{P}}}{x_{\mathrm{E}} - x_{\mathrm{P}}} \phi_{\mathrm{E}}, \tag{3.6}$$

where x_{f} and x_{C} are distances defined either globally or relative to $x_{\mathrm{P}} = 0$. This scheme estimates the value of ϕ_{e} by linear interpolation of the adjacent cell centers. However, as discussed by, among many others, Brooks and Hughes [3] or Fergizer and Perić (Chap. 4

in Ref. [1]), the application of central differencing to convective terms tends to result in unphysical, oscillatory profiles whenever $\mathrm{Pe} > 2$, i.e. in general CDS interpolations do not ensure boundedness.

The simplest alternative is the upwind differencing scheme (UDS),

$$\phi_{\mathrm{e}} = \begin{cases} \phi_{\mathrm{P}} & \text{if } \mathbf{u}\cdot\mathbf{n}_{\mathrm{e}} > 0 \\ \phi_{\mathrm{E}} & \text{if } \mathbf{u}\cdot\mathbf{n}_{\mathrm{e}} < 0 \end{cases}, \tag{3.7}$$

originally formulated by Courant et al. [4]. This scheme prevents the development of oscillatory profiles since it guarantees bounded solutions [5], and furthermore is also transportive (Chap. 5 in Ref. [2]) or convectively stable [6], i.e. for high Pe flows, the properties at face f are essentially only influenced by the upstream cells, particularly the cell C immediately upstream of f. However the method is only first-order accurate.

The CDS and UDS methods can be combined in different ways. For instance, the hybrid differencing scheme proposed by Spalding [7] switches between central differencing, when $\mathrm{Pe} < 2$, and upwind differencing, when $\mathrm{Pe} \geq 2$, with the Péclet number evaluated at cell face e. Alternatively, the linear upwind differencing scheme (LUDS), proposed by Price et al. [8], utilizes a computational molecule of the same size as the CDS method, shifted one cell upstream,

$$\phi_{\mathrm{e}} = \begin{cases} \dfrac{x_{\mathrm{e}} - x_{\mathrm{P}}}{x_{\mathrm{W}} - x_{\mathrm{P}}}\phi_{\mathrm{W}} + \dfrac{x_{\mathrm{e}} - x_{\mathrm{W}}}{x_{\mathrm{P}} - x_{\mathrm{W}}}\phi_{\mathrm{P}} & \text{if } \mathbf{u}\cdot\mathbf{n}_{\mathrm{e}} > 0 \\ \dfrac{x_{\mathrm{e}} - x_{\mathrm{EE}}}{x_{\mathrm{E}} - x_{\mathrm{EE}}}\phi_{\mathrm{E}} + \dfrac{x_{\mathrm{e}} - x_{\mathrm{E}}}{x_{\mathrm{EE}} - x_{\mathrm{E}}}\phi_{\mathrm{EE}} & \text{if } \mathbf{u}\cdot\mathbf{n}_{\mathrm{e}} < 0 \end{cases}, \tag{3.8}$$

therefore incorporating the notion of upwinding in a second-order scheme. Both the hybrid and linear upwind strategies improve on previous techniques, although without completely solving some of the outstanding difficulties. Namely, for $\mathrm{Pe} \gg 2$, the hybrid scheme exhibits the same inaccuracies as the UDS method, and the LUDS interpolation, particularly for multidimensional flows, does not ensure boundedness.

3.1.2 Advection and Polynomial Interpolation

The inaccuracy of the UDS and LUDS schemes stems from their relatively low order of convergence, respectively, first- and second-order. Following the logical progression in complexity, the next improvement would be to estimate ϕ_e using a quadratic interpolation. Before proceeding, a few remarks on notation and interpolation techniques are made.

First, to avoid stating two formulas whenever upwinding is used, the face targeted by the interpolation is denoted by d, the first cell downstream is denoted by D, the first cell upstream is denoted by C and the second cell upstream is denoted by U. Figure 3.2 illustrates how this notation automatically adjusts to the direction of the mass flux.

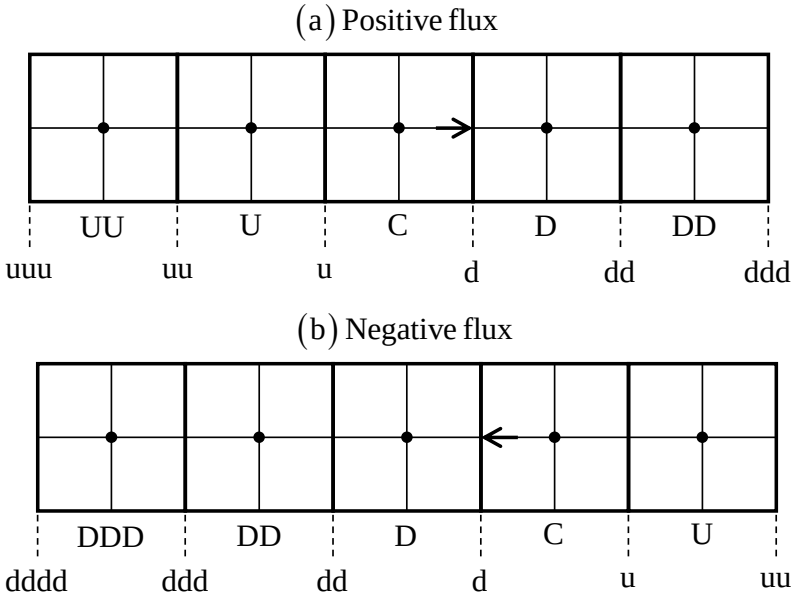

Figure 3.2 – Finite volume discretization with cell and face labels defined by the direction of the mass flux.

Second, to simplify the formulation of interpolations, Lagrange polynomials are used. The lowest order Lagrange polynomial $L(x)$ that fits a set of $k+1$ data points, $(x_0,\phi_0),\ldots,(x_j,\phi_j),\ldots,(x_k,\phi_k)$, is a linear combination of the basis polynomials $l_j(x)$,

$$L(x)=\sum_{j=0}^{k}\phi_j l_j(x), \tag{3.9}$$

$$l_j(x)=\prod_{\substack{0\le m\le k\\ m\neq j}}\frac{x-x_m}{x_j-x_m}. \tag{3.10}$$

Leonard [6] introduced the quadratic upstream interpolation for convective kinematics, or QUICK scheme,

$$\phi_{\mathrm{d}}=\frac{x_{\mathrm{d}}-x_{\mathrm{C}}}{x_{\mathrm{D}}-x_{\mathrm{C}}}\frac{x_{\mathrm{d}}-x_{\mathrm{U}}}{x_{\mathrm{D}}-x_{\mathrm{U}}}\phi_{\mathrm{D}}+\frac{x_{\mathrm{d}}-x_{\mathrm{D}}}{x_{\mathrm{C}}-x_{\mathrm{D}}}\frac{x_{\mathrm{d}}-x_{\mathrm{U}}}{x_{\mathrm{C}}-x_{\mathrm{U}}}\phi_{\mathrm{C}}+\frac{x_{\mathrm{d}}-x_{\mathrm{D}}}{x_{\mathrm{U}}-x_{\mathrm{D}}}\frac{x_{\mathrm{d}}-x_{\mathrm{C}}}{x_{\mathrm{U}}-x_{\mathrm{C}}}\phi_{\mathrm{U}}, \tag{3.11}$$

shown here in a form different from what is usually presented in the literature, owing to the construction using Lagrange polynomials. The scheme is third-order accurate and upwind biased, since it uses the center values of two cells upwind and one cell downwind of face d. One might easily envision other upwind biased, higher order polynomial interpolations. As discussed by Gaskell and Lau [9] or Leonard and Drummond [10], higher order interpolations such as the QUICK scheme perform well in regions where $\phi(x)$ is smooth. However, the approximation of sharp gradients, such as a step profile, tends to result in overshoots/undershoots, e.g. the estimated value of ϕ before/after a sudden decrease is higher/lower than the exact solution, illustrating the unboundedness of simple polynomial schemes. These overshoots/undershoots are particularly problematic if ϕ represents a quantity such as the concentration of a solute, leading to scenarios in which simulations yield unphysical negative values.

3.1.3 Advection and the Normalized Variable Approach

The problems with the aforementioned schemes are best illustrated via the normalized variable approach developed by Gaskell and Lau [9] and Leonard [11] for uniform meshes and generalized to non-uniform grids by Darwish and Moukalled [12]. Using the following normalization rules,

$$\tilde{x} = \frac{x - x_{\mathrm{U}}}{x_{\mathrm{D}} - x_{\mathrm{U}}}, \tag{3.12}$$

$$\tilde{\phi} = \frac{\phi - \phi_{\mathrm{U}}}{\phi_{\mathrm{D}} - \phi_{\mathrm{U}}}, \tag{3.13}$$

and further noting that $\tilde{x}_{\mathrm{U}} = \tilde{\phi}_{\mathrm{U}} = 0$ and $\tilde{x}_{\mathrm{D}} = \tilde{\phi}_{\mathrm{D}} = 1$, the CDS, UDS, LUDS and QUICK schemes are rewritten accordingly,

$$\begin{cases} \mathrm{CDS}: \ \tilde{\phi}_{\mathrm{d}} = \dfrac{\tilde{x}_{\mathrm{d}} - 1}{\tilde{x}_{\mathrm{C}} - 1}\tilde{\phi}_{\mathrm{C}} + \dfrac{\tilde{x}_{\mathrm{d}} - \tilde{x}_{\mathrm{C}}}{1 - \tilde{x}_{\mathrm{C}}} \\ \mathrm{UDS}: \ \tilde{\phi}_{\mathrm{d}} = \tilde{\phi}_{\mathrm{C}} \\ \mathrm{LUDS}: \ \tilde{\phi}_{\mathrm{d}} = \dfrac{\tilde{x}_{\mathrm{d}}}{\tilde{x}_{\mathrm{C}}}\tilde{\phi}_{\mathrm{C}} \\ \mathrm{QUICK}: \ \tilde{\phi}_{\mathrm{d}} = \dfrac{\tilde{x}_{\mathrm{d}} - \tilde{x}_{\mathrm{C}}}{1 - \tilde{x}_{\mathrm{C}}}\tilde{x}_{\mathrm{d}} + \dfrac{\tilde{x}_{\mathrm{d}} - 1}{\tilde{x}_{\mathrm{C}} - 1}\dfrac{\tilde{x}_{\mathrm{d}}}{\tilde{x}_{\mathrm{C}}}\tilde{\phi}_{\mathrm{C}} \end{cases}. \tag{3.14}$$

For a uniform mesh, $\tilde{x}_{\mathrm{C}} = 1/2$ and $\tilde{x}_{\mathrm{d}} = 3/4$, therefore,

$$\begin{cases} \mathrm{CDS}: \ \tilde{\phi}_{\mathrm{d}} = \dfrac{1}{2}\tilde{\phi}_{\mathrm{C}} + \dfrac{1}{2} \\ \mathrm{UDS}: \ \tilde{\phi}_{\mathrm{d}} = \tilde{\phi}_{\mathrm{C}} \\ \mathrm{LUDS}: \ \tilde{\phi}_{\mathrm{d}} = \dfrac{3}{2}\tilde{\phi}_{\mathrm{C}} \\ \mathrm{QUICK}: \ \tilde{\phi}_{\mathrm{d}} = \dfrac{3}{8} + \dfrac{3}{4}\tilde{\phi}_{\mathrm{C}} \end{cases}. \tag{3.15}$$

All the schemes are now written in the generic form $\tilde{\phi}_{\mathrm{d}} = f\left(\tilde{\phi}_{\mathrm{C}}\right)$, which serves as a basis for the convection boundedness criterion (CBC) formulated by Gaskell and Lau [9]. The CBC states that $f\left(\tilde{\phi}_{\mathrm{C}}\right)$, in addition to being a continuously increasing function or piecewise union of functions, should meet the following requirements,

$$\begin{cases} \text{i}: & \tilde{\phi}_C \le f\left(\tilde{\phi}_C\right) \le 1 \text{ if } 0 \le \tilde{\phi}_C \le 1 \\ \text{ii}: & f\left(\tilde{\phi}_C\right) = \tilde{\phi}_C \text{ if } \tilde{\phi}_C < 0 \text{ or } \tilde{\phi}_C > 1 \end{cases}, \tag{3.16}$$

with a third and fourth conditions, $f(0)=0$ and $f(1)=1$, often listed independently, although they are already implied by the continuity of $f\left(\tilde{\phi}_C\right)$ in conjunction with the other requirements. Figure 3.3 shows the normalized variable diagram (NVD) [11], on a uniform mesh, for the interpolation schemes discussed so far. Similar plots for non-uniform mesh segments can be constructed using the normalized variable and space formulation (NVSF) [12]. Conventionally, interpolation methods that satisfy the CBC are referred to as high resolution schemes (HRS). The requirements of the CBC are worthy of further examination: (i) ensures that monotonic profiles remain bounded, whereas (ii) prescribes the UDS interpolation for non-monotonic profiles. Hence, regardless of the order of convergence in regions where ϕ is monotonic, any scheme that satisfies the CBC is first-order accurate in local maxima or minima.

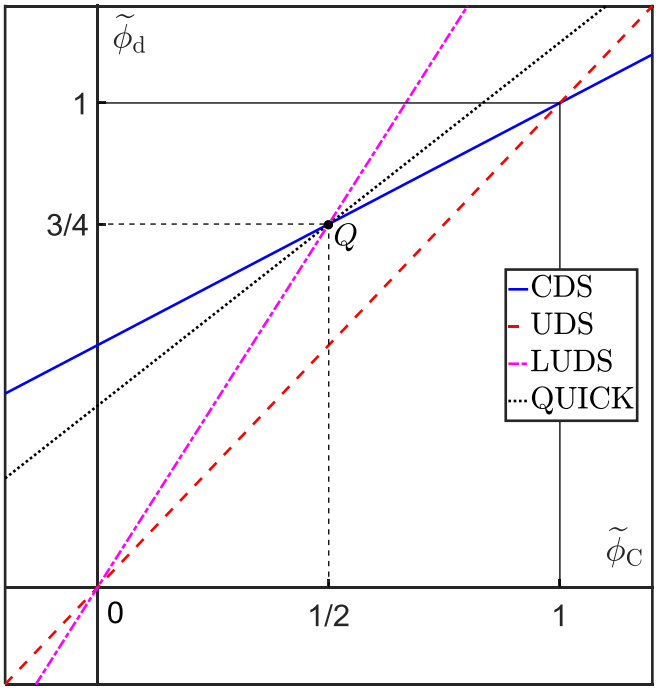

Figure 3.3 – Normalized variable diagram showing $\tilde{\phi}_d = f\left(\tilde{\phi}_C\right)$ for various simple interpolation schemes. A uniform mesh is assumed.

Of the schemes shown in Figure 3.3, the UDS interpolation is the only method that globally satisfies the CBC. Leonard [11] enunciated additional requirements for higher order schemes. Namely, any interpolation method that satisfies $f\left(1/2\right)=3/4$, denoted by point Q in Figure 3.3, or in a non-uniform mesh [12],

$$f\left(\tilde{x}_{\mathrm{C}}\right)=\tilde{x}_{\mathrm{d}}, \tag{3.17}$$

is second-order accurate, and if in addition the slope of the representation in the NVD satisfies $f'\left(1/2\right)=3/4$, or in a non-uniform mesh [12],

$$f'\left(\tilde{x}_{\mathrm{C}}\right)=\frac{\tilde{x}_{\mathrm{d}}-1}{\tilde{x}_{\mathrm{C}}-1}\frac{\tilde{x}_{\mathrm{d}}}{\tilde{x}_{\mathrm{C}}}, \tag{3.18}$$

the scheme is third-order accurate.

A few examples of CBC compliant schemes are shown in Figures 3.4 and 3.5 for uniform meshes. These are the MINMOD [13], CLAM [14] and MUSCL [15] second-order schemes, and the SMART [9] and NOTABLE [16] third-order schemes. Alternatively, the schemes are shown below in their NVSF variant, as derived by Darwish and Moukalled [12] or in Chap. 4.6.2 of Ref. [17].

MINMOD:

$$\tilde{\phi}_{\mathrm{d}}=\begin{cases}\dfrac{\tilde{x}_{\mathrm{d}}}{\tilde{x}_{\mathrm{C}}}\tilde{\phi}_{\mathrm{C}} & \text{if} \quad 0\le\tilde{\phi}_{\mathrm{C}}<\tilde{x}_{\mathrm{C}} \\ \dfrac{\tilde{x}_{\mathrm{C}}-\tilde{x}_{\mathrm{d}}}{\tilde{x}_{\mathrm{C}}-1}+\dfrac{\tilde{x}_{\mathrm{d}}-1}{\tilde{x}_{\mathrm{C}}-1}\tilde{\phi}_{\mathrm{C}} & \text{if} \quad \tilde{x}_{\mathrm{C}}\le\tilde{\phi}_{\mathrm{C}}\le 1 \\ \tilde{\phi}_{\mathrm{C}} & \text{elsewhere}\end{cases} \tag{3.19}$$

CLAM:

$$\tilde{\phi}_{\mathrm{d}} = \begin{cases} \dfrac{\tilde{x}_{\mathrm{C}}^2 - \tilde{x}_{\mathrm{d}}}{\tilde{x}_{\mathrm{C}}\left(\tilde{x}_{\mathrm{C}} - 1\right)}\tilde{\phi}_{\mathrm{C}} + \dfrac{\tilde{x}_{\mathrm{d}} - \tilde{x}_{\mathrm{C}}}{\tilde{x}_{\mathrm{C}}\left(\tilde{x}_{\mathrm{C}} - 1\right)}\tilde{\phi}_{\mathrm{C}}^2 & \text{if} \quad 0 \le \tilde{\phi}_{\mathrm{C}} \le 1 \\ \tilde{\phi}_{\mathrm{C}} & \text{elsewhere} \end{cases} \tag{3.20}$$

MUSCL:

$$\tilde{\phi}_{\mathrm{d}} = \begin{cases} \dfrac{2\tilde{x}_{\mathrm{d}} - \tilde{x}_{\mathrm{C}}}{\tilde{x}_{\mathrm{C}}}\tilde{\phi}_{\mathrm{C}} & \text{if} \quad 0 \le \tilde{\phi}_{\mathrm{C}} < \dfrac{\tilde{x}_{\mathrm{C}}}{2} \\ \tilde{x}_{\mathrm{d}} - \tilde{x}_{\mathrm{C}} + \tilde{\phi}_{\mathrm{C}} & \text{if} \quad \dfrac{\tilde{x}_{\mathrm{C}}}{2} \le \tilde{\phi}_{\mathrm{C}} < 1 + \tilde{x}_{\mathrm{C}} - \tilde{x}_{\mathrm{d}} \\ 1 & \text{if} \quad 1 + \tilde{x}_{\mathrm{C}} - \tilde{x}_{\mathrm{d}} \le \tilde{\phi}_{\mathrm{C}} \le 1 \\ \tilde{\phi}_{\mathrm{C}} & \text{elsewhere} \end{cases} \tag{3.21}$$

N.B. There is a typo in the MUSCL formula by Darwish and Moukalled [12].

SMART:

$$\tilde{\phi}_{\mathrm{d}} = \begin{cases} -\dfrac{\tilde{x}_{\mathrm{d}}\left(1 - 3\tilde{x}_{\mathrm{C}} + 2\tilde{x}_{\mathrm{d}}\right)}{\tilde{x}_{\mathrm{C}}\left(\tilde{x}_{\mathrm{C}} - 1\right)}\tilde{\phi}_{\mathrm{C}} & \text{if} \quad 0 \le \tilde{\phi}_{\mathrm{C}} < \dfrac{\tilde{x}_{\mathrm{C}}}{3} \\ \dfrac{\tilde{x}_{\mathrm{d}}\left(\tilde{x}_{\mathrm{d}} - \tilde{x}_{\mathrm{C}}\right)}{1 - \tilde{x}_{\mathrm{C}}} + \dfrac{\tilde{x}_{\mathrm{d}}\left(\tilde{x}_{\mathrm{d}} - 1\right)}{\tilde{x}_{\mathrm{C}}\left(\tilde{x}_{\mathrm{C}} - 1\right)}\tilde{\phi}_{\mathrm{C}} & \text{if} \quad \dfrac{\tilde{x}_{\mathrm{C}}}{3} \le \tilde{\phi}_{\mathrm{C}} < \dfrac{\tilde{x}_{\mathrm{C}}}{\tilde{x}_{\mathrm{d}}}\left(1 + \tilde{x}_{\mathrm{d}} - \tilde{x}_{\mathrm{C}}\right) \\ 1 & \text{if} \quad \dfrac{\tilde{x}_{\mathrm{C}}}{\tilde{x}_{\mathrm{d}}}\left(1 + \tilde{x}_{\mathrm{d}} - \tilde{x}_{\mathrm{C}}\right) \le \tilde{\phi}_{\mathrm{C}} \le 1 \\ \tilde{\phi}_{\mathrm{C}} & \text{elsewhere} \end{cases} \tag{3.22}$$

NOTABLE:

$$\tilde{\phi}_{\mathrm{d}} = \begin{cases} \dfrac{\tilde{\phi}_{\mathrm{C}}}{\tilde{x}_{\mathrm{C}}^2\left[\tilde{x}_{\mathrm{C}}\left(2 - \tilde{x}_{\mathrm{C}}\right) - 1\right]}\left(\begin{array}{l} \left[\tilde{x}_{\mathrm{d}}\left(2\tilde{x}_{\mathrm{C}} - \tilde{x}_{\mathrm{d}}\right) - \tilde{x}_{\mathrm{C}}^2\right]\tilde{\phi}_{\mathrm{C}}^2 \\ + \left[\begin{array}{l} \left(\tilde{x}_{\mathrm{d}} - \tilde{x}_{\mathrm{C}}\right)\left(1 - 3\tilde{x}_{\mathrm{C}}^2\right) \\ + \tilde{x}_{\mathrm{C}}\left(1 - \tilde{x}_{\mathrm{C}}^2\right) \\ - \tilde{x}_{\mathrm{d}}\left(1 - \tilde{x}_{\mathrm{d}}\right)\left(1 + \tilde{x}_{\mathrm{C}}\right) \end{array}\right]\tilde{\phi}_{\mathrm{C}} \\ + \left[\tilde{x}_{\mathrm{d}}\tilde{x}_{\mathrm{C}}\left(3\tilde{x}_{\mathrm{C}} - \tilde{x}_{\mathrm{d}} - 1\right) - \tilde{x}_{\mathrm{C}}^4\right] \end{array}\right) & \text{if} \quad 0 \le \tilde{\phi}_{\mathrm{C}} \le 1 \\ \tilde{\phi}_{\mathrm{C}} & \text{elsewhere} \end{cases} \tag{3.23}$$

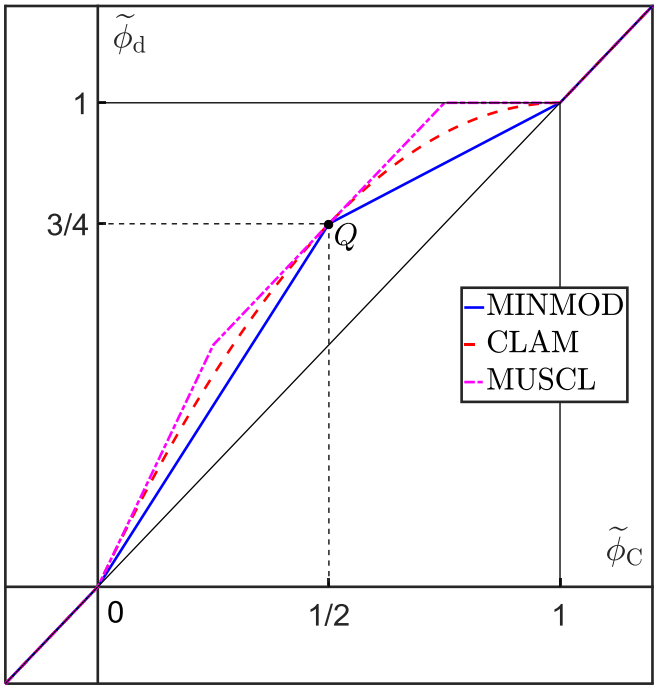

Figure 3.4 – Normalized variable diagram showing $\tilde{\phi}_d = f\left(\tilde{\phi}_C\right)$ for some second-order, high resolution schemes. A uniform mesh is assumed.

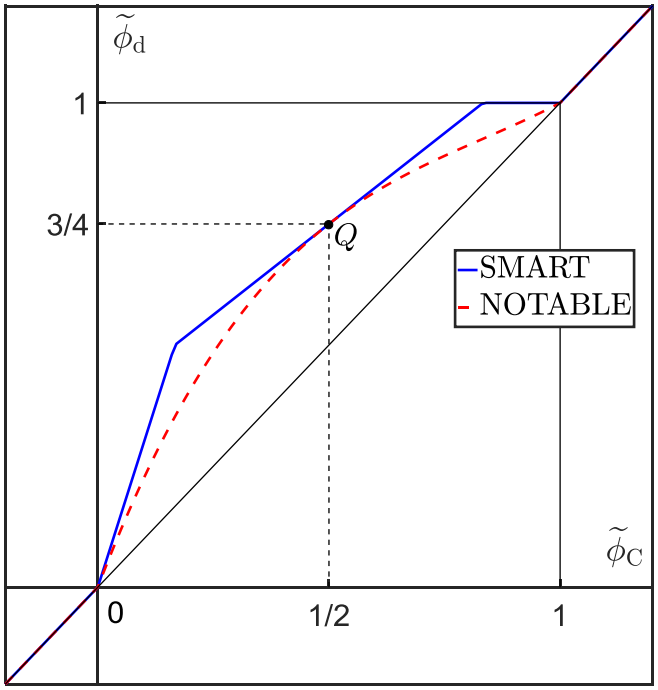

Figure 3.5 – Normalized variable diagram showing $\tilde{\phi}_d = f\left(\tilde{\phi}_C\right)$ for two, third-order, high resolution schemes. A uniform mesh is assumed.

3.1.4 Advection and Flux Limiters

The following logical tree is an equivalent statement of the convective boundedness criterion,

$$\begin{cases} \phi_{\mathrm{d}}\left(\phi_{\mathrm{U}},\phi_{\mathrm{C}},\phi_{\mathrm{D}}\right) \text{ is continuous} \\ \text{if } \phi(x) \text{ is monotonic} \\ \quad \text{then } \phi_{\mathrm{U}} \le \phi_{\mathrm{C}} \le \phi_{\mathrm{d}} \le \phi_{\mathrm{D}} \text{ or } \phi_{\mathrm{U}} \ge \phi_{\mathrm{C}} \ge \phi_{\mathrm{d}} \ge \phi_{\mathrm{D}} \\ \text{else } \phi_{\mathrm{d}} = \phi_{\mathrm{C}} \end{cases}.$$

If the scalar profile $\phi(x)$ is locally monotonic, then the range of possible estimates for ϕ_{d} must be limited to ensure that the interpolation scheme remains bounded. Waterson and Deconinck [18] reviewed the literature covering high resolution schemes and systematized the formulation of several dozen methods,

$$\begin{cases} \phi_{\mathrm{d}} = \phi_{\mathrm{C}} + \dfrac{x_{\mathrm{d}} - x_{\mathrm{u}}}{2}\Psi(r)\dfrac{\phi_{\mathrm{C}} - \phi_{\mathrm{U}}}{x_{\mathrm{C}} - x_{\mathrm{U}}} \\ \text{Uniform Mesh}: \phi_{\mathrm{d}} = \phi_{\mathrm{C}} + \dfrac{1}{2}\Psi(r)\left(\phi_{\mathrm{C}} - \phi_{\mathrm{U}}\right) \end{cases}, \tag{3.24}$$

where $\Psi(r)$ is a limiter function of the gradient ratio r,

$$\begin{cases} r = \dfrac{\phi_{\mathrm{D}} - \phi_{\mathrm{C}}}{x_{\mathrm{D}} - x_{\mathrm{C}}}\dfrac{x_{\mathrm{C}} - x_{\mathrm{U}}}{\phi_{\mathrm{C}} - \phi_{\mathrm{U}}} \\ \text{Uniform Mesh}: r = \dfrac{\phi_{\mathrm{D}} - \phi_{\mathrm{C}}}{\phi_{\mathrm{C}} - \phi_{\mathrm{U}}} \end{cases}. \tag{3.25}$$

Note that the gradient ratio defined by Waterson and Deconinck [18] is the reciprocal of the well-known gradient ratio proposed by Sweby [19], $r = 1/r_{\mathrm{Sweby}}$, leading to differences

in the form of non-symmetric limiters. Symmetric limiters, i.e. limiters that satisfy $\Psi(r)=r\Psi(1/r)$, remain unchanged. The limiter functions for several simple interpolation schemes are shown below,

$$\begin{cases} \text{CDS}: \Psi(r)=r \\ \text{UDS}: \Psi(r)=0 \\ \text{LUDS}: \Psi(r)=1 \\ \text{QUICK}: \Psi(r)=\dfrac{3}{4}r+\dfrac{1}{4} \end{cases}. \tag{3.26}$$

Harten [13] considered the simplified advection problem $\partial\phi/\partial t=-u\,\partial\phi/\partial x$ and noted that if $\phi(x)$ is assumed to be bounded, then any numerical approximation must be progressively less variable as it approaches convergence. For a finite volume discretization, the total variation, TV, of $\phi(x)$ is assessed by summation of the differences across cell faces,

$$\text{TV}\left(\phi^n\right)=\sum_{\text{all faces}}\left|\phi_{\text{P}}^n-\phi_{\text{F}}^n\right|, \tag{3.27}$$

where P and F are two adjacent control volumes and the superscript in ϕ^n represents either a given iteration or time step, for time marching or transient calculations, respectively. An interpolation scheme satisfies the total variation diminishing (TVD) condition if,

$$\text{TV}\left(\phi^{n+1}\right)\le\text{TV}\left(\phi^n\right). \tag{3.28}$$

Sweby [19] translated the TVD criterion into a set of boundaries on the limiter function $\Psi(r)$,

$$0 \le \Psi(r) \le \min(2r, 2) \quad \text{if} \quad r \ge 0. \tag{3.29}$$

As with the CBC, if the scalar profile is non-monotonic, i.e. $r < 0$, then $\phi_d = \phi_C$. Furthermore, since any second-order scheme constructed using only the cells $\{U, C, D\}$ must be a weighted average of the CDS and LUDS interpolations, Sweby [19] deduced the following additional restrictions for a second-order TVD scheme,

$$\min(r, 1) \le \Psi(r) \le \min(2, \max(r, \min(1, 2r))) \quad \text{if} \quad r \ge 0, \tag{3.30}$$

illustrated by the shaded area in Figure 3.6.

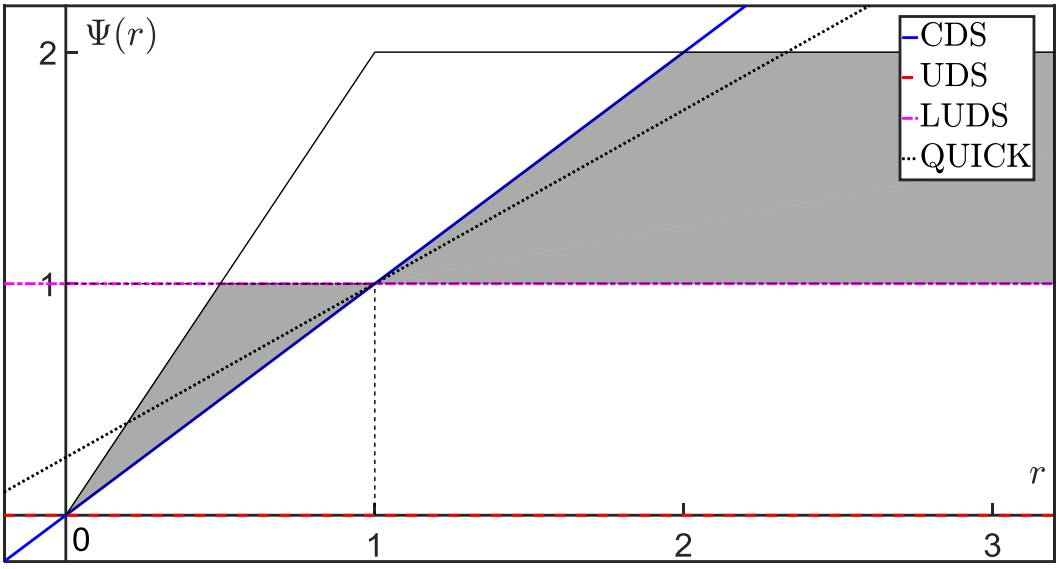

Figure 3.6 – Sweby diagram for various simple interpolation schemes. The shaded area denotes the second-order TVD region.

The high resolution schemes listed earlier using normalized variables can alternatively be written using flux limiters [18], and are represented in a Sweby diagram in Figures 3.7 and 3.8.

$$\text{MINMOD}: \Psi(r) = \max\left(0, \min(r, 1)\right), \tag{3.31}$$

$$\text{CLAM}: \Psi(r) = \max\left(0, \frac{r + |r|}{r + 1}\right), \tag{3.32}$$

$$\text{MUSCL}: \Psi(r) = \max\left(0, \min\left(2r, \frac{r+1}{2}, 2\right)\right), \tag{3.33}$$

$$\text{SMART}: \Psi(r) = \max\left(0, \min\left(2r, \frac{3r+1}{4}, 4\right)\right), \tag{3.34}$$

$$\text{NOTABLE}: \Psi(r) = \max\left(0, \frac{(r + |r|)(3r+1)}{2(r+1)^2}\right). \tag{3.35}$$

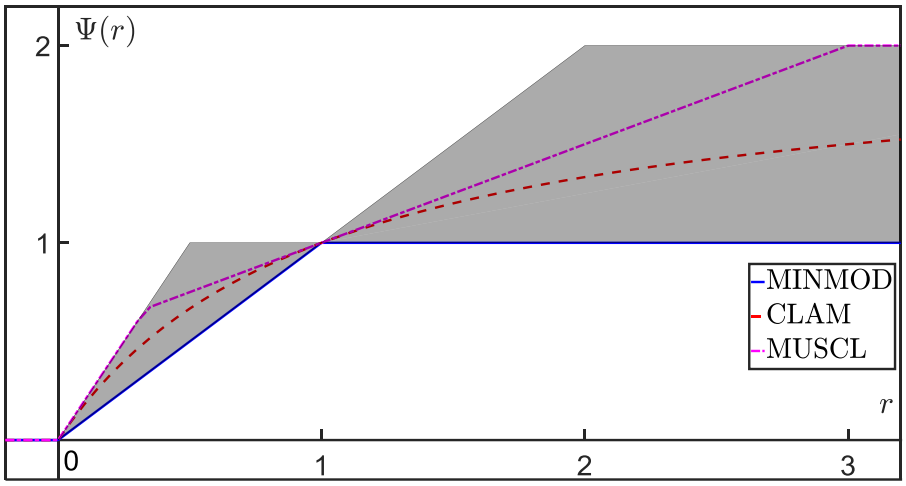

Figure 3.7 – Sweby diagram for some second-order, CBC compliant schemes.

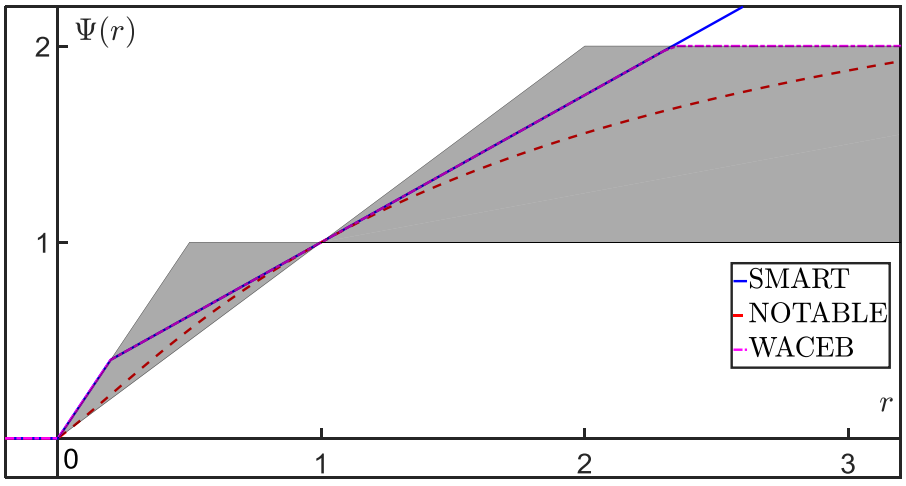

Figure 3.8 – Sweby diagram for some third-order, CBC compliant schemes.

The development of flux limiters predates the normalized variable diagram. Not coincidentally, over time many methods have been reinvented in either framework, such as e.g. the MINMOD, also known as SOUCUP [20] or the CLAM, known also as HPLA [21] or as van Leer's Harmonic limiter, highlighting the need for equivalency rules between the two approaches. On the other hand, the SMART and NOTABLE schemes are not TVD compliant,

$$\begin{cases} \Psi_{\text{SMART}}\left(r > 7/3\right) > 2 \\ \Psi_{\text{NOTABLE}}\left(r > \left(3+\sqrt{17}\right)/2\right) > 2 \end{cases}, \tag{3.36}$$

although the modifications needed to render them TVD are straightforward,

$$\text{SMART} \rightarrow \text{WACEB}: \Psi\left(r\right) = \max\left(0, \min\left(2r, \frac{3r+1}{4}, 2\right)\right) \text{ [22]}, \tag{3.37}$$

$$\text{NOTABLE} \rightarrow \text{NOTABLE 2.0}: \Psi\left(r\right) = \max\left(0, \min\left(\frac{\left(r+|r|\right)\left(3r+1\right)}{2\left(r+1\right)^2}, 2\right)\right). \tag{3.38}$$

The modified limiters are now TVD. The WACEB scheme is third-order accurate [22], however to assess if the novel NOTABLE 2.0 scheme retains third-order accuracy in the NVD, a set of conversion rules is necessary. As denoted by Leonard [23], the normalization of variables can also be applied to the formulation of flux limiters. For simplicity, a uniform mesh is assumed,

$$\tilde{\phi}_{\text{d}} = \tilde{\phi}_{\text{C}} + \frac{1}{2}\Psi\left(r\right)\tilde{\phi}_{\text{C}}, \tag{3.39}$$

$$r = \frac{1-\tilde{\phi}_{\text{C}}}{\tilde{\phi}_{\text{C}}}. \tag{3.40}$$

Therefore, by substituting eq. 3.40 into a limiter function, then substituting $\Psi(r)$ into eq. 3.39 and finally working out the intersections between the piecewise segments of $\Psi(r)$, $\tilde{\phi}_{\mathrm{d}} = f\left(\tilde{\phi}_{\mathrm{C}}\right)$ is recovered. Thus,

NOTABLE 2.0 :

$$\tilde{\phi}_{\mathrm{d}} = \begin{cases} 2\tilde{\phi}_{\mathrm{C}} & \text{if} \quad 0 \le \tilde{\phi}_{\mathrm{C}} < \dfrac{5-\sqrt{17}}{4} \\ \tilde{\phi}_{\mathrm{C}}\left(\tilde{\phi}_{\mathrm{C}}^2 - \dfrac{5}{2}\tilde{\phi}_{\mathrm{C}} + \dfrac{5}{2}\right) & \text{if} \quad \dfrac{5-\sqrt{17}}{4} \le \tilde{\phi}_{\mathrm{C}} \le 1 \\ \tilde{\phi}_{\mathrm{C}} & \text{elsewhere} \end{cases}, \tag{3.41}$$

and since $f(1/2) = 3/4$ and $f'(1/2) = 3/4$, NOTABLE 2.0 is third-order accurate. A similar procedure can be applied to the constraints imposed on $\Psi(r)$ by Sweby [19], yielding the TVD criterion in the normalized variable diagram [23].

3.1.5 Advection and the CUBISTA Scheme

Compiling all the requirements enunciated in sections 3.1.3 and 3.1.4, a scheme is third-order TVD if it satisfies,

$$\begin{cases} \text{i}: & \tilde{\phi}_{\mathrm{d}} = f\left(\tilde{\phi}_{\mathrm{C}}\right) \text{ is continuous} \\ \text{ii}: & \tilde{\phi}_{\mathrm{C}} \le f\left(\tilde{\phi}_{\mathrm{C}}\right) \le \min\left(2\tilde{\phi}_{\mathrm{C}}, 1\right) \text{ if } \tilde{\phi}_{\mathrm{C}} \in [0,1] \\ \text{iii}: & f\left(\tilde{x}_{\mathrm{C}}\right) = \tilde{x}_{\mathrm{d}} \\ \text{iv}: & f'\left(\tilde{x}_{\mathrm{C}}\right) = \dfrac{\tilde{x}_{\mathrm{d}} - 1}{\tilde{x}_{\mathrm{C}} - 1}\dfrac{\tilde{x}_{\mathrm{d}}}{\tilde{x}_{\mathrm{C}}} \end{cases}, \tag{3.42}$$

and if $\tilde{\phi}_C \notin [0,1]$, then $f(\tilde{\phi}_C) = \tilde{\phi}_C$. In addition to these constraints, the design of a scheme is informed by a set of desirable properties. In this section, the CUBISTA [24] scheme, used throughout this thesis, is examined in greater detail.

The TVD condition was developed for explicit time-dependent calculations [19]. For a given Courant number, $0 \le c \le 1$,

$$0 \le \Psi(r) \le \min\left(2r(1-c), 2(1-c)\right) \quad \text{if} \quad r \ge 0, \tag{3.43}$$

or alternatively, using normalized variables [23],

$$\tilde{\phi}_C \le f(\tilde{\phi}_C) \le \min\left((2-c)\tilde{\phi}_C, 1-c(1-\tilde{\phi}_C)\right) \text{ if } \tilde{\phi}_C \in [0,1], \tag{3.44}$$

where $c = |u|\Delta t/\Delta x$. For $c > 1$, explicit methods are unstable. The boundaries implied in eq. 3.43 are progressively less restrictive as c approaches zero, hence why the TVD condition is commonly stated for $c \to 0$, as was the case in section 3.1.4. Alves et al. [24] formulated an advection scheme by intercalating the QUICK scheme with the restrictions imposed by the generic TVD criterion,

$$\begin{aligned} \Psi(r) &= \max\left(0, \min\left(2r(1-c), \frac{3}{4}r + \frac{1}{4}, 2(1-c)\right)\right) \\ \Leftrightarrow \tilde{\phi}_d &= \begin{cases} (2-c)\tilde{\phi}_C & \text{if} \quad 0 \le \tilde{\phi}_C < \dfrac{3}{10-8c} \\ \dfrac{3}{4}\tilde{\phi}_C + \dfrac{3}{8} & \text{if} \quad \dfrac{3}{10-8c} \le \tilde{\phi}_C < \dfrac{8c-5}{8c-6} \\ 1-c(1-\tilde{\phi}_C) & \text{if} \quad \dfrac{8c-5}{8c-6} \le \tilde{\phi}_C \le 1 \\ \tilde{\phi}_C & \text{elsewhere} \end{cases} . \end{aligned} \tag{3.45}$$

As noted in section 3.1.2, the QUICK scheme may produce overshoots or undershoots when approximating the value of $\tilde{\phi}_{\mathrm{d}}$ near steep gradients, as a result of the non-monotonicity of quadratic polynomials. Considering a uniform mesh, the NVD formulation of the QUICK scheme for any point in the range $\tilde{x} \in [0,1]$ is as follows,

$$\tilde{\phi}(\tilde{x}) = 2\tilde{x}(\tilde{x} - 1/2) - 4\tilde{x}(\tilde{x} - 1)\tilde{\phi}_{\mathrm{C}}. \tag{3.46}$$

According to the CBC, $\tilde{\phi}(\tilde{x})$ must be a monotonic increasing function in $\tilde{x} \in [0,1]$, therefore the maximum of the second degree polynomial depicted in eq. 3.46 can at most be located at $\tilde{x} = 1$,

$$\left.\frac{\partial \tilde{\phi}(\tilde{x})}{\partial \tilde{x}}\right|_{\tilde{x}=1} = 4 - 1 - 8\tilde{\phi}_{\mathrm{C}} + 4\tilde{\phi}_{\mathrm{C}} = 0 \Leftrightarrow \tilde{\phi}_{\mathrm{C}} = \frac{3}{4}, \tag{3.47}$$

which serves as the upper boundary of the QUICK segment in eq. 3.45, leading to $c = 1/4$.

CUBISTA limiter:

$$\Psi(r) = \max\left(0, \min\left(\frac{3}{2}r, \frac{3}{4}r + \frac{1}{4}, \frac{3}{2}\right)\right) \tag{3.48}$$

CUBISTA scheme:

$$\tilde{\phi}_{\mathrm{d}} = \begin{cases} \frac{7}{4}\tilde{\phi}_{\mathrm{C}} & \text{if} \quad 0 \le \tilde{\phi}_{\mathrm{C}} < \frac{3}{8} \\ \frac{3}{4}\tilde{\phi}_{\mathrm{C}} + \frac{3}{8} & \text{if} \quad \frac{3}{8} \le \tilde{\phi}_{\mathrm{C}} < \frac{3}{4} \\ \frac{1}{4}\tilde{\phi}_{\mathrm{C}} + \frac{3}{4} & \text{if} \quad \frac{3}{4} \le \tilde{\phi}_{\mathrm{C}} \le 1 \\ \tilde{\phi}_{\mathrm{C}} & \text{elsewhere} \end{cases} \tag{3.49}$$

3.2 Computational Rheology

An important development in Rheology was the introduction of computational techniques, beginning in the late 1960s. As reviewed by Crochet and Walters [25], the initial attempts to simulate experimental flows were more successful whenever elasticity played at most a marginal role, and the early literature can be organized into three broad categories. First, shear dominated flows which can be modelled, to a reasonable degree of accuracy, using a shear-thinning generalized Newtonian fluid (GNF) model. Duda and Ventras [26] pioneered this category with their simulations of creeping flow in a 4:1 two-dimensional contraction, based on a finite difference implementation, and in general, methods developed for Newtonian Computational Fluid Dynamics (CFD) can be used with a variable viscosity function $\eta(\dot{\gamma})$ without added complications.

Second, slow flows or slightly elastic fluids. The Deborah number De is defined as the ratio between the relaxation time of the fluid λ and a characteristic time of the flow t_c, which is often obtained via a characteristic length L and velocity U,

$$\mathrm{De} = \lambda \frac{U}{L}. \tag{3.50}$$

Incidentally, Crochet and Walters [25] refer to this dimensionless group as the Weissenberg number Wi, which although formally defined as the ratio of elastic to viscous stresses, coincides with the Deborah number whenever the dynamics of a flow are primarily determined by one length scale [27]. Flows with low De, either because of low flow rates or low elasticity, may be successfully modeled using a retarded motion expansion (see Chap. 6 in Ref. [28]), that is, an expansion of Newton's law of viscosity incorporating higher order derivatives of the rate-of-strain tensor $\dot{\boldsymbol{\gamma}}$. For instance, consider the constitutive equation for the second order fluid,

$$\boldsymbol{\sigma} = b_1 \dot{\boldsymbol{\gamma}} + b_2 \overset{\nabla}{\dot{\boldsymbol{\gamma}}} + b_{11} \left(\dot{\boldsymbol{\gamma}} \cdot \dot{\boldsymbol{\gamma}} \right), \tag{3.51}$$

where b_1, b_2 and b_{11} are retarded motion constants. If $b_2 = b_{11} = 0$, then $b_1 = \mu$ and Newtonian behavior is recovered. Early numerical results using higher order fluids were obtained by Walters and co-workers, e.g. [29], who used a hybrid analytical approach to study edge effects in rheological measurements, by Crochet and co-workers, e.g. [30], using a finite difference method to study the flow in a lid-driven cavity and by Datta and Strauß [31] who simulated the flow in a contraction using a finite element implementation.

Third, nearly viscometric flows. A viscometric flow is defined as "a laminar shear flow in which fluid particles on any streamline are always the same distance apart" [32], and may be either shear driven, e.g. Couette flow, or pressure driven, e.g. Poiseuille flow. Certain weakly elastic flows can be regarded as perturbations about a viscometric flow field. This approach was pioneered by Barnes et al. [33], who studied the pipe flow of viscoelastic fluids in industrially relevant conditions, by modeling the fluctuating pressure gradient generated by conventional pumping systems as a perturbation about a steady state. To this end, Barnes et al. employed a simplified Oldroyd 8-constant model [34], applicable to simple shear flows, in order to derive an expression for the effective viscosity which would then be substituted into a constitutive equation of the GNF type $\boldsymbol{\sigma} = \eta(\dot{\gamma})\dot{\boldsymbol{\gamma}}$,

$$\begin{cases} \lambda_1 = \mu_1 \\ \lambda_2 = \mu_2 \\ \nu_1 = \nu_2 = 0 \\ \Rightarrow \eta(\dot{\gamma}) = \eta_0 \dfrac{1+\lambda_2\mu_0\dot{\gamma}^2}{1+\lambda_1\mu_0\dot{\gamma}^2} \end{cases}, \tag{3.52}$$

where $\{\eta_0, \lambda_1, \lambda_2, \mu_0, \mu_1, \mu_2, \nu_1, \nu_2\}$ are material constants. The Oldroyd 8-constant model is an expansion of the Oldroyd-B model including all possible quadratic terms involving products of the polymeric extra stress tensor $\boldsymbol{\tau}$ and rate-of-strain tensor $\dot{\boldsymbol{\gamma}}$, and of $\dot{\boldsymbol{\gamma}}$ with itself. The method developed by Barnes et al. therefore indirectly accounts for elasticity, assuming that deformations are small, i.e. that viscoelasticity is linear.

3.2.1 The High Weissenberg Number Problem (HWNP)

The initial concern with flows wherein elasticity plays a small role stems in part from the analytical intractability of nonlinear viscoelastic boundary value problems. In separate assessments of the state of non-Newtonian fluid mechanics in the 1970s, Astarita [35] and Walters [36], while acknowledging the importance of early contributions, urge the community to focus on complex flows with strong elastic effects, of the kind common in the plastics industry. Simultaneously, the processing speed and memory of computers were increasing at a rapid pace, for the first time allowing the simulation of nonlinear viscoelastic flows. However, it soon became apparent that numerical work was limited to low levels of elasticity, either because simulations would diverge above $\mathrm{De} \approx O(1)$, different methods would yield radically different results or in the few instances were a broader range of De was attainable, numerical work failed to reproduce experimental observations. Furthermore, failure occurred regardless of numerical method, flow geometry or constitutive model. This systematic numerical divergence became known as the High Weissenberg Number Problem (HWNP), and is reviewed in detail in Chap. 7 of Ref. [37]. The naming of the phenomenon is itself somewhat of a misnomer, since most studies at the time used the Deborah number as a measure of relative elasticity.

Many contributions in the early to mid-1980s addressed the HWNP, such as Mendelson et al. [38], Crochet and Walters [25], Davies [39], Brown et al. [40] and Keunings [41], to name a few of the more notable publications. Opinions on the causes of the HWNP were diverse but, for the purposes of this discussion, the classification proposed by Brown et al. [40] is adopted. Sources of numerical divergence were categorized in one of two groups: mathematical loss of existence or uniqueness of solutions, or excessive approximation error. The first group concerns various processes of an analytical nature, referred to as inherent instabilities by Davies [39], which stem from the choice of constitutive model, boundary conditions, flow geometry or other parameters. It should be noted that in the 1970s and 1980s, computational rheology was primarily concerned with two-dimensional, steady state flows. In some instances the cause of the HWNP may indeed have been a bifurcation, in which a single solution family branches into separate paths with increasing Deborah number, leading to the loss of uniqueness of the steady state solution. For example, for the Taylor-Couette flow of an

UCM fluid, an analytical investigation by Renardy et al. [42] uncovered a family of potential bifurcations at the terminus of stationary flow. Alternatively, at relatively low De, many viscoelastic flows become time-dependent, leading to the loss of existence of the steady state solution, even in very simple geometries, as shown by e.g. the linear stability analysis of viscoelastic channel flows by Wilson et al. [43],[44]. Both phenomena are recurring elements of this thesis, and have been experimentally documented in several variants of the cross-slot geometry e.g. [45],[46],[47]. In their review, Crochet and Walters [25] mentioned the inadequacy of constitutive equations, specifically concerning the prevalence of the Oldroyd-B and upper-convected Maxwell models and their known unbounded extensional viscosity. However, it is now apparent that at least some of the instabilities, which were thought to be modeling artifacts, are integral to the physical nature of viscoelastic flows.

3.2.2 The HWNP and Approximation Error

The second group proposed by Brown et al. [40] refers to causes of a numerical nature, or as Davies [39] put it, induced instabilities. In the opening plenary lecture of the XIIIth International Congress on Rheology [48], held in 2000, Keunings outlined three sources of approximation error: (1) local changes in the mathematical type of the coupled system of governing equations, namely from elliptic to hyperbolic; (2) the non-integrability of stress singularities, a problem which also exists in Newtonian fluid mechanics but is exacerbated by viscoelasticity; (3) the emergence of stress boundary layers in geometries where a Newtonian flow is smooth. The first source of error was studied in greater detail by Joseph et al. [49],[50], who postulated that for models without a solvent viscosity contribution, such as the upper-convected Maxwell (UCM) fluid, the vorticity equation changes type whenever the viscoelastic Mach number, M, exceeds one. This is defined as,

$$M = \frac{U}{c} = \frac{U}{\sqrt{\eta/(\rho\lambda)}}, \tag{3.53}$$

where U is the velocity of the unperturbed uniform flow, c is the velocity of propagation of shear wave fronts, ρ is the density of the fluid, and η and λ are the viscosity and relaxation time of the UCM model, respectively. Should this change in type occur, the flow problem is no longer well-posed, meaning that a solution may no longer exist or be unique, or that the flow field is unstable in the Hadamard sense, i.e. the solution no longer evolves continuously with the initial conditions. However, Joseph et al. [50] noted that the addition of a Newtonian solvent contribution to the constitutive equations should regularize the aforementioned Hadamard instabilities. A more comprehensive treatment of the mathematical theory of viscoelasticity is presented in Chap. 3 of Ref. [37].

The second source of approximation error is the non-integrability of stress singularities. Historically, a greater amount of attention has been devoted to the reentrant corner in contraction flows. As described by Hinch [51], although the velocity tends to zero near a reentrant corner, the velocity gradient in the limit $r \to 0$ is infinite, where r is the radius in the 270° arc around the corner. As a result, and perhaps counterintuitively, the residence time of polymer molecules in the corner region tends to zero, yet the polymer deforms affinely with the fluid, hence the large velocity gradient in turn generates a large normal stress gradient. Based on the construction of a similarity solution, Hinch [51] inferred that the normal stress scales as $r^{-2/3}$ for an Oldroyd-B fluid. Renardy [52] studied the same problem for a UCM fluid, and assuming a Newtonian velocity field, calculated an asymptotic growth of the normal stress proportional to $r^{-0.74}$. Davies and Devlin [53] constructed several perturbation series which are exact solutions of the governing equations for the creeping flow of an Oldroyd-B fluid near reentrant corners, and arrived at a normal stress scaling of $r^{-0.613}$. Although the predicted rate of growth differs for each analytical method, the scaling of the normal stress near reentrant corners is uncontroversially asymptotic.

The third source of approximation error is the emergence of stress boundary layers. As described by Renardy [54], for high Weissenberg number flows, the convected derivative terms of the constitutive equations become important at a short distance from the walls. Since inherently there is no convection at walls, this leads to sharp boundary layers. Additionally, Harlen et al. [55] explored the formation and evolution of so-called birefringence strands in elongational flows, i.e. localized changes in the refractive index of polymer solutions or melts as a result of stretching. Provided the extension rate of the flow, $\dot{\varepsilon}$, is sufficiently large to overcome the inverse of the relaxation time of the

polymer, λ, polymer molecules undergo a coil-stretch transition [56] when passing close to a stagnation point, and depending on the relaxation time and flow rate, remain stretched some distance downstream. One of the classical benchmark problems, flow past a cylinder in a channel (see e.g. Chap. 9 in Ref. [37]), displays both types of stress concentration, along the edge of the cylinder and downstream of the stagnation point in the wake [57]. Experimental setups such as the opposed jets device, the four roll mill or several variants of the cross-slot geometry [58] are characterized by the existence of a free stagnation point, which in turn generates a birefringent strand detached from any walls, posing many of the same numerical challenges as a stress boundary layer. For constitutive equations with unbounded extensional viscosity, such as the UCM or Oldroyd-B models, free stagnation points of the cross-slot kind are singular in normal stress whenever $\dot{\varepsilon} \geq 1/(2\lambda)$.

3.2.3 The HWNP and Finite Element Methods

As reviewed by Baaijens [59], Owens and Phillips (Chap. 7 in Ref. [37]) and Coronado (Chap. 3 in Ref. [60]), throughout the 1980s and 1990s advances in computational rheology were primarily driven by attempts to defeat the high Weissenberg number problem using finite element implementations. A detailed discussion of these methods would fall outside the scope of this thesis, in which a finite volume implementation is used. However, two important methods are mentioned. Concerning the potentially mixed elliptic-hyperbolic character of the system of governing equations, Rajagopalan et al. [61] proposed the Elastic Viscous Split Stress (EVSS) formulation. Using the Oldroyd-B model as an example, this formulation splits the extra stress tensor $\boldsymbol{\sigma}$ in two components, one which aggregates the viscous contributions of both polymer and solvent, $\boldsymbol{\sigma}_v$, and a second component comprised only of the elastic contribution of the polymer, $\boldsymbol{\sigma}_e$,

$$\begin{cases} \boldsymbol{\sigma} = \boldsymbol{\sigma}_v + \boldsymbol{\sigma}_e \\ \boldsymbol{\sigma}_v = \eta_0 \dot{\boldsymbol{\gamma}} \\ \boldsymbol{\sigma}_e = \boldsymbol{\tau} - \eta_p \dot{\boldsymbol{\gamma}} \end{cases}, \tag{3.54}$$

where $\eta_0 = \eta_s + \eta_p$. Rewriting the governing equations accordingly, for an incompressible flow,

$$\begin{cases} \text{Continuity}: \ \nabla \cdot \mathbf{u} = 0 \\ \text{Momentum}: \ \rho\left(\dfrac{\partial \mathbf{u}}{\partial t} + \mathbf{u} \cdot \nabla \mathbf{u}\right) = -\nabla p + \eta_0 \nabla^2 \mathbf{u} + \nabla \cdot \boldsymbol{\sigma}_e \ . \\ \text{Oldroyd-B}: \ \boldsymbol{\sigma}_e + \lambda \overset{\nabla}{\boldsymbol{\sigma}}_e = -\lambda \eta_p \overset{\nabla}{\dot{\boldsymbol{\gamma}}} \end{cases} \tag{3.55}$$

In essence, the elastic-viscous separation adds a diffusive term to the momentum equations, $\eta_p \nabla^2 \mathbf{u}$, which was removed from the constitutive equations, therefore ensuring that the former remain elliptic even when $\eta_s = 0$ while the latter are strictly hyperbolic [61].

Another important method used in finite element discretizations concerns the suppression of spurious oscillations which emerge when the advective terms in the constitutive equations are dominant, as is the case in high Weissenberg number flows. In a manner analogous to upwinding schemes applied to the momentum equations, the streamline upwind Petrov-Galerkin (SUPG) method, which, not coincidentally, was first devised by Brooks and Hughes [3] for the treatment of advection in Newtonian problems, was applied by Marchal and Crochet [62] to the constitutive equations. The SUPG method entails the following weak formulation of the Oldroyd-B model,

$$\int_\Omega \left(\boldsymbol{\tau} + \lambda \overset{\nabla}{\boldsymbol{\tau}} - \eta_p \dot{\boldsymbol{\gamma}} \right) : \left(\mathbf{S} + \alpha \mathbf{u} \cdot \nabla \mathbf{S} \right) \mathrm{d}\Omega = 0, \ \forall \mathbf{S} \in \Sigma \, , \tag{3.56}$$

where Ω is a bounded domain, Σ is the function space for the polymeric extra stress and $\alpha = h/U$ is a parameter incorporating a characteristic length scale h associated with the finite element discretization and a characteristic velocity U which is e.g. the norm of $\mathbf{u}$ at the center of an element. The test function of the Galerkin weak formulation, $\mathbf{S}$, is

augmented in the SUPG method with the advective term $\alpha\mathbf{u}\cdot\nabla\mathbf{S}$, imposing streamline upwinding on the stress field, without adding crosswind diffusion.

The EVSS and SUPG methods, or their variants, are normally used in conjunction and remain popular today. However, convection is weaker near walls, thus the term $\alpha\mathbf{u}\cdot\nabla\mathbf{S}$ tends to vanish, leading to difficulties in the resolution of stress boundary layers. Wall attached singularities in particular produce the kind of spurious oscillations that the SUPG method was devised to remedy [63]. Traditionally, these obstacles have been dealt with by either reducing the size of elements near walls, and therefore increasing computational demand, or by adding additional diffusive terms to the governing equations. Concerning the latter strategy, Keunings [48] reasoned that artificial diffusion changes the nature of the problem, in such a way that numerical results obtained using artificial diffusion are generally not a reasonable approximation of the flow under investigation.

3.2.4 The HWNP and the Log-Conformation Representation (LCR)

The difficulties generated by hyperbolic governing equations, stress boundary layers or stress singularities can be traced to the inability of polynomial interpolations or reconstructions to approximate exponentially or asymptotically growing stress profiles. To remedy this problem, Fattal and Kupferman [64],[65],[66] proposed a logarithmic transformation of the constitutive equation. The crux of their method is the decomposition of the velocity gradient into extensional and rotational components, proven in Ref. [64],

$$\left(\nabla\mathbf{u}\right)^{\dagger} = \boldsymbol{\Omega} + \mathbf{B} + \mathbf{N}\mathbf{A}^{-1}$$

where $\boldsymbol{\Omega}$ is the rotational component, $\mathbf{B}$ is the extensional component, $\mathbf{N}$ is an auxiliary matrix that vanishes when the decomposition is substituted into the constitutive equation and $\mathbf{A}^{-1}$ is the inverse of the conformation tensor. Furthermore, $\boldsymbol{\Omega}$ and $\mathbf{N}$ are antisymmetric, therefore $-\boldsymbol{\Omega} = \boldsymbol{\Omega}^{\dagger}$ and $-\mathbf{N} = \mathbf{N}^{\dagger}$, and $\mathbf{B}$ is diagonal and commutes with $\mathbf{A}$, $\mathbf{AB} = \mathbf{BA}$. In their proof, Fattal and Kupferman defined $\left(\nabla\mathbf{u}\right)_{ij} = \partial u_i / \partial x_j$, whereas

this thesis uses the convention $\left(\nabla \mathbf{u}\right)_{ij} = \partial u_j / \partial x_i$ [67],[68], leading to slight differences in notation. Writing the Oldroyd-B model in conformation tensor notation,

$$\begin{cases} \lambda \overset{\nabla}{\mathbf{A}} = -\left(\mathbf{A} - \mathbf{I}\right) \\ \boldsymbol{\tau} = \dfrac{\eta_p}{\lambda}\left(\mathbf{A} - \mathbf{I}\right) \end{cases}, \tag{3.57}$$

followed by substitution of the velocity gradient decomposition leads to [64],

$$\frac{\partial \mathbf{A}}{\partial t} + \mathbf{u} \cdot \nabla \mathbf{A} - \left(\boldsymbol{\Omega}\mathbf{A} - \mathbf{A}\boldsymbol{\Omega}\right) - 2\mathbf{B}\mathbf{A} = -\frac{1}{\lambda}\left(\mathbf{A} - \mathbf{I}\right). \tag{3.58}$$

Since $\mathbf{A}$ is symmetric positive definite, it can be diagonalized as follows,

$$\mathbf{A} = \mathbf{R}\boldsymbol{\Lambda}\mathbf{R}^{\dagger}, \tag{3.59}$$

where the columns of $\mathbf{R}$ are the eigenvectors of $\mathbf{A}$ and the diagonal matrix $\boldsymbol{\Lambda}$ contains the corresponding eigenvalues. Given this decomposition, the natural logarithm of $\mathbf{A}$ is calculated as,

$$\boldsymbol{\Theta} = \ln\left(\mathbf{A}\right) = \mathbf{R}\ln\left(\boldsymbol{\Lambda}\right)\mathbf{R}^{\dagger}. \tag{3.60}$$

Following the procedure outlined by Fattal and Kupferman [64], the constitutive equation for $\boldsymbol{\Theta}$ is as follows,

$$\frac{\partial \boldsymbol{\Theta}}{\partial t} + \mathbf{u} \cdot \nabla \boldsymbol{\Theta} - \left(\boldsymbol{\Omega}\boldsymbol{\Theta} - \boldsymbol{\Theta}\boldsymbol{\Omega}\right) - 2\mathbf{B} = \frac{1}{\lambda}\left(e^{-\boldsymbol{\Theta}} - \mathbf{I}\right). \tag{3.61}$$

Since $\boldsymbol{\Theta}$ is also symmetric positive definite, recovery of the conformation tensor is straightforward,

$$\mathbf{A} = e^{\boldsymbol{\Theta}} = \mathbf{R} e^{\boldsymbol{\Lambda}_\Theta} \mathbf{R}^\dagger, \tag{3.62}$$

where $\boldsymbol{\Lambda}_\Theta$ is the diagonal matrix of the eigenvalues of $\boldsymbol{\Theta}$. As discussed by Habla et al. [69], the eigenvectors $\mathbf{R}$ are the same for both $\boldsymbol{\Theta}$ and $\mathbf{A}$, and furthermore $\boldsymbol{\Lambda} = e^{\boldsymbol{\Lambda}_\Theta}$, therefore the eigenvalues and eigenvectors of $\boldsymbol{\Theta}$ can be saved and reused to diagonalize $\mathbf{A}$ at the start of the next iteration or time loop.

The key property of the log-conformation representation is the conversion of exponential stress growth into linear growth, an observation made clear by a comparison of the terms containing the extensional component $\mathbf{B}$ of the velocity gradient [64],

$$\begin{cases} \dfrac{\partial \mathbf{A}}{\partial t} = 2\mathbf{B}\mathbf{A} \Rightarrow \mathbf{A}(t) = \mathbf{A}(0) e^{2\mathbf{B}t} \\ \dfrac{\partial \boldsymbol{\Theta}}{\partial t} = 2\mathbf{B} \Rightarrow \boldsymbol{\Theta}(t) = \boldsymbol{\Theta}(0) + 2\mathbf{B}t \end{cases}. \tag{3.63}$$

$\boldsymbol{\Theta}$ profiles are smooth and can in principle be approximated with low order polynomials, ensuring the stability of simulations. However, a high level of resolution may still be necessary to ensure the accuracy of numerical results [65]. Furthermore, the onset of numerical instabilities has been observed to coincide with the loss of positive definiteness of $\mathbf{A}$ [70], whereas with a formulation based on $\ln(\mathbf{A})$, positivity is guaranteed [64]. Other transformations of the constitutive equation have been proposed, such as the square-root-conformation [71] or the more general kernel-conformation [72] methods, which remain less popular than the log-conformation representation (LCR). The LCR method is used throughout this thesis.

3.3 Purely Elastic Instabilities

The first documented purely elastic instability was reported in 1966 by Giesekus [73] while studying the Taylor-Couette flow of a shear-thinning solution of polyisobutylene in decalin. At a negligible Reynolds number, $\mathrm{Re} = 0.01$, and above an unspecified Deborah number, Giesekus noted the formation of cellular structures reminiscent of Taylor vortices [74]. Taylor-Couette flows subsequently became the source of initial insight into the dynamics of nearly inertialess, elasticity driven flow transitions, in a series of studies conducted by Larson, Muller and Shaqfeh, beginning in 1989 [75],[76],[77],[78],[79]. Other flow configurations have also proven conducive to the development of purely elastic instabilities, such as: Poiseuille flow through a curved channel, otherwise known as Dean flow [80]; lid-driven cavity flow [81]; cone-and-plate and parallel-plate flows of the kind common in rheometry [82]; or flow in the wake of a confined cylinder [83]. Shaqfeh [84] reviewed the early literature concerning these instabilities, with particular emphasis on viscometric flows.

All of the above examples seem to indicate that elastic instabilities preferentially occur in flows with at least some degree of curvature. Additionally, viscoelastic flows are linearly stable to infinitesimal perturbations [85], although it is possible to disturb a viscoelastic flow in a straight channel, using e.g. a series of obstacles [86], triggering nonlinear instabilities that do not decay further along the downstream direction. Nevertheless, this method can be thought of as a way to introduce curvature in an otherwise stable flow [87]. McKinley et al. [81],[88] pondered the relation between curvature and elasticity and developed a dimensionless criterion for the onset of instabilities based on an earlier micromechanical model proposed by Larson et al. [76], depicted in Figure 3.9. The Pakdel-McKinley criterion, M, is defined as follows,

$$M = \sqrt{\frac{\lambda U}{R}\frac{\tau_{ss}}{\eta_0 \dot{\gamma}}}, \tag{3.64}$$

where λ is the (principal) relaxation time of the fluid, U is a characteristic streamwise velocity, R is a characteristic radius of curvature, τ_{ss} is the streamwise tensile stress, η_0

is the zero-shear-rate viscosity and $\dot{\gamma}$ is a characteristic local deformation rate. The onset of purely elastic instabilities occurs whenever M reaches a certain critical value, usually $1 < M_{crit} < 10$, depending on the flow geometry [81],[88],[89],[90],[91].

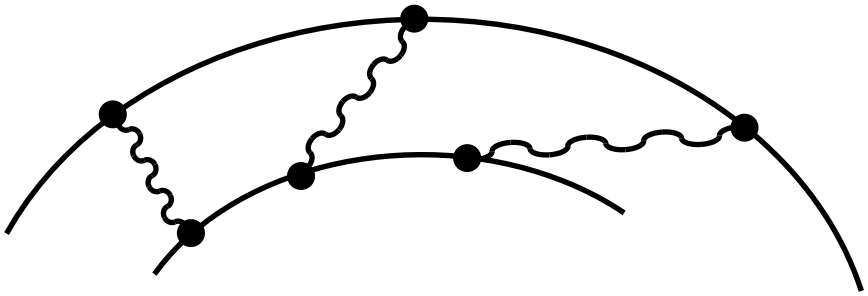

Figure 3.9 – Illustrative model of the coupling between elastic stress and curved streamlines. Polymer molecules not fully aligned with the underlying streamlines generate additional stress.

Both Shaqfeh [84] and McKinley et al. [88] acknowledged the existence of different types of instability, especially concerning their temporal behavior. As a given control parameter is varied, typically the Weissenberg or Deborah number, a flow problem may bifurcate, i.e. experience changes in the number and stability of solutions. Bifurcations are ubiquitous in physical systems, as extensively reviewed by Cross and Hohenberg [92]. In a dynamic system, a stable equilibrium or periodic cycle is referred to as an attractor, whereas an unstable solution is designated as a repellor. Two types of transition are especially relevant to this thesis, pitchfork and Hopf bifurcations, as they encapsulate the recurring distinction between stationary and time-dependent instabilities, respectively. The simplest state equation capable of generating a pitchfork bifurcation is the first-order ordinary differential equation (ODE) of the form [92],

$$\begin{aligned} &\text{(a) supercritical}: \dot{x}(t) = px(t) - x^3(t) \\ &\text{(b) subcritical}: \quad \dot{x}(t) = px(t) + x^3(t) \end{aligned}, \tag{3.65}$$

where $x(t)$ is a dependent variable and p is a parameter with critical value $p_{crit} = 0$. The supercritical and subcritical variants of the bifurcation are depicted in Figure 3.10, and are interpreted as collisions of equilibria [93]. Physically, and within the context of purely

elastic instabilities, supercritical pitchfork bifurcations are often identifiable by the formation of stationary flow asymmetries, as documented by e.g. Galindo-Rosales et al. [94] for a variety of micro-scale geometries.

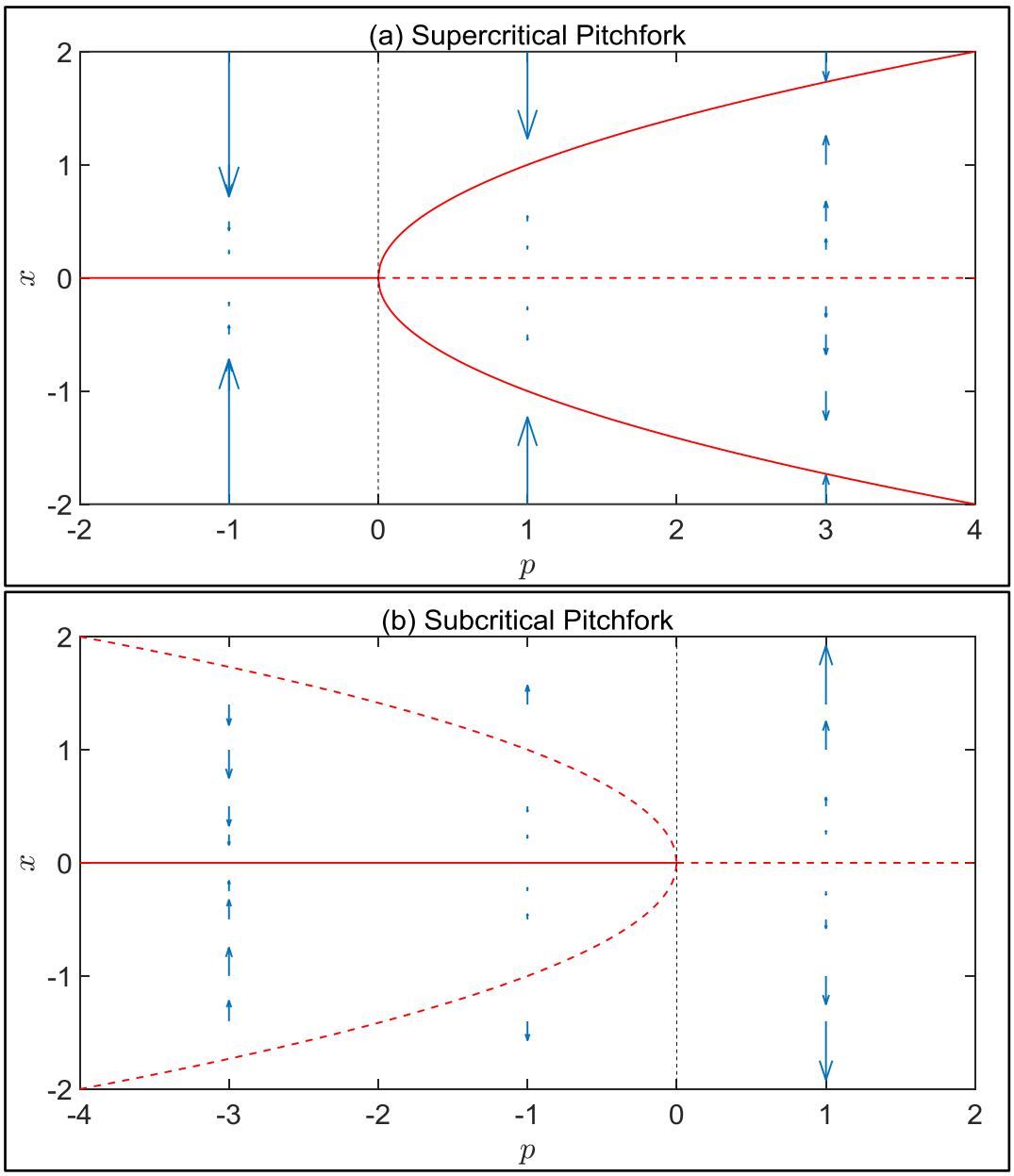

Figure 3.10 – Pitchfork bifurcations obtained from eqs. 3.65. The arrows, scaled to 90% of their real length, represent $\dot{x}(0) = f\left(x(0), p\right)$ and indicate the trajectory of the system towards stable, or away from unstable, equilibria. **(a)** For $p \to 0^{+}$, the attractors $x(t) = \pm\sqrt{p}$ collide with the repellor $x(t) = 0$, degenerating into the single attractor $x(t) = 0$ for $p < 0$. **(b)** For $p \to 0^{-}$, the repellors $x(t) = \pm\sqrt{-p}$ collide with the attractor $x(t) = 0$, degenerating into the single repellor $x(t) = 0$ for $p > 0$.

Hopf bifurcations only occur in systems with at least two ODEs, and the simplest possible state equations are [92],

$$\begin{aligned}
&\text{(a) supercritical}: \begin{cases} \dot{x}_1(t) = p x_1(t) - x_2(t) - \|\mathbf{x}(t)\|^2 x_1(t) \\ \dot{x}_2(t) = x_1(t) + p x_2(t) - \|\mathbf{x}(t)\|^2 x_2(t) \end{cases} \\
&\text{(b) subcritical}: \begin{cases} \dot{x}_1(t) = p x_1(t) - x_2(t) + \|\mathbf{x}(t)\|^2 x_1(t) \\ \dot{x}_2(t) = x_1(t) + p x_2(t) + \|\mathbf{x}(t)\|^2 x_2(t) \end{cases}
\end{aligned}, \tag{3.66}$$

where $\mathbf{x} = (x_1, x_2)$ is the dependent variable vector and p is a parameter with critical value $p_{crit} = 0$. The state equations may alternatively be expressed in polar coordinates [93],

$$\begin{aligned}
&\text{(a) supercritical}: \begin{cases} \dot{r}(t) = p r(t) - r^3(t) \\ \dot{\varphi}(t) = 1 \end{cases} \\
&\text{(b) subcritical}: \begin{cases} \dot{r}(t) = p r(t) + r^3(t) \\ \dot{\varphi}(t) = 1 \end{cases}
\end{aligned}, \tag{3.67}$$

where r and φ denote the radial and angular coordinates, respectively. The expressions for $\dot{r}(t)$ are identical to the state equations of a pitchfork bifurcation (cf. eqs. 3.65), therefore a Hopf bifurcation can be visualized by axial rotation of the plots in Figure 3.10 about $x = 0$, as shown in Figure 3.11. In the supercritical case, for $p > p_{crit}$, instead of a stationary equilibrium the system settles into a periodic orbit, otherwise referred to as a limit-cycle. The early instances of purely elastic instabilities reviewed by Shaqfeh [84] and McKinley et al. [88] were predominantly of the periodic kind, and although the existence of stationary asymmetric or time-dependent aperiodic flows was acknowledged in both reviews, investigations concerning these alternative types of instability would only proliferate in the early 2000s, largely due to the popularization of microfluidics [95],[96] and the discovery of elastic turbulence [97],[98].

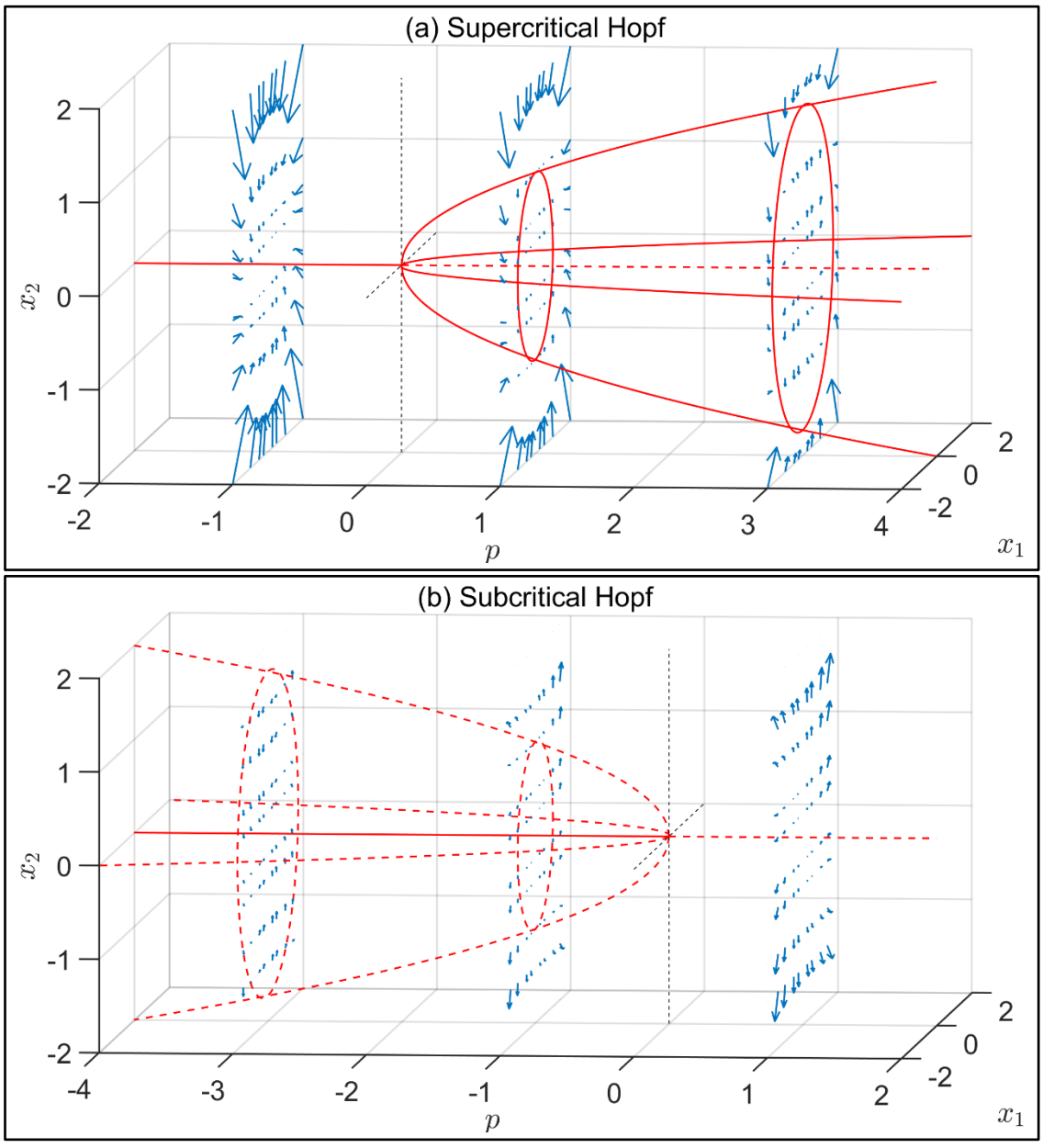

Figure 3.11 – Hopf bifurcations obtained from eqs. 3.66. The arrows, scaled to 200% of their real length, represent $\dot{\mathbf{x}}(0) = f(\mathbf{x}(0), p)$ and indicate the trajectory of the system towards stable, or away from unstable, equilibria. **(a)** For $p \to 0^+$, the attractor limit-cycle $\|\mathbf{x}(t)\| = \sqrt{p}$ collides with the repellor $\|\mathbf{x}(t)\| = 0$, degenerating into the attractor $\|\mathbf{x}(t)\| = 0$ for $p < 0$. **(b)** For $p \to 0^-$, the repellor limit-cycle $\|\mathbf{x}(t)\| = \sqrt{-p}$ collides with the attractor $\|\mathbf{x}(t)\| = 0$, degenerating into the repellor $\|\mathbf{x}(t)\| = 0$ for $p > 0$.

3.3.1 Microfluidics

The main challenge posed by the study of purely elastic instabilities, and consequently the reason why such phenomena have only been brought to the forefront of fluid dynamics research in the past 30 years, is the interfering effect of inertia. The Reynolds number quantifies the ratio of inertial to viscous forces [99],

$$\mathrm{Re} = \frac{\rho U d}{\eta}, \tag{3.68}$$

where ρ is the density of the fluid, U is a characteristic velocity, d is a characteristic length scale of the flow geometry, usually the spanwise width of some vessel, and η is the shear viscosity of the fluid. With the exception of some specialized flows common in the polymer industry, such as melt extrusion or fiber spinning [100], it is no coincidence that the earliest reports documenting purely elastic instabilities stem from attempted measurements in devices which may be used to quantify viscosity, such as Taylor-Couette cells, or cone-and-plate or plate-and-plate rheometers. Since any apparatus designed to measure viscosity should ideally require only a small sample, the gap between bounding walls is small, hence the Reynolds number is much lower than in a typical pipe flow. Another important contribution was the development of Boger fluids [101], originally prepared by adding a small amount of poly(acrylamide) to a concentrated solution of maltose, yielding a viscoelastic fluid with (nearly) constant shear viscosity. Although Boger's intent was to avoid the confounding effect of shear-thinning in rheological experiments, the fluid he had created was also highly viscous, further contributing to a lower Reynolds number. Boger fluids with lower viscosity would eventually be developed, e.g. by Odell and Carrington [102] who prepared a dilute solution of atactic poly(styrene) dissolved in dioctyl phthalate, yet the popularity of Boger's original fluid would contribute substantially to the advancement of research on purely elastic flow instabilities, such as in the work by Groisman and Steinberg [97] that uncovered the existence of elastic turbulence, initially detected in a parallel-plate rheometer.

The growing interest in elastic instabilities throughout the 1980s and 1990s coincided with the development of miniaturized channels with characteristic length scales lower than one millimeter. Microfluidic devices and the associated optical detection techniques were originally devised in an attempt to decrease the sample volumes required by conventional analytical methods, such as high-performance liquid chromatography or capillary electrophoresis, and later became important tools in the development of high-throughput DNA sequencing technologies [96]. Early designs relied on glass or silicon etching, yet glass is not permeable to gases, rendering the material unsuitable for certain biotechnology applications, and furthermore silicon is opaque to visible and ultraviolet light, nullifying the detection capabilities of optical techniques [96]. Both concerns were addressed with the development of soft lithography fabrication methods using primarily poly(dimethylsiloxane) (PDMS) [103]. PDMS is transparent and permeable to gases, and although the prototyping of a negative template requires specialized photolithography equipment, the template can then be used repeatedly under benchtop conditions, expediting the development of a significant number of applications, documented in e.g. [95],[104]. Nevertheless, glass or even steel are still often used in particularly deep or shallow microchannels, e.g. [105], to circumvent issues caused by the buckling of elastomeric walls. Of special interest to this thesis is the application of microfluidic devices to the study of extensional flows.

The purely elastic instabilities reviewed by Shaqfeh [84] and McKinley et al. [88] occur in flows which are either shear dominated, such as in plate-and-plate rheometers, or are characterized by a complex superposition of shear and extensional kinematics, e.g. the sudden contraction. With the aforementioned fabrication techniques, the miniaturization of some of the specialized extensional flows became possible. Of the classical setups discussed by Keller and Odell [106], some are not amenable to downscaling, either because they rely on moving parts, such as the four roll mill, or because the setup is immersed in a fluid, such as the opposed-jets device, leaving the cross-slot geometry, depicted in Figure 3.12, as one of the few extensional rheometers that can be easily replicated using soft lithography. Furthermore, considering the definition of the Elasticity number – the ratio of elastic to inertial forces – given by Squires and Quake [95],

$$\mathrm{El} = \frac{\mathrm{De}}{\mathrm{Re}} = \frac{\lambda \eta}{\rho d^2}, \tag{3.69}$$

the miniaturization of flow geometries not only reduces the effect of inertia but also enhances the role of elasticity, since $\mathrm{El} \propto d^{-2}$, which is especially relevant in extensional flows.

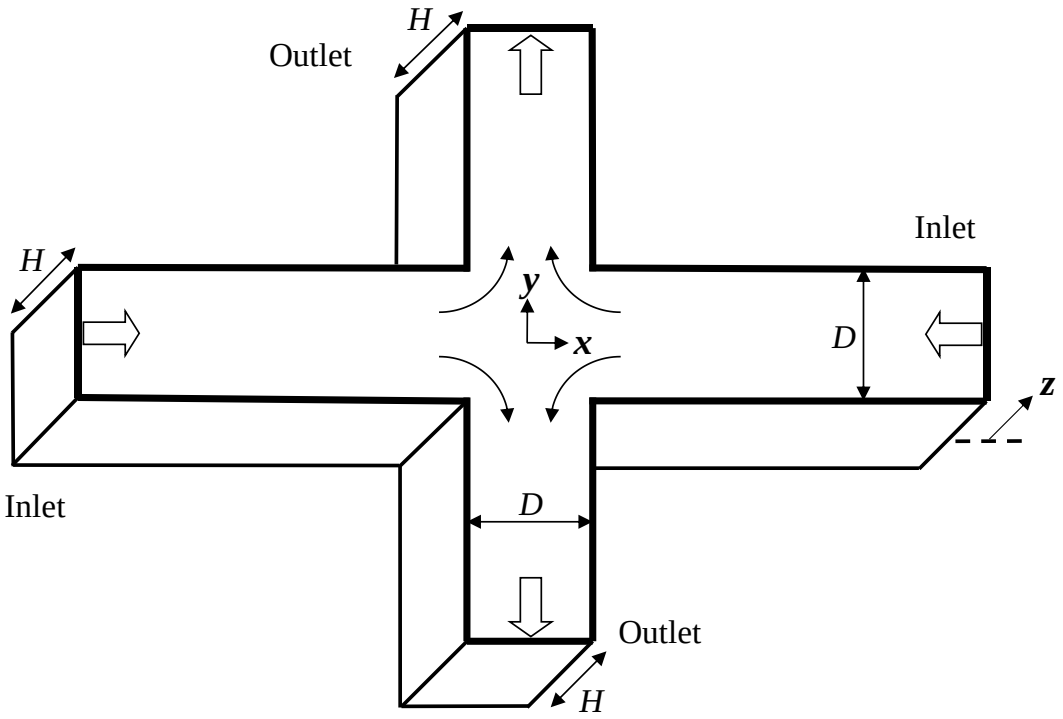

Figure 3.12 – Prototypical cross-slot geometry. The aspect ratio of the geometry is commonly defined as $AR = H/D$, where H is the depth and D is the width.

3.3.2 The Cross-Slot Geometry and the Genesis of this Thesis

The primary topic of this thesis is the computational investigation of purely elastic flow instabilities in microscale cross-slots, sometimes also referred to as crossed-slots or crossed microchannels. At the very center of the flow geometry shown in Figure 3.12, the two inflow streams meet and then diverge around a free stagnation point. Polymer molecules passing near this point experience significant stretching along the outflow axis, provided the Weissenberg number is sufficiently large, $\mathrm{Wi} \geq 0.5$, defined as,

$$\mathrm{Wi} = \lambda \dot{\varepsilon}, \tag{3.70}$$

where $\dot{\varepsilon}$ is the rate of extension Alternatively, $\mathrm{Wi}_{crit} = \lambda \dot{\gamma} = 1$, if the rate of deformation is used instead. Experimentally, the stretching of polymer chains causes a localized change in the refractive index of the solution, hence the band of extended molecules along the outflow axis is commonly referred to as birefringence strand. Historically, cross-slot devices have been used as extensional rheometers for the characterization of polymer solutions [107] or melts [108]. The two examples cited also illustrate alternative applications. Gardner et al. [107] reported the first indirect evidence of instability in the configuration of the birefringence strand, hinted at by asymmetric downstream velocity profiles. On the other hand, van Meerveld et al. [108] studied the crystallization of polymer melts, induced by the aforementioned stretching and alignment of polymer molecules. Another well-known application of cross-slot flows is the study of single polymer dynamics, such as the measurements on the unfolding of individual DNA molecules, reported by Perkins et al. [109].

The study by Gardner et al. [107] is to some extent a distant precursor to this thesis. A more immediate primer is the sequence of instabilities reported by Arratia et al. [45]. Using a fluid prepared by adding 200 ppm of high molecular weight poly(acrylamide) to a 97% glycerol aqueous solution, the authors demonstrated the existence of a stationary elastic instability, wherein at sufficiently high Deborah number the flow field becomes asymmetric as a result of accumulated extensional stress along the outlet centerline of the slot, forming a thin layer of large normal stresses, the aforementioned birefringence strand. Further increases in flow rate cause a transition to time-dependent flow. These instabilities were shortly after confirmed to be purely elastic in nature, by a set of inertialess simulations using the UCM model, on a two-dimensional, i.e. $H \gg D$ (cf. Figure 3.12), planar cross-slot, reported by Poole et al. [110]. The same study also demonstrated that the stationary asymmetric transition is a type of supercritical pitchfork bifurcation. For inlet and outlet channels with the same width D, an asymmetry parameter DQ may be defined,

$$DQ = \frac{q_2 - q_1}{Q}, \tag{3.71}$$

where Q is the total flow rate per unit depth at one of the inlets – and is the same for both inlet channels – which is then split between the two outlets, with the corresponding flow rates represented by q_1 and q_2, such that $Q = q_1 + q_2$. Thus, for a symmetric flow field, $q_1 = q_2 = Q/2 \Rightarrow DQ = 0$, and conversely for a fully asymmetric flow field, $q_1 = 0 \wedge q_2 = Q \Rightarrow DQ = 1$ or $q_1 = Q \wedge q_2 = 0 \Rightarrow DQ = -1$. Poole et al. [110] then showed that this asymmetry parameter is a square-root function of the Deborah number, $\mathrm{De} = \lambda U/D = \lambda Q/D^2$, which is characteristic of pitchfork bifurcations (cf. Figure 3.10),

$$DQ = \pm A\sqrt{\mathrm{De} - \mathrm{De}_{crit}}, \tag{3.72}$$

where A is a fit constant and De_{crit} is the critical transition De. Furthermore, Poole et al. [110] demonstrated that the asymmetric transition leads to a reduction in energy dissipation, by defining a Couette correction C,

$$C = \frac{\Delta p - \Delta p_{fd}}{2\tau_w}, \tag{3.73}$$

where Δp is the pressure drop between the inlets and outlets, Δp_{fd} is the corresponding pressure drop for a hypothetical fully developed flow, i.e. without the central slot, and τ_w is the wall shear stress under similar idealized conditions. The Couette correction represents an additional pressure loss incurred by the presence of the slot, which, for the definition given in eq. 3.73, is equivalent to extending the length of the idealized channel flow by C channel widths, and was shown to decrease after the asymmetric transition [110].

These stationary asymmetries remained unreported – with the arguable exception of Gardner et al. [107] – until the early 21st century, most likely due to the non-negligible

inertia in experimental setups preceding the popularization of microfluidics. This argument is further supported by experimental results for wormlike micellar surfactant flows, published by Pathak and Hudson [111] in the same year as Arratia et al. [45], again in a microfluidic cross-slot, in which the steady asymmetry and subsequent transition to time-dependent flow were also observed. Since 2006, other publications have reported steady-state asymmetries in cross-slot flows of wormlike micellar solutions, including fully asymmetric flow [111],[112], $\mathrm{Wi}-\mathrm{Re}$ stability diagrams delimiting different flow behaviors [112],[113] and also the formation of lip vortices in the inlet channels for strongly viscoelastic fluids [112],[114]. Additionally, earlier computational work in the cross-slot device, by e.g. Harris and Rallison [115] or Remmelgas et al. [116], was performed on truncated meshes, such that only a quarter or half of the full cross-slot was simulated, with symmetry boundary conditions imposed as a way to reduce the computational burden, thus precluding the emergence of flow asymmetries. Similarly, analytical studies such as the work of Öztekin et al. [89] focused only on a portion of the extensional flow equivalent to one of the cross-slot outlets, in order to assess the characteristics of the time-dependent flow transition in the absence of asymmetries, which had not been reported at the time.

In addition to a well-defined flow transition, the planar cross-slot possess other noteworthy features. The flow contains an internal stagnation point where a fluid element is subjected to large extensional stresses, a trait that facilitates the testing of numerical methods away from any influence of boundary conditions, namely by analysis of the mesh-wise convergence of the local Weissenberg number (eq. 3.70), calculated at the stagnation point, or of the aforementioned asymmetry parameter DQ. This feature differentiates the planar cross-slot from classical benchmark problems, such as the 4:1 sudden contraction [117], which despite the extensional character of the flow in the contraction, also contains an important shear contribution and a strong dependence on the boundary conditions, namely on the effect of the reentrant corner. Another important benchmark problem, the flow around a confined cylinder [66] – which is arguably shear dominated – has two wall-bounded stagnation points, upstream and downstream along the cylinder surface, the latter of which is capable of generating a birefringence strand. Comparatively, the principal characteristic of the planar cross-slot is the strong extensional nature of the flow in a region far away from walls. Indeed, while compiling a list of important unresolved problems in non-Newtonian fluid mechanics, Wilson [118]

names the loss of symmetry in the planar cross-slot, specifically citing the unidentified linear instability which should underlie the supercritical pitchfork bifurcation, a transition that triggers a change in the type of flow, in and immediately around the stagnation point, from extension to shearing.

The properties enumerated above, and also the ease with which purely elastic instabilities can be studied either computationally or, crucially, experimentally, all led to the proposal of the two-dimensional, planar cross-slot as a new benchmark flow problem, as documented in Chap. 5 of this thesis [119].

3.3.3 The Cross-Slot Geometry and Energy Dissipation

The steady asymmetries observed in two-dimensional cross-slots are known to result from a pitchfork bifurcation, and lead to a decreased flow resistance and thus a reduction in dissipated energy [119],[120]. Depending on the rheological characteristics of the fluid, the two-dimensional flow may also transition from a steady symmetric to a time-dependent state [121]. Although the steady flow bifurcation has been comprehensively studied from a two-dimensional (2D) perspective, and the results show an energy dissipation decrease in the form of a reduced pressure drop, a mechanistic understanding of the phenomenon may benefit from an exploration of the three-dimensional (3D) nature of the flow bifurcation. Although there is a computational study which considers a 3D six-arm variant of the standard cross-slot [122], the mechanism of the bifurcation phenomenon is not explored in depth and the geometry *per se* is inherently not the same as the conventional four-arm planar cross-slot typically used in microfluidic devices. However, stationary viscoelastic creeping flow bifurcations are not unique to cross-slot geometries, and have been studied experimentally [83],[123] and computationally [124] for flow past a confined cylinder, in flow-focusing devices [125], in T-shaped microchannels [126] and in mixing-separating cells [127]. Notably, the three-dimensional nature of the phenomenon in the flow past a confined cylinder has been explored in detail, and experimental studies report the formation of steady 3D flow cells in the cylinder wake upon bifurcation [83],[123],[124], with a subsequent transition to time-dependent flow for increasing Deborah number, as also observed for cross-slot geometries [45],[110],[119],[120]. The cellular structure found in the cylinder wake is characterized

by spanwise, spatial-periodic asymmetries relative to the wake neutral axis and the convergence of streamlines into bundles, also arranged in a spatial-periodic manner (cf. Figure 4 in Ref. [124]). This would indicate that the fluid, upon steady bifurcation, selects a set of optimal flow paths, an idea consistent with the lower energy dissipation observed in bifurcated 2D cross-slot creeping flow, and which may hint at the mechanism of bifurcation in 3D cross-slots. Furthermore, McKinley et al. [83] showed that the critical bifurcation De decreases as the cylinder blockage ratio increases, an observation suggesting an aspect ratio dependence of critical conditions for 3D cross-slots. Here, the cylinder blockage ratio and the cross-slot aspect ratio, AR, are compared on the basis that the fluid is forced through a narrower gap for higher cylinder blockage ratios or lower cross-slot aspect ratios, therefore producing increased shear rates. In fact, earlier computational work [128] suggests a possible linear relation between the critical De and the aspect ratio, for $AR<1$, implicitly invoking the Pakdel-McKinley criterion [81],[88] due to the progressively larger tensile stress and velocity gradient near the cross-slot corners as the channel depth decreases. It should be noted however that for $AR<1$, usually the flow field transitions directly from a steady symmetric to a time-dependent state, omitting the intermediate, stationary asymmetric configuration. Incidentally, it was also previously shown, for electro-osmotic viscoelastic flows in 2D cross-slots, that the instability of the flow can be explained by a simplified model of flow around corners and the application of the Pakdel-McKinley criterion therein [129].

In Chap. 6 of this thesis [130], I systematically study the three-dimensional nature of the cross-slot steady flow bifurcation and also attempt to provide insights into the steady-unsteady transition. Using UCM [131] and simplified linearized PTT [132] constitutive equations, under creeping-flow conditions $\left(\mathrm{Re}\to 0\right)$, I simulate the flow in standard, four-arm cross-slots, with aspect ratios ranging from close to the shallow, Hele-Shaw flow limit [133] up to very deep channels.

3.3.4 A Cross-Slot Device and the Interaction of Different Instabilities

Since the work by Arratia et al. [45], renewed interest has emerged in the cross-slot geometry. Further computational work has confirmed that the stationary asymmetric instability is a type of supercritical pitchfork bifurcation, and that it may occur for shear-

thinning PTT fluids [119] or other bounded extensional viscosity model fluids, such as the FENE model with either Peterlin (-P) or Chilcott-Rallison (-CR) closures [120]. Rocha et al. [120] have also studied the effect of solvent viscosity ratio, $\beta = \eta_s / \left(\eta_s + \eta_p \right)$, where η_s and η_p are respectively the solvent and polymer viscosities, and extensibility, L^2, and concluded that the onset of the pitchfork bifurcation occurs at lower De for lower β and/or higher L^2. Xi and Graham [121] also simulated the flow of a FENE-P fluid in a cross-slot device and have not found a stationary instability, instead reporting a direct transition to time-dependent flow. Their choice of a high solvent viscosity ratio, $\beta = 0.95,$ together with the previously mentioned effects of β and L^2 on the onset of stationary instabilities, suggests that a minimum threshold in the relative strength of extensional flow relative to shearing effects is necessary to trigger the steady asymmetric transition. Experimental work performed on cross-slot flows of wormlike micellar solutions [112],[113] seems to confirm this hypothesis: highly viscoelastic fluids sequentially undergo both transitions, whereas weakly viscoelastic fluids directly evolve from steady symmetric to unsteady flow as the flow rate increases. This is further supported by the experimental work of Sousa et al. [47] who studied the flow stability of various viscoelastic fluids with different β. Furthermore, Xi and Graham [121] demonstrated that the time-dependent flow that is observed at high De is the result of a supercritical Hopf bifurcation. Experimental [47] and computational [130] investigations of cross-slot flows with different channel aspect ratios have shown that the steady supercritical pitchfork bifurcation only occurs in channels with sufficient depth, i.e. high aspect ratio, whereas channels which are relatively shallow usually evolve directly from steady symmetric to unsteady flow as De is increased. The relative proximity of the top and bottom bounding walls in shallow channels causes an increase in the relative magnitude of shear effects [47], therefore suppressing the pitchfork bifurcation to steady asymmetric flow that is linked to the extensional nature of the flow. However, as the aspect ratio decreases, the second, time-dependent transition occurs at progressively lower Deborah numbers [130], indicating that the additional shear-induced normal stresses near the corners are themselves destabilizing, although leading to a different type of instability.

Whether it be by manipulation of fluid rheology or the geometric aspect ratio of the cross-slot device, evidence suggests extension and shear compete in order to

determine the nature of flow instabilities. However, studying the two effects separately has proven to be difficult. According to the Pakdel-McKinley criterion [88], elastic instabilities are a consequence of curved streamlines acting on polymer chains not fully aligned with the streamwise direction, causing them to stretch and produce tensile stress (cf. Figure 3.9). Disturbances in the alignment of polymers are thus amplified, eventually leading to unstable flow. Alternatively, as discussed in Ref. [130], a flow which is rotational in nature, despite having curved streamlines, cannot generate the aforementioned differential stretching of polymer chains owing to the uniform angular velocity of the flow field, or for that matter, the lack of extension thought to be the cause of the steady asymmetric transition. Ideally, isolating the influence of shear and extension in elastic instabilities would require a flow geometry capable of producing a nearly purely extensional field while retaining streamline curvature. Attempts made by Cruz et al. [119] and Rocha et al. [120] to reduce the influence of shear by rounding the corners of the cross-slot geometry have also caused the pitchfork bifurcation to be postponed to higher flow rates, slightly when the curvature of rounded corners is 5% of the channel width D [119] and pronouncedly for rounding curvature equivalent to 50% of D [120]. Thus the extensional character of standard planar cross-slot flows is also predicated on the sharpness of its corners.

Introduced by Alves [134] and experimentally validated by Haward et al. [105],[135], the Optimized Shape Cross-slot Extensional Rheometer, or OSCER device, depicted in Figure 3.13, is a variant of the cross-slot geometry, numerically optimized to produce an homogeneous extensional field $\left(u_x, u_y\right) = \left(\dot{\varepsilon}x, -\dot{\varepsilon}y\right)$ with deformation rate $\dot{\varepsilon} = 1.5U_0/\left(15H\right)$ along a wide region in the center of the geometry (cf. Figure 1.b in Ref. [105]) and, consequently, a well-defined homogeneous birefringence strand along the outlet axis. Although initially proposed as an extensional rheometer, the OSCER device has also been used as a platform for the investigation of elastic instabilities. Haward et al. [46] measured the birefringence strand formed by the flow of various poly(ethylene oxide) solutions with varying proportions of glycerol and of hyaluronic acid aqueous solutions. Depending on the magnitude of the Elasticity number, representative of the ratio between elastic and inertial forces, which due to the shear-thinning nature of the test fluids was defined at a flow rate corresponding to the respective critical Weissenberg number Wi_{crit} of each flow transition, flows may either become steady asymmetric for

$El_{crit} > 1$, or undergo a transition into a time-dependent, inertio-elastic regime for $El_{crit} < 1$, with both Reynolds number $Re_{crit} > 10$ and $Wi_{crit} > 1$. While the high elasticity transition is analogous to the supercritical pitchfork bifurcation observed in standard planar cross-slots, the low elasticity transition is characterized by what appears to be rapid oscillation of the birefringence strand, in a manner which resembles the behavior of a vibrating taut string [46].

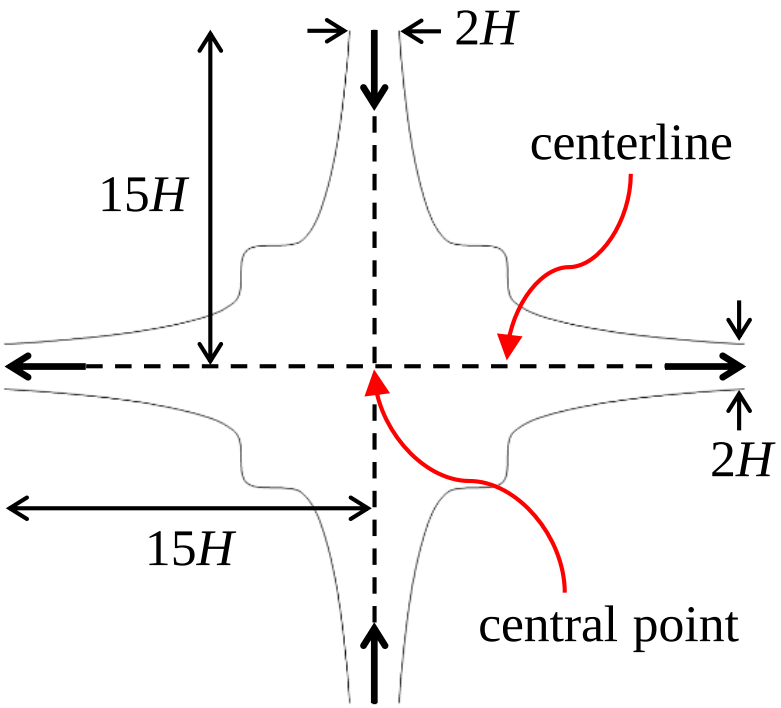

Figure 3.13 – Optimized Cross-Slot Extensional Rheometer, or OSCER device. The half-width H is the characteristic length scale of the geometry.

Furthermore, Haward et al. [136] studied the flow in the OSCER device using monodisperse, dilute atactic polystyrene dissolved in dioctyl phthalate. Their test fluids were weakly shear-thinning, and despite having a relatively high solvent viscosity ratio $\beta > 0.5$, generate strong yet thin birefringence strands due to the large extensibility of polymer chains. The authors reported a new type of instability [136], wherein the stagnation point becomes laterally displaced and oscillates between the central position of the slot and one of the outlets. Further increases in flow rate cause a symmetry breaking transition, analogous to the pitchfork bifurcation in standard cross-slots. However, the flow is unsteady in what appears to be a superposition of the lateral displacement

oscillations with a base asymmetric flow field, mixed with aperiodic modes of fluctuation (cf. supplementary movie S4 in Ref. [136]).

The observation of symmetry breaking transitions in the OSCER device [46],[136] indicates that the shearing produced by the corners in a standard cross-slot is not a necessary condition for the underlying supercritical pitchfork bifurcation. Furthermore, in the near absence of inertia or shearing effects, of which the latter is an integral part of the micromechanical model of elastic instabilities proposed by Larson et al. [76], hitherto unknown time-dependent instabilities [136] may occur and eventually become superimposed on an asymmetry flow field. In Chap. 7 of this thesis, I simulate the two-dimensional (2D) flow of dilute, highly extensible, FENE-CR fluids in the OSCER device, under conditions of low to negligible inertia, and attempt to characterize the various emerging transitions and their superimposed states. Considering the high aspect ratio of the OSCER device, specifically $AR = \text{depth}/\text{width} = 10.5$ [105], 2D flow simulations are a reasonable approximation of experimental flows, since the influence of the top and bottom bounding walls should be negligible near the center plane of the device.

3.3.5 Elastic Turbulence (ET)

Turbulent flows are usually identified by three hallmark features: (i) increased resistance to flow, which can be detected via measurements of pressure drop in pressure-driven flows or by quantification of shear stress in shear-driven flows; (ii) enhanced mixing, which is commonly assessed by tracking a passive scalar quantity, such as the concentration of a dye; (iii) a broad range of excited spatial and temporal scales, which are typically quantified by spectral analysis of fluctuations in velocity or other relevant flow variables [137]. Groisman and Steinberg [97] reported a sudden increase in the resistance to flow, by a factor of $20\times$, in a plate-and-plate rheometer using a Boger fluid [101] – 80 ppm of poly(acrylamide) dissolved in a 65% sucrose aqueous solution – and further complemented this result via spectral analysis of velocity fluctuations, obtaining a power-law decay with exponent $\alpha \approx -3.5$. Since the experiment was performed under creeping flow conditions, the authors concluded that they had discovered a new type of turbulence, which was denominated elastic turbulence (ET). Shortly thereafter [98], the

remaining main feature of turbulence – mixing – was confirmed on a curvilinear channel with two adjacent inlets injected with the same Boger fluid as previously, with one of the inlets dyed so that mixing could be tracked. Using the solvent as a control, complete mixing was attained on a time scale three orders of magnitude lower than the expected diffusion time. Analysis of velocity fluctuations yielded a power-law decay with exponent $\alpha \approx -3.3$. The topic of mixing via ET has since drawn considerable attention, e.g. [95],[138], given the potential applications in the field of microfluidics.

The experimental evidence of ET was soon complemented with theoretical predictions of the aforementioned spectral decay. Fouxon and Lebedev [139] developed a hydrodynamic theory concerning the stretching of Hookean polymers in turbulent flows, including an analysis of isotropic, unbounded, homogeneous ET based principally on the following two assumptions: (i) both viscous and stress relaxation contributions to the dissipation of elastic energy are of the same order; (ii) due to the feedback (or back reaction) of the elastic stress on the flow, the velocity field reaches a statistically stationary state. Consequently, the normalized elastic stress was expected to saturate at a value of $\sigma_e \lambda/\eta \approx 1$, evaluated locally, and furthermore the power-law decay of velocity fluctuations in ET was predicted to be,

$$|\alpha| > 3. \tag{3.74}$$

This result was consistent with the earlier observations by Groisman and Steinberg [97],[98], and has since been confirmed by several studies: experimental torsional plate-and-plate flow of Boger fluids [140]; experimental Taylor-Couette flows of wormlike micellar solutions [141]; computational two-dimensional periodic Kolmogorov flow of Oldroyd-B fluids [142],[143]; and computational straight channel flow of Oldroyd-B fluids with cylindrical obstacles [144]. Usually, $-4 < \alpha < -3$, although in the study by Grilli et al. [144], the power-law decay had a slope of -4.3 for a velocity signal sampled along the gap between the cylinder and the wall.

In an extended account of their experimental work, Groisman and Steinberg [145] reported a succession of two decay regimes, one with a slope of -1.1 for lower frequencies, followed by a higher slope, -2.2, for higher frequencies, in a Taylor-Couette

flow using the same Boger fluid as earlier. This inconsistency with Fouxon and Lebedev's theory was also reported by Beaumont et al. [146], for Taylor-Couette flows of betaine-based wormlike micellar solutions, with measured spectral decays between -1 and -3, depending on the applied shear stress or shear rate, although in the latter study there are several confounding effects, principally shear-banding. Ghanbari and Khomami [147] addressed this issue, using linear stability analysis to determine the influence of thermal sensitivity and gap ratio on the critical Wi for the onset of purely elastic instabilities in the Taylor-Couette flow of Oldroyd-B and FENE-P fluids. Under anisothermal conditions, Wi_{crit} decreases by one to two orders of magnitude relative to isothermal conditions, which led the authors to propose the concept of thermo-elastic turbulence. However, there is debate on whether linear stability analysis is appropriate or useful in the study of turbulence. For instance, the straight pipe flow of a Newtonian fluid is linearly stable for all Re, and yet the transition to inertial turbulence occurs typically at $\mathrm{Re} \approx 2000$ [148]. As mentioned by Morozov and van Saarloos [148], viscoelastic flows are subjected to nonlinear instabilities, as the classical rod-climbing effect demonstrates. For example, a polymer molecule may stretch in a region where the shear rate is high, only to release the stored elastic energy downstream, in a region where shear rate is low. As demonstrated experimentally by Pan et al. [86] and computationally by Grilli et al. [144], cylinder arrays in straight microchannels are capable of producing persistent perturbations. Given a sufficiently long channel, any linear perturbation should be dampened, irrespective of the initial amplitude or frequency. Even considering the memory of viscoelastic fluids, and thus the potential for hysteresis, one may argue that if the fluid has travelled sufficiently far from the source of the perturbation, say after ten relaxation times have elapsed, then the unstable flow should decay to a laminar state. Thus, as inferred by Pan et al. [86] and also by Morozov and van Saarloos [148], ET is the result of a subcritical transition, i.e. a bifurcation which results in the complete loss of attractors. Several studies have addressed the sequence of events when a flow transitions from a steady state into ET. Fardin et al. [141], while studying shear-banding wormlike micelles, observed a transition range wherein the interface between sheared bands oscillates periodically, and this periodicity scales with the size of the high shear rate band, with subsequent work supporting this observation [149],[150]. The transition regime for polymer solutions appears to be significantly more complex. Schiamberg et al. [151] observed at least six different modes in the creeping flow of a Boger fluid in a

torsional plate-and-plate rheometer, as Wi is increased: stable base flow, stationary ring, competing spirals, multi-spiral chaotic, spiral bursting, and finally elastic turbulence (cf. Figures 4 and 5 in Ref. [151]). This sequence of distinct instabilities suggests the sequential emergence and perhaps superposition of different types of bifurcations as the flow rate is increased.

Although the predicted power-law decay, $|\alpha| > 3$, has often been verified, the core assumptions of the theory developed by Fouxon and Lebedev [139] have occasionally been shown to be inconsistent with the dynamics of ET in a finite vessel, namely because of the unsaturated nature of velocity fluctuations [140],[152] and elastic stress [153], which appear to grow with the locally evaluated Weissenberg number, but also due to the disproportionally large role of stress relaxation in the dissipation of elastic energy, when compared to the viscous contribution [142],[153],[154]. In a recent publication, Jun and Steinberg [155] assessed the status of ET research, and suggested that the inconsistencies between the earlier theoretical and experimental contributions may be explained by the bounded, anisotropic and inhomogeneous nature of ET in realistic flow geometries. Any finite vessel necessarily imposes boundaries on a fluid, and whatever method may be used to drive the flow also leads to a non-zero average velocity. Although these issues are also noteworthy when comparing theoretical and experimental work on inertial turbulence, the small length scales required for the emergence of ET tend to exacerbate them. For instance, theoretical predictions concerning the properties of unbounded, isotropic inertial turbulence may well be applicable to large scale phenomena such as oceanic or atmospheric flows. On the other hand, ET is strongly influenced by the stress boundary layers along the walls of bounding vessels, with a growing body of evidence suggesting that the source of inhomogeneity in ET is the accumulation of elastic stress in boundary layers, which is then randomly injected into the bulk flow [140],[152],[156],[157]. As tentatively argued by Steinberg [158], this type of interaction between boundary layers and the fluid bulk may also be the cause of turbulent drag reduction, since a large proportion of the momentum that would be transferred to the wall is instead stored in stretched polymer molecules near the wall and randomly injected back into the bulk, leading to an overall reduction in the dissipation of momentum. It is worth noting that the literature covering ET focuses primarily on shear dominated flows, with, to the best of my knowledge and as of late 2017, no assessments of the possibility of ET in strongly extensional stagnation point flows, in geometries such as the planar cross-slot.

A recent theoretical investigation by Belan et al. [159] on the characteristics of boundary layers in ET, in the limit of large Weissenberg number, and without assuming any specific form for the spring constant of modelled polymers beyond the imposition of a maximum extensibility R_m, yielded the following relation,

$$\frac{U_L}{u_L} \propto nR_0R_m^2, \tag{3.75}$$

where U_L is the mean velocity of the flow at the border between the boundary layer and the bulk, u_L is the characteristic wall-normal fluctuating velocity at the same border, n is the polymer concentration and R_0 is the radius of gyration of the polymer molecule. As discussed by the authors [159], this ratio differs from the corresponding result for inertial turbulence, where the mean and fluctuating velocity components at the border of the viscous sublayer are of the same order. Additionally, since the extensibility of test polymers is usually large, one may reasonably expect that $U_L/u_L \gg 1$. Belan et al. [159] also argue that the elimination of the boundary layer width L during the derivation of eq. 3.75 suggests that L is a function of the vessel width, as previously reported for ET in a curvilinear channel [152].

In Chap. 8 of this thesis, I simulate the transition to elastic turbulence in a two-dimensional planar cross-slot geometry, identified via the analysis of the spectral decay of velocity fluctuations and also through the observation of the ejection of excessive elastic stresses concentrated in the boundary layers along the walls of the outlet channels.

3.4 References

[1] J.H. Fergizer, M. Perić, Computational Methods for Fluid Dynamics, 3rd ed., Springer-Verlag, Berlin, 2002.

[2] H.K. Versteeg, W. Malalasekera, An Introduction to Computational Fluid Dynamics - The Finite Volume Method, Longman Scientific & Technical, Harlow, 1995.

[3] A.N. Brooks, T.J.R. Hughes, Streamline upwind/Petrov-Galerkin formulations for convection dominated flows with particular emphasis on the incompressible Navier-Stokes equations, Comput. Methods Appl. Mech. Eng. 32 (1982) 199–259. doi:10.1016/0045-7825(82)90071-8.

[4] R. Courant, E. Isaacson, M. Rees, On the solution of nonlinear hyperbolic differential equations by finite differences, Commun. Pure Appl. Math. 5 (1952) 243–255. doi:10.1002/cpa.3160050303.

[5] S.K. Godunov, A difference method for numerical calculation of discontinuous solutions of the equations of hydrodynamics, Mat. Sb. 89 (1959) 271–306.

[6] B.P. Leonard, A stable and accurate convective modelling procedure based on quadratic upstream interpolation, Comput. Methods Appl. Mech. Eng. 19 (1979) 59–98. doi:10.1016/0045-7825(79)90034-3.

[7] D.B. Spalding, A novel finite difference formulation for differential expressions involving both first and second derivatives, Int. J. Numer. Methods Eng. 4 (1972) 551–559. doi:10.1002/nme.1620040409.

[8] H.S. Price, R.S. Varga, J.E. Warren, Application of Oscillation Matrices to Diffusion-Convection Equations, J. Math. Phys. 45 (1966) 301–311. doi:10.1002/sapm1966451301.

[9] P.H. Gaskell, A.K.C. Lau, Curvature-compensated convective transport: SMART, A new boundedness- preserving transport algorithm, Int. J. Numer. Meth. Fluids. 8 (1988) 617–641. doi:10.1002/fld.1650080602.

[10] B.P. Leonard, J.E. Drummond, Why you should not use 'Hybrid', 'Power-Law' or related exponential schemes for convective modelling—there are much better alternatives, Int. J. Numer. Meth. Fluids. 20 (1995) 421–442. doi:10.1002/fld.1650200602.

[11] B.P. Leonard, Simple high-accuracy resolution program for convective modelling of discontinuities, Int. J. Numer. Meth. Fluids. 8 (1988) 1291–1318. doi:10.1002/fld.1650081013.

[12] M.S. Darwish, F.H. Moukalled, Normalized variable and space formulation methodology for high-resolution schemes, Numer. Heat Transf. Part B Fundam. 26 (1994) 79–96. doi:10.1080/10407799408914918.

[13] A. Harten, High resolution schemes for hyperbolic conservation laws, J. Comput. Phys. 49 (1983) 357–393. doi:10.1016/0021-9991(83)90136-5.

[14] B. van Leer, Towards the ultimate conservative difference scheme. II. Monotonicity and conservation combined in a second-order scheme, J. Comput. Phys. 14 (1974) 361–370. doi:10.1016/0021-9991(74)90019-9.

[15] B. van Leer, Towards the ultimate conservative difference scheme. V. A second-order sequel to Godunov's method, J. Comput. Phys. 32 (1979) 101–136. doi:10.1016/0021-9991(79)90145-1.

[16] A. Pascau, C. Pérez, D. Sánchez, A well- behaved scheme to model strong convection in a general transport equation, Int. J. Numer. Methods Heat Fluid Flow. 5 (1995) 75–87. doi:10.1108/EUM0000000004058.

[17] M.A. Alves, Escoamentos de Fluidos Viscoelásticos em Regime Laminar - Análise Numérica, Teórica e Experimental, PhD Thesis, Universidade do Porto, 2004.

[18] N.P. Waterson, H. Deconinck, Design principles for bounded higher-order convection schemes – a unified approach, J. Comput. Phys. 224 (2007) 182–207. doi:10.1016/j.jcp.2007.01.021.

[19] P.K. Sweby, High Resolution Schemes Using Flux Limiters for Hyperbolic Conservation Laws, SIAM J. Numer. Anal. 21 (1984) 995–1011. doi:10.1137/0721062.

[20] J. Zhu, W. Rodi, A low dispersion and bounded convection scheme, Comput. Methods Appl. Mech. Eng. 92 (1991) 87–96. doi:10.1016/0045-7825(91)90199-G.

[21] J. Zhu, On the higher-order bounded discretization schemes for finite volume computations of incompressible flows, Comput. Methods Appl. Mech. Eng. 98 (1992) 345–360. doi:10.1016/0045-7825(92)90003-3.

[22] B. Song, G.R. Liu, K.Y. Lam, R.S. Amano, On a higher-order bounded discretization scheme, Int. J. Numer. Meth. Fluids. 32 (2000) 881–897. doi:10.1002/(SICI)1097-0363(20000415)32:7<881::AID-FLD2>3.0.CO;2-6.

[23] B.P. Leonard, The ULTIMATE conservative difference scheme applied to unsteady one-dimensional advection, Comput. Methods Appl. Mech. Eng. 88

(1991) 17–74. doi:10.1016/0045-7825(91)90232-U.

[24] M.A. Alves, P.J. Oliveira, F.T. Pinho, A convergent and universally bounded interpolation scheme for the treatment of advection, Int. J. Numer. Meth. Fluids. 41 (2003) 47–75. doi:10.1002/fld.428.

[25] M.J. Crochet, K. Walters, Numerical Methods in Non-Newtonian Fluid Mechanics, Annu. Rev. Fluid Mech. 15 (1983) 241–260. doi:10.1146/annurev.fl.15.010183.001325.

[26] J.L. Duda, J.S. Vrentas, Entrance Flows of Non- Newtonian Fluids, Trans. Soc. Rheol. 17 (1973) 89–108. doi:10.1122/1.549297.

[27] R. Poole, The Deborah and Weissenberg numbers, Rheol. Bull. 53 (2012) 32–39.

[28] R.B. Bird, R.C. Armstrong, O. Hassager, Dynamics of Polymeric Liquids, Vol. 1 - Fluids Mechanics, 2nd ed., Jonh Wiley & Sons, New York, 1987.

[29] D.F. Griffiths, D.T. Jones, K. Walters, A flow reversal due to edge effects, J. Fluid Mech. 36 (1969) 161. doi:10.1017/S0022112069001571.

[30] M.J. Crochet, G. Pilate, Numerical study of the flow of a fluid of second grade in a square cavity, Comput. Fluids. 3 (1975) 283–291. doi:10.1016/0045-7930(75)90001-8.

[31] A.B. Datta, K. Strauß, Slow flow of a viscoelastic fluid through a contraction, Rheol. Acta. 15 (1976) 403–410. doi:10.1007/BF01574495.

[32] A. Atkins, M. Escudier, A Dictionary of Mechanical Engineering, Oxford University Press, Oxford, 2013.

[33] H.A. Barnes, P. Townsend, K. Walters, On pulsatile flow of non-Newtonian liquids, Rheol. Acta. 10 (1971) 517–527. doi:10.1007/BF03396402.

[34] J.G. Oldroyd, Non-Newtonian Effects in Steady Motion of Some Idealized Elastico-Viscous Liquids, Proc. R. Soc. A Math. Phys. Eng. Sci. 245 (1958) 278–297. doi:10.1098/rspa.1958.0083.

[35] G. Astarita, Is non-newtonian fluid mechanics a culturally autonomous subject?, J. Non-Newt. Fluid Mech. 1 (1976) 203–206. doi:10.1016/0377-0257(76)80020-1.

[36] K. Walters, Developments in non-Newtonian fluid mechanics — a personal view,

J. Non-Newt. Fluid Mech. 5 (1979) 113–124. doi:10.1016/0377-0257(79)85007-7.

[37] R.G. Owens, T.N. Phillips, Computational Rheology, Imperial College Press, London, 2002.

[38] M.A. Mendelson, P.-W. Yeh, R.A. Brown, R.C. Armstrong, Approximation error in finite element calculation of viscoelastic fluid flows, J. Non-Newt. Fluid Mech. 10 (1982) 31–54. doi:10.1016/0377-0257(82)85003-9.

[39] A.R. Davies, Numerical filtering and the high weissenberg number problem, J. Non-Newt. Fluid Mech. 16 (1984) 195–209. doi:10.1016/0377-0257(84)85010-7.

[40] R.A. Brown, R.C. Armstrong, A.N. Beris, P.-W. Yeh, Galerkin finite element analysis of complex viscoelastic flows, Comput. Methods Appl. Mech. Eng. 58 (1986) 201–226. doi:10.1016/0045-7825(86)90096-4.

[41] R. Keunings, On the high Weissenberg number problem, J. Non-Newt. Fluid Mech. 20 (1986) 209–226. doi:10.1016/0377-0257(86)80022-2.

[42] M. Renardy, Y. Renardy, R. Sureshkumar, A.N. Beris, Hopf-Hopf and steady-Hopf mode interactions in Taylor-Couette flow of an upper convected Maxwell liquid, J. Non-Newt. Fluid Mech. 63 (1996) 1–31. doi:10.1016/0377-0257(95)01415-2.

[43] H.J. Wilson, M. Renardy, Y. Renardy, Structure of the spectrum in zero Reynolds number shear flow of the UCM and Oldroyd-B liquids, J. Non-Newt. Fluid Mech. 80 (1999) 251–268. doi:10.1016/S0377-0257(98)00087-1.

[44] H.J. Wilson, J.M. Rallison, Instability of channel flow of a shear-thinning White-Metzner fluid, J. Non-Newt. Fluid Mech. 87 (1999) 75–96. doi:10.1016/S0377-0257(99)00012-9.

[45] P.E. Arratia, C.C. Thomas, J. Diorio, J.P. Gollub, Elastic Instabilities of Polymer Solutions in Cross-Channel Flow, Phys. Rev. Lett. 96 (2006) 144502. doi:10.1103/PhysRevLett.96.144502.

[46] S.J. Haward, G.H. McKinley, Instabilities in stagnation point flows of polymer solutions, Phys. Fluids. 25 (2013) 083104. doi:10.1063/1.4818151.

[47] P.C. Sousa, F.T. Pinho, M.S.N. Oliveira, M.A. Alves, Purely elastic flow

instabilities in microscale cross-slot devices, Soft Matter. 11 (2015) 8856–8862. doi:10.1039/C5SM01298H.

[48] R. Keunings, A survey of computational rheology, in: Proc. XIIIth Int. Congr. Rheol., 2000: pp. 7–14. doi:10.1080/17489720701624618.

[49] D. Joseph, M. Renardy, J.-C. Saut, Hyperbolicity and change of type in the flow of viscoelastic fluids, Arch. Ration. Mech. Anal. 87 (1985) 67–83. doi:10.1007/BF00250725.

[50] D.D. Joseph, J.C. Saut, Change of type and loss of evolution in the flow of viscoelastic fluids, J. Non-Newt. Fluid Mech. 20 (1986) 117–141. doi:10.1016/0377-0257(86)80018-0.

[51] E.J. Hinch, The flow of an Oldroyd fluid around a sharp corner, J. Non-Newt. Fluid Mech. 50 (1993) 161–171. doi:10.1016/0377-0257(93)80029-B.

[52] M. Renardy, The stresses of an upper convected Maxwell fluid in a Newtonian velocity field near a re-entrant corner, J. Non-Newt. Fluid Mech. 50 (1993) 127–134. doi:10.1016/0377-0257(93)80027-9.

[53] A.R. Davies, J. Devlin, On corner flows of Oldroyd-B fluids, J. Non-Newt. Fluid Mech. 50 (1993) 173–191. doi:10.1016/0377-0257(93)80030-F.

[54] M. Renardy, High weissenberg number boundary layers for the upper convected Maxwell fluid, J. Non-Newt. Fluid Mech. 68 (1997) 125–132. doi:10.1016/S0377-0257(96)01491-7.

[55] O.G. Harlen, E.J. Hinch, J.M. Rallison, Birefringent pipes: the steady flow of a dilute polymer solution near a stagnation point, J. Non-Newt. Fluid Mech. 44 (1992) 229–265. doi:10.1016/0377-0257(92)80052-Y.

[56] P.G. De Gennes, Coil-stretch transition of dilute flexible polymers under ultrahigh velocity gradients, J. Chem. Phys. 60 (1974) 5030. doi:10.1063/1.1681018.

[57] M. Renardy, Asymptotic structure of the stress field in flow past a cylinder at high Weissenberg number, J. Non-Newt. Fluid Mech. 90 (2000) 13–23. doi:10.1016/S0377-0257(99)00050-6.

[58] F.J. Galindo-Rosales, M. a. Alves, M.S.N. Oliveira, Microdevices for extensional rheometry of low viscosity elastic liquids: a review, Microfluid. Nanofluidics. 14

(2012) 1–19. doi:10.1007/s10404-012-1028-1.

[59] F.P.T. Baaijens, Mixed finite element methods for viscoelastic flow analysis: a review, J. Non-Newt. Fluid Mech. 79 (1998) 361–385. doi:10.1016/S0377-0257(98)00122-0.

[60] O.M. Coronado, Finite Element Methods for Viscoelastic Fluid Flow Simulations: Formulations and Applications, PhD Thesis, Rice University, 2009.

[61] D. Rajagopalan, R.C. Armstrong, R.A. Brown, Finite element methdos for calculation of steady, viscoelastic flow using constitutive equations with a Newtonian viscosity, J. Non-Newt. Fluid Mech. 36 (1990) 159–192. doi:10.1016/0377-0257(90)85008-M.

[62] J.M. Marchal, M.J. Crochet, A new mixed finite element for calculating viscoelastic flow, J. Non-Newt. Fluid Mech. 26 (1987) 77–114. doi:10.1016/0377-0257(87)85048-6.

[63] R.C. King, M.R. Apelian, R.C. Armstrong, R.A. Brown, Numerically stable finite element techniques for viscoelastic calculations in smooth and singular geometries, J. Non-Newt. Fluid Mech. 29 (1988) 147–216. doi:10.1016/0377-0257(88)85054-7.

[64] R. Fattal, R. Kupferman, Constitutive laws for the matrix-logarithm of the conformation tensor, J. Non-Newt. Fluid Mech. 123 (2004) 281–285. doi:10.1016/j.jnnfm.2004.08.008.

[65] R. Fattal, R. Kupferman, Time-dependent simulation of viscoelastic flows at high Weissenberg number using the log-conformation representation, J. Non-Newt. Fluid Mech. 126 (2005) 23–37. doi:10.1016/j.jnnfm.2004.12.003.

[66] M.A. Hulsen, R. Fattal, R. Kupferman, Flow of viscoelastic fluids past a cylinder at high Weissenberg number: Stabilized simulations using matrix logarithms, J. Non-Newt. Fluid Mech. 127 (2005) 27–39. doi:10.1016/j.jnnfm.2005.01.002.

[67] A.M. Afonso, P.J. Oliveira, F.T. Pinho, M.A. Alves, The log-conformation tensor approach in the finite-volume method framework, J. Non-Newt. Fluid Mech. 157 (2009) 55–65. doi:10.1016/j.jnnfm.2008.09.007.

[68] F. Pimenta, M.A. Alves, Stabilization of an open-source finite-volume solver for viscoelastic fluid flows, J. Non-Newt. Fluid Mech. 239 (2017) 85–104.

doi:10.1016/j.jnnfm.2016.12.002.

[69] F. Habla, M.W. Tan, J. Haßlberger, O. Hinrichsen, Numerical simulation of the viscoelastic flow in a three-dimensional lid-driven cavity using the log-conformation reformulation in OpenFOAM®, J. Non-Newt. Fluid Mech. 212 (2014) 47–62. doi:10.1016/j.jnnfm.2014.08.005.

[70] T.. Phillips, A.. Williams, Comparison of creeping and inertial flow of an Oldroyd B fluid through planar and axisymmetric contractions, J. Non-Newt. Fluid Mech. 108 (2002) 25–47. doi:10.1016/S0377-0257(02)00123-4.

[71] N. Balci, B. Thomases, M. Renardy, C.R. Doering, Symmetric factorization of the conformation tensor in viscoelastic fluid models, J. Non-Newt. Fluid Mech. 166 (2011) 546–553. doi:10.1016/j.jnnfm.2011.02.008.

[72] A.M. Afonso, F.T. Pinho, M.A. Alves, The kernel-conformation constitutive laws, J. Non-Newt. Fluid Mech. 167–168 (2011) 30–37. doi:10.1016/j.jnnfm.2011.09.008.

[73] H. Giesekus, Zur Stabilität von Strömungen viskoelastischer Flüssigkeiten, Rheol. Acta. 5 (1966) 239–252. doi:10.1007/BF01982435.

[74] G.I. Taylor, Stability of a Viscous Liquid Contained between Two Rotating Cylinders, Philos. Trans. R. Soc. A Math. Phys. Eng. Sci. 223 (1923) 289–343. doi:10.1098/rsta.1923.0008.

[75] S.J. Muller, R.G. Larson, E.S.G. Shaqfeh, A purely elastic transition in Taylor-Couette flow, Rheol. Acta. 28 (1989) 499–503. doi:10.1007/BF01332920.

[76] R.G. Larson, E.S.G. Shaqfeh, S.J. Muller, A purely elastic instability in Taylor–Couette flow, J. Fluid Mech. 218 (1990) 573–600. doi:10.1017/S0022112090001124.

[77] E.S.G. Shaqfeh, S.J. Muller, R.G. Larson, The effects of gap width and dilute solution properties on the viscoelastic Taylor-Couette instability, J. Fluid Mech. 235 (1992) 285. doi:10.1017/S0022112092001113.

[78] S.J. Muller, E.S.G. Shaqfeh, R.G. Larson, Experimental studies of the onset of oscillatory instability in viscoelastic Taylor-Couette flow, J. Non-Newt. Fluid Mech. 46 (1993) 315–330. doi:10.1016/0377-0257(93)85053-D.

[79] R.G. Larson, S.J. Muller, E.S.G. Shaqfeh, The effect of fluid rheology on the elastic Taylor-Couette instability, J. Non-Newt. Fluid Mech. 51 (1994) 195–225. doi:10.1016/0377-0257(94)85012-7.

[80] Y.L. Joo, E.S.G. Shaqfeh, Viscoelastic Poiseuille flow through a curved channel: A new elastic instability, Phys. Fluids A Fluid Dyn. 3 (1991) 2043–2046. doi:10.1063/1.857886.

[81] P. Pakdel, G.H. McKinley, Elastic Instability and Curved Streamlines, Phys. Rev. Lett. 77 (1996) 2459–2462. doi:10.1103/PhysRevLett.77.2459.

[82] G.H. McKinley, J.A. Byars, R.A. Brown, R.C. Armstrong, Observations on the elastic instability in cone-and-plate and parallel-plate flows of a polyisobutylene Boger fluid, J. Non-Newt. Fluid Mech. 40 (1991) 201–229. doi:10.1016/0377-0257(91)85013-9.

[83] G.H. McKinley, R.C. Armstrong, R.A. Brown, The Wake Instability in Viscoelastic Flow past Confined Circular Cylinders, Philos. Trans. R. Soc. A Math. Phys. Eng. Sci. 344 (1993) 265–304. doi:10.1098/rsta.1993.0091.

[84] E.S.G. Shaqfeh, Purely Elastic Instabilities in Viscometric Flows, Annu. Rev. Fluid Mech. 28 (1996) 129–185. doi:10.1146/annurev.fl.28.010196.001021.

[85] T.C. Ho, M.M. Denn, Stability of plane poiseuille flow of a highly elastic liquid, J. Non-Newt. Fluid Mech. 3 (1977) 179–195. doi:10.1016/0377-0257(77)80048-7.

[86] L. Pan, A. Morozov, C. Wagner, P.E. Arratia, Nonlinear Elastic Instability in Channel Flows at Low Reynolds Numbers, Phys. Rev. Lett. 110 (2013) 174502. doi:10.1103/PhysRevLett.110.174502.

[87] A.N. Morozov, W. van Saarloos, Subcritical Finite-Amplitude Solutions for Plane Couette Flow of Viscoelastic Fluids, Phys. Rev. Lett. 95 (2005) 024501. doi:10.1103/PhysRevLett.95.024501.

[88] G.H. McKinley, P. Pakdel, A. Öztekin, Rheological and geometric scaling of purely elastic flow instabilities, J. Non-Newt. Fluid Mech. 67 (1996) 19–47. doi:10.1016/S0377-0257(96)01453-X.

[89] A. Öztekin, B. Alakus, G.H. McKinley, Stability of planar stagnation flow of a highly viscoelastic fluid, J. Non-Newt. Fluid Mech. 72 (1997) 1–29.

doi:10.1016/S0377-0257(97)00021-9.

[90] R.J. Poole, F.T. Pinho, M.A. Alves, P.J. Oliveira, The effect of expansion ratio for creeping expansion flows of UCM fluids, J. Non-Newt. Fluid Mech. 163 (2009) 35–44. doi:10.1016/j.jnnfm.2009.06.004.

[91] J. Zilz, R.J. Poole, M.A. Alves, D. Bartolo, B. Levaché, A. Lindner, Geometric scaling of a purely elastic flow instability in serpentine channels, J. Fluid Mech. 712 (2012) 203–218. doi:10.1017/jfm.2012.411.

[92] M.C. Cross, P.C. Hohenberg, Pattern formation outside of equilibrium, Rev. Mod. Phys. 65 (1993) 851–1112. doi:10.1103/RevModPhys.65.851.

[93] F. Dercole, S. Rinaldi, Dynamical Systems and Their Bifurcations, in: Adv. Methods Biomed. Signal Process., John Wiley & Sons, Inc., Hoboken, NJ, USA, 2011: pp. 291–325. doi:10.1002/9781118007747.ch12.

[94] F.J. Galindo-Rosales, L. Campo-Deaño, P.C. Sousa, V.M. Ribeiro, M.S.N. Oliveira, M.A. Alves, et al., Viscoelastic instabilities in micro-scale flows, Exp. Therm. Fluid Sci. 59 (2014) 128–139. doi:10.1016/j.expthermflusci.2014.03.004.

[95] T.M. Squires, S.R. Quake, Microfluidics: Fluid physics at the nanoliter scale, Rev. Mod. Phys. 77 (2005) 977–1026. doi:10.1103/RevModPhys.77.977.

[96] G.M. Whitesides, The origins and the future of microfluidics, Nature. 442 (2006) 368–373. doi:10.1038/nature05058.

[97] A. Groisman, V. Steinberg, Elastic turbulence in a polymer solution flow, Nature. 405 (2000) 53–55. doi:10.1038/35011019.

[98] A. Groisman, V. Steinberg, Efficient mixing at low Reynolds numbers using polymer additives., Nature. 410 (2001) 905–908. doi:10.1038/35073524.

[99] O. Reynolds, An Experimental Investigation of the Circumstances Which Determine Whether the Motion of Water Shall Be Direct or Sinuous, and of the Law of Resistance in Parallel Channels, Philos. Trans. R. Soc. London. 174 (1883) 935–982. doi:10.1098/rstl.1883.0029.

[100] R.G. Larson, Instabilities in viscoelastic flows, Rheol. Acta. 31 (1992) 213–263. doi:10.1007/BF00366504.

[101] D.V. Boger, A highly elastic constant-viscosity fluid, J. Non-Newt. Fluid Mech.

3 (1977) 87–91. doi:10.1016/0377-0257(77)80014-1.

[102] J.A. Odell, S.P. Carrington, Extensional flow oscillatory rheometry, J. Non-Newt. Fluid Mech. 137 (2006) 110–120. doi:10.1016/j.jnnfm.2006.03.010.

[103] J.C. McDonald, D.C. Duffy, J.R. Anderson, D.T. Chiu, H. Wu, O.J. Schueller, et al., Fabrication of microfluidic systems in poly(dimethylsiloxane), Electrophoresis. 21 (2000) 27–40. doi:10.1002/(SICI)1522-2683(20000101)21:1<27::AID-ELPS27>3.0.CO;2-C.

[104] H.A. Stone, A.D. Stroock, A. Ajdari, Engineering Flows In Small Devices: Microfluidics Toward a Lab-on-a-Chip, Annu. Rev. Fluid Mech. 36 (2004) 381–411. doi:10.1146/annurev.fluid.36.050802.122124.

[105] S.J. Haward, M.S.N. Oliveira, M.A. Alves, G.H. McKinley, Optimized cross-slot flow geometry for microfluidic extensional rheometry, Phys. Rev. Lett. 109 (2012) 128301. doi:10.1103/PhysRevLett.109.128301.

[106] A. Keller, J.A. Odell, The extensibility of macromolecules in solution; A new focus for macromolecular science, Colloid Polym. Sci. 263 (1985) 181–201. doi:10.1007/BF01415506.

[107] K. Gardner, E. Pike, M. Miles, A. Keller, K. Tanaka, Photon-correlation velocimetry of polystyrene solutions in extensional flow fields, Polymer. 23 (1982) 1435–1442. doi:10.1016/0032-3861(82)90240-3.

[108] J. van Meerveld, G.W.M. Peters, M. Hütter, Towards a rheological classification of flow induced crystallization experiments of polymer melts, Rheol. Acta. 44 (2004) 119–134. doi:10.1007/s00397-004-0382-7.

[109] T.T. Perkins, D.E. Smith, S. Chu, Single Polymer Dynamics in an Elongational Flow, Science (80-.). 276 (1997) 2016–2021. doi:10.1126/science.276.5321.2016.

[110] R.J. Poole, M.A. Alves, P.J. Oliveira, Purely Elastic Flow Asymmetries, Phys. Rev. Lett. 99 (2007) 164503. doi:10.1103/PhysRevLett.99.164503.

[111] J.A. Pathak, S.D. Hudson, Rheo-optics of Equilibrium Polymer Solutions: Wormlike Micelles in Elongational Flow in a Microfluidic Cross-Slot, Macromolecules. 39 (2006) 8782–8792. doi:10.1021/ma061355r.

[112] S.J. Haward, G.H. McKinley, Stagnation point flow of wormlike micellar

solutions in a microfluidic cross-slot device: Effects of surfactant concentration and ionic environment, Phys. Rev. E. 85 (2012) 031502. doi:10.1103/PhysRevE.85.031502.

[113] N. Dubash, P. Cheung, A.Q. Shen, Elastic instabilities in a microfluidic cross-slot flow of wormlike micellar solutions, Soft Matter. 8 (2012) 5847. doi:10.1039/c2sm25215e.

[114] S.J. Haward, T.J. Ober, M.S.N. Oliveira, M.A. Alves, G.H. McKinley, Extensional rheology and elastic instabilities of a wormlike micellar solution in a microfluidic cross-slot device, Soft Matter. 8 (2012) 536–555. doi:10.1039/C1SM06494K.

[115] O.J. Harris, J.M. Rallison, Instabilities of a stagnation point flow of a dilute polymer solution, J. Non-Newt. Fluid Mech. 55 (1994) 59–90. doi:10.1016/0377-0257(94)80060-X.

[116] J. Remmelgas, P. Singh, L.G. Leal, Computational studies of nonlinear elastic dumbbell models of Boger fluids in a cross-slot flow, J. Non-Newt. Fluid Mech. 88 (1999) 31–61. doi:10.1016/S0377-0257(99)00020-8.

[117] A.M. Afonso, P.J. Oliveira, F.T. Pinho, M.A. Alves, Dynamics of high-Deborah-number entry flows: a numerical study, J. Fluid Mech. 677 (2011) 272–304. doi:10.1017/jfm.2011.84.

[118] H.J. Wilson, Open mathematical problems regarding non-Newtonian fluids, Nonlinearity. 25 (2012) R45–R51. doi:10.1088/0951-7715/25/3/R45.

[119] F.A. Cruz, R.J. Poole, A.M. Afonso, F.T. Pinho, P.J. Oliveira, M.A. Alves, A new viscoelastic benchmark flow: Stationary bifurcation in a cross-slot, J. Non-Newt. Fluid Mech. 214 (2014) 57–68. doi:10.1016/j.jnnfm.2014.09.015.

[120] G.N. Rocha, R.J. Poole, M.A. Alves, P.J. Oliveira, On extensibility effects in the cross-slot flow bifurcation, J. Non-Newt. Fluid Mech. 156 (2009) 58–69. doi:10.1016/j.jnnfm.2008.06.008.

[121] L. Xi, M.D. Graham, A mechanism for oscillatory instability in viscoelastic cross-slot flow, J. Fluid Mech. 622 (2009) 145. doi:10.1017/S0022112008005119.

[122] A.M. Afonso, M.A. Alves, F.T. Pinho, Purely elastic instabilities in three-dimensional cross-slot geometries, J. Non-Newt. Fluid Mech. 165 (2010) 743–751.

doi:10.1016/j.jnnfm.2010.03.010.

[123] A.H. Shiang, A. Özkekin, J.-C. Lin, D. Rockwell, Hydroelastic instabilities in viscoelastic flow past a cylinder confined in a channel, Exp. Fluids. 28 (2000) 128–142. doi:10.1007/s003480050017.

[124] M. Sahin, Parallel large-scale numerical simulations of purely-elastic instabilities behind a confined circular cylinder in a rectangular channel, J. Non-Newt. Fluid Mech. 195 (2013) 46–56. doi:10.1016/j.jnnfm.2012.11.011.

[125] M.S.N. Oliveira, F.T. Pinho, R.J. Poole, P.J. Oliveira, M.A. Alves, Purely elastic flow asymmetries in flow-focusing devices, J. Non-Newt. Fluid Mech. 160 (2009) 31–39. doi:10.1016/j.jnnfm.2009.02.010.

[126] J. Soulages, M.S.N. Oliveira, P.C. Sousa, M.A. Alves, G.H. McKinley, Investigating the stability of viscoelastic stagnation flows in T-shaped microchannels, J. Non-Newt. Fluid Mech. 163 (2009) 9–24. doi:10.1016/j.jnnfm.2009.06.002.

[127] A.M. Afonso, M.A. Alves, R.J. Poole, P.J. Oliveira, F.T. Pinho, Viscoelastic flows in mixing-separating cells, J. Eng. Math. 71 (2011) 3–13. doi:10.1007/s10665-010-9384-x.

[128] R.J. Poole, M.A. Alves, A.M. Afonso, F.T. Pinho, P.J. Oliveira, Purely-elastic flow instabilities in a microfluidic cross-slot geometry, in: AIChE 2007 Annu. Meet., 2007.

[129] A.M. Afonso, F.T. Pinho, M.A. Alves, Electro-osmosis of viscoelastic fluids and prediction of electro-elastic flow instabilities in a cross slot using a finite-volume method, J. Non-Newt. Fluid Mech. 179–180 (2012) 55–68. doi:10.1016/j.jnnfm.2012.05.004.

[130] F.A. Cruz, R.J. Poole, A.M. Afonso, F.T. Pinho, P.J. Oliveira, M.A. Alves, Influence of channel aspect ratio on the onset of purely-elastic flow instabilities in three-dimensional planar cross-slots, J. Non-Newt. Fluid Mech. 227 (2016) 65–79. doi:10.1016/j.jnnfm.2015.11.008.

[131] J.G. Oldroyd, On the Formulation of Rheological Equations of State, Proc. R. Soc. A Math. Phys. Eng. Sci. 200 (1950) 523–541. doi:10.1098/rspa.1950.0035.

[132] N.P. Thien, R.I. Tanner, A new constitutive equation derived from network

theory, J. Non-Newt. Fluid Mech. 2 (1977) 353–365. doi:10.1016/0377-0257(77)80021-9.

[133] H.S. Hele-Shaw, The Flow of Water, Nature. 58 (1898) 34–36. doi:10.1038/058034a0.

[134] M.A. Alves, Design of a Cross-Slot Flow Channel for Extensional Viscosity Measurements, in: AIP Conf. Proc., AIP, 2008: pp. 240–242. doi:10.1063/1.2964648.

[135] S.J. Haward, A. Jaishankar, M.S.N. Oliveira, M.A. Alves, G.H. McKinley, Extensional flow of hyaluronic acid solutions in an optimized microfluidic cross-slot device, Biomicrofluidics. 7 (2013) 044108. doi:10.1063/1.4816708.

[136] S.J. Haward, G.H. McKinley, A.Q. Shen, Elastic instabilities in planar elongational flow of monodisperse polymer solutions, Sci. Rep. 6 (2016) 33029. doi:10.1038/srep33029.

[137] R.G. Larson, Fluid dynamics: Turbulence without inertia, Nature. 405 (2000) 27–28. doi:10.1038/35011172.

[138] R.J. Poole, B. Budhiraja, A.R. Cain, P.A. Scott, Emulsification using elastic turbulence, J. Non-Newt. Fluid Mech. 177–178 (2012) 15–18. doi:10.1016/j.jnnfm.2012.03.012.

[139] A. Fouxon, V. Lebedev, Spectra of turbulence in dilute polymer solutions, Phys. Fluids. 15 (2003) 2060–2072. doi:10.1063/1.1577563.

[140] T. Burghelea, E. Segre, V. Steinberg, Elastic turbulence in von Karman swirling flow between two disks, Phys. Fluids. 19 (2007) 053104. doi:10.1063/1.2732234.

[141] M.A. Fardin, D. Lopez, J. Croso, G. Grégoire, O. Cardoso, G.H. McKinley, et al., Elastic Turbulence in Shear Banding Wormlike Micelles, Phys. Rev. Lett. 104 (2010) 178303. doi:10.1103/PhysRevLett.104.178303.

[142] S. Berti, A. Bistagnino, G. Boffetta, A. Celani, S. Musacchio, Two-dimensional elastic turbulence, Phys. Rev. E. 77 (2008) 055306. doi:10.1103/PhysRevE.77.055306.

[143] S. Berti, G. Boffetta, Elastic waves and transition to elastic turbulence in a two-dimensional viscoelastic Kolmogorov flow, Phys. Rev. E. 82 (2010) 036314.

doi:10.1103/PhysRevE.82.036314.

[144] M. Grilli, A. Vázquez-Quesada, M. Ellero, Transition to Turbulence and Mixing in a Viscoelastic Fluid Flowing Inside a Channel with a Periodic Array of Cylindrical Obstacles, Phys. Rev. Lett. 110 (2013) 174501. doi:10.1103/PhysRevLett.110.174501.

[145] A. Groisman, V. Steinberg, Elastic turbulence in curvilinear flows of polymer solutions, New J. Phys. 6 (2004) 29–29. doi:10.1088/1367-2630/6/1/029.

[146] J. Beaumont, N. Louvet, T. Divoux, M.-A. Fardin, H. Bodiguel, S. Lerouge, et al., Turbulent flows in highly elastic wormlike micelles, Soft Matter. 9 (2013) 735–749. doi:10.1039/C2SM26760H.

[147] R. Ghanbari, B. Khomami, The onset of purely elastic and thermo-elastic instabilities in Taylor–Couette flow: Influence of gap ratio and fluid thermal sensitivity, J. Non-Newt. Fluid Mech. 208–209 (2014) 108–117. doi:10.1016/j.jnnfm.2014.04.004.

[148] A.N. Morozov, W. van Saarloos, An introductory essay on subcritical instabilities and the transition to turbulence in visco-elastic parallel shear flows, Phys. Rep. 447 (2007) 112–143. doi:10.1016/j.physrep.2007.03.004.

[149] M.A. Fardin, S. Lerouge, Instabilities in wormlike micelle systems, Eur. Phys. J. E. 35 (2012) 91. doi:10.1140/epje/i2012-12091-0.

[150] C. Perge, M.-A. Fardin, S. Manneville, Surfactant micelles: Model systems for flow instabilities of complex fluids, Eur. Phys. J. E. 37 (2014) 23. doi:10.1140/epje/i2014-14023-4.

[151] B.A. Schiamberg, L.T. Shereda, H. Hu, R.G. Larson, Transitional pathway to elastic turbulence in torsional, parallel-plate flow of a polymer solution, J. Fluid Mech. 554 (2006) 191. doi:10.1017/S0022112006009426.

[152] Y. Jun, V. Steinberg, Elastic turbulence in a curvilinear channel flow, Phys. Rev. E. 84 (2011) 056325. doi:10.1103/PhysRevE.84.056325.

[153] Y. Liu, V. Steinberg, Molecular sensor of elastic stress in a random flow, EPL (Europhysics Lett. 90 (2010) 44002. doi:10.1209/0295-5075/90/44002.

[154] S. Berti, A. Bistagnino, G. Boffetta, A. Celani, S. Musacchio, Small-scale

statistics of viscoelastic turbulence, Europhys. Lett. 76 (2006) 63–69. doi:10.1209/epl/i2006-10222-6.

[155] Y. Jun, V. Steinberg, Polymer concentration and properties of elastic turbulence in a von Karman swirling flow, Phys. Rev. Fluids. 2 (2017) 103301. doi:10.1103/PhysRevFluids.2.103301.

[156] T. Burghelea, E. Segre, V. Steinberg, Role of Elastic Stress in Statistical and Scaling Properties of Elastic Turbulence, Phys. Rev. Lett. 96 (2006) 214502. doi:10.1103/PhysRevLett.96.214502.

[157] Y. Liu, V. Steinberg, Stretching of polymer in a random flow: Effect of a shear rate, EPL (Europhysics Lett. 90 (2010) 44005. doi:10.1209/0295-5075/90/44005.

[158] V. Steinberg, Elastic stresses in random flow of a dilute polymer solution and the turbulent drag reduction problem, Comptes Rendus Phys. 10 (2009) 728–739. doi:10.1016/j.crhy.2009.10.015.

[159] S. Belan, A. Chernykh, V. Lebedev, Boundary layer of elastic turbulence, ArXiv:1708.05312. (2017) 1–5.

4 Finite Volume Method

This chapter presents a description of the numerical method used in this thesis. Minor modifications were made to the boundary conditions of the in-house viscoelastic flow solver as work progressed, duly noted in each chapter. The present method, initially developed by Oliveira et al. [1], is an implicit, second order accurate, finite volume implementation using a non-orthogonal mesh, and is based on the Semi-Implicit Method for Pressure Linked Equations-Consistent (SIMPLEC) algorithm proposed by van Doormal and Raithby [2]. The two core modifications of the previously Newtonian flow solver are (1) the collocated mesh arrangement of all dependent variables at the center of each control volume, and (2) the extension of the algorithm to include differential constitutive equations for the polymeric component of the extra stress tensor. Further improvements were later added to the method, principally the Convergent and Universally Bounded Interpolation Scheme for the Treatment of Advection (CUBISTA), developed by Alves et al. [3], and Fattal and Kupferman's log-conformation representation (LCR) of the polymeric extra stress tensor [4], implemented by Afonso et al. [5]. The Einstein summation convention, i.e. summation over repeated indices, is used throughout this chapter, except in the discretized formulation of the governing equations, where sums are made explicit.

4.1 Generalized Coordinates

Some of the flow geometries commonly used in both fundamental and applied investigations of viscoelastic flow feature curved boundaries, e.g. in the flow past a cylinder, hence a broadly applicable finite volume formulation should not rely on an orthogonal grid arrangement. The non-orthogonal computational mesh is described using generalized curvilinear coordinates, (see also Chap. 3 in Ref. [6] or Chap. 2 in Ref. [7]), according to the transformation depicted in Figure 4.1.

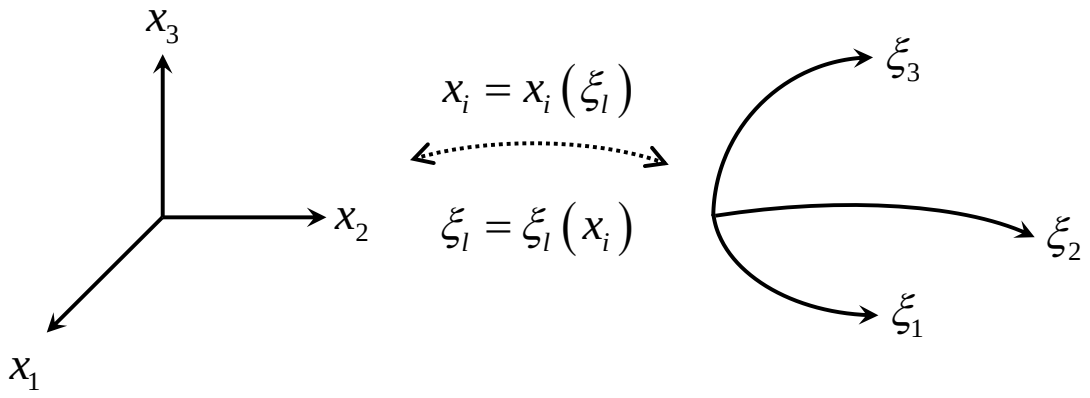

Figure 4.1 – Representation of the transformation of a Cartesian coordinate system, $\{x_i,\ i=1,2,3\}$, into a generalized coordinate system aligned with the curvature of the mesh, $\{\xi_l,\ l=1,2,3\}$.

Consequently, the governing equations must be expressed in generalized coordinates. Considering the Jacobian matrix $\mathbf{J}$ of the transformation,

$$J_{il} = \frac{\partial x_i}{\partial \xi_l}, \tag{4.1}$$

the following transformation rules lead to a set of governing equations written in strong conservation form [8],

$$\frac{\partial}{\partial t} = \frac{1}{J}\frac{\partial}{\partial t} J, \tag{4.2}$$

$$\frac{\partial}{\partial x_i} = \frac{\partial}{\partial \xi_l}\frac{\partial \xi_l}{\partial x_i} = \frac{1}{J}\frac{\partial}{\partial \xi_l}\beta_{li}, \tag{4.3}$$

where J is the determinant of the Jacobian matrix and β_{li} are metric coefficients defined as the entries in the cofactor matrix of $\mathbf{J}$. For isothermal, incompressible flow, the following continuity and momentum equations apply for a Cartesian coordinate system,

$$\frac{\partial \rho u_j}{\partial x_j} = 0, \tag{4.4}$$

$$\frac{\partial \rho u_i}{\partial t} + \frac{\partial \rho u_j u_i}{\partial x_j} = -\frac{\partial p}{\partial x_i} + \frac{\partial \sigma_{ij}}{\partial x_j}, \tag{4.5}$$

where u_i are the components of the velocity vector, ρ is the volumetric mass density of the fluid, p is the pressure and σ_{ij} are the components of the extra stress tensor. In the continuity equation, ρ is included for the sake of convenience. In the momentum equation, the body force term referring to the influence of gravity, ρg_i, was neglected, since there are no changes in the elevation of the fluid in the work discussed throughout in this thesis. Application of the transformation rules described by eqs. 4.2 and 4.3 yields the following conservation equations in generalized coordinates,

$$\frac{\partial \rho \beta_{lj} u_j}{\partial \xi_l} = 0, \tag{4.6}$$

$$\frac{\partial \rho J u_i}{\partial t} + \frac{\partial \rho \beta_{lj} u_j u_i}{\partial \xi_l} = -\frac{\partial \beta_{li} p}{\partial \xi_l} + \frac{\partial \beta_{lj} \sigma_{ij}}{\partial \xi_l}. \tag{4.7}$$

In eq. 4.7, generally the terms on the left hand side are calculated implicitly, whereas the terms on the right hand side are incorporated into the source term of the algebraic equation, as explained later. Several differential constitutive models are used in this thesis, namely the UCM, Oldroyd-B, simplified linearized PTT and FENE-CR models. For a Cartesian coordinate system, these models may be written using the following formulae,

$$\begin{cases} \sigma_{ij} = \eta_s \left(\dfrac{\partial u_i}{\partial x_j} + \dfrac{\partial u_j}{\partial x_i} \right) + \tau_{ij} \\ f\left(\mathrm{tr}(\boldsymbol{\tau})\right)\tau_{ij} + \lambda \left(\dfrac{\tau_{ij}}{g\left(\mathrm{tr}(\boldsymbol{\tau})\right)} \right)_{(1)} = \eta_p \left(\dfrac{\partial u_i}{\partial x_j} + \dfrac{\partial u_j}{\partial x_i} \right) \end{cases} \tag{4.8}$$

where η_s is the solvent shear viscosity, with $\eta_s = 0$ for the UCM model, τ_{ij} represents the components of the polymeric extra stress tensor, λ is the relaxation time of the fluid and η_p is the polymeric shear viscosity. The subscript $(\cdot)_{(1)}$ denotes the upper-convected time derivative,

$$\left(\frac{\tau_{ij}}{g\left(\mathrm{tr}(\boldsymbol{\tau})\right)}\right)_{(1)} = \frac{\partial}{\partial t}\left(\frac{\tau_{ij}}{g\left(\mathrm{tr}(\boldsymbol{\tau})\right)}\right) + \frac{\partial}{\partial x_k}\left(u_k \frac{\tau_{ij}}{g\left(\mathrm{tr}(\boldsymbol{\tau})\right)}\right) - \frac{\tau_{jk}}{g\left(\mathrm{tr}(\boldsymbol{\tau})\right)}\frac{\partial u_i}{\partial x_k} - \frac{\tau_{ik}}{g\left(\mathrm{tr}(\boldsymbol{\tau})\right)}\frac{\partial u_j}{\partial x_k}, \tag{4.9}$$

whereas $f\left(\mathrm{tr}(\boldsymbol{\tau})\right)$ and $g\left(\mathrm{tr}(\boldsymbol{\tau})\right)$ are functions of the trace of the polymeric extra stress tensor, and are equal to one except for the simplified linearized PTT and FENE-CR models, respectively,

$$\begin{cases} \text{simplified linearized PTT}: f\left(\mathrm{tr}(\boldsymbol{\tau})\right) = 1 + \dfrac{\lambda\varepsilon}{\eta_p}\mathrm{tr}(\boldsymbol{\tau}) \\ \text{other models}: f\left(\mathrm{tr}(\boldsymbol{\tau})\right) = 1 \end{cases}, \tag{4.10}$$

$$\begin{cases} \text{FENE-CR}: g\left(\mathrm{tr}(\boldsymbol{\tau})\right) = \dfrac{L^2 + \dfrac{\lambda}{\eta_p}\mathrm{tr}(\boldsymbol{\tau})}{L^2 - 3} \\ \text{other models}: g\left(\mathrm{tr}(\boldsymbol{\tau})\right) = 1 \end{cases}$$

where ε and L^2 are the extensibility parameters of the corresponding model. Rearranging eq. 4.8 and applying the transformation rules described in eqs. 4.2 and 4.3, the constitutive equation has the following form in a generalized coordinate system,

$$\begin{cases} \sigma_{ij} = \dfrac{\eta_s}{J}\left(\dfrac{\partial \beta_{lj} u_i}{\partial \xi_l} + \dfrac{\partial \beta_{li} u_j}{\partial \xi_l}\right) + \tau_{ij} \\ f\left(\mathrm{tr}(\boldsymbol{\tau})\right) J\tau_{ij} + \lambda\dfrac{\partial}{\partial t}\left(J\dfrac{\tau_{ij}}{g\left(\mathrm{tr}(\boldsymbol{\tau})\right)}\right) + \lambda\dfrac{\partial}{\partial \xi_l}\left(\beta_{lk} u_k \dfrac{\tau_{ij}}{g\left(\mathrm{tr}(\boldsymbol{\tau})\right)}\right) \\ \qquad = \eta_p\left(\dfrac{\partial \beta_{lj} u_i}{\partial \xi_l} + \dfrac{\partial \beta_{li} u_j}{\partial \xi_l}\right) + \lambda\left(\dfrac{\tau_{jk}}{g\left(\mathrm{tr}(\boldsymbol{\tau})\right)}\dfrac{\partial \beta_{lk} u_i}{\partial \xi_l} + \dfrac{\tau_{ik}}{g\left(\mathrm{tr}(\boldsymbol{\tau})\right)}\dfrac{\partial \beta_{lk} u_j}{\partial \xi_l}\right) \end{cases}. \tag{4.11}$$

4.2 Discretization of the Governing Equations

The computational domain is subdivided into contiguous cuboids, i.e. convex polyhedra with six convex quadrilateral faces, and the integration of the governing equations over each control volume is realized via the application of the Divergence Theorem,

$$\iiint_V (\nabla \cdot \mathbf{G}) \, \mathrm{d}V = \oiint_S (\mathbf{G} \cdot \mathbf{n}) \, \mathrm{d}S , \tag{4.12}$$

where $\mathbf{G}$ is a generic vector field and V is a control volume bounded by surface S with normal vector $\mathbf{n}$. Most terms in the governing equations are discretized using central differences, meaning that the cell face values needed for the application of the Divergence Theorem are calculated by linear interpolation of the appropriate cell center values obtained in the previous time-step or time-marching iteration. Alternatively, the cell face values corresponding to the advective terms in the momentum and constitutive equations are estimated using the CUBISTA scheme. Ultimately, the discretization yields a set of algebraic equations, relating the new cell center values of the variables with their counterparts in the adjacent cells.

The numerical integration of the governing equations written in generalized coordinates, eqs. 4.6, 4.7 and 4.11, requires a working knowledge of the notation explained in Figures 4.2 and 4.3 (see also Chap. 3 in Ref. [6] or Chap. 2 in Ref. [7]). Briefly, the Jacobian determinant J and the cofactors of the Jacobian matrix β_{li} may be written using finite differences, and are in this form readily interpreted, respectively, as the volume of the cell V and the corresponding surface area components B_{li} after integration. Additionally, the derivatives of the form $\partial\phi/\partial\xi_l$ are replaced by differences along direction l. For instance, for $l = 1 \equiv f$ as depicted in Figure 4.3, this derivative might be discretized either about a cell center or a face center. Using the notation described in Figure 4.2,

$$\left.\frac{\partial \phi}{\partial \xi_l}\right|_{l=1\equiv f}^{\mathrm{P}} = \left[\Delta\phi\right]_f^{\mathrm{P}} \equiv \phi_{\mathrm{f}^+} - \phi_{\mathrm{f}^-} \quad \text{or} \quad \left.\frac{\partial \phi}{\partial \xi_l}\right|_{l=1\equiv f}^{\mathrm{f}} = \left[\Delta\phi\right]_f^{\mathrm{f}} \equiv \phi_{\mathrm{F}^+} - \phi_{\mathrm{P}} . \tag{4.13}$$

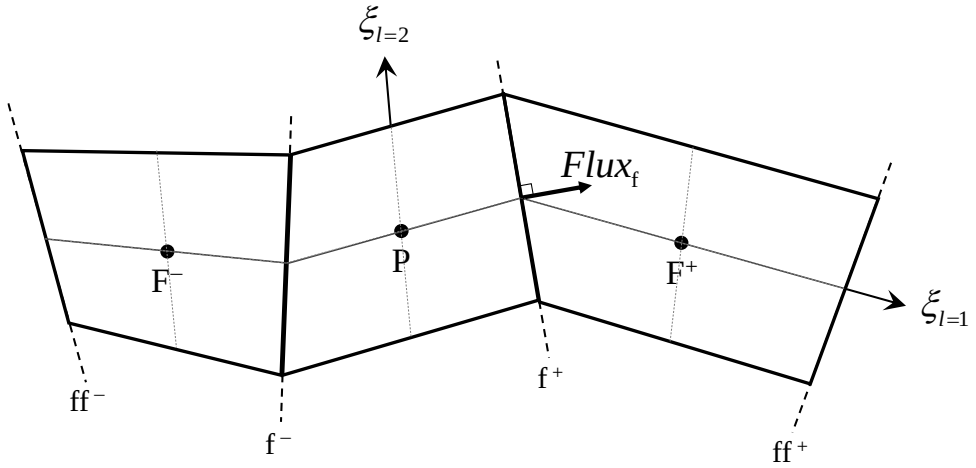

Figure 4.2 – Notation used in the discretization of the governing equations. Uppercase letters denote control volumes, or cells, and the corresponding center, whereas lowercase letters denote cell faces and face centers. The mass flow rate, or flux, across face f^+ is elsewhere denoted F_{f}, but was here written as $Flux_{\mathrm{f}}$ for the sake of clarity. ξ_l are the generalized coordinate axes.

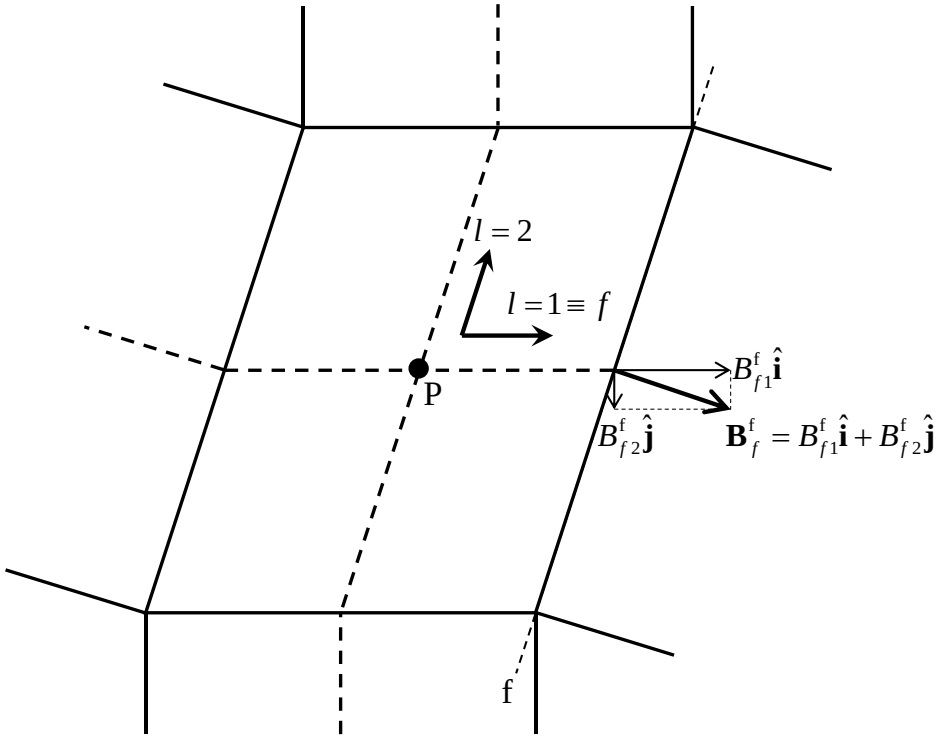

Figure 4.3 – Representation of the area components B_{li}. The superscript denotes the position where the area is evaluated, in this case at cell face f, whereas the subscript denotes the direction of the surface normal $\mathbf{n}_{\mathrm{f}}$, which coincides with one of the axes of the generalized coordinate system, in this example $l=1\equiv f$. $\mathbf{B}^{\mathrm{f}}_f$ is therefore the product of the area of face f with the normal vector $\mathbf{n}_{\mathrm{f}}$. Alternatively, the surface perpendicular to the axis $l=1\equiv f$, calculated at P, is denoted as $\mathbf{B}^{\mathrm{P}}_f = B^{\mathrm{P}}_{f1}\hat{\mathbf{i}}$, with $B^{\mathrm{P}}_{f2}=0$ from the geometry shown in this example, and the surface perpendicular to $l=2$ at the same location is denoted as $\mathbf{B}^{\mathrm{P}}_2 = B^{\mathrm{P}}_{21}\hat{\mathbf{i}} + B^{\mathrm{P}}_{22}\hat{\mathbf{j}}$.

The letter P denotes a generic cell where integration is performed, F refers to the first cell adjacent to P along the generalized direction f, or $l = f$, which in turn references the cell face f separating P and F. Continuing along direction f, the second neighbor of P is the cell FF, and the boundary between cells F and FF is denoted by ff. Using compass notation, the six cells that border P are referred to as W, E, S, N, B and T, which stand for West, East, South, North, Bottom and Top, and following the aforementioned naming conventions, the cell FF may be referred to as WW, EE, SS, NN, BB or TT. Similarly, the six faces of P are referred to as w, e, s, n, b and t, and so on for the faces between F and FF. The three axes of the compass, W-E, S-N and B-T, correspond to the three generalized directions, respectively, $l = \{1, 2, 3\}$. Alternatively, the neighbors of P may be numbered, such that $\mathrm{F} = \{1, 2, 3, 4, 5, 6\} \equiv \{\mathrm{W}, \mathrm{E}, \mathrm{S}, \mathrm{N}, \mathrm{B}, \mathrm{T}\}$, and a similar numbering system may also apply to the cell faces f. All of the implicitly treated terms of the governing equations refer only to the first set of neighbors around P, thus the algebraic equations always have a matrix of coefficients with $1 + 2\,\mathrm{dim}$ non-zero entries in each row, where $\mathrm{dim} = \{1, 2, 3\}$ for one-, two- or three-dimensional flows, respectively.

4.2.1 Continuity Equation

As a reminder, the summation convention over repeated indices is not used in the discretized equations, where sums are made explicit. Application of the Divergence Theorem to eq. 4.6, followed by the above mentioned discretization rules, yields the following expression for the continuity equation,

$$\int_{V_\mathrm{P}} \frac{\partial}{\partial \xi_l} \left(\rho \beta_{lj} u_j \right) \mathrm{d}V = \sum_{l=1}^{3} \left[\Delta \left(\sum_{j=1}^{3} \rho B_{lj} u_j \right) \right]_l^{\mathrm{P}} = \sum_{\mathrm{f}=1}^{6} \left(\sum_{j=1}^{3} \rho B_{lj}^{\mathrm{f}} \tilde{u}_{j,\mathrm{f}} \right) = 0 . \quad (4.14)$$

The special notation $\tilde{u}_{j,\mathrm{f}}$ is meant to convey that the components of the cell face velocity are not determined through linear interpolation, and are instead estimated via a Rhie-Chow interpolation [9], as explained later. Alternatively, mass flow rates F_f may be

defined for each cell face, leading to a simplified form of the discretized continuity equation,

$$F_{\mathrm{f}} = \sum_{j=1}^{3} \rho B_{fj}^{\mathrm{f}} \tilde{u}_{j,\mathrm{f}} \,, \tag{4.15}$$

$$\sum_{\mathrm{f}=1}^{6} F_{\mathrm{f}} = 0 \,. \tag{4.16}$$

4.2.2 Momentum Equation

Eq. 4.7 is first rewritten so that the extra stress tensor σ_{ij} is decomposed into a sum of solvent and polymeric contributions,

$$\underbrace{\frac{\partial \rho J u_i}{\partial t}}_{\text{Inertia}} + \underbrace{\frac{\partial \rho \beta_{lj} u_j u_i}{\partial \xi_l}}_{\text{Advection}} = \underbrace{-\frac{\partial \beta_{li} p}{\partial \xi_l}}_{\substack{\text{Pressure} \\ \text{Gradient}}} + \underbrace{\frac{\partial}{\partial \xi_l}\left[\beta_{lj}\frac{\eta_s}{J}\left(\frac{\partial \beta_{mj} u_i}{\partial \xi_m} + \frac{\partial \beta_{mi} u_j}{\partial \xi_m}\right)\right]}_{\text{Diffusion} \equiv \text{Newtonian Stress Divergence}} + \underbrace{\frac{\partial \beta_{lj} \tau_{ij}}{\partial \xi_l}}_{\substack{\text{Polymeric Stress} \\ \text{Divergence}}} \,. \tag{4.17}$$

The integration of each term in eq. 4.17 is described separately.

Inertia term

The inertial term is integrated using the following backward differencing scheme [10],

$$\int_{V_{\mathrm{P}}} \frac{\partial \rho J u_i}{\partial t} \mathrm{d}V = \frac{\rho V_{\mathrm{P}}}{\delta t}\left[(1+\alpha)u_{i,\mathrm{P}} - (1+2\alpha)u_{i,\mathrm{P}}^{(n-1)} + \alpha u_{i,\mathrm{P}}^{(n-2)}\right], \tag{4.18}$$

where δt is the time-step and the superscripts $^{(n-1)}$ and $^{(n-2)}$ denote the preceding time levels. The parameter α controls the accuracy of the time discretization, for $\alpha = 0$ the first order backward Euler method is recovered, which is utilized for stationary flow simulations. For $\alpha = 1/2$, second order backward differentiation is recovered, which is used for time-dependent flow simulations in order to increase the accuracy of the solver. Since the present method is fully implicit, all variables without the superscripts $^{(n-1)}$ or $^{(n-2)}$ refer to the new time level.

Advection term

The integration of the advective term is initially similar to the procedure applied to the continuity equation,

$$\int_{V_\mathrm{P}} \frac{\partial}{\partial \xi_l}\left(\rho \beta_{lj} u_j u_i\right) \mathrm{d}V = \sum_{l=1}^{3}\left[\Delta\left(u_i \sum_{j=1}^{3} \rho B_{lj} u_j\right)\right]_l^{\mathrm{P}} = \sum_{\mathrm{f}=1}^{6} F_\mathrm{f} \hat{u}_{i,\mathrm{f}} \,, \tag{4.19}$$

where F_f are the mass flow rates across each face, calculated via eq. 4.15, and the advected cell face velocity $\hat{u}_{i,\mathrm{f}}$ is estimated using a special procedure. First, an upwind differencing scheme (UDS) is implemented (see Figure 4.2 for the relevant notation),

$$\begin{cases} F_\mathrm{f}^{+} = \max\left(F_\mathrm{f}, 0\right) \\ F_\mathrm{f}^{-} = \min\left(F_\mathrm{f}, 0\right) \\ \hat{u}_{i,\mathrm{f}} = \dfrac{F_\mathrm{f}^{+} u_{i,\mathrm{P}} + F_\mathrm{f}^{-} u_{i,\mathrm{F}}}{F_\mathrm{f}} \equiv u_{i,\mathrm{f,UDS}} \end{cases}, \tag{4.20}$$

and the term $F_\mathrm{f} \hat{u}_{i,\mathrm{f}}$ in eq. 4.19 is treated implicitly. Second, a separate estimate of the advected cell face velocity is calculated via the CUBISTA scheme [3], denoted as

$u_{i,\mathrm{f}^+,\mathrm{CUBISTA}}$. The normalized variable approach was extensively discussed Chap. 3 of this thesis, hence here only a brief reminder of the relevant notation is given,

$$\left\{ \widehat{\xi}_{\mathrm{C}} = \frac{\xi_{\mathrm{C}} - \xi_{\mathrm{U}}}{\xi_{\mathrm{D}} - \xi_{\mathrm{U}}},\ \widehat{\xi}_{\mathrm{f}^+} = \frac{\xi_{\mathrm{f}^+} - \xi_{\mathrm{U}}}{\xi_{\mathrm{D}} - \xi_{\mathrm{U}}} \right\}, \tag{4.21}$$

$$\left\{ \widehat{u}_{i,\mathrm{C}} = \frac{u_{i,\mathrm{C}} - u_{i,\mathrm{U}}}{u_{i,\mathrm{D}} - u_{i,\mathrm{U}}},\ \widehat{u}_{i,\mathrm{f}^+} = \frac{u_{i,\mathrm{f}^+} - u_{i,\mathrm{U}}}{u_{i,\mathrm{D}} - u_{i,\mathrm{U}}} \right\}, \tag{4.22}$$

where D, C and U denote, respectively, the first downstream cell, the first upstream cell, and the second upstream cell relative to face f^+. Thus, according to the notation given in Figure 4.2, if the mass flow rate is positive, i.e. $F_{\mathrm{f}^+} \geq 0$, then $\{\mathrm{U},\mathrm{C},\mathrm{D}\} = \{\mathrm{F}^-,\mathrm{P},\mathrm{F}^+\}$, otherwise if $F_{\mathrm{f}^+} < 0$ then $\{\mathrm{U},\mathrm{C},\mathrm{D}\} = \{\mathrm{FF}^+,\mathrm{F}^+,\mathrm{P}\}$. For the sake of notational brevity, the subscript corresponding to the generalized coordinate axes, $l = \{1,2,3\}$, was not included in eqs. 4.21 and 4.22. The CUBISTA scheme yields the following interpolation for $\widehat{u}_{i,\mathrm{f}^+}$,

$$\widehat{u}_{i,\mathrm{f}^+,\mathrm{CUBISTA}} = \begin{cases} \left[1 + \dfrac{\widehat{\xi}_{\mathrm{f}^+} - \widehat{\xi}_{\mathrm{C}}}{3\left(1-\widehat{\xi}_{\mathrm{C}}\right)}\right]\dfrac{\widehat{\xi}_{\mathrm{f}^+}}{\widehat{\xi}_{\mathrm{C}}}\widehat{u}_{i,\mathrm{C}} & \text{if} \quad 0 \leq \widehat{u}_{i,\mathrm{C}} < \dfrac{3}{4}\widehat{\xi}_{\mathrm{C}} \\ \dfrac{\widehat{\xi}_{\mathrm{f}^+}\left(1-\widehat{\xi}_{\mathrm{f}^+}\right)}{\widehat{\xi}_{\mathrm{C}}\left(1-\widehat{\xi}_{\mathrm{C}}\right)}\widehat{u}_{i,\mathrm{C}} + \dfrac{\widehat{\xi}_{\mathrm{f}^+}\left(\widehat{\xi}_{\mathrm{f}^+} - \widehat{\xi}_{\mathrm{C}}\right)}{1-\widehat{\xi}_{\mathrm{C}}} & \text{if} \quad \dfrac{3}{4}\widehat{\xi}_{\mathrm{C}} \leq \widehat{u}_{i,\mathrm{C}} < \dfrac{1+2\left(\widehat{\xi}_{\mathrm{f}^+} - \widehat{\xi}_{\mathrm{C}}\right)}{2\widehat{\xi}_{\mathrm{f}^+} - \widehat{\xi}_{\mathrm{C}}}\widehat{\xi}_{\mathrm{C}} \\ 1 - \dfrac{1-\widehat{\xi}_{\mathrm{f}^+}}{2\left(1-\widehat{\xi}_{\mathrm{C}}\right)}\left(1-\widehat{u}_{i,\mathrm{C}}\right) & \text{if} \quad \dfrac{1+2\left(\widehat{\xi}_{\mathrm{f}^+} - \widehat{\xi}_{\mathrm{C}}\right)}{2\widehat{\xi}_{\mathrm{f}^+} - \widehat{\xi}_{\mathrm{C}}}\widehat{\xi}_{\mathrm{C}} \leq \widehat{u}_{i,\mathrm{C}} \leq 1 \\ \widehat{u}_{i,\mathrm{C}} & \text{elsewhere} \end{cases} \tag{4.23}$$

Finally, the normalization of $\widehat{u}_{i,\mathrm{f}^+,\mathrm{CUBISTA}}$ is reversed, and the estimate is incorporated in the source term of the discretized momentum equation, S_{u_i}, via deferred correction [11],

$$S_{u_i-\text{CUBISTA}} = -\sum_{\text{f}^+=1}^{3}\left[F_{\text{f}^+}^{+}\left(u_{i,\text{f}^+,\text{CUBISTA}} - u_{i,\text{f}^+,\text{UDS}}\right) + F_{\text{f}^+}^{-}\left(u_{i,\text{f}^+,\text{CUBISTA}} - u_{i,\text{f}^+,\text{UDS}}\right)\right] + \sum_{\text{f}^-=1}^{3}\left[F_{\text{f}^-}^{+}\left(u_{i,\text{f}^-,\text{CUBISTA}} - u_{i,\text{f}^-,\text{UDS}}\right) + F_{\text{f}^-}^{-}\left(u_{i,\text{f}^-,\text{CUBISTA}} - u_{i,\text{f}^-,\text{UDS}}\right)\right]. \quad (4.24)$$

The deferred correction procedure effectively compensates for the diffusiveness of the UDS method, given that a portion of the advected scalar is transferred between the source terms of sequential cells along the downstream direction.

Pressure Gradient term

Integration of the pressure gradient term is straightforward, and the resulting value is incorporated in the source term of the discretized momentum equation,

$$\int_{V_\text{P}}\left(-\frac{\partial \beta_{li} p}{\partial \xi_l}\right)\text{d}V = \sum_{l=1}^{3}\left(-B_{li}^{\text{P}}\left[\Delta p\right]_l^{\text{P}}\right) \equiv S_{u_i-\text{pressure}}. \quad (4.25)$$

Diffusion / Newtonian Stress Divergence term

The integration of the diffusive term is more complex than the corresponding operation for other terms, due to the presence of nested derivatives. For the sake of clarity, the following decomposition of the term is used,

$$\frac{\partial \beta_{lj}\eta_s \dot{\gamma}_{ij}}{\partial \xi_l}, \quad (4.26)$$

$$\dot{\gamma}_{ij} = \frac{1}{J}\frac{\partial}{\partial \xi_m}\left(\beta_{mj}u_i + \beta_{mi}u_j\right), \quad (4.27)$$

where $\dot{\gamma}_{ij}$ are the components of the rate-of-strain tensor. The integration of eq. 4.26 yields the following expression,

$$\int_{V_\mathrm{P}} \frac{\partial \beta_{lj} \eta_s \dot{\gamma}_{ij}}{\partial \xi_l} \mathrm{d}V = \sum_{l=1}^{3} \left[\Delta \left(\sum_{j=1}^{3} B_{lj} \eta_s \dot{\gamma}_{ij} \right) \right]_l^{\mathrm{P}} = \eta_s \sum_{\mathrm{f}=1}^{6} \left(\sum_{j=1}^{3} B_{\hat{f}j}^{\mathrm{f}} \hat{\dot{\gamma}}_{ij,\mathrm{f}} \right), \tag{4.28}$$

where $\hat{\dot{\gamma}}_{ij,\mathrm{f}}$ denotes a special integration procedure, over the volume of a pseudo cell centered at the face f, namely $V_\mathrm{f} = \sum_{j=1}^{3} B_{\hat{f}j}^{\mathrm{f}} \left[\Delta x_j \right]_f^{\mathrm{f}}$. From eq. 4.27,

$$\begin{aligned} \hat{\dot{\gamma}}_{ij,\mathrm{f}} = \int_{V_\mathrm{f}} \frac{1}{J} \frac{\partial}{\partial \xi_m} \left(\beta_{mj} u_i + \beta_{mi} u_j \right) \mathrm{d}V &= \frac{1}{V_\mathrm{f}} \sum_{m=1}^{3} \left[\Delta \left(\sum_{j=1}^{3} \left(B_{mj} u_i + B_{mi} u_j \right) \right) \right]_m^{\mathrm{f}} \\ &= \frac{1}{V_\mathrm{f}} \sum_{m=1}^{3} \left(\sum_{j=1}^{3} \left(B_{mj}^{\mathrm{f}} \left[\Delta u_i \right]_m^{\mathrm{f}} + B_{mi}^{\mathrm{f}} \left[\Delta u_j \right]_m^{\mathrm{f}} \right) \right) \end{aligned} . \tag{4.29}$$

Substituting eq. 4.29 into eq. 4.28 and rearranging,

$$\begin{aligned} &\int_{V_\mathrm{P}} \frac{\partial}{\partial \xi_l} \left[\beta_{lj} \frac{\eta_s}{J} \left(\frac{\partial \beta_{mj} u_i}{\partial \xi_m} + \frac{\partial \beta_{mi} u_j}{\partial \xi_m} \right) \right] \mathrm{d}V \\ &\quad = \eta_s \sum_{\mathrm{f}=1}^{6} \frac{1}{V_\mathrm{f}} \left(\sum_{j=1}^{3} \left(\sum_{m=1}^{3} B_{\hat{f}j}^{\mathrm{f}} B_{mj}^{\mathrm{f}} \left[\Delta u_i \right]_m^{\mathrm{f}} + \sum_{m=1}^{3} B_{\hat{f}j}^{\mathrm{f}} B_{mi}^{\mathrm{f}} \left[\Delta u_j \right]_m^{\mathrm{f}} \right) \right) \end{aligned} . \tag{4.30}$$

Furthermore, eq. 4.30 is split in two components. First, the diffusive flux aligned with the direction $m \equiv f$, i.e. normal to face f, which is evaluated implicitly,

$$-\eta_s \sum_{\mathrm{f}=1}^{6} \frac{1}{V_\mathrm{f}} \left(\sum_{j=1}^{3} B_{\hat{f}j}^{\mathrm{f}} B_{\hat{f}j}^{\mathrm{f}} \left[\Delta u_i \right]_f^{\mathrm{f}} \right) = -\sum_{\mathrm{f}=1}^{6} D_{\mathrm{f},s} \left(u_{i,\mathrm{F}} - u_{i,\mathrm{P}} \right), \tag{4.31}$$

where $D_{\mathrm{f},s} = \eta_s B_\mathrm{f}^2 / V_\mathrm{f}$ is the diffusive conductance of the solvent, and $B_\mathrm{f} = \left\| \mathbf{B}_f^\mathrm{f} \right\| = \sqrt{\sum_{j=1}^{3} B_{fj}^\mathrm{f} B_{fj}^\mathrm{f}}$ is the surface area of face f. Second, the remaining terms in eq. 4.30 are incorporated into the source term,

$$S_{u_i-\mathrm{diffusion}} = \eta_s \sum_{\mathrm{f}=1}^{6} \frac{1}{V_\mathrm{f}} \left(\sum_{j=1}^{3} \left(\sum_{\substack{m=1 \\ m \neq j}}^{3} B_{fj}^\mathrm{f} B_{mj}^\mathrm{f} \left[\Delta u_i \right]_m^\mathrm{f} + \sum_{m=1}^{3} B_{fj}^\mathrm{f} B_{mi}^\mathrm{f} \left[\Delta u_j \right]_m^\mathrm{f} \right) \right). \qquad (4.32)$$

The treatment of diffusion is explained in greater detail in Chap. 3 of Ref. [7].

Polymeric Stress Divergence term

The polymeric extra stress term is evaluated explicitly,

$$\int_{V_\mathrm{P}} \frac{\partial \beta_{lj} \tau_{ij}}{\partial \xi_l} \mathrm{d}V = \sum_{l=1}^{3} \left[\Delta \left(\sum_{j=1}^{3} B_{lj} \tau_{ij} \right) \right]_l^\mathrm{P} = \sum_{\mathrm{f}=1}^{6} \left(\sum_{j=1}^{3} B_{fj}^\mathrm{f} \tilde{\tau}_{ij,\mathrm{f}} \right) \equiv S_{u_i-\text{polymeric stress}}. \qquad (4.33)$$

Due to the collocated variable arrangement, and to avoid stress-velocity decoupling, $\tilde{\tau}_{ij,\mathrm{f}}$ is interpolated using a special procedure, originally introduced in Ref. [1] and later modified by Oliveira and Pinho [12] and by Matos et al. [13], as explained later.

Algebraic Equation

Re-grouping the various terms of the momentum equation leads to,

$$\frac{\rho V_{\mathrm{P}}}{\delta t}\left[(1+\alpha)u_{i,\mathrm{P}}-(1+2\alpha)u_{i,\mathrm{P}}^{(n-1)}+\alpha u_{i,\mathrm{P}}^{(n-2)}\right]+\sum_{\mathrm{f}=1}^{6}F_{\mathrm{f}}u_{i,\mathrm{f,UDS}}-\sum_{\mathrm{f}=1}^{6}D_{\mathrm{f},s}\left(u_{i,\mathrm{F}}-u_{i,\mathrm{P}}\right)$$
$$=\underbrace{S_{u_i-\mathrm{CUBISTA}}+S_{u_i-\mathrm{pressure}}+S_{u_i-\mathrm{diffusion}}+S_{u_i-\mathrm{polymeric\ stress}}}_{=S_{u_i}}. \qquad (4.34)$$

Alternatively, using matrix notation,

$$a_{\mathrm{P}}u_{i,\mathrm{P}}-\sum_{\mathrm{F}=1}^{6}a_{\mathrm{F}}u_{i,\mathrm{F}}=S_{u_i}-\frac{\rho V_{\mathrm{P}}}{\delta t}\left[-(1+2\alpha)u_{i,\mathrm{P}}^{(n-1)}+\alpha u_{i,\mathrm{P}}^{(n-2)}\right], \qquad (4.35)$$

where a_{P} are the entries of the matrix of coefficients, $u_{i,\mathrm{P}}$ are the entries in the vector of unknowns and the right hand side of eq. 4.35 is the source term of the linear system. The coefficients are defined as follows [1],

$$\begin{cases} a_{\mathrm{F}}=a_{\mathrm{F}}^{D}+a_{\mathrm{F}}^{C} \\ \quad a_{\mathrm{F}}^{D}=D_{\mathrm{f},s} \\ \quad a_{\mathrm{F}}^{C}=\begin{cases} +F_{\mathrm{f}}^{+}=+\max\left(F_{\mathrm{f}},0\right) & \text{for a negative face, } \mathrm{f}^{-} \\ -F_{\mathrm{f}}^{-}=-\min\left(F_{\mathrm{f}},0\right) & \text{for a positive face, } \mathrm{f}^{+} \end{cases} \\ a_{\mathrm{P}}=\dfrac{\rho V_{\mathrm{P}}}{\delta t}(1+\alpha)+\sum_{\mathrm{F}=1}^{6}a_{\mathrm{F}} \end{cases}, \qquad (4.36)$$

where the superscripts ^{D} and ^{C} denote diffusion and advection (or convection), respectively.

4.2.3 Constitutive Equation

The constitutive equation is treated using the Log-Conformation Representation (LCR) developed by Fattal and Kupferman [4], as discussed in Chap. 3 of this thesis. The

corresponding sequence of transformations is presented below. First, the constitutive equation is written in Cartesian coordinates for the polymeric extra stresses τ_{ij},

$$f\left(\mathrm{tr}\left(\boldsymbol{\tau}\right)\right)\tau_{ij}+\lambda\frac{\partial}{\partial t}\left(\frac{\tau_{ij}}{g\left(\mathrm{tr}\left(\boldsymbol{\tau}\right)\right)}\right)+\lambda\frac{\partial}{\partial x_k}\left(u_k\frac{\tau_{ij}}{g\left(\mathrm{tr}\left(\boldsymbol{\tau}\right)\right)}\right) -\lambda\left(\frac{\tau_{jk}}{g\left(\mathrm{tr}\left(\boldsymbol{\tau}\right)\right)}\frac{\partial u_i}{\partial x_k}+\frac{\tau_{ik}}{g\left(\mathrm{tr}\left(\boldsymbol{\tau}\right)\right)}\frac{\partial u_j}{\partial x_k}\right)=\eta_p\left(\frac{\partial u_i}{\partial x_j}+\frac{\partial u_j}{\partial x_i}\right) \quad . \quad (4.37)$$

Then, using the following relation between the polymeric extra stress tensor $\boldsymbol{\tau}$ and the conformation tensor $\mathbf{A}$,

$$\tau_{ij}=\frac{\eta_p}{\lambda/g\left(\mathrm{tr}\left(\mathbf{A}\right)\right)}\left(A_{ij}-\delta_{ij}\right), \quad (4.38)$$

where δ_{ij} is the Kronecker delta (i.e. $i=j\Rightarrow\delta_{ij}=1$ and $i\neq j\Rightarrow\delta_{ij}=0$), eq. 4.37 is converted into the conformation tensor formulation,

$$\frac{\partial A_{ij}}{\partial t}+\frac{\partial u_k A_{ij}}{\partial x_k}-\left(A_{jk}\frac{\partial u_i}{\partial x_k}+A_{ik}\frac{\partial u_j}{\partial x_k}\right)=-f\left(\mathrm{tr}\left(\mathbf{A}\right)\right)g\left(\mathrm{tr}\left(\mathbf{A}\right)\right)\frac{1}{\lambda}\left(A_{ij}-\delta_{ij}\right). \quad (4.39)$$

As noted earlier, the auxiliary functions $f\left(\mathrm{tr}\left(\cdot\right)\right)$ and $g\left(\mathrm{tr}\left(\cdot\right)\right)$ are equal to one, except for the following constitutive models,

$$\begin{cases}\text{simplified linearized PTT}: f\left(\mathrm{tr}\left(\boldsymbol{\tau}\right)\right)\equiv f\left(\mathrm{tr}\left(\mathbf{A}\right)\right)=1+\varepsilon\left(\mathrm{tr}\left(\mathbf{A}\right)-3\right)\\ \text{other models}: f\left(\mathrm{tr}\left(\boldsymbol{\tau}\right)\right)\equiv f\left(\mathrm{tr}\left(\mathbf{A}\right)\right)=1\end{cases}$$
$$\begin{cases}\text{FENE-CR}: g\left(\mathrm{tr}\left(\boldsymbol{\tau}\right)\right)\equiv g\left(\mathrm{tr}\left(\mathbf{A}\right)\right)=\dfrac{L^2}{L^2-\mathrm{tr}\left(\mathbf{A}\right)}\\ \text{other models}: g\left(\mathrm{tr}\left(\boldsymbol{\tau}\right)\right)\equiv g\left(\mathrm{tr}\left(\mathbf{A}\right)\right)=1\end{cases} \quad . \quad (4.40)$$

Subsequently, as explained in greater detail by Pimenta and Alves [14], the procedure outlined by Fattal and Kupferman [4] is implemented. Briefly, since the conformation tensor is symmetric positive definite, $\mathbf{A}$ may be diagonalized and transformed as follows,

$$\mathbf{A} = \mathbf{R}\boldsymbol{\Lambda}\mathbf{R}^{\dagger}, \tag{4.41}$$

$$\boldsymbol{\Theta} = \ln\left(\mathbf{A}\right) = \mathbf{R}\ln\left(\boldsymbol{\Lambda}\right)\mathbf{R}^{\dagger}, \tag{4.42}$$

where the columns of the tensor $\mathbf{R}$ are the eigenvectors of the conformation tensor, the diagonal matrix $\boldsymbol{\Lambda}$ contains the corresponding eigenvalues, and $\boldsymbol{\Theta}$ is the matrix-logarithm of $\mathbf{A}$. Note that $\mathbf{R}$ is orthogonal, i.e. $\mathbf{R}\mathbf{R}^{\dagger} = \mathbf{R}^{\dagger}\mathbf{R} = \mathbf{I}$, where $\mathbf{I}$ is the identity matrix. Furthermore, the transposed gradient of the velocity field $\left(\nabla\mathbf{u}\right)^{\dagger}$ is decomposed into an extensional component $\mathbf{E}$ and a rotational component $\boldsymbol{\Omega}$,

$$\mathbf{E} = \mathbf{R}\begin{bmatrix} M_{11} & 0 & 0 \\ 0 & M_{22} & 0 \\ 0 & 0 & M_{33} \end{bmatrix}\mathbf{R}^{\dagger} \quad \text{with} \quad \mathbf{M} = \mathbf{R}^{\dagger}\left(\nabla\mathbf{u}\right)^{\dagger}\mathbf{R}, \tag{4.43}$$

$$\boldsymbol{\Omega} = \mathbf{R}\begin{bmatrix} 0 & \omega_{12} & \omega_{13} \\ -\omega_{12} & 0 & \omega_{23} \\ -\omega_{13} & -\omega_{23} & 0 \end{bmatrix}\mathbf{R}^{\dagger} \quad \text{with} \quad \underbrace{\omega_{ij} = \frac{\Lambda_{jj}M_{ij} + \Lambda_{ii}M_{ji}}{\Lambda_{jj} - \Lambda_{ii}}}_{\text{no Einstein summation}}. \tag{4.44}$$

In this thesis, $\left(\nabla\mathbf{u}\right)_{ij} = \partial u_j / \partial x_i$. Combining all the elements of the LCR transformation, the following constitutive equation is obtained,

$$\begin{aligned} &\frac{\partial\Theta_{ij}}{\partial t} + \frac{\partial u_k\Theta_{ij}}{\partial x_k} - \left(\Omega_{ik}\Theta_{kj} - \Theta_{ik}\Omega_{kj}\right) - 2E_{ij} \\ &\qquad = f\left(\mathrm{tr}\left(e^{\boldsymbol{\Theta}}\right)\right) g\left(\mathrm{tr}\left(e^{\boldsymbol{\Theta}}\right)\right)\frac{1}{\lambda}\left(e^{-\Theta_{ij}} - \delta_{ij}\right) \end{aligned}, \tag{4.45}$$

where $e^{\boldsymbol{\Theta}} = \mathbf{A}$, which may then be rearranged and expressed in generalized coordinates,

$$\underbrace{\frac{\lambda}{g\left(\mathrm{tr}\left(\boldsymbol{\tau}\right)\right)}\frac{\partial J\Theta_{ij}}{\partial t}}_{\text{Transient term}} + \underbrace{\frac{\lambda}{g\left(\mathrm{tr}\left(\boldsymbol{\tau}\right)\right)}\frac{\partial \beta_{lk}u_k\Theta_{ij}}{\partial \xi_l}}_{\text{Advection}} = \frac{\lambda}{g\left(\mathrm{tr}\left(\boldsymbol{\tau}\right)\right)} J\left(\Omega_{ik}\Theta_{kj} - \Theta_{ik}\Omega_{kj}\right) + 2\frac{\lambda}{g\left(\mathrm{tr}\left(\boldsymbol{\tau}\right)\right)} JE_{ij} + f\left(\mathrm{tr}\left(\mathbf{A}\right)\right) J\left(e^{-\Theta_{ij}} - \delta_{ij}\right) \quad . \tag{4.46}$$

The auxiliary functions $f\left(\mathrm{tr}\left(\cdot\right)\right)$ and $g\left(\mathrm{tr}\left(\cdot\right)\right)$ have the same value regardless of the specific argument, be it $\boldsymbol{\tau}$, $\mathbf{A}$ or $e^{\boldsymbol{\Theta}}$, however eq. 4.46 denotes the exact argument used in the Fortran implementation. The two terms on the left hand side of eq. 4.46 are discretized in a manner analogous, respectively, to the inertia and advection terms of the momentum equation,

$$\text{Transient term}: \int_{V_\mathrm{P}} \frac{\lambda}{g\left(\mathrm{tr}\left(\boldsymbol{\tau}\right)\right)}\frac{\partial J\Theta_{ij}}{\partial t}\mathrm{d}V = \frac{\lambda_\mathrm{P} V_\mathrm{P}}{\delta t}\left[\left(1+\alpha\right)\Theta_{ij,\mathrm{P}} - \left(1+2\alpha\right)\Theta_{ij,\mathrm{P}}^{(n-1)} + \alpha\Theta_{ij,\mathrm{P}}^{(n-2)}\right] , \tag{4.47}$$

$$\text{Advection}: \int_{V_\mathrm{P}} \frac{\lambda}{g\left(\mathrm{tr}\left(\boldsymbol{\tau}\right)\right)}\frac{\partial \beta_{lk}u_k\Theta_{ij}}{\partial \xi_l}\mathrm{d}V = \frac{\lambda_\mathrm{P}}{\rho}\sum_{\mathrm{f}=1}^{6} F_\mathrm{f}\hat{\Theta}_{ij,\mathrm{f}} , \tag{4.48}$$

$$\text{Deferred Correction}: S_{\Theta_{ij}-\mathrm{CUBISTA}} = -\frac{\lambda_\mathrm{P}}{\rho}\sum_{\mathrm{f}^+=1}^{3}\left[F_{\mathrm{f}^+}^{+}\left(\Theta_{ij,\mathrm{f}^+,\mathrm{CUBISTA}} - \Theta_{ij,\mathrm{f}^+,\mathrm{UDS}}\right) + F_{\mathrm{f}^+}^{-}\left(\Theta_{ij,\mathrm{f}^+,\mathrm{CUBISTA}} - \Theta_{ij,\mathrm{f}^+,\mathrm{UDS}}\right)\right], \tag{4.49}$$
$$+\frac{\lambda_\mathrm{P}}{\rho}\sum_{\mathrm{f}^-=1}^{3}\left[F_{\mathrm{f}^-}^{+}\left(\Theta_{ij,\mathrm{f}^-,\mathrm{CUBISTA}} - \Theta_{ij,\mathrm{f}^-,\mathrm{UDS}}\right) + F_{\mathrm{f}^-}^{-}\left(\Theta_{ij,\mathrm{f}^-,\mathrm{CUBISTA}} - \Theta_{ij,\mathrm{f}^-,\mathrm{UDS}}\right)\right]$$

where $\lambda_\mathrm{P} = \lambda / g\left(\mathrm{tr}\left(\boldsymbol{\tau}_\mathrm{P}\right)\right)$ is the effective relaxation time of the FENE-CR model or $\lambda_\mathrm{P} = \lambda$ for the other constitutive models used in this thesis, and, for convenience, the treatment of the convective term, eqs. 4.48 and 4.49, employs the mass flow rates F_f, therefore requiring an additional division by the density ρ. The right hand side of eq. 4.46 is treated explicitly,

$$\int_{V_\mathrm{P}} \frac{\lambda}{g\left(\mathrm{tr}\left(\boldsymbol{\tau}\right)\right)} J\left(\Omega_{ik}\Theta_{kj}-\Theta_{ik}\Omega_{kj}\right)+2\frac{\lambda}{g\left(\mathrm{tr}\left(\boldsymbol{\tau}\right)\right)} JE_{ij}+f\left(\mathrm{tr}\left(\mathbf{A}\right)\right)J\left(e^{-\Theta_{ij}}-\delta_{ij}\right)\mathrm{d}V$$
$$=\lambda_\mathrm{P} V_\mathrm{P}\left(\Omega_{ik,\mathrm{P}}\Theta_{kj,\mathrm{P}}-\Theta_{ik,\mathrm{P}}\Omega_{kj,\mathrm{P}}\right)+2\lambda_\mathrm{P} V_\mathrm{P} E_{ij,\mathrm{P}} \qquad . \qquad (4.50)$$
$$+f\left(\mathrm{tr}\left(\mathbf{A}_\mathrm{P}\right)\right)V_\mathrm{P}\left(e^{-\Theta_{ij,\mathrm{P}}}-\delta_{ij}\right)\equiv S_{\Theta_{ij}-\text{other terms}}$$

Finally, the algebraic equation for the constitutive equation is assembled [5],

$$a_\mathrm{P}^\Theta\Theta_{ij,\mathrm{P}}-\sum_{\mathrm{F}=1}^{6}a_\mathrm{F}^\Theta\Theta_{ij,\mathrm{F}}=S_{\Theta_{ij}}-\frac{\lambda_\mathrm{P}V_\mathrm{P}}{\delta t}\left[-\left(1+2\alpha\right)\Theta_{ij,\mathrm{P}}^{(n-1)}+\alpha\Theta_{ij,\mathrm{P}}^{(n-2)}\right], \qquad (4.51)$$

with the following definitions for the coefficients [1] and source term,

$$\begin{cases} a_\mathrm{F}^\Theta=\begin{cases}+\dfrac{\lambda_\mathrm{P}}{\rho}F_\mathrm{f}^{+}=+\dfrac{\lambda_\mathrm{P}}{\rho}\max\left(F_\mathrm{f},0\right) & \text{for a negative face, f}^{-}\\ -\dfrac{\lambda_\mathrm{P}}{\rho}F_\mathrm{f}^{-}=-\dfrac{\lambda_\mathrm{P}}{\rho}\min\left(F_\mathrm{f},0\right) & \text{for a positive face, f}^{+}\end{cases} \\ a_\mathrm{P}^\Theta=\dfrac{\lambda_\mathrm{P}V_\mathrm{P}}{\delta t}\left(1+\alpha\right)_\mathrm{P}+\sum_{\mathrm{F}=1}^{6}a_\mathrm{F}^\Theta \\ S_{\Theta_{ij}}=S_{\Theta_{ij}-\mathrm{CUBISTA}}+S_{\Theta_{ij}-\text{other terms}}\end{cases} \qquad . \qquad (4.52)$$

After solving eq. 4.51, and since $\boldsymbol{\Theta}$ is symmetric positive definite, recovery of the conformation tensor is straightforward,

$$\begin{aligned}&\boldsymbol{\Theta}=\mathbf{R}_\Theta\boldsymbol{\Lambda}_\Theta\mathbf{R}_\Theta^{\dagger}\\ &\Rightarrow\mathbf{A}=e^{\boldsymbol{\Theta}}=\mathbf{R}_\Theta e^{\boldsymbol{\Lambda}_\Theta}\mathbf{R}_\Theta^{\dagger}\end{aligned}, \qquad (4.53)$$

where the columns of the tensor $\mathbf{R}_\Theta$ are the eigenvectors of $\boldsymbol{\Theta}$ and the diagonal matrix $\boldsymbol{\Lambda}_\Theta$ contains the corresponding eigenvalues. Subsequent application of the relation described by eq. 4.38 yields the polymeric extra stress tensor $\boldsymbol{\tau}$. It should be noted that, for the same time level, $\boldsymbol{\Theta}$ and $\mathbf{A}$ have the same eigenvectors and the corresponding eigenvalues satisfy $\boldsymbol{\Lambda} = e^{\boldsymbol{\Lambda}_\Theta}$ [15].

4.3 Pressure-Velocity Coupling

In the present method, the pressure field is computed from the continuity equation, using a pressure (and velocity) correction procedure, as explained later. As discussed by Fergizer and Perić (Chaps. 7 and 8 in Ref. [16]), the collocated arrangement of variables simplifies the discretization of the governing equations in a non-orthogonal mesh, and consequently, the simulation of flow in complex geometries. However, unlike with a staggered grid arrangement, where the pressure and velocity nodal values are staggered by half a cell width, and in order to ensure a strong pressure-velocity coupling, the special interpolation procedure proposed by Rhie and Chow [9] is required for the calculation of the mass flow rates F_f across cell faces, or more specifically, as per eq. 4.15, the evaluation of the corresponding velocity components $\left(\tilde{u}_{i,\mathrm{f}}, \tilde{u}_{j,\mathrm{f}}, \tilde{u}_{k,\mathrm{f}}\right)$. The formulation devised by Issa and Oliveira [17] is adopted in this thesis. First, the pressure gradient is segregated from the remaining source term of the momentum equation, and for the sake of clarity, an auxiliary function $H_\mathrm{P}\left(u_i\right)$ is defined,

$$S_{u_i} = \sum_{l=1}^{3}\left(-B_{li}^{\mathrm{P}}\left[\Delta p\right]_l^{\mathrm{P}}\right) + S'_{u_i}\,, \tag{4.54}$$

$$H_\mathrm{P}\left(u_i\right) = \sum_{\mathrm{F}=1}^{6} a_\mathrm{F} u_{i,\mathrm{F}}\,. \tag{4.55}$$

The algebraic momentum equations for cells P and F can then be rewritten as follows,

$$a_{\mathrm{P}}u_{i,\mathrm{P}} = H_{\mathrm{P}}\left(u_i\right) + \sum_{l=1}^{3}\left(-B_{li}^{\mathrm{P}}\left[\Delta p\right]_l^{\mathrm{P}}\right) + S'_{u_i,\mathrm{P}} - \frac{\rho V_{\mathrm{P}}}{\delta t}\left[-\left(1+2\alpha\right)u_{i,\mathrm{P}}^{(n-1)} + \alpha u_{i,\mathrm{P}}^{(n-2)}\right], \quad (4.56)$$

$$\begin{aligned} a_{\mathrm{P=F}}u_{i,\mathrm{P=F}} &= H_{\mathrm{P=F}}\left(u_i\right) + \sum_{l=1}^{3}\left(-B_{li}^{\mathrm{P=F}}\left[\Delta p\right]_l^{\mathrm{P=F}}\right) \\ &\quad + S'_{u_i,\mathrm{P=F}} - \frac{\rho V_{\mathrm{P=F}}}{\delta t}\left[-\left(1+2\alpha\right)u_{i,\mathrm{P=F}}^{(n-1)} + \alpha u_{i,\mathrm{P=F}}^{(n-2)}\right] \\ \Leftrightarrow a_{\mathrm{F}}u_{i,\mathrm{F}} &= H_{\mathrm{F}}\left(u_i\right) + \sum_{l=1}^{3}\left(-B_{li}^{\mathrm{F}}\left[\Delta p\right]_l^{\mathrm{F}}\right) \\ &\quad + S'_{u_i,\mathrm{F}} - \frac{\rho V_{\mathrm{F}}}{\delta t}\left[-\left(1+2\alpha\right)u_{i,\mathrm{F}}^{(n-1)} + \alpha u_{i,\mathrm{F}}^{(n-2)}\right] \end{aligned} \quad (4.57)$$

To avoid confusion, eq. 4.57 denotes the algebraic momentum equation for cell F. According to the Rhie-Chow special interpolation [9],[17], $\tilde{u}_{i,\mathrm{f}}$ is evaluated by averaging the momentum eqs. 4.56 and 4.57, except for the pressure gradient term which is calculated using the procedure normally applicable to staggered grids,

$$\begin{aligned} \frac{a_{\mathrm{P}} + a_{\mathrm{F}}}{2}\tilde{u}_{i,\mathrm{f}} &= \frac{H_{\mathrm{P}}\left(u_i\right) + H_{\mathrm{F}}\left(u_i\right)}{2} - B_{fi}^{\mathrm{f}}\left[\Delta p\right]_f^{\mathrm{f}} \\ &\quad + \sum_{\substack{l=1 \\ l\neq f}}^{3}\left(\frac{-B_{li}^{\mathrm{P}}\left[\Delta p\right]_l^{\mathrm{P}} - B_{li}^{\mathrm{F}}\left[\Delta p\right]_l^{\mathrm{F}}}{2}\right) + \frac{S'_{u_i,\mathrm{P}} + S'_{u_i,\mathrm{F}}}{2} \\ &\quad - \frac{\rho}{\delta t}\frac{V_{\mathrm{P}} + V_{\mathrm{F}}}{2}\left[-\left(1+2\alpha\right)\tilde{u}_{i,\mathrm{f}}^{(n-1)} + \alpha\tilde{u}_{i,\mathrm{f}}^{(n-2)}\right] \quad , \\ \Leftrightarrow \overline{a_{\mathrm{P}}}\tilde{u}_{i,\mathrm{f}} &= \overline{H_{\mathrm{P}}\left(u_i\right)} - B_{fi}^{\mathrm{f}}\left[\Delta p\right]_f^{\mathrm{f}} + \sum_{\substack{l=1 \\ l\neq f}}^{3}\overline{\left(-B_{li}^{\mathrm{P}}\left[\Delta p\right]_l^{\mathrm{P}}\right)} + \overline{S'_{u_i,\mathrm{P}}} \\ &\quad - \frac{\rho}{\delta t}\overline{V_{\mathrm{P}}}\left[-\left(1+2\alpha\right)\tilde{u}_{i,\mathrm{f}}^{(n-1)} + \alpha\tilde{u}_{i,\mathrm{f}}^{(n-2)}\right] \end{aligned} \quad (4.58)$$

where the overbar denotes the arithmetic mean. Subtraction of the arithmetic mean of eqs. 4.56 and 4.57 from eq. 4.58 yields the final form of the special interpolation,

$$\tilde{u}_{i,\mathrm{f}} = \frac{\left[\begin{array}{c} \overline{a_{\mathrm{P}}u_{i,\mathrm{P}}} - B_{fi}^{\mathrm{f}}\left[\Delta p\right]_f^{\mathrm{f}} + \overline{B_{fi}^{\mathrm{P}}\left[\Delta p\right]_f^{\mathrm{P}}} \\ -\frac{\rho}{\delta t}\left(\overline{V_{\mathrm{P}}}\left[-\left(1+2\alpha\right)\tilde{u}_{i,\mathrm{f}}^{(n-1)} + \alpha\tilde{u}_{i,\mathrm{f}}^{(n-2)}\right] - \overline{V_{\mathrm{P}}\left[-\left(1+2\alpha\right)u_{i,\mathrm{P}}^{(n-1)} + \alpha u_{i,\mathrm{P}}^{(n-2)}\right]}\right) \end{array}\right]}{\overline{a_{\mathrm{P}}}}, \quad (4.59)$$

which is then substituted into eq. 4.15.

4.4 Stress-Velocity Coupling

The application of a special procedure for the interpolation of the cell face polymeric extra stress components $\tilde{\tau}_{ij,\mathrm{f}}$ is required to ensure a strong stress-velocity coupling. This may be illustrated with a simple example. Consider the discretization of the derivative $\partial \tau_{ij} / \partial x_f$ about cell P, in a uniform orthogonal mesh,

$$\left.\frac{\partial \tau_{ij}}{\partial x_f}\right|_{\mathrm{P}} = \frac{\tau_{ij,\mathrm{f}^+} - \tau_{ij,\mathrm{f}^-}}{x_{f,\mathrm{f}^+} - x_{f,\mathrm{f}^-}} = \frac{1}{\Delta x_f}\left[\frac{\tau_{ij,\mathrm{F}^+} + \tau_{ij,\mathrm{P}}}{2} - \frac{\tau_{ij,\mathrm{P}} + \tau_{ij,\mathrm{F}^-}}{2}\right] = \frac{1}{2\Delta x_f}\left[\tau_{ij,\mathrm{F}^+} - \tau_{ij,\mathrm{F}^-}\right]. \quad (4.60)$$

Since the application of central differencing leads to the evaluation of the derivative in cell P based exclusively in the values of τ_{ij} in the adjacent cells, a possible stress-velocity decoupling may occur due to the polymeric extra stress divergence term in the momentum equation. This is traditionally not an issue for the Newtonian component of the stress, since this term is usually formulated using the Laplace operator,

$$\eta_s \left.\frac{\partial^2 u_i}{\partial x_f^2}\right|_{\mathrm{P}} = \frac{\eta_s}{\Delta x_f}\left[\left.\frac{\partial u_i}{\partial x_f}\right|_{\mathrm{f}^+} - \left.\frac{\partial u_i}{\partial x_f}\right|_{\mathrm{f}^-}\right] = \frac{\eta_s}{\left(\Delta x_f\right)^2}\left[u_{i,\mathrm{F}^+} - 2u_{i,\mathrm{P}} + u_{i,\mathrm{F}^-}\right]. \quad (4.61)$$

Consequently, a special interpolation procedure is required for the estimation of $\tilde{\tau}_{ij,\mathrm{f}}$ in eq. 4.33. The methodology developed by Oliveira et al. [1] and later refined by Oliveira and Pinho [12] was subsequently modified by Matos et al. [13], in order to eliminate the influence of the time-step value δt on the interpolated values $\tilde{\tau}_{ij,\mathrm{f}}$. First, the algebraic constitutive equation is rewritten for τ_{ij}, instead of Θ_{ij},

$$a_{\mathrm{P}}^{\tau}\tau_{ij,\mathrm{P}} - \sum_{\mathrm{F}=1}^{6} a_{\mathrm{F}}^{\tau}\tau_{ij,\mathrm{F}} = S_{\tau_{ij}} - \frac{\lambda_{\mathrm{P}} V_{\mathrm{P}}}{\delta t}\left[-\left(1+2\alpha\right)\tau_{ij,\mathrm{P}}^{(n-1)} + \alpha\tau_{ij,\mathrm{P}}^{(n-2)}\right], \quad (4.62)$$

with coefficients $a_{\mathrm{F}}^{\tau} = a_{\mathrm{F}}^{\Theta}$ and $a_{\mathrm{P}}^{\tau} = f\left(\mathrm{tr}\left(\boldsymbol{\tau}_{\mathrm{P}}\right)\right)V_{\mathrm{P}} + \sum_{\mathrm{F}=1}^{6} a_{\mathrm{F}}^{\tau} + \frac{\lambda_{\mathrm{P}} V_{\mathrm{P}}}{\delta t}\left(1+\alpha\right)$. The source term $S_{\tau_{ij}}$ is obtained from eq. 4.11 using the aforementioned discretization rules,

$$\begin{aligned} S_{\tau_{ij}} = & \sum_{l=1}^{3}\left(\eta_p B_{lj}^{\mathrm{P}}\left[\Delta u_i\right]_l^{\mathrm{P}} + \eta_p B_{li}^{\mathrm{P}}\left[\Delta u_j\right]_l^{\mathrm{P}}\right) \\ & + \sum_{l=1}^{3}\left(\lambda_{\mathrm{P}}\sum_{k=1}^{3}\tau_{jk,\mathrm{P}} B_{lk}^{\mathrm{P}}\left[\Delta u_i\right]_l^{\mathrm{P}} + \lambda_{\mathrm{P}}\sum_{k=1}^{3}\tau_{ik,\mathrm{P}} B_{lk}^{\mathrm{P}}\left[\Delta u_j\right]_l^{\mathrm{P}}\right) + S_{\tau_{ij}-\mathrm{CUBISTA}} \end{aligned}, \quad (4.63)$$

Additionally, the auxiliary function $H_{\mathrm{P}}^{\tau}\left(\tau_{ij}\right)$ is defined as,

$$H_{\mathrm{P}}^{\tau}\left(\tau_{ij}\right) = \sum_{\mathrm{F}=1}^{6} a_{\mathrm{F}}^{\tau}\tau_{ij,\mathrm{F}} + S_{\tau_{ij,\mathrm{P}}-\mathrm{CUBISTA}}\,. \quad (4.64)$$

Subsequently, the algebraic constitutive equation (4.62), is recast for the pair of adjacent cells P and F,

$$\begin{aligned} a_{\mathrm{P}}^{\tau}\tau_{ij,\mathrm{P}} = & H_{\mathrm{P}}^{\tau}\left(\tau_{ij}\right) + \sum_{l=1}^{3}\left(\eta_p B_{lj}^{\mathrm{P}}\left[\Delta u_i\right]_l^{\mathrm{P}} + \eta_p B_{li}^{\mathrm{P}}\left[\Delta u_j\right]_l^{\mathrm{P}}\right) \\ & + \sum_{l=1}^{3}\left(\lambda_{\mathrm{P}}\sum_{k=1}^{3}\tau_{jk,\mathrm{P}} B_{lk}^{\mathrm{P}}\left[\Delta u_i\right]_l^{\mathrm{P}} + \lambda_{\mathrm{P}}\sum_{k=1}^{3}\tau_{ik,\mathrm{P}} B_{lk}^{\mathrm{P}}\left[\Delta u_j\right]_l^{\mathrm{P}}\right), \\ & - \frac{\lambda_{\mathrm{P}} V_{\mathrm{P}}}{\delta t}\left[-\left(1+2\alpha\right)\tau_{ij,\mathrm{P}}^{(n-1)} + \alpha\tau_{ij,\mathrm{P}}^{(n-2)}\right] \end{aligned} \quad (4.65)$$

$$\begin{aligned} a_{\mathrm{F}}^{\tau}\tau_{ij,\mathrm{F}} = & H_{\mathrm{F}}^{\tau}\left(\tau_{ij}\right) + \sum_{l=1}^{3}\left(\eta_p B_{lj}^{\mathrm{F}}\left[\Delta u_i\right]_l^{\mathrm{F}} + \eta_p B_{li}^{\mathrm{F}}\left[\Delta u_j\right]_l^{\mathrm{F}}\right) \\ & + \sum_{l=1}^{3}\left(\lambda_{\mathrm{F}}\sum_{k=1}^{3}\tau_{jk,\mathrm{F}} B_{lk}^{\mathrm{F}}\left[\Delta u_i\right]_l^{\mathrm{F}} + \lambda_{\mathrm{F}}\sum_{k=1}^{3}\tau_{ik,\mathrm{F}} B_{lk}^{\mathrm{F}}\left[\Delta u_j\right]_l^{\mathrm{F}}\right). \\ & - \frac{\lambda_{\mathrm{F}} V_{\mathrm{F}}}{\delta t}\left[-\left(1+2\alpha\right)\tau_{ij,\mathrm{F}}^{(n-1)} + \alpha\tau_{ij,\mathrm{F}}^{(n-2)}\right] \end{aligned} \quad (4.66)$$

As with the special interpolation of the cell face velocity components $\tilde{u}_{i,\mathrm{f}}$, eq. 4.66 denotes the algebraic constitutive equation for cell F. Following the procedure described by Matos et al. [13], all of the terms in eqs. 4.65 and 4.66 are then divided by the cell volume, V_{P} and V_{F} respectively, and then averaged, except for those terms in the first summation on the right-hand side of eqs. 4.65 and 4.66 which correspond to the generalized direction $l = f$,

$$\begin{aligned}\overline{\frac{1}{V_{\mathrm{P}}} a_{\mathrm{P}}^{\tau} \tilde{\tau}_{ij,\mathrm{f}}} = {} & \overline{\frac{1}{V_{\mathrm{P}}} H_{\mathrm{P}}^{\tau}\left(\tau_{ij}\right)} + \frac{1}{V_{\mathrm{f}}}\left(\eta_p B_{lj}^{\mathrm{f}}\left[\Delta u_i\right]_l^{\mathrm{f}} + \eta_p B_{li}^{\mathrm{f}}\left[\Delta u_j\right]_l^{\mathrm{f}}\right) \\ & + \overline{\frac{1}{V_{\mathrm{P}}} \sum_{\substack{l=1 \\ l \neq f}}^{3}\left(\eta_p B_{lj}^{\mathrm{P}}\left[\Delta u_i\right]_l^{\mathrm{P}} + \eta_p B_{li}^{\mathrm{P}}\left[\Delta u_j\right]_l^{\mathrm{P}}\right)} \\ & + \overline{\frac{1}{V_{\mathrm{P}}} \sum_{l=1}^{3}\left(\left(\lambda_{\mathrm{P}} \sum_{k=1}^{3} \tau_{jk,\mathrm{P}} B_{lk}^{\mathrm{P}}\right)\left[\Delta u_i\right]_l^{\mathrm{P}} + \left(\lambda_{\mathrm{P}} \sum_{k=1}^{3} \tau_{ik,\mathrm{P}} B_{lk}^{\mathrm{P}}\right)\left[\Delta u_j\right]_l^{\mathrm{P}}\right)} \\ & - \overline{\frac{\lambda_{\mathrm{P}}}{\delta t}\left[-\left(1+2\alpha\right)\tau_{ij,\mathrm{P}}^{(n-1)} + \alpha \tau_{ij,\mathrm{P}}^{(n-2)}\right]}\end{aligned} . \tag{4.67}$$

where $V_{\mathrm{f}} = \sum_{j=1}^{3} B_{fj}^{\mathrm{f}}\left[\Delta x_j\right]_f^{\mathrm{f}}$, introduced earlier in the discretization of the diffusive term of the momentum equation, is the volume of a pseudo cell centered at face f. Subtraction of the arithmetic mean of eqs. 4.65 and 4.66 from eq. 4.67 yields the final form of the special interpolation,

$$\tilde{\tau}_{ij,\mathrm{f}} = \frac{\left[\begin{array}{c} \overline{\frac{1}{V_{\mathrm{P}}} a_{\mathrm{P}}^{\tau} \tau_{ij,\mathrm{P}}} - \overline{\frac{1}{V_{\mathrm{P}}}\left(\eta_p B_{fj}^{\mathrm{P}}\left[\Delta u_i\right]_f^{\mathrm{P}} + \eta_p B_{fi}^{\mathrm{P}}\left[\Delta u_j\right]_f^{\mathrm{P}}\right)} \\ + \frac{1}{V_{\mathrm{f}}}\left(\eta_p B_{lj}^{\mathrm{f}}\left[\Delta u_i\right]_l^{\mathrm{f}} + \eta_p B_{li}^{\mathrm{f}}\left[\Delta u_j\right]_l^{\mathrm{f}}\right) \end{array}\right]}{\overline{a_{\mathrm{P}}^{\tau} / V_{\mathrm{P}}}}, \tag{4.68}$$

which is then substituted into eq. 4.33.

4.5 Solution Algorithm

The solution algorithm is based on the SIMPLEC procedure developed by van Doormal and Raithby [2], derived from Patankar and Spalding's SIMPLE algorithm [18]. Since the momentum equations, which explicitly contain a pressure gradient term, are used to calculate the velocity field, the pressure is computed indirectly from the continuity equation. The SIMPLEC procedure was devised for iterative marching, however, with the modifications described by Issa and Oliveira [17], the method used in this thesis is instead time-marching, allowing the simulation of both transient and stationary flows. Typically, for a stationary flow, the simulations are interrupted whenever the residuals associated with each variable decay by several orders of magnitude. Oliveira et al. [1] extended the method further with the incorporation of differential constitutive equations for the calculation of the polymeric extra stress, evaluated prior to the computation of the velocity field, and finally the implementation of the log-conformation representation described by Afonso et al. [5] implied additional adjustments to the procedure. The following is a summary of the algorithm in its current form.

The first of three major steps is the solution of the algebraic constitutive equations. As explained in section 4.2.3, the polymeric extra stress tensor $\tau_{ij}^{(n-1)}$ is first converted into the conformation tensor $A_{ij}^{(n-1)}$, which is then transformed into the matrix-logarithm $\Theta_{ij}^{(n-1)}$ using the velocity field of the previous time level. The six components Θ_{ij} are then calculated implicitly,

$$a_{\mathrm{P}}^{\Theta}\Theta_{ij,\mathrm{P}} - \sum_{\mathrm{F}=1}^{6} a_{\mathrm{F}}^{\Theta}\Theta_{ij,\mathrm{F}} = \underbrace{S_{\Theta_{ij}} - \frac{\lambda_{\mathrm{P}} V_{\mathrm{P}}}{\delta t}\left[-\left(1+2\alpha\right)\Theta_{ij,\mathrm{P}}^{(n-1)} + \alpha\Theta_{ij,\mathrm{P}}^{(n-2)}\right]}_{\text{source term}}, \qquad (4.69)$$

where the source term is shown in an expanded form. The updated conformation tensor A_{ij} and subsequently the polymeric extra stress tensor τ_{ij} are then recovered.

The second major step is the solution of the algebraic momentum equations. The three components u_i^*, which do not generally satisfy the continuity equation, are calculated implicitly,

$$a_{\mathrm{P}}u_{i,\mathrm{P}}^{*}-\sum_{\mathrm{F}=1}^{6}a_{\mathrm{F}}u_{i,\mathrm{F}}^{*}=\underbrace{\begin{array}{c}S_{u_i-\text{other terms}}+S_{u_i-\text{polymeric stress}}+\sum_{l=1}^{3}\left(-B_{li}^{\mathrm{P}}\left[\Delta p^{(n-1)}\right]_{l}^{\mathrm{P}}\right)\\ -\dfrac{\rho V_{\mathrm{P}}}{\delta t}\left[-\left(1+2\alpha\right)u_{i,\mathrm{P}}^{(n-1)}+\alpha u_{i,\mathrm{P}}^{(n-2)}\right]\end{array}}_{\text{source term}},\qquad(4.70)$$

where the terms on the right-hand side are calculated explicitly. The polymeric extra stress divergence term, $S_{u_i-\text{polymeric stress}}$, is computed using the cell face extra stresses $\tilde{\tau}_{ij,\mathrm{f}}$, obtained via the special interpolation described in section 4.4, hence why the constitutive equations are solved first. Also, the pressure gradient term appears segregated from the remaining source term for the sake of convenience.

The third major step is the correction of u_i^{*} and simultaneously the calculation of the pressure field. Eq. 4.70 is first rewritten as follows,

$$\begin{array}{l}\overbrace{\left\{\dfrac{\rho V_{\mathrm{P}}}{\delta t}\left(1+\alpha\right)u_{i,\mathrm{P}}+\left(\sum_{\mathrm{F}=1}^{6}a_{\mathrm{F}}\right)u_{i,\mathrm{P}}^{*}\right\}}^{\text{from } a_{\mathrm{P}}u_{i,\mathrm{P}}^{*}}-\sum_{\mathrm{F}=1}^{6}a_{\mathrm{F}}u_{i,\mathrm{F}}^{*}\\ =\underbrace{S_{u_i-\text{other terms}}+S_{u_i-\text{polymeric stress}}+\sum_{l=1}^{3}\left(-B_{li}^{\mathrm{P}}\left[\Delta p\right]_{l}^{\mathrm{P}}\right)-\dfrac{\rho V_{\mathrm{P}}}{\delta t}\left[-\left(1+2\alpha\right)u_{i,\mathrm{P}}^{(n-1)}+\alpha u_{i,\mathrm{P}}^{(n-2)}\right]}_{\text{source term}}\end{array},\qquad(4.71)$$

where the term $a_{\mathrm{P}}^{(n-1)}u_{i,\mathrm{P}}^{*}$ has been expanded and modified according to the SIMPLEC algorithm [2], so that the corrected, new time level velocity components $u_{i,\mathrm{P}}$ appear and the pressure drop Δp now refers to the new time level as well. Subtracting eq. 4.70 from eq. 4.71,

$$\begin{array}{l}\dfrac{\rho V_{\mathrm{P}}}{\delta t}\left(1+\alpha\right)\left[u_{i,\mathrm{P}}-u_{i,\mathrm{P}}^{*}\right]=\sum_{l=1}^{3}\left(-B_{li}^{\mathrm{P}}\left(\left[\Delta p\right]_{l}^{\mathrm{P}}-\left[\Delta p^{(n-1)}\right]_{l}^{\mathrm{P}}\right)\right)\\ \qquad\qquad=\sum_{l=1}^{3}\left(-B_{li}^{\mathrm{P}}\left(\left[\Delta p'\right]_{l}^{\mathrm{P}}\right)\right)\end{array},\qquad(4.72)$$

where $p' = p - p^{(n-1)}$ denotes the pressure correction. As inferred by Patankar and Spalding [18], the mass flow rate correction, $F_\mathrm{f}' = F_\mathrm{f} - F_\mathrm{f}^*$, should be proportional to the pressure drop correction,

$$\begin{aligned} &-a_\mathrm{F}^p \left[\Delta p'\right]_f^\mathrm{f} = F_\mathrm{f}' \\ &\Leftrightarrow -a_\mathrm{F}^p \left(p_\mathrm{F}' - p_\mathrm{P}'\right) = F_\mathrm{f} - F_\mathrm{f}^* \end{aligned}, \tag{4.73}$$

where F_f^* is computed from eq. 4.15 using the uncorrected velocity components $\tilde{u}_{i,\mathrm{f}}^*$, formulated as described in section 4.3, and is also a function of the pressure in the previous time level, $p^{(n-1)}$. The coefficients a_F^p used in this thesis were derived by Issa and Oliveira [17],

$$a_\mathrm{F}^p = \frac{\rho B_\mathrm{f}^2}{\left(\frac{\rho V_\mathrm{P}}{\delta t}\left(1+\alpha\right)\right)_\mathrm{f}} = \frac{B_\mathrm{f}^2}{\frac{1}{\delta t}\left(1+\alpha\right)\frac{V_\mathrm{P}+V_\mathrm{F}}{2}}. \tag{4.74}$$

The corrected mass flow rates are then forced to satisfy the continuity equation, $\sum_{\mathrm{f}=1}^{6} F_\mathrm{f} = 0,$ yielding the algebraic pressure correction equation,

$$\begin{aligned} &\sum_{\mathrm{F}=1}^{6}\left(-a_\mathrm{F}^p \left(p_\mathrm{F}' - p_\mathrm{P}'\right)\right) = \sum_{\mathrm{f}=1}^{6}\left(F_\mathrm{f} - F_\mathrm{f}^*\right) \\ &\Leftrightarrow a_\mathrm{P}^p p_\mathrm{P}' - \sum_{\mathrm{F}=1}^{6} a_\mathrm{F}^p p_\mathrm{F}' = -\sum_{\mathrm{f}=1}^{6} F_\mathrm{f}^* \\ &\text{with} \quad a_\mathrm{P}^p = \sum_{\mathrm{F}=1}^{6} a_\mathrm{F}^p \end{aligned}. \tag{4.75}$$

The values of p' obtained by solving eq. 4.75 are then used to updated the pressure and correct the velocity components,

$$p_{\mathrm{P}} = p'_{\mathrm{P}} + p_{\mathrm{P}}^{(n-1)}, \tag{4.76}$$

$$u_{i,\mathrm{P}} = \frac{1}{\dfrac{\rho V_{\mathrm{P}}}{\delta t}\left(1+\alpha\right)} \sum_{l=1}^{3}\left(-B_{li}^{\mathrm{P}}\left(\left[\Delta p'\right]_{l}^{\mathrm{P}}\right)\right) + u_{i,\mathrm{P}}^{*}. \tag{4.77}$$

This completes the algorithm.

The algebraic momentum and constitutive equations are solved using a bi-conjugate gradient method [19], whereas the algebraic pressure correction equation is solved using a symmetric gradient method [19]. In either case, the matrix of coefficients is pre-conditioned using an incomplete LU factorization, also described in Ref. [19].

4.6 Boundary Conditions

Boundary conditions are set for the velocity components along the inlets, outlets, symmetry planes and walls. The constitutive equations are hyperbolic, therefore only the inlet values of the polymeric extra stress need to be specified, however approximate wall values may be prescribed to reduce the computational time. The absolute values of the pressure are unimportant for incompressible flow problems, hence $p = 0$ is prescribed at a particular cell, commonly at an inlet, and the pressure field is initially set to zero, and subsequently updated by the SIMPLEC algorithm.

4.6.1 Inlets

Dirichlet boundary conditions are prescribed for the velocity and polymeric extra stress components. Often, the inlet velocity profile is uniform along the streamwise direction and null in the spanwise direction, whereas the inlet polymeric extra stress profile is usually equal to zero. Sufficiently long inlet channels ensure the full development of variable profiles. Alternatively, the inlet values may be derived from analytical solutions of the flow in a straight channel.

4.6.2 Outlets

Neumann boundary conditions of the form $\mathbf{n}_{\text{out}} \cdot \nabla \phi = 0$ are prescribed for the velocity, polymeric extra stress and pressure gradient, which is equivalent to assuming an ad infinitum continuation of the mesh. Sufficiently long outlet channels ensure that any hypothetical perturbations at the outlet are not felt near the relevant segment of the flow domain. Numerically, the boundary conditions are implemented by setting the values at the outlet cell faces equal to those of the corresponding upstream cell center, except for pressure which is linearly extrapolated from the two upstream cell centers.

4.6.3 Symmetry Planes

Symmetry boundary conditions are utilized as a way to facilitate the simulation of two-dimensional flows with symmetry. This is accomplished via the application of reflection rules in fictitious symmetric cells (see Chap. 3.4 of Ref. [7]), depicted in Figure 4.4.

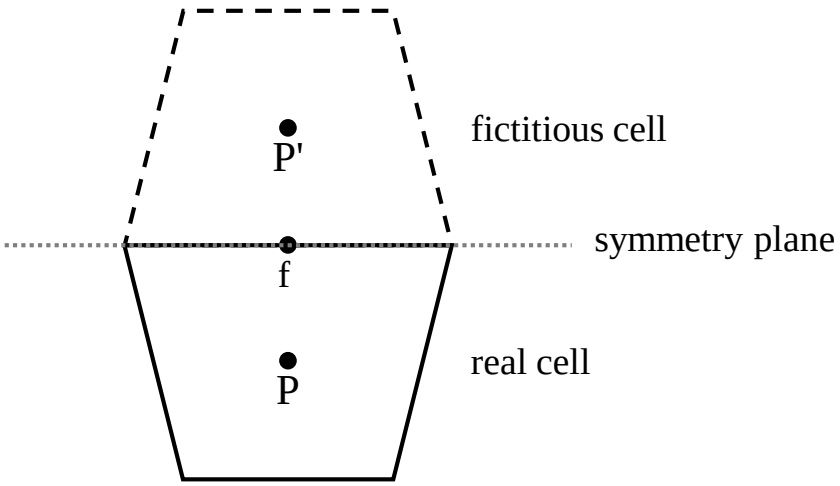

Figure 4.4 – Illustration of a fictitious reflected cell P'.

The convective and diffusive fluxes must vanish across a symmetry plane, leading to the following set of boundary conditions. The velocity vector stored at cell P is written as a combination of wall-normal and tangential components,

$$\mathbf{u}_{\mathrm{P}} = u_{n,\mathrm{P}}\mathbf{n}_{\mathrm{f}} + \underbrace{\left(\mathbf{u}_{\mathrm{P}} - u_{n,\mathrm{P}}\mathbf{n}_{\mathrm{f}}\right)}_{\text{tangential component}}, \tag{4.78}$$

where $\mathbf{n}_{\mathrm{f}}$ is the unit vector normal to the symmetry plane along face f in Figure 4.4, and the wall-normal component is given by $u_{n,\mathrm{P}} = \mathbf{u}_{\mathrm{P}} \cdot \mathbf{n}_{\mathrm{f}}$. The tangential component is the same for both P and the fictitious cell P' across f, whereas the normal component is symmetric,

$$\begin{aligned} & u_{n,\mathrm{P}'} = -u_{n,\mathrm{P}} \\ & \Rightarrow \mathbf{u}_{\mathrm{P}'} = -u_{n,\mathrm{P}}\mathbf{n}_{\mathrm{f}} + \left(\mathbf{u}_{\mathrm{P}} - u_{n,\mathrm{P}}\mathbf{n}_{\mathrm{f}}\right) = \mathbf{u}_{\mathrm{P}} - 2u_{n,\mathrm{P}}\mathbf{n}_{\mathrm{f}} \end{aligned}. \tag{4.79}$$

Given $\mathbf{u}_{\mathrm{P}}$ and $\mathbf{u}_{\mathrm{P}'}$, the velocity along the symmetry plane is calculated by linear interpolation, which, considering that P and P' are symmetric, amounts to an arithmetic mean,

$$\begin{aligned} & \mathbf{u}_{\mathrm{f}} = \frac{\mathbf{u}_{\mathrm{P}} + \mathbf{u}_{\mathrm{P}'}}{2} = \mathbf{u}_{\mathrm{P}} - u_{n,\mathrm{P}}\mathbf{n}_{\mathrm{f}} \\ & \Leftrightarrow u_{i,\mathrm{f}} = u_{i,\mathrm{P}} - \left(\sum_{j=1}^{3} u_{j,\mathrm{P}} n_{j,\mathrm{f}}\right) n_{i,\mathrm{f}} \end{aligned}. \tag{4.80}$$

For any scalar quantity, including the pressure, the reflection law is obtained from eq. 4.80 by setting $u_{n,\mathrm{P}} = 0$,

$$\begin{aligned} & \phi_{\mathrm{f}} = \phi_{\mathrm{P}} \\ & \Rightarrow p_{\mathrm{f}} = p_{\mathrm{P}} \end{aligned}. \tag{4.81}$$

The symmetry boundary conditions for the polymeric extra stress are derived using the traction vector $\mathbf{T}$,

$$T_i = \sum_{j=1}^{3} \tau_{ij} n_j \,, \tag{4.82}$$

which may be written as a combination of wall-normal and tangential components,

$$\mathbf{T}_\mathrm{P} = T_{n,\mathrm{P}} \mathbf{n}_\mathrm{f} + \underbrace{\left(\mathbf{T}_\mathrm{P} - T_{n,\mathrm{P}} \mathbf{n}_\mathrm{f} \right)}_{\text{tangential component}} . \tag{4.83}$$

Since the polymeric extra stress is a function of the gradient of the velocity field, the reflection rules for the traction vector are reversed, i.e. the wall-normal component is the same for both P and the fictitious cell P' across f, whereas the tangential component is symmetric. Consequently,

$$\mathbf{T}_{\mathrm{P}'} = T_{n,\mathrm{P}} \mathbf{n}_\mathrm{f} - \left(\mathbf{T}_\mathrm{P} - T_{n,\mathrm{P}} \mathbf{n}_\mathrm{f} \right) = -\mathbf{T}_\mathrm{P} + 2 T_{n,\mathrm{P}} \mathbf{n}_\mathrm{f} \,, \tag{4.84}$$

and, by linear interpolation,

$$\begin{aligned} &\mathbf{T}_\mathrm{f} = \frac{\mathbf{T}_\mathrm{P} + \mathbf{T}_{\mathrm{P}'}}{2} = T_{n,\mathrm{P}} \mathbf{n}_\mathrm{f} \\ &\Leftrightarrow T_{i,\mathrm{f}} = \left(\sum_{j=1}^{3} T_{j,\mathrm{P}} n_{j,\mathrm{f}} \right) n_{i,\mathrm{f}} \\ &\Leftrightarrow \sum_{j=1}^{3} \tau_{ij,\mathrm{f}} n_{j,\mathrm{f}} = \left(\sum_{j=1}^{3} \left(\sum_{k=1}^{3} \tau_{jk,\mathrm{P}} n_{k,\mathrm{f}} \right) n_{j,\mathrm{f}} \right) n_{i,\mathrm{f}} \end{aligned} \,. \tag{4.85}$$

By definition, $n_{j,\mathrm{f}} = B^{\mathrm{f}}_{fj} / B_{\mathrm{f}}$, with $B_{\mathrm{f}} = \left\| \mathbf{B}^{\mathrm{f}}_{f} \right\| = \sqrt{\sum_{j=1}^{3} B^{\mathrm{f}}_{fj} B^{\mathrm{f}}_{fj}}$, so the left-hand side of eq. 4.85 is rewritten as follows,

$$\frac{1}{B_{\mathrm{f}}} \sum_{j=1}^{3} B^{\mathrm{f}}_{fj} \tau_{ij,\mathrm{f}} = \frac{1}{B_{\mathrm{f}}} \left(S_{u_i - \text{polymeric stress}} \right)_{\mathrm{f}} , \tag{4.86}$$

hence the symmetry boundary condition for the polymeric extra stress is implemented via the source term of the momentum equation,

$$\left(S_{u_i - \text{polymeric stress}} \right)_{\mathrm{f}} = B_{\mathrm{f}} \left(\sum_{j=1}^{3} \left(\sum_{k=1}^{3} \tau_{jk,\mathrm{P}} n_{k,\mathrm{f}} \right) n_{j,\mathrm{f}} \right) n_{i,\mathrm{f}} . \tag{4.87}$$

For the sake of clarity, the full polymeric extra stress source term is written for a cell along a symmetry plane,

$$S_{u_i - \text{polymeric stress}} = \sum_{\substack{\mathrm{f}=1 \\ \mathrm{f} \neq \text{sym.p.}}}^{6} \left(\sum_{j=1}^{3} B^{\mathrm{f}}_{fj} \tilde{\tau}_{ij,\mathrm{f}} \right) + \underbrace{B_{\mathrm{f}} \left(\sum_{j=1}^{3} \left(\sum_{k=1}^{3} \tau_{jk,\mathrm{P}} n_{k,\mathrm{f}} \right) n_{j,\mathrm{f}} \right) n_{i,\mathrm{f}}}_{\mathrm{f} = \text{symmetry plane}} . \tag{4.88}$$

4.6.4 Walls

At the walls, no-slip boundary conditions are assumed for the velocity components, and furthermore no moving walls are considered in this thesis,

$$u_{i,\mathrm{f}} = u_{i,\text{wall}} = 0 . \tag{4.89}$$

The pressure at the walls is formulated either by linear extrapolation or using the procedure devised by Oliveira [20],

$$p_{\mathrm{f}} = \left(p_{\mathrm{f}}\right)_{\text{lin. extrap.}} + \frac{a_{\mathrm{P}}}{B_{\mathrm{f}}} \sum_{i=1}^{3} u_{i,\mathrm{P}} n_{i,\mathrm{f}} \,, \tag{4.90}$$

where a_{P} is the central coefficient of the algebraic momentum equation, $\left(p_{\mathrm{f}}\right)_{\text{lin. extrap.}}$ denotes the pressure at the wall obtained by linear extrapolation based on the first two cells along the wall-normal direction, and $\sum_{i=1}^{3} u_{i,\mathrm{P}} n_{i,\mathrm{f}} = u_{n,\mathrm{P}}$ is the wall-normal velocity component. As shown by Oliveira [20], for fluids with non-zero second normal stress difference coefficient, such as a Giesekus fluid, the formulation of the pressure at the walls based solely on linear extrapolation, a common practice in Newtonian CFD, may lead to unphysical oscillations of the velocity field near the wall. Since only the pressure gradient appears in the discretized momentum equations, eq. 4.90 is implemented as a correction to Δp,

$$\left[\Delta p\right]_f^{\mathrm{P}} = \left(\left[\Delta p\right]_f^{\mathrm{P}}\right)_{\text{lin. extrap.}} + \frac{a_{\mathrm{P}}}{B_{\mathrm{f}}} u_{n,\mathrm{P}} \,. \tag{4.91}$$

The polymeric extra stress components at the walls are currently estimated via linear extrapolation of the first two cells along the wall-normal direction. Previously, including in the early stages of this thesis [21], the extra stresses at the walls were evaluated assuming a viscometric flow parallel to the wall planes, an approach that may introduce local errors for unsteady flows. Habla et al. [22] compared two different formulations, linear extrapolation and a zero gradient assumption along the wall-normal direction, which amounts to setting the values at the wall face equal to those of the corresponding cell center. The two types of boundary condition are second- and first-order accurate, respectively, although their method was shown to be more robust using the zero gradient assumption. The numerical divergence associated with the linear extrapolation boundary condition in Ref. [22] was shown to occur due to the loss of

positivity of the conformation tensor $\mathbf{A}$. With the log-conformation representation, the positivity of the matrix-logarithm $\boldsymbol{\Theta}$ is ensured, hence the divergence phenomenon reported by Habla et al. [22] is no longer prevalent.

4.7 References

[1] P.J. Oliveira, F.T. Pinho, G.A. Pinto, Numerical simulation of non-linear elastic flows with a general collocated finite-volume method, J. Non-Newt. Fluid Mech. 79 (1998) 1–43. doi:10.1016/S0377-0257(98)00082-2.

[2] J.P. van Doormaal, G.D. Raithby, Enhancements of the simple method for predicting incompressible fluid flows, Numer. Heat Transf. 7 (1984) 147–163. doi:10.1080/01495728408961817.

[3] M.A. Alves, P.J. Oliveira, F.T. Pinho, A convergent and universally bounded interpolation scheme for the treatment of advection, Int. J. Numer. Meth. Fluids. 41 (2003) 47–75. doi:10.1002/fld.428.

[4] R. Fattal, R. Kupferman, Constitutive laws for the matrix-logarithm of the conformation tensor, J. Non-Newt. Fluid Mech. 123 (2004) 281–285. doi:10.1016/j.jnnfm.2004.08.008.

[5] A.M. Afonso, P.J. Oliveira, F.T. Pinho, M.A. Alves, The log-conformation tensor approach in the finite-volume method framework, J. Non-Newt. Fluid Mech. 157 (2009) 55–65. doi:10.1016/j.jnnfm.2008.09.007.

[6] M. Perić, A Finite Volume Method for the Prediction of Three-dimensional Fluid Flow in Complex Ducts, PhD Thesis, 1985.

[7] P.J. Oliveira, Computer Modelling of Multidimensional Multiphase Flow and Application to T-Juntions, PhD Thesis, 1992.

[8] M. Vinokur, An analysis of finite-difference and finite-volume formulations of conservation laws, J. Comput. Phys. 81 (1989) 1–52. doi:10.1016/0021-9991(89)90063-6.

[9] C.M. Rhie, W.L. Chow, Numerical study of the turbulent flow past an airfoil with trailing edge separation, AIAA J. 21 (1983) 1525–1532. doi:10.2514/3.8284.

[10] P.J. Oliveira, Method for time-dependent simulations of viscoelastic flows: vortex shedding behind cylinder, J. Non-Newt. Fluid Mech. 101 (2001) 113–137. doi:10.1016/S0377-0257(01)00146-X.

[11] P.K. Khosla, S.G. Rubin, A diagonally dominant second-order accurate implicit scheme, Comput. Fluids. 2 (1974) 207–209. doi:10.1016/0045-7930(74)90014-0.

[12] P.J. Oliveira, F.T. Pinho, Numerical procedure for the computation of fluid flow with arbitrary stress-strain relationships, Numer. Heat Transf. Part B Fundam. 35 (1999) 295–315. doi:10.1080/104077999275884.

[13] H.M. Matos, M.A. Alves, P.J. Oliveira, New Formulation for Stress Calculation: Application to Viscoelastic Flow in a T-Junction, Numer. Heat Transf. Part B Fundam. 56 (2010) 351–371. doi:10.1080/10407790903507972.

[14] F. Pimenta, M.A. Alves, Stabilization of an open-source finite-volume solver for viscoelastic fluid flows, J. Non-Newt. Fluid Mech. 239 (2017) 85–104. doi:10.1016/j.jnnfm.2016.12.002.

[15] F. Habla, M.W. Tan, J. Haßlberger, O. Hinrichsen, Numerical simulation of the viscoelastic flow in a three-dimensional lid-driven cavity using the log-conformation reformulation in OpenFOAM®, J. Non-Newt. Fluid Mech. 212 (2014) 47–62. doi:10.1016/j.jnnfm.2014.08.005.

[16] J.H. Fergizer, M. Perić, Computational Methods for Fluid Dynamics, 3rd ed., Springer-Verlag, Berlin, 2002.

[17] R.I. Issa, P.J. Oliveira, Numerical prediction of phase separation in two-phase flow through T-junctions, Comput. Fluids. 23 (1994) 347–372. doi:10.1016/0045-7930(94)90045-0.

[18] S.V. Patankar, D.B. Spalding, A calculation procedure for heat, mass and momentum transfer in three-dimensional parabolic flows, Int. J. Heat Mass Transf. 15 (1972) 1787–1806. doi:10.1016/0017-9310(72)90054-3.

[19] J.A. Meijerink, H.A. van der Vorst, An iterative solution method for linear systems of which the coefficient matrix is a symmetric M-matrix, Math. Comput. 31 (1977) 148–162. doi:10.1090/S0025-5718-1977-0438681-4.

[20] P.J. Oliveira, On the numerical implementation of nonlinear viscoelastic models in a finite-volume method, Numer. Heat Transf. Part B Fundam. 40 (2001) 283–

301. doi:10.1080/104077901317091695.

[21] F.A. Cruz, R.J. Poole, A.M. Afonso, F.T. Pinho, P.J. Oliveira, M.A. Alves, A new viscoelastic benchmark flow: Stationary bifurcation in a cross-slot, J. Non-Newt. Fluid Mech. 214 (2014) 57–68. doi:10.1016/j.jnnfm.2014.09.015.

[22] F. Habla, A. Woitalka, S. Neuner, O. Hinrichsen, Development of a methodology for numerical simulation of non-isothermal viscoelastic fluid flows with application to axisymmetric 4:1 contraction flows, Chem. Eng. J. 207–208 (2012) 772–784. doi:10.1016/j.cej.2012.07.060.

5 The Planar Cross-Slot as a Benchmark Problem

5.1 Summary

The cross-slot geometry is proposed as a candidate for a numerical benchmark flow problem for viscoelastic fluids. Extensive data of quantified accuracy is provided, obtained via Richardson extrapolation to the limit of infinite refinement using results for three different mesh resolutions, for the upper-convected Maxwell, Oldroyd-B and the linear form of the simplified Phan-Thien–Tanner constitutive models. Furthermore, two types of flow geometry are considered, having either sharp or rounded corners, the latter with a radius of curvature equal to 5% of the channel's width. For all models the inertialess steady symmetric flow is shown to undergo a bifurcation to a steady asymmetric configuration, followed by a second transition to time-dependent flow, which is in qualitative agreement with previous experimental observations for low Reynolds number flows. The critical Deborah number for both transitions is quantified and a set of standard parameters is proposed for benchmarking purposes.

5.2 Numerical Methods

The cross-slot flow is assumed to be inertialess $(\mathrm{Re} \to 0)$, two-dimensional, isothermal and incompressible. Under these conditions, the equations that need to be solved are the continuity equation,

$$\nabla \cdot \mathbf{u} = 0, \tag{5.1}$$

and the momentum equation,

$$-\nabla p + \nabla \cdot \boldsymbol{\tau} + \eta_s \nabla^2 \mathbf{u} = \mathbf{0}, \tag{5.2}$$

together with a suitable equation for the polymeric extra stress tensor $\boldsymbol{\tau}$. The Phan-Thien–Tanner constitutive model is chosen [2],[3] – in its simplified, linearized form often denoted as sPTT – of which the UCM and Oldroyd-B models are limiting cases,

$$\left(1+\frac{\lambda\varepsilon}{\eta_p}\mathrm{Tr}(\boldsymbol{\tau})\right)\boldsymbol{\tau}+\lambda\left[\frac{\partial\boldsymbol{\tau}}{\partial t}+\nabla\cdot\mathbf{u}\boldsymbol{\tau}\right]=\eta_p\left(\nabla\mathbf{u}+(\nabla\mathbf{u})^{\dagger}\right)+\lambda\left(\boldsymbol{\tau}\cdot\nabla\mathbf{u}+(\nabla\mathbf{u})^{\dagger}\cdot\boldsymbol{\tau}\right). \tag{5.3}$$

In these equations the constant model parameters are the relaxation time of the polymer λ, the zero-shear-rate polymer viscosity η_p, the solvent viscosity η_s, and the extensibility parameter ε. For both the Oldroyd-B and sPTT models, the viscosity ratio β, defined as the ratio of solvent viscosity to total zero-shear-rate viscosity ($\eta_0 = \eta_s + \eta_p$), was kept constant at $\beta = \eta_s / \eta_0 = 1/9$. Two typical values of the extensibility parameter ε are used to assess its effect on the onset of instabilities, ε=0.02 and ε=0.25 (note that extensibility is larger for lower values of ε). Although a number of shortcomings exist in both the UCM and Oldroyd-B models, most notably the unbounded nature of the steady-state extensional stresses above a critical strain rate $\dot{\varepsilon} = 1/(2\lambda)$ and their inability to predict shear-thinning behavior, they are probably the simplest differential models of an elastic fluid which can capture qualitatively many features of highly-elastic flows (e.g. [4],[5]). These particular deficiencies are absent in the sPTT model.

A fully implicit, second-order, finite-volume numerical method is applied to solve the governing equations. The log-conformation technique, introduced by Fattal and Kupferman [6], is used to solve eq. 5.3 after it is converted to the log-conformation representation as detailed in Ref. [7]. The original numerical method and subsequent developments have been described in great detail elsewhere [7],[8],[9]. Boundary conditions for the traction vector $\mathbf{T} = \boldsymbol{\tau} \cdot \hat{\mathbf{n}}$ at the walls, where $\hat{\mathbf{n}}$ is the wall-normal unit vector, which are needed to evaluate the stress divergence term in the momentum equation, are based on local analytical solutions. With the present constitutive models, these are equivalent to assuming a viscometric flow along the wall planes,

$$\begin{cases} T_s = \eta(\dot{\gamma})\dfrac{\partial u_s}{\partial n} \\ \eta(\dot{\gamma}) = \eta_s + \dfrac{\eta_p}{1+\varepsilon\dfrac{\lambda}{\eta_p}\tau_{ss}}, \\ T_{\text{other components}} = 0 \end{cases} \tag{5.4}$$

where T_s, u_s and τ_{ss} are the streamwise components of the traction vector, velocity field and extra stress tensor, respectively, which, given the viscometric flow assumption, are tangential to the wall plane, and ∂n denotes differentiation along the wall-normal direction. No finite disturbances are introduced in the numerical simulations to induce the onset of flow asymmetries. Instead, asymmetric solutions were found to develop naturally in the simulations, most likely from accumulation of round-off error at machine level precision – double precision in Fortran was used for all calculations.

In the computational mesh the inlet and outlet arms are ten channel widths (*D*) in length for all fluid models (cf. Figure 5.1.a). Fully-developed velocity (average value *U*) and stress profiles are applied at the inlets and Neumann boundary conditions are assumed at the outlets for all variables including the pressure gradient. In the central square a uniform mesh with cell spacing $\Delta x_{\min} = \Delta y_{\min}$ is used, while in each arm the minimum cell spacing is the same as this minimum value in cells bordering the central square but becomes progressively larger away from this region. An odd number of cells across each arm, and in the central square, enable the calculation of variables exactly along the centerline and at the stagnation point. Consistent mesh refinement, in which the minimum cell spacing is halved in each direction, was used to enable the computation of the Richardson extrapolation [10] for the asymmetry parameter *DQ*, Weissenberg number Wi_o at the cross-slot center and Couette correction *C*. The Richardson extrapolation is a sequence acceleration method. For a given step size *h*, a numerical procedure generates an approximation φ_h to the exact value $\varphi_{h\to 0}$,

$$\begin{aligned} &\varphi_{h\to 0} = \varphi_h + a_0 h^p + a_1 h^{p+1} + a_2 h^{p+2} + \ldots \\ &\Leftrightarrow \varphi_{h\to 0} = \varphi_h + a_0 h^p + \mathrm{O}\left(h^{p+1}\right) \end{aligned}, \tag{5.5}$$

where p is the order of convergence, the coefficients a_i are unknown and the error terms are progressively smaller, $a_i h^{p+i} > a_{i+1} h^{p+i+1}$. Alternatively, eq. 5.5 may be written for a step size $2h$,

$$\varphi_{h\to 0} = \varphi_{2h} + a_0 2^p h^p + \mathrm{O}\left(h^{p+1}\right). \tag{5.6}$$

Multiplying eq. 5.5 by 2^p and then subtracting the result from eq. 5.6, the largest error term, $a_0 h^p$, is eliminated,

$$\varphi_{h\to 0} = \frac{2^p \varphi_h - \varphi_{2h}}{2^p - 1} + \mathrm{O}\left(h^{p+1}\right). \tag{5.7}$$

Eq. 5.7 might instead be derived for the pair of approximations φ_{2h} and φ_{4h}, leading to an expression for the calculation of the order of convergence p,

$$\begin{aligned} &\frac{2^p \varphi_h - \varphi_{2h}}{2^p - 1} = \frac{2^p \varphi_{2h} - \varphi_{4h}}{2^p - 1} + \mathrm{O}\left(h^{p+1}\right) \\ &\Leftrightarrow p = \frac{\ln\left(\dfrac{\varphi_{2h} - \varphi_{4h}}{\varphi_h - \varphi_{2h}}\right)}{\ln 2} + \mathrm{O}\left(h^{p+1}\right) \end{aligned}. \tag{5.8}$$

Table 5.1 documents the minimum cell spacing, total number of cells, degrees of freedom and corner radius of curvature for the six meshes used. The availability of data for rounded corners should allow the benchmarking of spectral or other higher-order computational methods, as well as a direct evaluation of the significance of cross-slot

corners, and indeed wall boundary conditions, on the steady flow bifurcation. Furthermore, simulations were conducted at progressively higher Deborah number, De, and in smaller increments as the time-dependent flow regime was approached, such that the critical Deborah number for the second transition could also be estimated accurately.

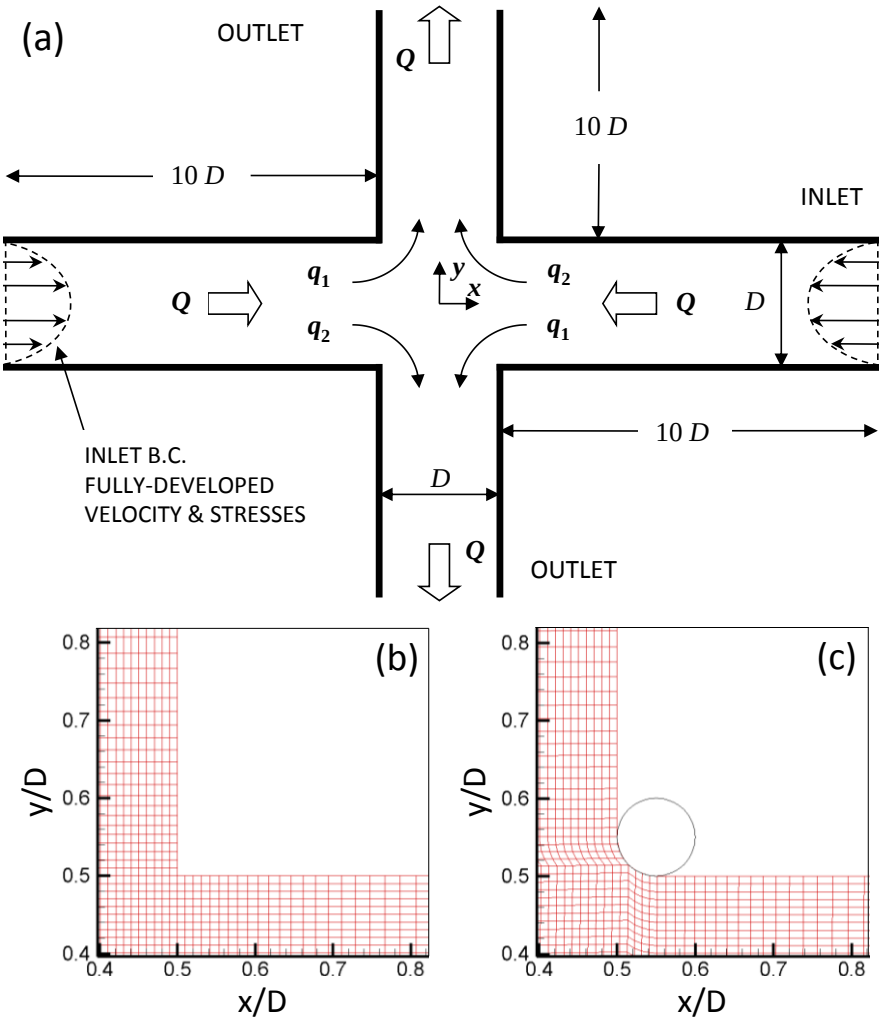

Figure 5.1 – **(a)** Schematics of the cross-slot geometry. **(b,c)** Close-up view of the meshes near the corners of the **(b)** sharp and **(c)** rounded geometries, for meshes M2-R0 and M2-R5, respectively (see Table 5.1 for details). The rounded corner has a radius of curvature of 5% of the channel width, as illustrated by the superimposed circle to the lower left.

Table 5.1 – Characteristics of the computational meshes. NC – number of cells; DOF – degrees of freedom; RCC – radius of curvature of corners; D – channel width.

Mesh	**NC**	**DOF**	**RCC**	$\frac{\Delta x_{min}}{D} = \frac{\Delta y_{min}}{D}$
M1-R0	12801	76806	0	0.02
M2-R0	50601	303606	0	0.01
M3-R0	201201	1207206	0	0.005
M1-R5	12801	76806	0.05 D	0.02
M2-R5	50601	303606	0.05 D	0.01
M3-R5	201201	1207206	0.05 D	0.005

5.3 Numerical Results and Discussion

Streamlines for some representative cases obtained using mesh M3-R0 are plotted in Figure 5.2.a-j, where R0 denotes the geometry with sharp corners (see Table 5.1), superimposed upon contours of the dimensionless first normal-stress difference. The experimentally observed asymmetry can be captured with the UCM, Oldroyd-B and sPTT models, at least if ε is sufficiently small (cf. Figure 1 of [11] for experimental asymmetry patterns), as reported for geometrically similar flow-focusing devices [12]. In Figure 5.2 the degree of elasticity increases from left to right along each row. For the UCM model, the highest De which results in a steady symmetric flow is represented in **(a)** at De=0.31, along with the lowest De flow for steady asymmetry **(b)** at De=0.315, followed by the highest De case prior to the onset of time-dependent flow **(c)** at De=0.33. These three reference states are also represented for the Oldroyd-B model with $\beta = 1/9$, at **(d)** De=0.36, **(e)** De=0.37 and **(f)** De=0.42 and the sPTT model with $\beta = 1/9$ and ε=0.02, at **(g)** De=0.50, **(h)** De=0.51 and **(i)** De=0.92. Between the second and third plot of each triplet, the flow becomes increasingly more asymmetric. As implied in Figure 5.2, the asymmetry may occur as either a clockwise or counter-clockwise rotation of the birefringence strand around the cross-slot center, depending on numerical noise that induces the onset of flow asymmetry. Represented is also the **(j)** sPTT model with $\beta = 1/9$ and ε=0.25 at De=1.20, which remains steady and symmetric in the range of De tested – up to De=1.20, with no hints of asymmetries or time-dependent flow. Figure 5.3 provides contour maps of normalized velocity magnitude, relative pressure and extra-stress tensor component τ_{xy}, at De=0.36 and De=0.42, for the Oldroyd-B fluid.

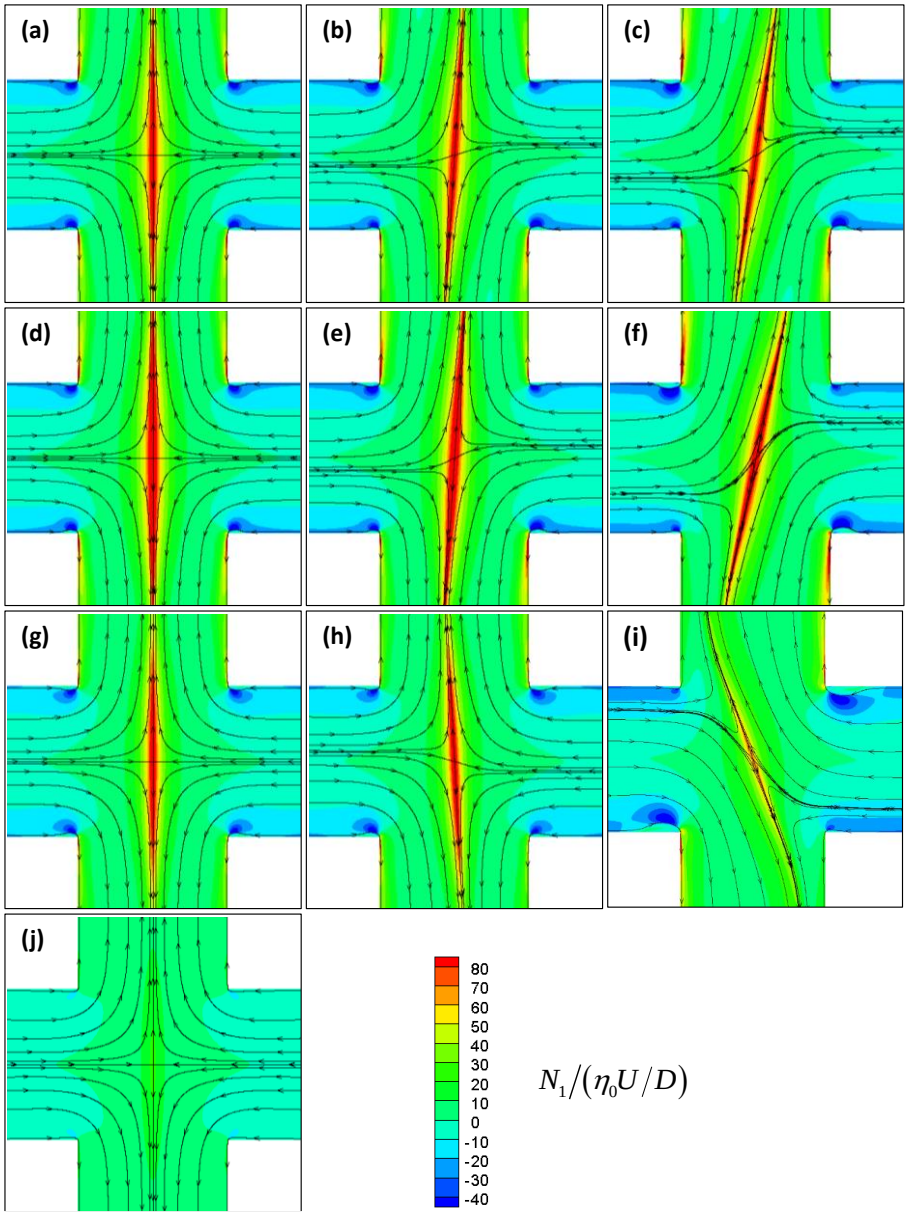

Figure 5.2 – Streamline patterns superimposed onto contour plots of the normalized polymeric first normal stress difference $\left(\tau_{yy}-\tau_{xx}\right)/\left(\eta_0 U/D\right)$. Represented are the highest De steady-state symmetric cases (left column), the lowest De steady-state asymmetric cases (middle column) and the highest De steady-state asymmetric cases prior to the transition to time-dependent flow (right column): UCM model at **(a)** De=0.31, **(b)** De=0.315 and **(c)** De=0.33; Oldroyd-B model with β=1/9 at **(d)** De=0.36, **(e)** De=0.37 and **(f)** De=0.42; sPTT model with β=1/9 and ε=0.02 at **(g)** De=0.50, **(h)** De=0.51 and **(i)** De=0.92. The first normal stress difference reaches its maximum value at the highest De prior to the onset of steady asymmetric flow, with subsequent post-transition stress relief. Results for the **(j)** sPTT model with β=1/9 and ε=0.25 at De=1.20, the highest simulated Deborah number, are also shown. Illustrations are provided for calculations on mesh M3-R0 (see Table 5.1 for details).

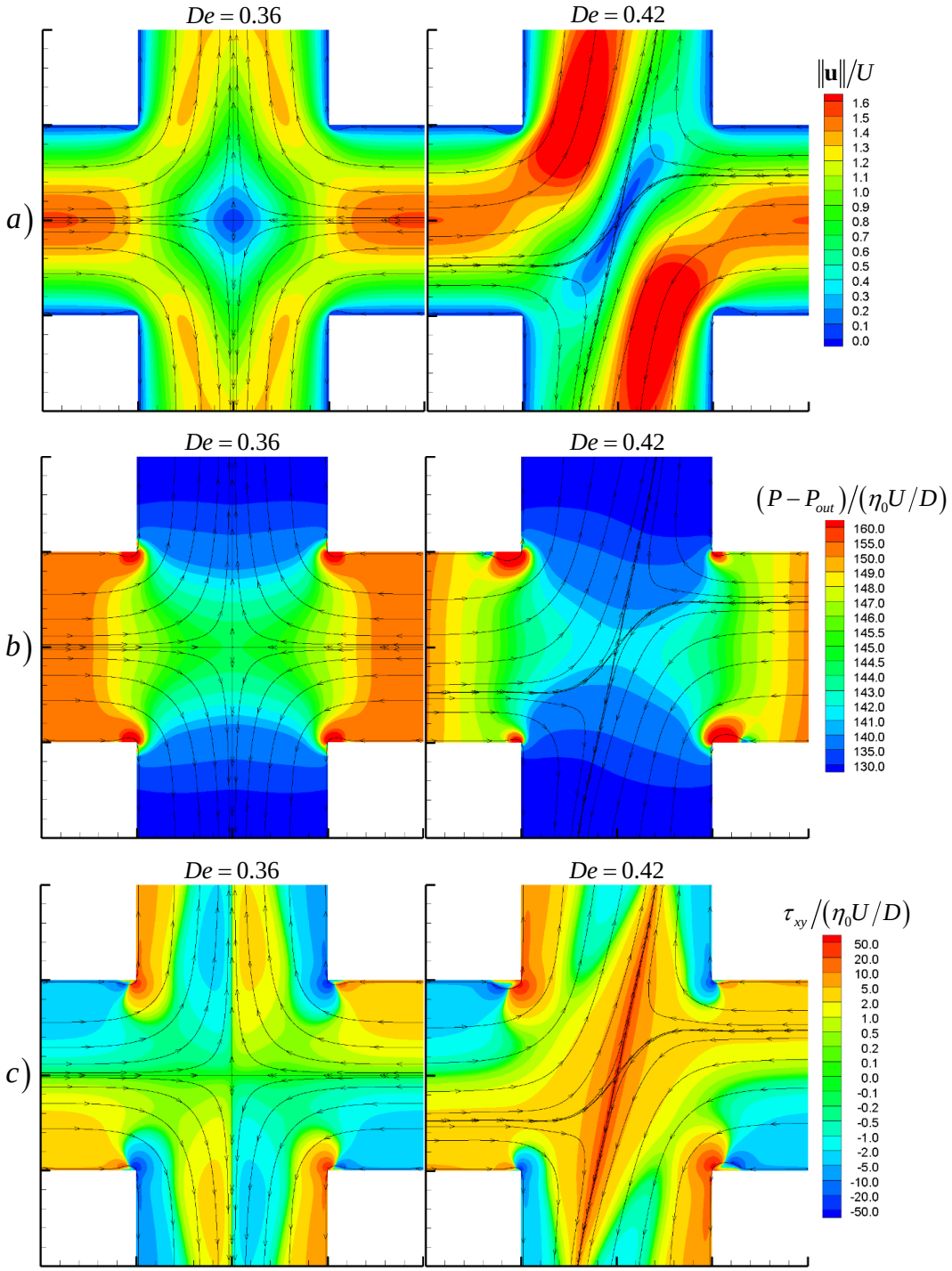

Figure 5.3 – Contour plots, with superimposed streamlines, of normalized: **a)** velocity magnitude ||**u**||; **b)** relative pressure P-P_{out}; **c)** extra-stress component τ_{xy}. Data is provided for the Oldroyd-B model with β=1/9 at De=0.36, the highest steady symmetric case, and De=0.42, the highest steady asymmetric case. Illustrations are provided for calculations on mesh M3-R0 (see Table 5.1 for details).

Based on the numerical results it is possible to determine a local Weissenberg number, $\mathrm{Wi}_o = \lambda \dot{\varepsilon}_o$, which is presented as the first benchmark variable, calculated using the strain rate $\dot{\varepsilon}_o$ at the central stagnation point $(x = y = 0)$,

$$\dot{\varepsilon}_o = \sqrt{\left(\left.\frac{\partial u}{\partial x}\right|_o\right)^2 + \left.\frac{\partial u}{\partial y}\right|_o \left.\frac{\partial v}{\partial x}\right|_o} \,. \tag{5.9}$$

In the vicinity of the stagnation point the two-dimensional velocity field can, in general, be regarded as linear, and may thus be approximated as $[u,v] = [ax+by, cx-ay]$, with $a = -(\partial u/\partial x)\big|_o = (\partial v/\partial y)\big|_o$, $b = (\partial u/\partial y)\big|_o$ and $c = (\partial v/\partial x)\big|_o$. In matricial form the velocity field is written as $\mathbf{u} = \mathbf{A}\,\mathbf{x}$. The positive eigenvalue of this linear transformation is the extensional strain rate depicted in eq. 5.9, while the corresponding eigenvectors represent the principal axes defined by the streamlines that cross the stagnation point, which are not normal to each other in a stationary asymmetric flow field. For symmetric flows the strain rate at the stagnation point simplifies to $\dot{\varepsilon}_o = -(\partial u/\partial x)\big|_o = (\partial v/\partial y)\big|_o$.

The mesh-wise convergence and Richardson extrapolation of Wi at the stagnation point is demonstrated in Figure 5.4, for the sPTT model with ε=0.02, for both the sharp and rounded corner configurations, while in Figure 5.5 extrapolated results for all models and geometries are presented. The average order of convergence of Wi_o is p=2.2, which follows closely the expected second-order accuracy of the numerical method. Notably for both the UCM and Oldroyd-B models the local Weissenberg number at the stagnation point exceeds the theoretical critical value of $1/2$. Therefore, at this point, the extensional stresses can become unbounded, since the residence time is infinitely large – for the sPTT model, for which the normal stresses are bounded, this concern is not an issue. Steady-state solutions can still be obtained because at the stagnation point, although singular, the stresses remain integrable (see the interesting discussion in Rallison and Hinch [13]). That the stresses become unbounded well below the critical De for the asymmetric transition, in conjunction with the fact that the asymmetry is also observed for the sPTT model, shows that the loss of symmetry is not directly related to this local stress singularity. Rocha et al. [14] examined the influence of finite extensibility upon the bifurcation

phenomenon and concluded that, even though higher extensibility promotes steady asymmetries at lower De, infinite extensibility such as in the UCM and Oldroyd-B models is not a necessary condition for the steady asymmetric transition.

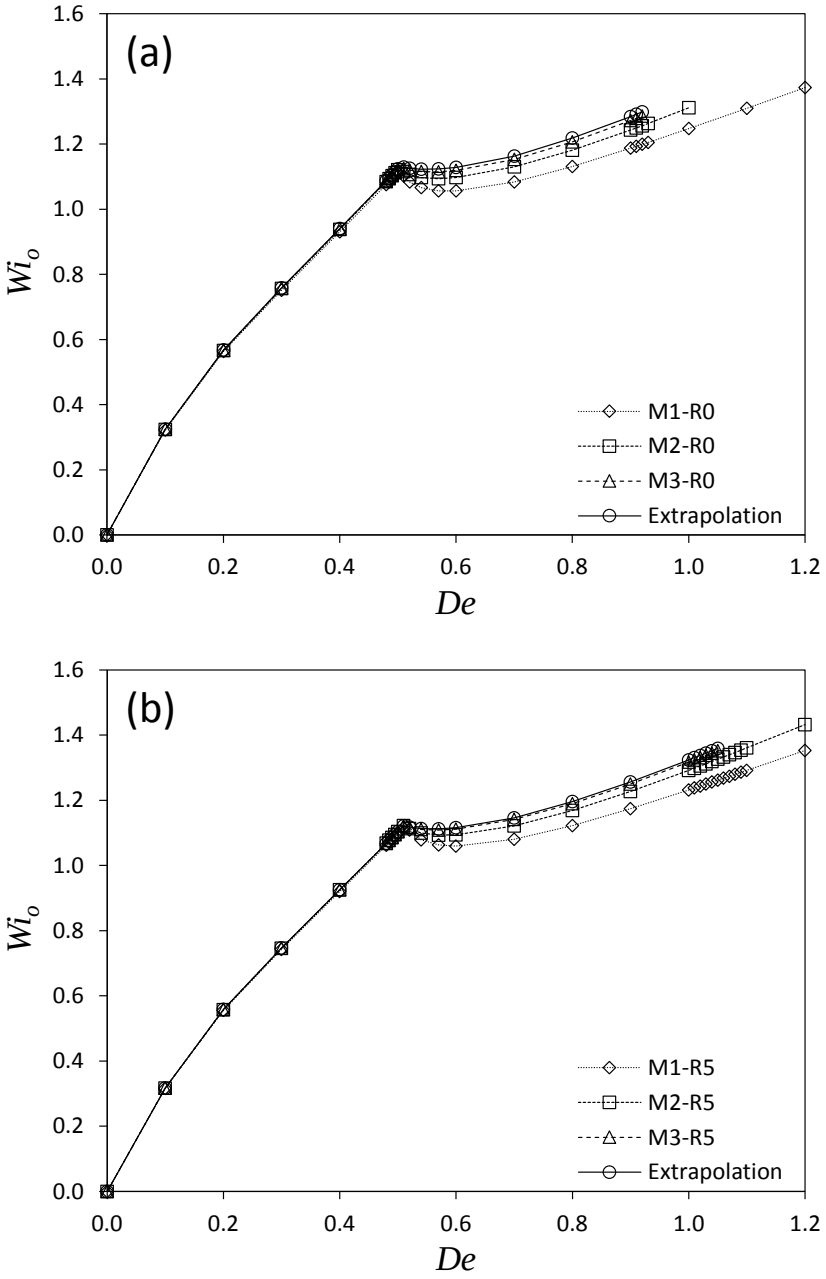

Figure 5.4 – Convergence with mesh refinement, for the sPTT model with β=1/9 and ε=0.02, of the Weissenberg number Wi_o as a function of De, calculated as the product of the relaxation time and strain rate at the stagnation point, $\mathrm{Wi}_o = \lambda\dot{\varepsilon}_o$. M1, M2 and M3 are progressively finer meshes whose results converge towards the Richardson extrapolation limit with approximately second-order accuracy. Convergence is demonstrated for both the sharp corner (**a**) and rounded corner (**b**) meshes (see Table 5.1 for details). The curves are simply a guide to the eye.

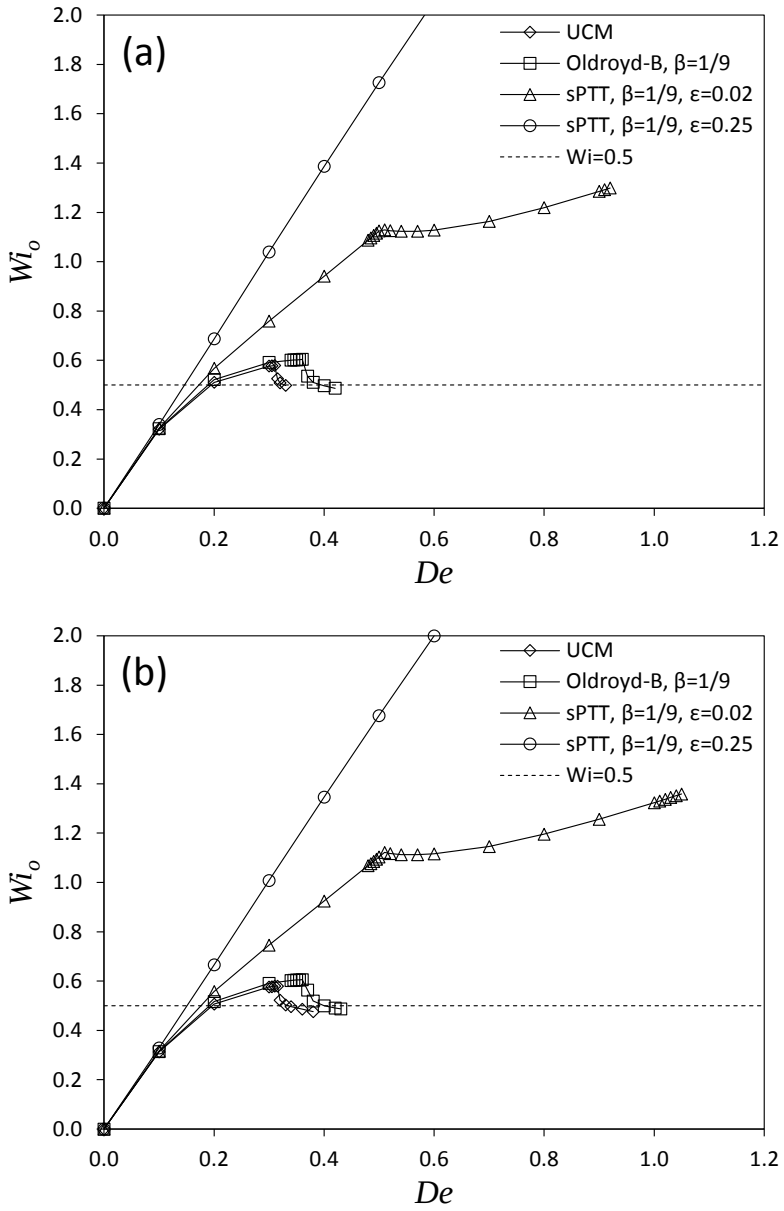

Figure 5.5 – Extrapolated values of the normalized strain rate at the stagnation point, Wi_o, as a function of De for all simulated models, $\mathrm{Wi}_o = \lambda\dot{\varepsilon}_o$. Both the sharp corner (**a**) and rounded corner (**b**) geometries are represented (see Table 5.1 for details). The curves are simply a guide to the eye.

In Figure 5.6 the variation of the polymeric component of stress τ_{yy} is plotted along the horizontal (upstream) centerline for mesh M3-R0 (see Table 5.1), demonstrating the asymptotically singular nature of the UCM and Oldroyd-B models near the stagnation point. Given the characteristics of the present flow, i.e. $\mathrm{Wi}_0 > 0.5$, the normal stress τ_{yy} is unbounded in the region along the outlet centerline for both the UCM and the Oldroyd-B models. Thus, there is a local loss of accuracy near the stagnation

point in the numerical solution, which predicts a very large, yet bounded normal stress. This loss of accuracy is limited to a narrow region near the stagnation point, and therefore is not of significant concern. Further mesh refinement would lead to an increase of τ_{yy} in the vicinity of the cross-slot center, with $\tau_{yy,o} \to \infty$ for cell spacing $\Delta x_{\min}, \Delta y_{\min} \to 0,$ for the UCM and Oldroyd-B models.

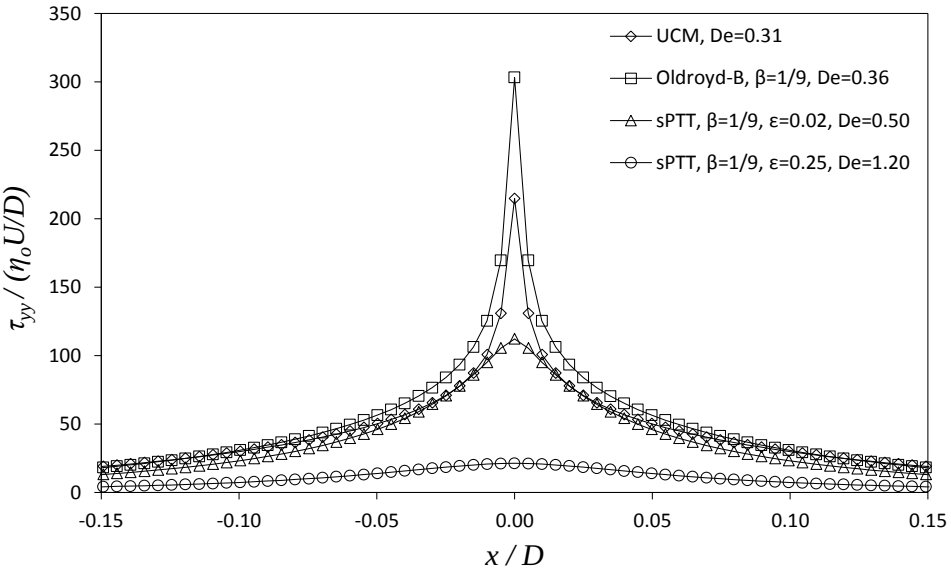

Figure 5.6 – Variation of the polymeric normalized normal stress τ_{yy} along the horizontal centerline (y=0) for the highest De immediately prior to the transition to steady asymmetric flow or at the highest De simulated $\left(\mathrm{De} = 1.20\right)$ if no transition was observed. Data is provided for mesh M3-R0 (see Table 5.1 for details). The curves are simply a guide to the eye.

Although the streamline plots of Figure 5.2 provide a qualitative visual indication of the degree of flow asymmetry, a suitable quantitative parameter is necessary as a reliable benchmark variable. An intuitive measure of the degree of asymmetry is the relative split of flow from an inlet arm heading towards each outlet arm, which in a symmetric flow would be 50%. This relative split may be calculated using the flow asymmetry parameter proposed by Poole et al. [15],

$$DQ = \frac{q_2 - q_1}{q_1 + q_2}. \tag{5.10}$$

The total flow rate per unit depth supplied to each inlet channel, $Q = UD = q_1 + q_2$, is split amongst two outlet streams. For instance, for the west inlet arm, as illustrated in Figure 5.1.a the inbound fluid is split between the north outflow arm, q_1, and the south outflow arm, q_2. For a symmetric flow $DQ = 0$ and for a fully asymmetric flow $|DQ| = 1$, i.e. flow from one inlet channel goes completely to a single outlet channel. The total flow rate Q leaving each outlet arm remains unaltered in both the symmetric and asymmetric states, since the latter has an anti-symmetric nature. The Richardson extrapolation of this asymmetry parameter as a function of De is provided in Figure 5.7, for both sharp and rounded corners.

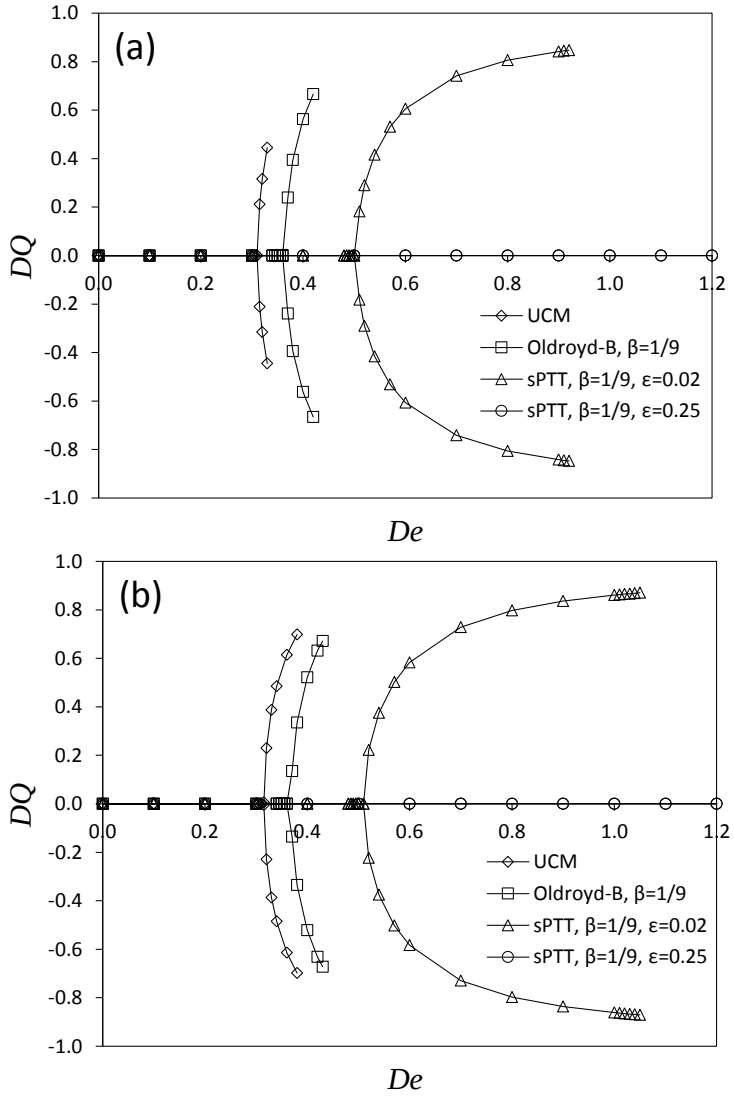

Figure 5.7 – Asymmetry parameter *DQ*, obtained by Richardson extrapolation, as a function of De, for both the sharp corner (**a**) and rounded corner (**b**) geometries (see Table 5.1 for details). Critical De values for both bifurcation and time-dependent flow are available in Tables 5.2 and 5.3, respectively. No bifurcation is detected for the sPTT model with ε=0.25 up to De=1.20. The curves are simply a guide to the eye.

The average order of convergence for DQ is 2.1, in agreement with the second-order accuracy of the numerical method. In order to accurately determine the critical conditions of the flow transition, the first three post-bifurcation points of the function $DQ = f(\mathrm{De})$ were fitted with the characteristic square-root formula for a supercritical pitchfork bifurcation [16], $DQ = A\sqrt{\mathrm{De} - \mathrm{De}_{CR}}$, where A is a scale factor and De_{CR} is the critical transition Deborah number. Fitted parameters and error are given in Table 5.2. As expected from previous work [14], rounded corners with a radius of curvature equivalent to 5% of the channel width have a negligible influence on the critical De for the onset of steady asymmetric flow.

Table 5.2 – Square root fit, $DQ = A\sqrt{\mathrm{De} - \mathrm{De}_{CR}}$, for De above the first critical value. The first three points after bifurcation (see Figure 5.7) were fitted and the minimization of the sum of the point-wise relative error was used as the objective function. S_r is the point-wise average relative error. *Rounded* refers to the meshes whose corners have been rounded to a radius of curvature equivalent to 5% of the channel's width.

Model	**Corner**	A	De_{CR}	S_r
UCM	Sharp	3.20	0.311	0.6%
Oldroyd-B, β=1/9	Sharp	2.94	0.363	1.3%
sPTT, β=1/9, ε=0.02	Sharp	2.16	0.503	0.9%
sPTT, β=1/9, ε=0.25	Sharp	No bifurcation up to De=1.20		
UCM	Rounded	3.20	0.315	2.4%
Oldroyd-B, β=1/9	Rounded	2.91	0.368	1.5%
sPTT, β=1/9, ε=0.02	Rounded	2.01	0.508	1.2%
sPTT, β=1/9, ε=0.25	Rounded	No bifurcation up to De=1.20		

The determination of the second critical Deborah number, which governs the transition to time-dependent flow, is based on an approximate method which relies on the identification of the highest steady De and lowest unsteady De flows for each fluid, using data obtained from the finer meshes available, M3-R0 and M3-R5 (see Table 5.1 for details). By increasing the Deborah number in small increments, $\Delta\mathrm{De} = 0.01$, the second critical De can thus be determined with an absolute error of ±0.005. As seen in Table 5.3, a radius of curvature of only 5% of the channel width is sufficient to significantly delay the onset of time-dependent flow for the UCM and sPTT (at ε=0.02) models to higher De

values. This indicates a distinct source for the two transitions in the cross-slot system: the steady bifurcation occurs as a result of the accumulation of normal stresses in the birefringence strand, while the unsteady flow transition seems to result from instabilities generated along curved streamlines near the corners, as predicted by the Larson micromechanical model [17], which are quantifiable using the Pakdel-McKinley criterion [18]. However, for the Oldroyd-B model, only a relatively small increase in the second critical De was observed for the rounded corner simulations (see Table 5.3).

Table 5.3 – Estimated values of De for the second critical transition, from steady asymmetric flow to time-dependent behavior, obtained from the more refined meshes, M3-R0 and M3-R5. *Rounded* refers to the M3-R5 meshes whose corners have been rounded to a radius of curvature equivalent to 5% of the channel width.

Model	**Corner**	**Highest steady De**	**Lowest unsteady De**	**Estimated critical De**
UCM	Sharp	0.330	0.340	0.335
Oldroyd-B, β=1/9	Sharp	0.420	0.430	0.425
sPTT, β=1/9, ε=0.02	Sharp	0.920	0.930	0.925
sPTT, β=1/9, ε=0.25	Sharp	Steady flow up to De=1.20		
UCM	Rounded	0.380	0.390	0.385
Oldroyd-B, β=1/9	Rounded	0.430	0.440	0.435
sPTT, β=1/9, ε=0.02	Rounded	1.050	1.060	1.055
sPTT, β=1/9, ε=0.25	Rounded	Steady flow up to De=1.20		

The additional pressure drop that arises due to the strong extensional flow within the cross-slot is quantified using the Couette correction, the third proposed benchmark variable, defined as,

$$C \equiv \frac{\Delta p - \Delta p_{fd}}{2\tau_w}, \tag{5.11}$$

where Δp is the overall pressure drop between two points located far away from the central region – one upstream and one downstream – under fully developed flow conditions, including the central slot region; τ_w is the total wall shear stress, (solvent plus

polymer contributions), in the fully-developed channel flows; and Δp_{fd} is the pressure-drop required to drive that same fully-developed flow in a straight channel, in the absence of the slot, i.e. simple-shear flow between the two points chosen to determine Δp, not accounting for the length of the central square. Thus one may think of the Couette correction as the number of additional channel widths by which the length of the planar channel would have to be extended to produce the same pressure drop as induced by the central slot. Note that $2\tau_w = -\left(\mathrm{d}\,p/\mathrm{d}\,x\right)_{fd} D = \left(\mathrm{d}\,p/\mathrm{d}\,y\right)_{fd} D$. The variation of this measure of the additional pressure drop with De is shown in Figure 5.8 for both geometries.

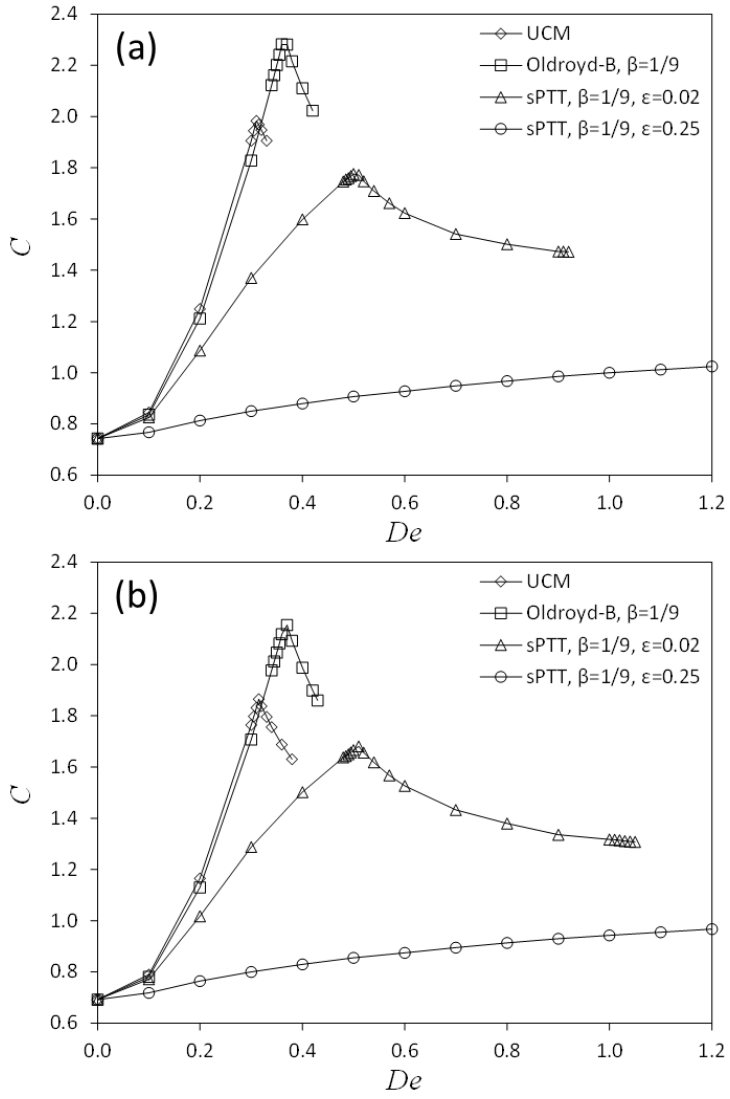

Figure 5.8 – Couette correction *C*, obtained by Richardson extrapolation, as a function of De. At the onset of steady asymmetric flow the Couette correction decreases, indicating a relative decrease in flow resistance. Data is provided for both the sharp corner (**a**) and rounded corner (**b**) geometries (see Table 5.1 for details). The curves are simply a guide to the eye.

The average order of convergence for *C* is 1.2, somewhat lower than the expected value for a second-order method, because additional errors are introduced in the calculation procedure for *C*, namely the extrapolation used to determine the fully developed pressure drop and the difference between two small quantities. Upon bifurcation the viscoelastic fluid dissipates less energy as it flows through the cross-slot, relative to both the pre-bifurcation flow and the hypothetical continuation of the symmetric flow field, in agreement with previous results for two-dimensional cross-slot flows [14],[15] and uniaxial extension in a three-dimensional device [19]. For the sPTT model with $\varepsilon = 0.25$, for which no bifurcation was observed up to $\mathrm{De} = 1.20$, the sudden decrease in the Couette correction is not observed. Also, as expected, rounding the cross-slot corners slightly decreases the pressure drop necessary to drive the flow.

In the spirit of this benchmark-proposing chapter, all previously discussed data is provided in detail in tabular form in section 5.5. For sharp corner geometries, Tables 5.4 and 5.5 include data on the three benchmark parameters – Wi_o, *DQ* and *C* – for the UCM and Oldroyd-B models, respectively, while Tables 5.6 and 5.7 provide the same data for the sPTT model, with $\varepsilon = 0.02$ and $\varepsilon = 0.25$, respectively. Similarly, data for rounded corners is given in Tables 5.8 and 5.9 for the UCM and Oldroyd-B models, respectively, while data for the sPTT model, with $\varepsilon = 0.02$ and $\varepsilon = 0.25$, can be found in Tables 5.10 and 5.11, respectively. Furthermore, as discussed, the critical values of De for the first and second flow transitions are listed in Tables 5.2 and 5.3, respectively.

5.4 References

[1] F.A. Cruz, R.J. Poole, A.M. Afonso, F.T. Pinho, P.J. Oliveira, M.A. Alves, A new viscoelastic benchmark flow: Stationary bifurcation in a cross-slot, J. Non-Newt. Fluid Mech. 214 (2014) 57–68. doi:10.1016/j.jnnfm.2014.09.015.

[2] N.P. Thien, R.I. Tanner, A new constitutive equation derived from network theory, J. Non-Newt. Fluid Mech. 2 (1977) 353–365. doi:10.1016/0377-0257(77)80021-9.

[3] N. Phan- Thien, A Nonlinear Network Viscoelastic Model, J. Rheol. 22 (1978) 259–283. doi:10.1122/1.549481.

[4] J. Zilz, R.J. Poole, M.A. Alves, D. Bartolo, B. Levaché, A. Lindner, Geometric scaling of a purely elastic flow instability in serpentine channels, J. Fluid Mech. 712 (2012) 203–218. doi:10.1017/jfm.2012.411.

[5] M.A. Alves, R.J. Poole, Divergent flow in contractions, J. Non-Newt. Fluid Mech. 144 (2007) 140–148. doi:10.1016/j.jnnfm.2007.04.003.

[6] R. Fattal, R. Kupferman, Constitutive laws for the matrix-logarithm of the conformation tensor, J. Non-Newt. Fluid Mech. 123 (2004) 281–285. doi:10.1016/j.jnnfm.2004.08.008.

[7] A.M. Afonso, P.J. Oliveira, F.T. Pinho, M.A. Alves, The log-conformation tensor approach in the finite-volume method framework, J. Non-Newt. Fluid Mech. 157 (2009) 55–65. doi:10.1016/j.jnnfm.2008.09.007.

[8] M.A. Alves, P.J. Oliveira, F.T. Pinho, A convergent and universally bounded interpolation scheme for the treatment of advection, Int. J. Numer. Meth. Fluids. 41 (2003) 47–75. doi:10.1002/fld.428.

[9] P.J. Oliveira, F.T. Pinho, G.A. Pinto, Numerical simulation of non-linear elastic flows with a general collocated finite-volume method, J. Non-Newt. Fluid Mech. 79 (1998) 1–43. doi:10.1016/S0377-0257(98)00082-2.

[10] J.H. Ferziger, M. Perić, Further discussion of numerical errors in CFD, Int. J. Numer. Meth. Fluids. 23 (1996) 1263–1274. doi:10.1002/(SICI)1097-0363(19961230)23:12<1263::AID-FLD478>3.0.CO;2-V.

[11] P.E. Arratia, C.C. Thomas, J. Diorio, J.P. Gollub, Elastic Instabilities of Polymer Solutions in Cross-Channel Flow, Phys. Rev. Lett. 96 (2006) 144502. doi:10.1103/PhysRevLett.96.144502.

[12] M.S.N. Oliveira, F.T. Pinho, R.J. Poole, P.J. Oliveira, M.A. Alves, Purely elastic flow asymmetries in flow-focusing devices, J. Non-Newt. Fluid Mech. 160 (2009) 31–39. doi:10.1016/j.jnnfm.2009.02.010.

[13] J.M. Rallison, E.J. Hinch, Do we understand the physics in the constitutive equation?, J. Non-Newt. Fluid Mech. 29 (1988) 37–55. doi:10.1016/0377-0257(88)85049-3.

[14] G.N. Rocha, R.J. Poole, M.A. Alves, P.J. Oliveira, On extensibility effects in the cross-slot flow bifurcation, J. Non-Newt. Fluid Mech. 156 (2009) 58–69.

doi:10.1016/j.jnnfm.2008.06.008.

[15] R.J. Poole, M.A. Alves, P.J. Oliveira, Purely Elastic Flow Asymmetries, Phys. Rev. Lett. 99 (2007) 164503. doi:10.1103/PhysRevLett.99.164503.

[16] H.J. Wilson, Open mathematical problems regarding non-Newtonian fluids, Nonlinearity. 25 (2012) R45–R51. doi:10.1088/0951-7715/25/3/R45.

[17] R.G. Larson, E.S.G. Shaqfeh, S.J. Muller, A purely elastic instability in Taylor–Couette flow, J. Fluid Mech. 218 (1990) 573–600. doi:10.1017/S0022112090001124.

[18] G.H. McKinley, P. Pakdel, A. Öztekin, Rheological and geometric scaling of purely elastic flow instabilities, J. Non-Newt. Fluid Mech. 67 (1996) 19–47. doi:10.1016/S0377-0257(96)01453-X.

[19] A.M. Afonso, M.A. Alves, F.T. Pinho, Purely elastic instabilities in three-dimensional cross-slot geometries, J. Non-Newt. Fluid Mech. 165 (2010) 743–751. doi:10.1016/j.jnnfm.2010.03.010.

5.5 Appendix: Benchmark Tables

Table 5.4 – UCM model data for a cross-slot with sharp corners. *Osc.* stands for oscillatory flow.

De	$\mathrm{Wi}_o = \lambda\dot{\varepsilon}_o$				$\lvert DQ \rvert$				C			
	M1	M2	M3	Extrap.	M1	M2	M3	Extrap.	M1	M2	M3	Extrap.
0.000	0.000	0.000	0.000	0.000	0.000	0.000	0.000	0.000	0.735	0.738	0.741	0.743
0.100	0.318	0.319	0.320	0.320	0.000	0.000	0.000	0.000	0.831	0.839	0.842	0.845
0.200	0.507	0.509	0.511	0.511	0.000	0.000	0.000	0.000	1.232	1.245	1.247	1.249
0.300	0.571	0.574	0.575	0.576	0.000	0.000	0.000	0.000	1.905	1.911	1.908	1.906
0.305	0.572	0.576	0.577	0.577	0.000	0.000	0.000	0.000	1.944	1.949	1.946	1.944
0.310	0.574	0.577	0.578	0.579	0.000	0.000	0.000	0.000	1.984	1.988	1.985	1.983
0.315	0.552	0.535	0.528	0.526	0.138	0.203	0.209	0.211	1.994	1.976	1.972	1.969
0.320	0.529	0.515	0.511	0.509	0.270	0.312	0.315	0.315	1.972	1.951	1.949	1.947
0.330	0.509	0.502	0.500	0.499	0.415	0.441	0.444	0.445	1.929	1.910	1.908	1.905
0.340	0.499	0.494	*Osc.*	-	0.508	0.527	*Osc.*	-	1.893	1.875	*Osc.*	-
0.360	0.485	0.481	*Osc.*	-	0.631	0.646	*Osc.*	-	1.831	1.816	*Osc.*	-
0.380	0.472	0.468	*Osc.*	-	0.712	0.724	*Osc.*	-	1.781	1.767	*Osc.*	-
0.400	0.460	0.456	*Osc.*	-	0.770	0.780	*Osc.*	-	1.741	1.729	*Osc.*	-
0.500	0.407	*Osc.*	*Osc.*	-	0.907	*Osc.*	*Osc.*	-	1.643	*Osc.*	*Osc.*	-
0.600	*Osc.*	*Osc.*	*Osc.*	-	*Osc.*	*Osc.*	*Osc.*	-	*Osc.*	*Osc.*	*Osc.*	-

Table 5.5 – Oldroyd-B model data, with $\beta = 1/9$, for a cross-slot with sharp corners. *Osc.* stands for oscillatory flow.

De	$\mathrm{Wi}_o = \lambda\dot{\varepsilon}_o$				$\lvert DQ \rvert$				C			
	M1	M2	M3	Extrap.	M1	M2	M3	Extrap.	M1	M2	M3	Extrap.
0.000	0.000	0.000	0.000	0.000	0.000	0.000	0.000	0.000	0.733	0.738	0.741	0.743
0.100	0.320	0.321	0.322	0.322	0.000	0.000	0.000	0.000	0.822	0.829	0.833	0.835
0.200	0.519	0.521	0.522	0.522	0.000	0.000	0.000	0.000	1.195	1.207	1.209	1.211
0.300	0.588	0.590	0.591	0.591	0.000	0.000	0.000	0.000	1.830	1.836	1.832	1.828
0.340	0.598	0.600	0.600	0.600	0.000	0.000	0.000	0.000	2.135	2.134	2.128	2.123
0.345	0.599	0.601	0.601	0.601	0.000	0.000	0.000	0.000	2.175	2.173	2.167	2.162
0.350	0.600	0.602	0.602	0.602	0.000	0.000	0.000	0.000	2.215	2.212	2.206	2.201
0.355	0.600	0.602	0.602	0.602	0.001	0.000	0.000	0.000	2.255	2.252	2.246	2.241
0.360	0.601	0.602	0.603	0.603	0.002	0.007	0.000	0.002	2.296	2.291	2.286	2.282
0.370	0.561	0.543	0.538	0.537	0.221	0.260	0.244	0.239	2.291	2.264	2.274	2.281
0.380	0.530	0.518	0.512	0.511	0.381	0.401	0.396	0.394	2.226	2.206	2.211	2.215
0.400	0.507	0.500	0.498	0.497	0.550	0.563	0.563	0.562	2.124	2.107	2.109	2.111
0.420	0.493	0.488	0.487	0.487	0.653	0.664	0.665	0.666	2.038	2.026	2.024	2.023
0.430	0.486	0.482	*Osc.*	-	0.692	0.702	*Osc.*	-	2.002	1.991	*Osc.*	-
0.500	0.445	*Osc.*	*Osc.*	-	0.850	*Osc.*	*Osc.*	-	1.823	*Osc.*	*Osc.*	-
0.600	0.390	*Osc.*	*Osc.*	-	0.934	*Osc.*	*Osc.*	-	1.720	*Osc.*	*Osc.*	-
0.700	*Osc.*	*Osc.*	*Osc.*	-	*Osc.*	*Osc.*	*Osc.*	-	*Osc.*	*Osc.*	*Osc.*	-

Table 5.6 – sPTT model data, with $\beta = 1/9$ and $\varepsilon = 0.02$, for a cross-slot with sharp corners. *Osc.* stands for oscillatory flow.

De	$\mathrm{Wi}_o = \lambda\dot{\varepsilon}_o$				$\lvert DQ \rvert$				C			
	M1	M2	M3	Extrap.	M1	M2	M3	Extrap.	M1	M2	M3	Extrap.
0.000	0.000	0.000	0.000	0.000	0.000	0.000	0.000	0.000	0.733	0.738	0.741	0.743
0.100	0.322	0.324	0.324	0.324	0.000	0.000	0.000	0.000	0.812	0.819	0.822	0.825
0.200	0.563	0.566	0.567	0.568	0.000	0.000	0.000	0.000	1.075	1.084	1.085	1.087
0.300	0.751	0.756	0.758	0.758	0.000	0.000	0.000	0.000	1.372	1.374	1.372	1.370
0.400	0.931	0.938	0.940	0.940	0.000	0.000	0.000	0.000	1.619	1.611	1.604	1.598
0.480	1.075	1.084	1.086	1.087	0.000	0.000	0.000	0.000	1.774	1.761	1.753	1.746
0.485	1.084	1.094	1.096	1.096	0.000	0.000	0.000	0.000	1.783	1.769	1.761	1.755
0.490	1.093	1.103	1.105	1.105	0.001	0.001	0.000	0.000	1.792	1.778	1.768	1.760
0.495	1.102	1.112	1.114	1.115	0.001	0.001	0.001	0.001	1.801	1.786	1.776	1.768
0.500	1.111	1.121	1.123	1.124	0.001	0.003	0.001	0.001	1.809	1.795	1.784	1.776
0.510	1.102	1.115	1.125	1.128	0.173	0.194	0.184	0.181	1.804	1.784	1.777	1.772
0.520	1.084	1.106	1.120	1.124	0.282	0.295	0.291	0.290	1.784	1.764	1.755	1.747
0.540	1.066	1.097	1.115	1.120	0.405	0.417	0.417	0.416	1.746	1.727	1.717	1.710
0.570	1.057	1.094	1.115	1.121	0.518	0.530	0.531	0.531	1.698	1.681	1.670	1.661
0.600	1.057	1.097	1.119	1.125	0.593	0.604	0.606	0.606	1.663	1.645	1.633	1.623
0.700	1.084	1.130	1.153	1.160	0.727	0.738	0.741	0.742	1.590	1.567	1.552	1.541
0.800	1.131	1.181	1.207	1.215	0.791	0.802	0.805	0.806	1.556	1.528	1.513	1.501
0.900	1.187	1.243	1.272	1.280	0.828	0.838	0.841	0.842	1.527	1.504	1.487	1.473
0.910	1.193	1.250	1.279	1.287	0.831	0.841	0.844	0.845	1.526	1.503	1.486	1.473
0.920	1.199	1.256	1.286	1.294	0.834	0.844	0.847	0.847	1.549	1.501	1.485	1.472
0.930	1.205	1.263	*Osc.*	-	0.836	0.846	*Osc.*	-	1.538	1.504	*Osc.*	-
1.000	1.248	1.311	*Osc.*	-	0.852	0.861	*Osc.*	-	1.523	1.495	*Osc.*	-
1.100	1.310	*Osc.*	*Osc.*	-	0.868	*Osc.*	*Osc.*	-	1.534	*Osc.*	*Osc.*	-
1.200	1.373	*Osc.*	*Osc.*	-	0.879	*Osc.*	*Osc.*	-	1.548	*Osc.*	*Osc.*	-

Table 5.7 – sPTT model data, with $\beta = 1/9$ and $\varepsilon = 0.25$, for a cross-slot with sharp corners.

De	$\mathrm{Wi}_o = \lambda\dot{\varepsilon}_o$				$\lvert DQ \rvert$				C			
	M1	M2	M3	Extrap.	M1	M2	M3	Extrap.	M1	M2	M3	Extrap.
0.000	0.000	0.000	0.000	0.000	0.000	0.000	0.000	0.000	0.733	0.738	0.741	0.743
0.100	0.337	0.338	0.339	0.339	0.000	0.000	0.000	0.000	0.757	0.762	0.765	0.767
0.200	0.681	0.685	0.686	0.687	0.000	0.000	0.000	0.000	0.803	0.808	0.811	0.813
0.300	1.030	1.036	1.038	1.038	0.000	0.000	0.000	0.000	0.840	0.846	0.848	0.850
0.400	1.375	1.383	1.385	1.386	0.000	0.000	0.000	0.000	0.877	0.878	0.879	0.880
0.500	1.712	1.722	1.725	1.726	0.000	0.000	0.000	0.000	0.900	0.905	0.906	0.906
0.600	2.040	2.052	2.056	2.057	0.000	0.000	0.000	0.000	0.927	0.930	0.929	0.927
0.700	2.361	2.375	2.379	2.380	0.000	0.000	0.000	0.000	0.948	0.949	0.949	0.949
0.800	2.674	2.690	2.695	2.696	0.000	0.000	0.000	0.000	0.966	0.968	0.968	0.967
0.900	2.982	3.000	3.005	3.006	0.000	0.000	0.000	0.000	0.985	0.986	0.985	0.985
1.000	3.284	3.304	3.309	3.311	0.000	0.000	0.000	0.000	1.001	1.000	1.000	0.999
1.100	3.581	3.603	3.610	3.611	0.000	0.000	0.000	0.000	1.014	1.014	1.013	1.012
1.200	3.874	3.899	3.906	3.908	0.000	0.000	0.000	0.000	1.027	1.026	1.025	1.024

Table 5.8 – UCM model data for a cross-slot with rounded corners with a radius of curvature equal to 5% of the channel width. *Osc.* stands for oscillatory flow.

De	$\mathrm{Wi}_o = \lambda\dot{\varepsilon}_o$				$\lvert DQ \rvert$				C			
	M1	M2	M3	Extrap.	M1	M2	M3	Extrap.	M1	M2	M3	Extrap.
0.000	0.000	0.000	0.000	0.000	0.000	0.000	0.000	0.000	0.694	0.694	0.693	0.692
0.100	0.312	0.313	0.313	0.313	0.000	0.000	0.000	0.000	0.789	0.791	0.791	0.790
0.200	0.504	0.506	0.506	0.506	0.000	0.000	0.000	0.000	1.173	1.173	1.169	1.166
0.300	0.571	0.575	0.576	0.576	0.000	0.000	0.000	0.000	1.818	1.797	1.779	1.765
0.305	0.573	0.576	0.577	0.578	0.000	0.000	0.000	0.000	1.855	1.833	1.814	1.798
0.310	0.574	0.578	0.579	0.579	0.000	0.000	0.000	0.000	1.893	1.869	1.848	1.832
0.315	0.576	0.579	0.580	0.580	0.000	0.002	0.004	0.005	1.931	1.906	1.883	1.865
0.320	0.554	0.537	0.526	0.523	0.132	0.199	0.221	0.228	1.943	1.892	1.861	1.837
0.330	0.517	0.508	0.504	0.503	0.351	0.377	0.384	0.387	1.897	1.847	1.818	1.796
0.340	0.504	0.499	0.497	0.496	0.463	0.480	0.484	0.485	1.857	1.807	1.779	1.756
0.360	0.489	0.486	0.486	0.486	0.603	0.612	0.614	0.614	1.790	1.740	1.711	1.688
0.380	0.476	0.474	0.476	0.476	0.691	0.698	0.698	0.698	1.737	1.686	1.655	1.630
0.390	0.471	0.469	*Osc.*	-	0.725	0.730	*Osc.*	-	1.713	1.663	*Osc.*	-
0.400	0.465	0.463	*Osc.*	-	0.754	0.758	*Osc.*	-	1.692	1.641	*Osc.*	-
0.500	0.414	*Osc.*	*Osc.*	-	0.898	*Osc.*	*Osc.*	-	1.572	*Osc.*	*Osc.*	-
0.600	0.378	*Osc.*	*Osc.*	-	0.947	*Osc.*	*Osc.*	-	1.540	*Osc.*	*Osc.*	-
0.700	*Osc.*	*Osc.*	*Osc.*	-	*Osc.*	*Osc.*	*Osc.*	-	*Osc.*	*Osc.*	*Osc.*	-

Table 5.9 – Oldroyd-B model data, with $\beta = 1/9$, for a cross-slot with rounded corners with a radius of curvature equal to 5% of the channel width. *Osc.* stands for oscillatory flow.

De	$\mathrm{Wi}_o = \lambda\dot{\varepsilon}_o$				$\lvert DQ \rvert$				C			
	M1	M2	M3	Extrap.	M1	M2	M3	Extrap.	M1	M2	M3	Extrap.
0.000	0.000	0.000	0.000	0.000	0.000	0.000	0.000	0.000	0.694	0.695	0.693	0.692
0.100	0.314	0.314	0.315	0.315	0.000	0.000	0.000	0.000	0.779	0.781	0.781	0.781
0.200	0.515	0.517	0.517	0.517	0.000	0.000	0.000	0.000	1.134	1.135	1.132	1.130
0.300	0.589	0.591	0.591	0.591	0.000	0.000	0.000	0.000	1.738	1.727	1.716	1.708
0.340	0.600	0.602	0.602	0.602	0.000	0.000	0.000	0.000	2.029	2.008	1.991	1.977
0.345	0.601	0.603	0.603	0.603	0.000	0.000	0.000	0.000	2.066	2.044	2.026	2.012
0.350	0.602	0.604	0.604	0.604	0.000	0.000	0.000	0.000	2.104	2.081	2.062	2.047
0.355	0.603	0.605	0.605	0.605	0.000	0.000	0.000	0.000	2.143	2.118	2.098	2.082
0.360	0.603	0.605	0.606	0.606	0.000	0.000	0.000	0.000	2.182	2.155	2.134	2.118
0.370	0.590	0.578	0.566	0.563	0.063	0.090	0.123	0.133	2.244	2.209	2.178	2.154
0.380	0.549	0.531	0.521	0.519	0.289	0.321	0.331	0.335	2.199	2.147	2.117	2.093
0.400	0.514	0.506	0.501	0.500	0.500	0.514	0.519	0.521	2.089	2.042	2.011	1.987
0.420	0.499	0.493	0.492	0.491	0.619	0.627	0.630	0.631	1.998	1.952	1.922	1.899
0.430	0.492	0.488	0.487	0.487	0.662	0.669	0.671	0.672	1.958	1.913	1.883	1.860
0.440	0.486	0.483	*Osc.*	-	0.699	0.705	*Osc.*	-	1.922	1.877	*Osc.*	-
0.500	0.452	0.449	*Osc.*	-	0.835	0.838	*Osc.*	-	1.761	1.711	*Osc.*	-
0.600	0.401	0.392	*Osc.*	-	0.925	0.927	*Osc.*	-	1.625	1.564	*Osc.*	-
0.700	*Osc.*	*Osc.*	*Osc.*	-	*Osc.*	*Osc.*	*Osc.*	-	*Osc.*	*Osc.*	*Osc.*	-

Table 5.10 – sPTT model data, with $\beta = 1/9$ and $\varepsilon = 0.02$, for a cross-slot with rounded corners with a radius of curvature equal to 5% of the channel width. *Osc.* stands for oscillatory flow.

De	$\mathrm{Wi}_o = \lambda\dot{\varepsilon}_o$				$\lvert DQ \rvert$				C			
	M1	M2	M3	Extrap.	M1	M2	M3	Extrap.	M1	M2	M3	Extrap.
0.000	0.000	0.000	0.000	0.000	0.000	0.000	0.000	0.000	0.694	0.695	0.693	0.693
0.100	0.316	0.316	0.317	0.317	0.000	0.000	0.000	0.000	0.770	0.772	0.772	0.772
0.200	0.556	0.558	0.558	0.558	0.000	0.000	0.000	0.000	1.022	1.023	1.020	1.017
0.300	0.743	0.746	0.746	0.746	0.000	0.000	0.000	0.000	1.308	1.302	1.294	1.287
0.400	0.920	0.925	0.925	0.925	0.000	0.000	0.000	0.000	1.545	1.528	1.513	1.502
0.480	1.062	1.068	1.068	1.068	0.000	0.000	0.000	0.000	1.698	1.671	1.652	1.637
0.485	1.071	1.077	1.077	1.077	0.000	0.000	0.000	0.000	1.707	1.679	1.658	1.642
0.490	1.080	1.086	1.086	1.086	0.000	0.000	0.000	0.000	1.715	1.687	1.666	1.650
0.495	1.089	1.095	1.095	1.095	0.000	0.000	0.000	0.000	1.723	1.694	1.673	1.657
0.500	1.098	1.104	1.104	1.104	0.000	0.000	0.000	0.000	1.732	1.702	1.682	1.667
0.510	1.115	1.122	1.122	1.121	0.000	0.000	0.000	0.000	1.748	1.717	1.697	1.681
0.520	1.109	1.113	1.116	1.117	0.157	0.202	0.217	0.221	1.747	1.703	1.677	1.656
0.540	1.079	1.099	1.110	1.113	0.342	0.364	0.372	0.374	1.707	1.664	1.638	1.618
0.570	1.063	1.093	1.108	1.113	0.478	0.495	0.500	0.501	1.658	1.614	1.588	1.568
0.600	1.059	1.094	1.111	1.116	0.563	0.578	0.582	0.583	1.620	1.574	1.547	1.527
0.700	1.080	1.121	1.141	1.147	0.713	0.724	0.728	0.729	1.530	1.485	1.456	1.433
0.800	1.122	1.169	1.190	1.196	0.783	0.793	0.796	0.797	1.484	1.436	1.405	1.380
0.900	1.174	1.227	1.250	1.257	0.822	0.832	0.835	0.836	1.462	1.408	1.368	1.336
1.000	1.232	1.292	1.317	1.324	0.847	0.857	0.860	0.861	1.453	1.388	1.348	1.317
1.010	1.238	1.298	1.324	1.331	0.849	0.859	0.862	0.863	1.452	1.386	1.347	1.316
1.020	1.244	1.305	1.331	1.338	0.851	0.860	0.864	0.865	1.451	1.385	1.345	1.314
1.030	1.250	1.312	1.338	1.345	0.853	0.862	0.866	0.867	1.434	1.384	1.343	1.312
1.040	1.256	1.319	1.345	1.352	0.855	0.864	0.867	0.868	1.433	1.383	1.342	1.310
1.050	1.262	1.326	1.352	1.359	0.857	0.866	0.869	0.870	1.432	1.382	1.341	1.308
1.060	1.268	1.333	*Osc.*	-	0.858	0.867	*Osc.*	-	1.445	1.382	*Osc.*	-
1.070	1.274	1.340	*Osc.*	-	0.860	0.869	*Osc.*	-	1.445	1.382	*Osc.*	-
1.080	1.280	1.347	*Osc.*	-	0.861	0.871	*Osc.*	-	1.444	1.381	*Osc.*	-
1.090	1.286	1.354	*Osc.*	-	0.863	0.872	*Osc.*	-	1.433	1.380	*Osc.*	-
1.100	1.292	1.361	*Osc.*	-	0.864	0.873	*Osc.*	-	1.435	1.379	*Osc.*	-
1.200	1.353	1.432	*Osc.*	-	0.877	0.886	*Osc.*	-	1.440	1.377	*Osc.*	-

Table 5.11 – sPTT model data, with $\beta = 1/9$ and $\varepsilon = 0.25$, for a cross-slot with rounded corners with a radius of curvature equal to 5% of the channel width.

De	$\mathrm{Wi}_o = \lambda\dot{\varepsilon}_o$				$\lvert DQ \rvert$				C			
	M1	M2	M3	Extrap.	M1	M2	M3	Extrap.	M1	M2	M3	Extrap.
0.000	0.000	0.000	0.000	0.000	0.000	0.000	0.000	0.000	0.694	0.695	0.693	0.693
0.100	0.328	0.329	0.329	0.329	0.000	0.000	0.000	0.000	0.718	0.720	0.719	0.719
0.200	0.664	0.666	0.666	0.666	0.000	0.000	0.000	0.000	0.765	0.766	0.765	0.764
0.300	1.005	1.008	1.008	1.008	0.000	0.000	0.000	0.000	0.804	0.803	0.802	0.800
0.400	1.343	1.346	1.346	1.346	0.000	0.000	0.000	0.000	0.834	0.833	0.831	0.829
0.500	1.673	1.677	1.677	1.677	0.000	0.000	0.000	0.000	0.863	0.859	0.857	0.855
0.600	1.995	2.000	2.000	2.000	0.000	0.000	0.000	0.000	0.886	0.883	0.878	0.874
0.700	2.309	2.316	2.315	2.315	0.000	0.000	0.000	0.000	0.905	0.901	0.898	0.895
0.800	2.616	2.624	2.623	2.623	0.000	0.000	0.000	0.000	0.923	0.920	0.916	0.913
0.900	2.917	2.926	2.925	2.925	0.000	0.000	0.000	0.000	0.941	0.936	0.932	0.930
1.000	3.213	3.223	3.223	3.222	0.000	0.000	0.000	0.000	0.956	0.950	0.946	0.943
1.100	3.504	3.516	3.515	3.515	0.000	0.000	0.000	0.000	0.969	0.962	0.959	0.956
1.200	3.791	3.805	3.804	3.804	0.000	0.000	0.000	0.000	0.981	0.974	0.970	0.967

6 Stationary Instabilities in Cross-Slots with Different Aspect Ratio

6.1 Summary

Creeping flow simulations of upper-convected Maxwell and simplified linearized Phan-Thien–Tanner fluids are performed in order to study the purely-elastic steady bifurcation and transition to time-dependent flow in three-dimensional planar cross-slots. By analyzing the flow in geometries with aspect ratios ranging from the near Hele-Shaw flow like limit, up to the very deep, two-dimensional limit, the mechanism of the cross-slot bifurcation is characterized with significant detail. The bifurcation mechanism is shown to be similar to a buckling instability, by which fluid is redirected via paths of least resistance, resulting in the emergence of peripheral stagnation points, above and below the central stagnation point. The intake of matter at the center via the inlet axis is thus reduced, being compensated by fluid flowing through low resistance corridors along the central vertical axis, above and below the central point. Furthermore, a modified Pakdel-McKinley criterion is propose and locally computed, thereby producing a scalar stability field and suggesting emergent peripheral stagnation points also indirectly contribute to the onset of time-dependent flow.

6.2 Numerical Methods

Inertialess (Re→0), isothermal and incompressible three-dimensional (3D) flow is assumed. The governing equations are the continuity equation,

$$\nabla \cdot \mathbf{u} = 0, \tag{6.1}$$

the momentum equation,

$$-\nabla p + \nabla \cdot \boldsymbol{\tau} + \eta_s \nabla^2 \mathbf{u} = \mathbf{0}, \tag{6.2}$$

and a constitutive equation needed for the computation of the polymeric extra stress-tensor $\boldsymbol{\tau}$,

$$\left(1+\frac{\lambda\varepsilon}{\eta_p}\mathrm{Tr}\left(\boldsymbol{\tau}\right)\right)\boldsymbol{\tau}+\lambda\left[\frac{\partial\boldsymbol{\tau}}{\partial t}+\nabla\cdot\mathbf{u}\boldsymbol{\tau}\right]=\eta_p\left(\nabla\mathbf{u}+\nabla\mathbf{u}^{\dagger}\right)+\lambda\left(\boldsymbol{\tau}\cdot\nabla\mathbf{u}+\nabla\mathbf{u}^{\dagger}\cdot\boldsymbol{\tau}\right), \quad (6.3)$$

representative of the simplified Phan-Thien–Tanner model with linear stress function, henceforth denoted sPTT [2],[3], where λ is the zero-shear-rate polymeric relaxation time, η_p is the zero-shear-rate polymer viscosity, η_s is the solvent viscosity and ε is the extensibility parameter. Should the extensibility parameter ε be equal to zero, i.e. polymer chains have unlimited extensibility, the constitutive model simplifies to an Oldroyd-B fluid [4], which is further simplified to the UCM model for solvent viscosity η_s equal to zero. Only two constitutive models are investigated in this chapter, the UCM fluid and the sPTT fluid with $\varepsilon=0.02$ and $\beta=1/9$, where β is the solvent viscosity ratio, defined as $\beta=\eta_s/\left(\eta_s+\eta_p\right)=\eta_s/\eta_0$, with η_0 being the zero-shear-rate solution viscosity. The shear-thinning behavior of the sPTT formulation is noted here, expressed by $\lambda_{eff}=\lambda/g\left(\boldsymbol{\tau}\right)$ and $\eta_{p,eff}=\eta_p/g\left(\boldsymbol{\tau}\right)$, with the subscript *eff* denoting effective values and the function $g\left(\boldsymbol{\tau}\right)$ given by

$$g\left(\boldsymbol{\tau}\right)=1+\frac{\lambda\varepsilon}{\eta_p}\mathrm{Tr}\left(\boldsymbol{\tau}\right). \quad (6.4)$$

An implicit, second-order, finite volume numerical method is used to solve the governing equations, as extensively described elsewhere [5],[6],[7], and to improve numerical stability the log-conformation technique [8] is applied. For each constitutive model-geometry pair, simulations were performed at progressively higher Deborah numbers, $\mathrm{De}=\lambda U/D$, where U is the average velocity in the four arms and D is the channel width, until unsteady flow conditions are attained. Viscometric flow is assumed at the wall planes, fully-developed velocity and stress profiles are given at the inlets and Neumann boundary conditions are assumed at the outlets for all variables, except pressure which is linearly extrapolated from the two upstream cells. No finite disturbances are introduced in the simulations to induce the onset of flow asymmetries or other

instabilities. Instead, these solutions develop naturally from the accumulation of round-off error at machine level precision – double precision Fortran is used for all calculations. A total of eleven meshes are used, all with the basic geometry shown in Figure 6.1.a. Each mesh has a different aspect ratio *AR*, defined as the ratio of height-to-width, $AR = H/D$, and is composed of five blocks, one for each arm and a fifth block for the central slot, each with 51^3 control volumes, totaling 663255 computational cells. All meshes have the same total number of cells. To facilitate the representation of the widest possible range of aspect ratios, a normalized aspect ratio *ARn* is defined,

$$ARn = \frac{AR}{AR+1} = \frac{H}{H+D}. \tag{6.5}$$

The limits $ARn \to 0$ and $ARn \to 1$ correspond to the shallow and deep cross-slots, respectively. The former is the Hele-Shaw flow limit, while the latter is nominally equivalent to a two-dimensional (2D) geometry. Truly 2D simulations are denoted by $ARn = 1.0$ whereas 3D simulations in deep channels refer to the corresponding asymptotic limit, $ARn \to 1$. The exact range of aspect ratios covered is given in Table 6.1, alongside other mesh characteristics. For the shallowest geometries, $ARn = 0.01$ and $ARn = 0.1$, acceptable resolution of velocity gradients near the cross-slot corners requires localized mesh refinement (cf. Figure 6.1.c).

Table 6.1 – Characteristics of the computational meshes. All meshes are composed of five blocks, each with 51^3 cells, for a total of 663255 cells. Cells along the z-direction are uniformly spaced, see Figure 6.1 for cell spacing along the x- and y-directions.

ARn	*AR*	$\Delta z/D$
0.01	0.010	0.00020
0.1	0.11	0.0022
0.2	0.25	0.0049
0.3	0.43	0.0084
0.4	0.67	0.013
0.5	1.0	0.020
0.6	1.5	0.029
0.7	2.3	0.046
0.8	4.0	0.078
0.9	9.0	0.18
1.0	$\to \infty$	2D

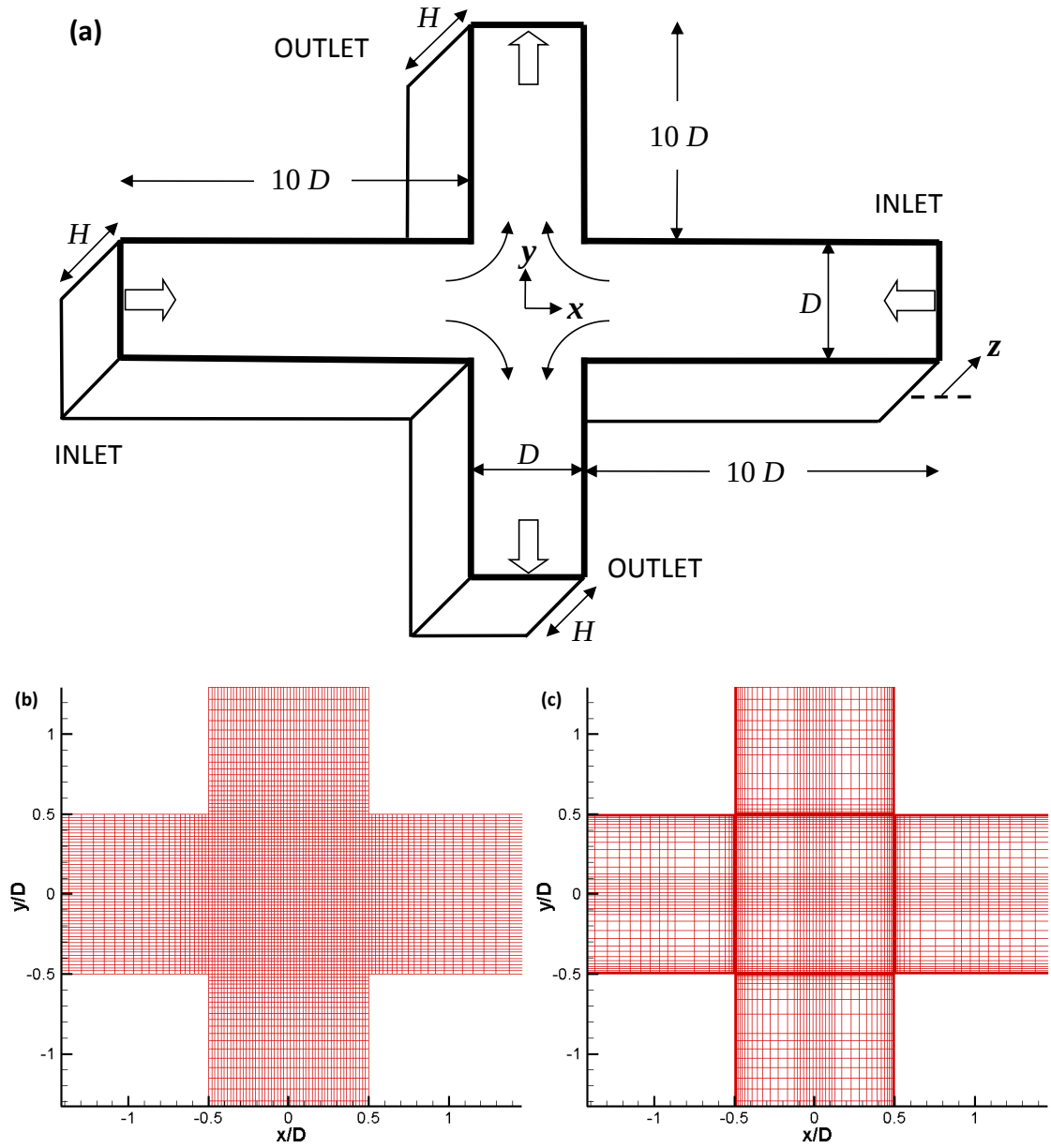

Figure 6.1 – **(a)** Schematic of the three-dimensional planar cross-slot geometry. **(b,c)** Zoomed-in, bird's eye view of the computational meshes. Mesh **(b)** is used for aspect ratios ranging from $ARn = 0.2$ to $ARn = 1.0$. Mesh **(c)** is used for $ARn = 0.01$ and $ARn = 0.1$; note the local refinement near the corners and lateral walls, obtained at the expense of a local coarsening away from the walls; care was taken to preserve cell density along the centerlines of the x- and y-axes. Cells in the four arms are progressively larger in the streamwise direction towards the inlets and outlets.

To facilitate the assessment of several important flow parameters, the eigenvalues and eigenvectors of the tensor $\left(\nabla\mathbf{u}^{\dagger}\right)_{ij} = \partial u_i/\partial x_j$ are computed at the stagnation point located at the geometric center of the cross-slot. Assuming a linear velocity field in the vicinity of the central stagnation point, $\mathbf{u} = \nabla\mathbf{u}^{\dagger}\cdot\mathbf{x}$, the unit eigenvectors $\hat{\mathbf{v}}_n$ and eigenvalues ξ_n of $\nabla\mathbf{u}^{\dagger}$ represent the directions of the stagnation streamlines and the corresponding velocity gradients in streamline coordinates $\mathrm{d}\|\mathbf{u}\|/\mathrm{d}s_n$. For incompressible creeping Newtonian flow, the three eigenvectors are the Cartesian unit vectors $\left(\hat{\mathbf{i}},\hat{\mathbf{j}},\hat{\mathbf{k}}\right)$ and the corresponding strain-rates are $\left(-\dot{\varepsilon}_{stretch},\dot{\varepsilon}_{stretch},0\right)$, for inlets along the x-direction and outlets along the y-direction, as sketched in Figure 6.1. Furthermore, the continuity equation dictates that the sum of the three eigenvalues is equal to zero, regardless of flow configuration, and thus it is possible that up to two of the strain-rates are either positive or negative, implying the potential for stretching in more than one direction. The second eigenvalue ξ_2, along outlet direction $\hat{\mathbf{j}}$ for Newtonian flow or symmetric viscoelastic flow, represents the magnitude of the extension-rate $\dot{\varepsilon}_{stretch}$. In the following, $\hat{\mathbf{k}}$ along the z-axis is referred to as the vertical direction, with the 3D cross-slot orientated in the XY center plane as shown in Figure 6.1. The coordinate system defined by the eigenvectors $\left(\hat{\mathbf{v}}_1,\hat{\mathbf{v}}_2,\hat{\mathbf{v}}_3\right)$ of $\nabla\mathbf{u}^{\dagger}$ can be distinct from the standard Cartesian unit vectors $\left(\hat{\mathbf{i}},\hat{\mathbf{j}},\hat{\mathbf{k}}\right)$, specifically if the flow field is asymmetric at the central stagnation point. It should be noted, however, that at the central stagnation point, $\hat{\mathbf{k}} \equiv \hat{\mathbf{v}}_3$ across the present data range.

6.3 Numerical Results and Discussion

6.3.1 Qualitative analysis of results and stability maps

Figures 6.2 and 6.3 illustrate typical results for both UCM and sPTT models, respectively, presented for the same normalized aspect ratio $\left(ARn = 0.7\right)$ to facilitate comparison. Represented are streamlines along the XY center plane $\left(z = 0\right)$ and crossing the central

vertical axis at various heights, as well as the polymeric component of the first normal stress difference, $N_1 = \tau_{yy} - \tau_{xx}$, in dimensionless form. The highest De flows for this aspect ratio are represented, both prior to the steady bifurcation – **(a)**,**(b)** in both figures – and to the onset of time-dependent flow – **(c)**,**(d)**. Several observations may be drawn from Figures 6.2 and 6.3, which are qualitatively similar, so the following applies to both. In panel **(a)**, the predominantly extensional nature of flow is noticeable along the outlet axis ($\hat{\mathbf{v}}_2$ direction). Accordingly, in panel **(b)** there is a well-defined region of large N_1, with the approximate shape of an ellipsoid, aligned with the YZ center plane. Furthermore, streamlines drawn along the vertical central axis tend to redirect matter away from the stagnation point $(\xi_3 > 0)$, as expected in a vertical stretch scenario. Regions of large normal stresses are also seen around the corners in panel **(b)**. In a bifurcated state, the flow structure changes significantly. From the streamline distribution along the vertical axis in panel **(d)**, two additional stagnation points are visible, one in the upper half $(z > 0)$ and the other in the lower half $(z < 0)$ of the slot. In-between these peripheral stagnation points and the center of the channel, along the vertical z-direction, streamlines appear to show a redirection of matter towards the center, which, by continuity, implies that the flow along the XY center plane will have a tendency to avoid the principal stagnation point. Interestingly, despite the asymmetries along the horizontal middle-plane, vertical symmetry is seen relative to $z = 0$. Furthermore, large regions of high N_1 are seen in panel **(d)**. The above mentioned birefringence ellipsoid strand has rotated around the z-axis to be aligned with the asymmetric flow pattern, and regions of high normal stresses around the corners have expanded significantly, especially on the concave side of the asymmetry. Notably, the central region of large N_1 is now caused primarily by shear at the interface between the two dominant flow branches, which although a fundamentally different flow type from the previously symmetric extensional flow, is also capable of stretching polymer molecules, thus generating large normal stresses. On that note, one of the few differences between Figures 6.2 and 6.3 is the increase/decrease in size of the N_1 iso-surface, respectively, likely due to the stress unbounded nature of the UCM model in extensional flows vs. the bounded extensional viscosity and shear-thinning behavior for the sPTT fluid.

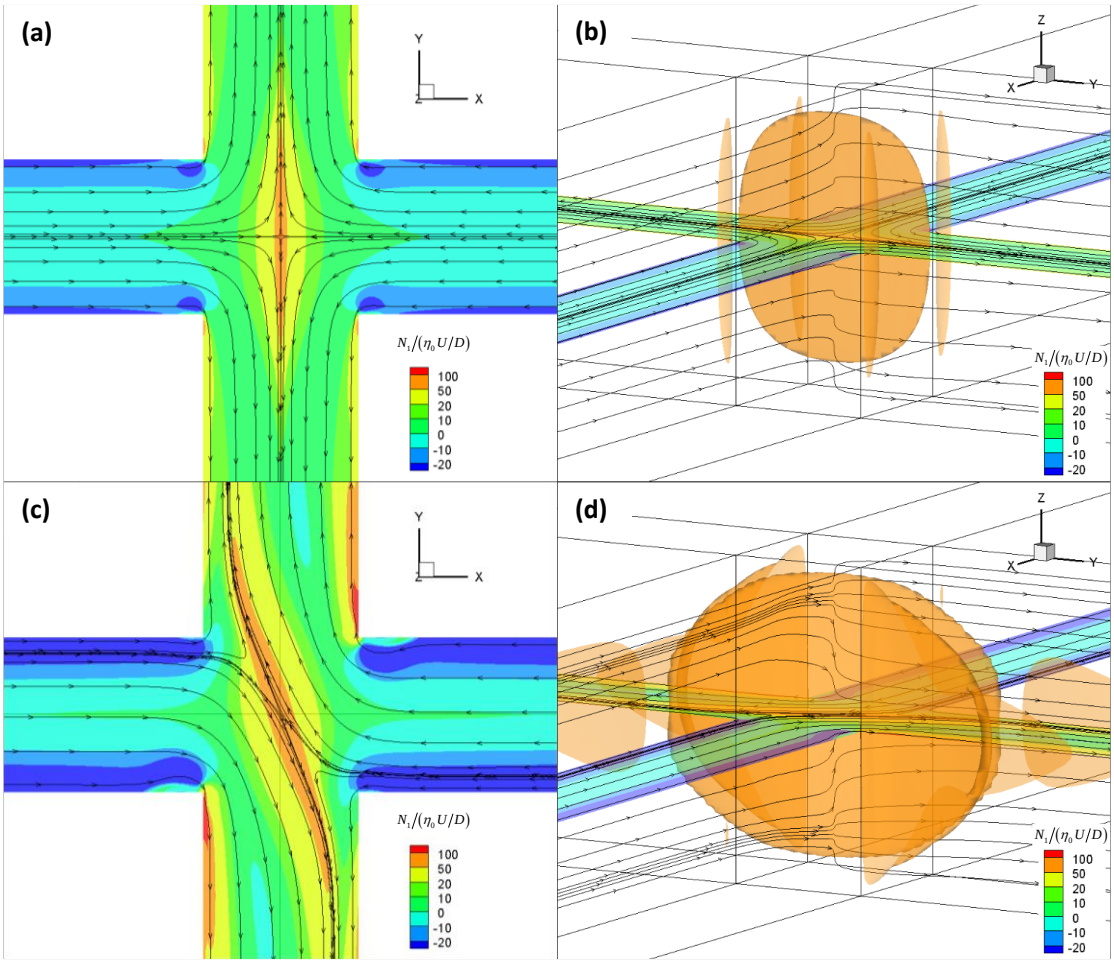

Figure 6.2 – Example of creeping-flow of an UCM fluid in a cross-slot channel with normalized aspect ratio $ARn = 0.7$. The flow is **(a**,**b)** steady symmetric at $\mathrm{De} = 0.2$ and **(c**,**d)** steady asymmetric at $\mathrm{De} = 0.4$. Panels **(a**,**c)** show the XY center plane, at $z = 0$, with streamlines superimposed onto contour plots of the first normal stress difference, $N_1 = \tau_{yy} - \tau_{xx}$. Panels **(b**,**d)** show the respective three-dimensional iso-surface at $N_1/(\eta_0 U/D) = 50$ and streamlines originating on the $y = 0$ plane inside the inlet channel and crossing the central z-axis at various heights. The streamlines in panels (a,c) do not leave the center plane.

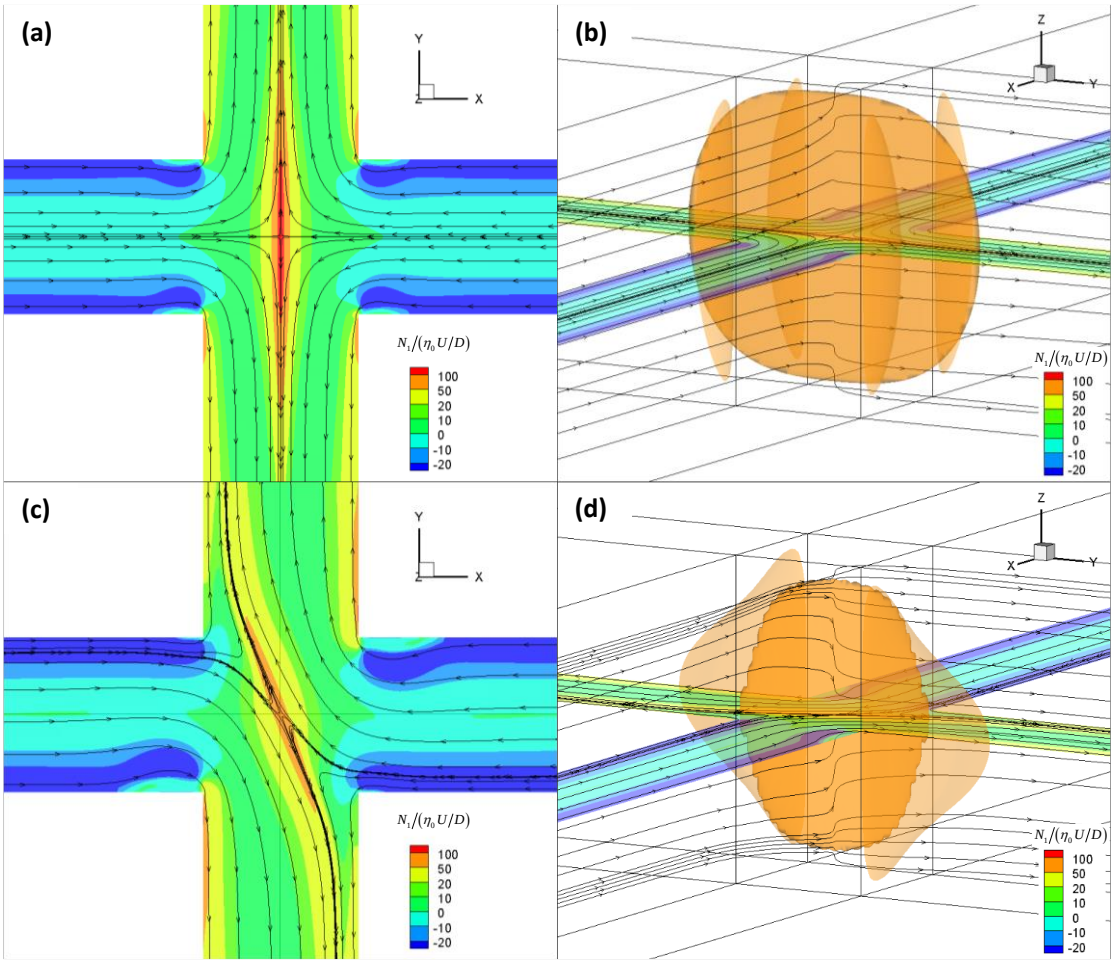

Figure 6.3 – Example of creeping flow of an sPTT fluid with $\varepsilon = 0.02$ and $\beta = 1/9$ in a cross-slot channel with normalized aspect ratio $ARn = 0.7$. Flow is **(a**,**b)** steady symmetric at $\mathrm{De} = 0.5$ and **(c**,**d)** steady asymmetric at $\mathrm{De} = 1.1$. Panels **(a**,**c)** show the XY center plane, at $z = 0$, with streamlines superimposed onto contour plots of the polymeric first normal stress difference, $N_1 = \tau_{yy} - \tau_{xx}$. Panels **(b**,**d)** show the respective three-dimensional iso-surface at $N_1/(\eta_0 U/D) = 50$ and streamlines originating on the $y = 0$ plane inside the inlet channel and crossing the central z-axis at various heights. The streamlines in panels **(a,c)** do not leave the center plane.

The qualitative picture described above is consistent throughout the simulated parameter space, so further plots as given in Figures 6.2 and 6.3 for different ARn would be redundant. Understanding the bifurcation mechanism thus requires the computation of characteristic parameters such as those given in Ref. [9]. Critically, a quantitative measure of flow asymmetry is needed. However, the absence of a scalar streamfunction in 3D flows invalidates the straightforward computation of the asymmetry parameter DQ proposed in Ref. [9]. Considering the vertical symmetry about the XY middle-plane, observed for all simulations in this chapter, and taking advantage of the eigenvector/eigenvalue calculations described in section 6.2, a suitable asymmetry parameter is the cosine of the angle between the two non-vertical eigenvectors of $\nabla\mathbf{u}^{\dagger}$ at the central stagnation point, $\cos(\theta)=\hat{\mathbf{v}}_1\cdot\hat{\mathbf{v}}_2$. For symmetric flow, these correspond to the Cartesian unit vectors $\left(\hat{\mathbf{i}},\hat{\mathbf{j}}\right)$ and $\cos(\theta)=0$. Stability diagrams are provided in Figures 6.4 and 6.5, for the UCM and sPTT models, respectively. The sequence of flow states, types of transitions and the corresponding De_{crit} strongly depend on the aspect ratio of the cross-slot. Roughly, for both models, at $ARn>0.5$, two types of flow transition are present: steady bifurcation and, at higher De, the onset of time-dependent flow. However, for $ARn<0.5$, approximately, there is a single, direct transition from steady symmetric flow to unsteady flow. This is an interesting cut-off, since it separates geometries in two broad categories: deep channels, i.e. $H>D$, and shallow channels, i.e. $H<D$.

Looking specifically at the UCM model, in Figure 6.4, for the shallow half of the stability diagram, the single De_{crit} appears to vary approximately linearly with the normalized aspect ratio, suggesting a progressively lower De_{crit} as $AR\to 0$, that is, viscoelastic flow is highly prone to instabilities for very shallow channels, a prediction which may be experimentally tested using e.g. a highly elastic Boger fluid [10] in a Hele-Shaw cell [11]. Indeed, in their studies of viscoelastic creeping-flow past a cylinder, McKinley and co-workers [12] used a highly elastic polyisobutylene solution – colloquially known as the MIT Boger fluid and extensively characterized elsewhere [13] – and showed a progressively lower De_{crit} with increasing blockage ratio, or in other words, with decreasing cylinder-to-wall gap and therefore elevated shear-rate, similar to what is observed for progressively shallower planar cross-slots. This relation between

De_{crit} and blockage ratio is further demonstrated in Ref. [14], where it is shown that $1/\mathrm{De}_{crit} = \tilde{a} + \tilde{b}/\Lambda$, with Λ being the inverse blockage ratio and $\tilde{a}$ and $\tilde{b}$ constants determined by data fitting. For clarity, this comparison between blockage ratio in flow past a cylinder and aspect ratio in a cross-slot is made on the basis of similar shear-rate trends: if $\Lambda \to 1$, the shear-rate increases in the cylinder-to-wall gap; if $AR \to 0$, the shear-rate increases in a cross-slot; in both geometries, the additional shear-rate leads to instability. As for the deep half $(ARn > 0.5)$ of the stability map in Figure 6.4, the borders separating the symmetric-asymmetric and the asymmetric-unsteady regions appear, although with some variance, to have a constant De_{crit}. Once the channel is sufficiently deep, it seems the UCM fluid behaves as though the channel were infinitely deep. This observed response above a certain AR for UCM or more generally Oldroyd-B type fluids may be one of the reasons why three-dimensional effects have generally gone unreported, since microfluidic channels usually are not very shallow (see Ref. [15] for examples of five different geometries).

Regarding the stability map for the sPTT fluid (Figure 6.5), for the shallow segment of the map $(ARn < 0.5)$, again there is a direct transition from steady symmetric to unsteady flow above a critical De, which also decreases concomitantly with the decrease of ARn. As for the deep half $(ARn > 0.5)$ of the stability map in Figure 6.5, De_{crit} for the symmetric-asymmetric transition is approximately constant for $ARn \geq 0.7$. For the steady-unsteady flow transition a different scenario is observed. Although the stability map in Figure 6.5 ranges from $\mathrm{De} = 0$ up to $\mathrm{De} = 1.8$, further simulations for the two-dimensional, $ARn = 1.0$ case show the steady-unsteady transition occurs at $\mathrm{De}_{crit} = 3.75 \pm 0.05$. Since this transition occurs at $\mathrm{De}_{crit} = 1.65 \pm 0.05$ for $ARn = 0.9$, it appears the stability boundary continues to evolve, even for already fairly deep channels. In contrast, the UCM flow exhibits an approximately constant De_{crit} starting at $ARn = 0.5$. Since the parameters of the sPTT model were set at $\varepsilon = 0.02$ and $\beta = 1/9$, ergo the extensibility is large but finite and the solvent contribution to viscosity is small but not zero, the comparison with the UCM case indicates that the depth at which a cross-slot channel may be considered a good approximation to a 2D geometry is strongly dependent on the rheological properties of the test fluid.

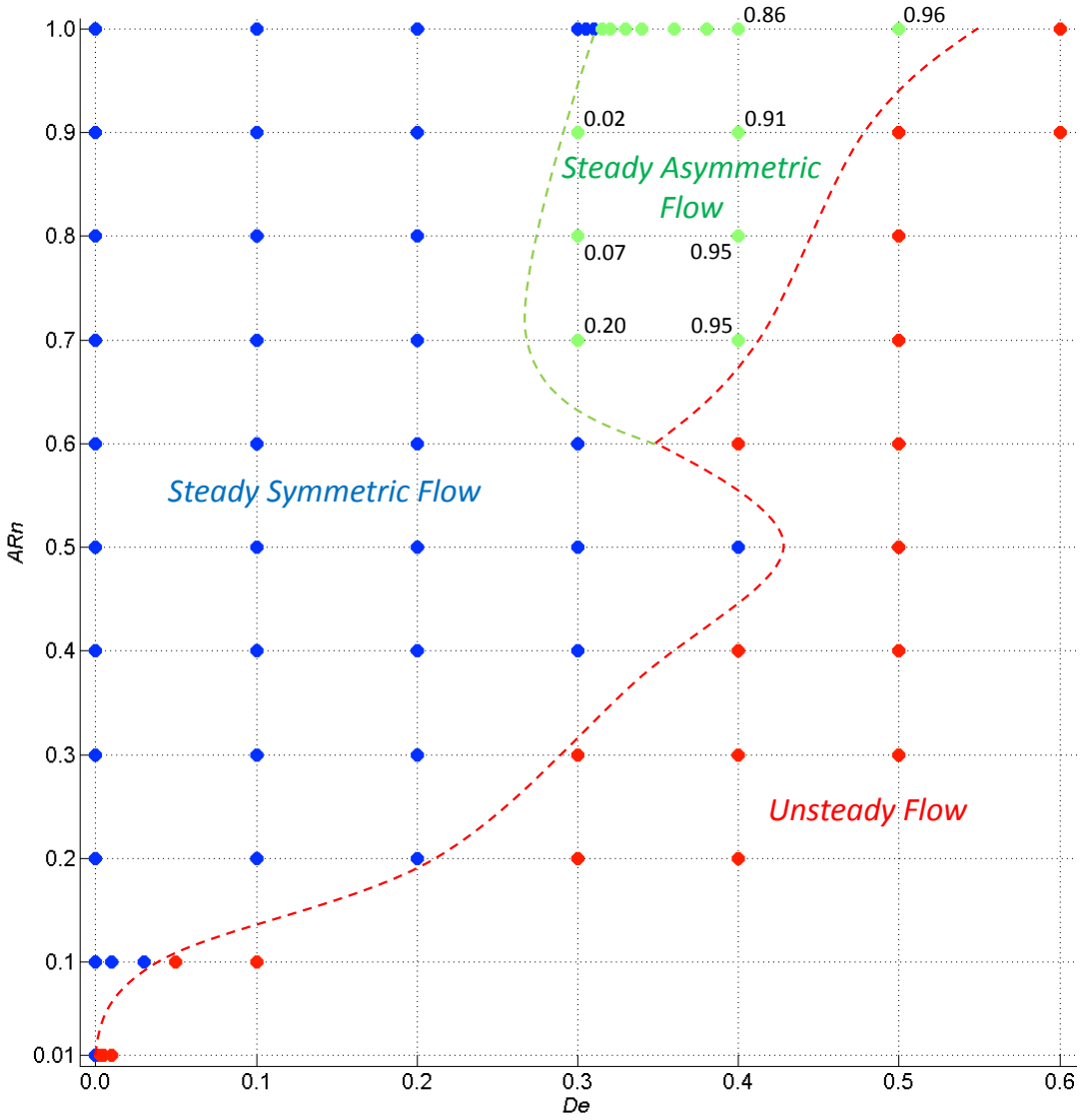

Figure 6.4 – Stability diagram for the UCM fluid. Values are given for the cosine of the angle between non-vertical eigenvectors $(\hat{\mathbf{v}}_1, \hat{\mathbf{v}}_2)$ of $\nabla \mathbf{u}^{\dagger}$ at the center of the cross-slot. The dashed lines are a guide to the eye.

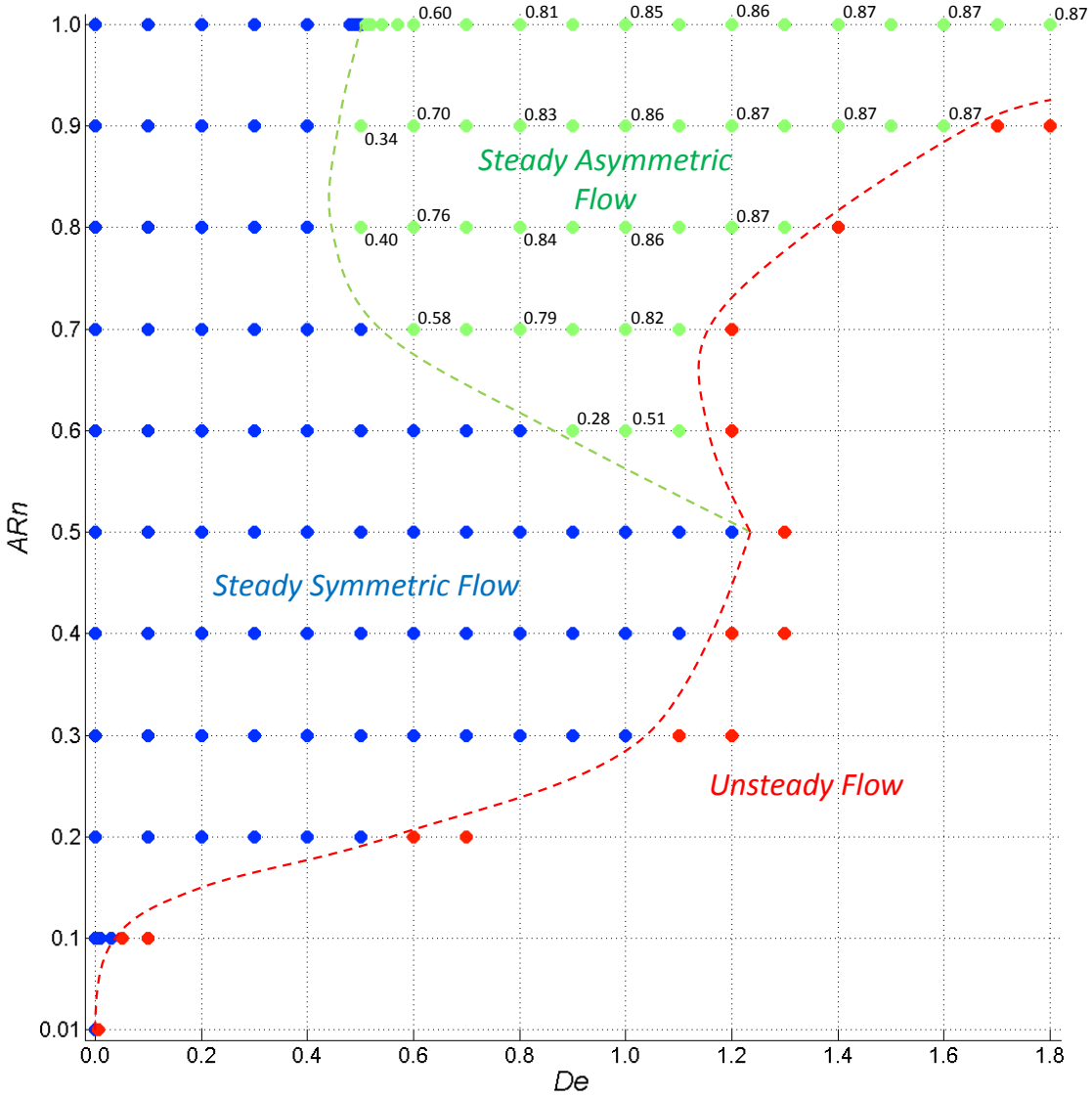

Figure 6.5 – Stability diagram for the sPTT fluid with $\varepsilon = 0.02$ and $\beta = 1/9$. Values are given for the cosine of the angle between non-vertical eigenvectors $(\hat{\mathbf{v}}_1, \hat{\mathbf{v}}_2)$ of $\nabla \mathbf{u}^{\dagger}$ at the center of the cross-slot. The dashed lines are a guide to the eye.

6.3.2 Bifurcation lowers resistance to flow

In previous publications concerning the viscoelastic cross-slot bifurcation, the observation that asymmetric flow states are accompanied by a reduction of energy dissipation is often mentioned as a justification for the phenomenon [16],[17],[18]. If this is the case, a hypothetical reduction in energy dissipation upon bifurcation should occur regardless of aspect ratio. Data for the extra pressure drop is given in Figure 6.6. The extra energy dissipation due to the central slot, relative to the dissipation occurring in the arms is expressed via the Couette correction C,

$$C = \frac{\Delta p - \Delta p_{fd}}{4\tau_{w,fd}}, \tag{6.6}$$

where the subscript *fd* refers to fully-developed flow, meaning Δp_{fd} would be the pressure drop if the cross-slot had no central slot, i.e. considering just fully-developed flow in the inlet and outlet arms. Thus one may think of the Couette correction as an additional pressure loss, equivalent to the pressure drop incurred by extending the length of the fully-developed channel flow by C hydraulic diameters, $d_h = 2D.ARn$. The average corresponding wall shear stress $\tau_{w,fd}$ may be expressed as,

$$2\tau_{w,fd} = D\left|\frac{\Delta p}{L}\right|_{fd} ARn, \tag{6.7}$$

where $\left|\Delta p/L\right|_{fd}$ denotes the constant pressure gradient in the inlet and outlet arms, which are geometrically identical, implying $\left|\mathrm{d}p/\mathrm{d}x\right|_{fd} = \left|\mathrm{d}p/\mathrm{d}y\right|_{fd} = \left|\Delta p/L\right|_{fd}$; and L is the distance over which Δp is calculated. Inspection of Figure 6.6 shows a decrease in excess pressure drop upon bifurcation for all aspect ratios where the symmetric-asymmetric transition occurs, in agreement with previous literature.

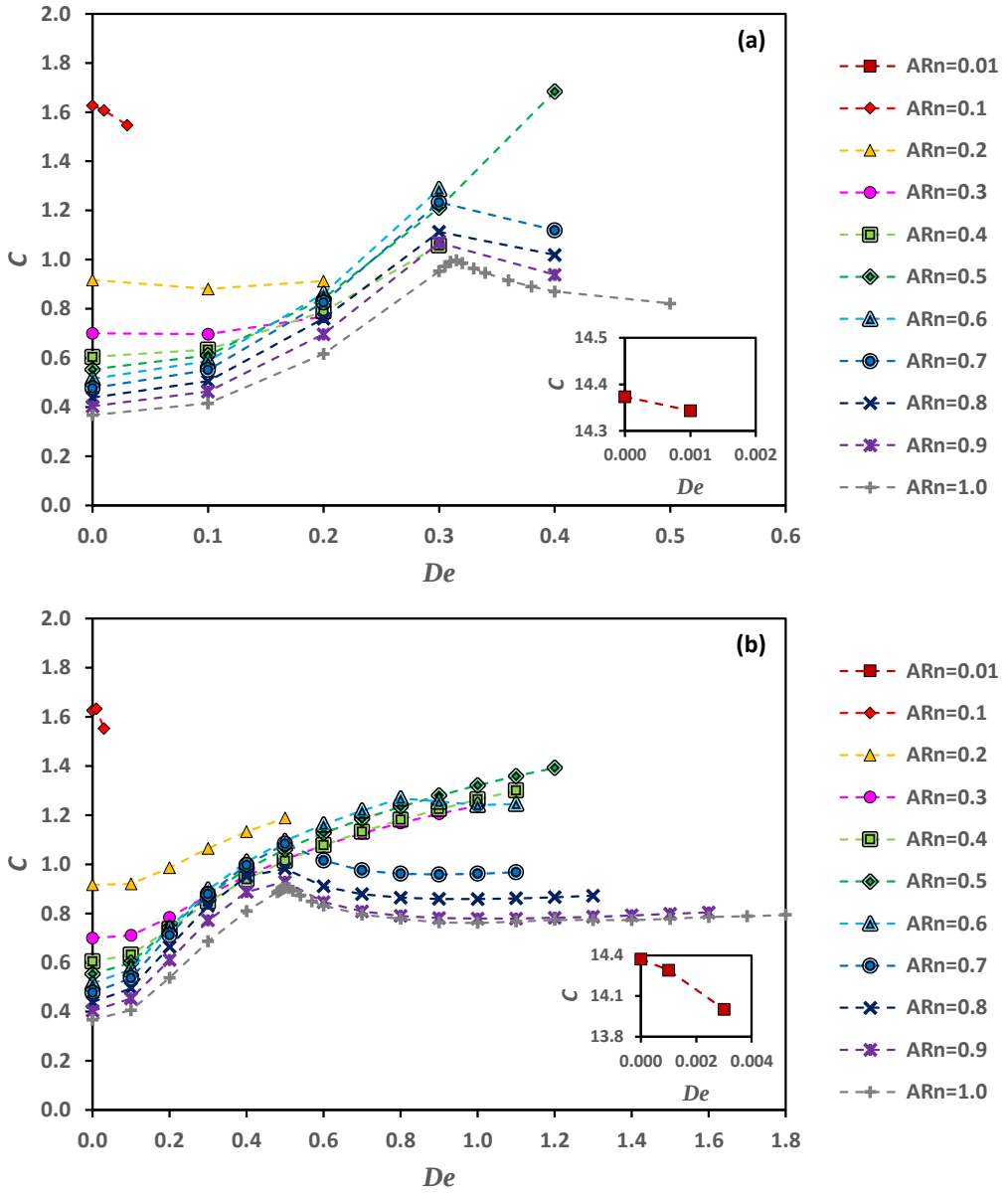

Figure 6.6 – Extra pressure drop, as indicated by the Couette correction C, for the steady state flow of **(a)** the UCM fluid and **(b)** the sPTT fluid with $\varepsilon = 0.02$ and $\beta = 1/9$.

6.3.3 Mechanism of bifurcation in 3D cross-slots

The illustrative results in Figures 6.2 and 6.3 show the emergence of peripheral stagnation points along the z-axis upon bifurcation, which direct matter towards the central stagnation point along the vertical z-direction. By continuity, this implies that some of the matter headed towards the center along the x-direction changes trajectory, with streamlines buckling around it. A more consistent way to characterize this 3D effect is to look at the strain-rate along the z-axis at the central stagnation point. At the center, one

of the eigenvectors of $\nabla\mathbf{u}^{\dagger}$ is always parallel to the z-axis, for all simulated cases, and the other two are normal to the z-axis. The corresponding eigenvalue $\dot{\varepsilon}_{z,0}$ is given in Figure 6.7, normalized by $\dot{\varepsilon}_{stretch}$ to provide an indication of the relative weight of this vertical component. Furthermore, to illustrate the flow of matter along the central z-axis, velocity profiles of the z-component of velocity are given in Figures 6.8 and 6.9 for UCM and sPTT models, respectively, with stagnation points identifiable by a change in the sign of this velocity component. In general, $\dot{\varepsilon}_{z,0} \to 0$ for the Newtonian limit or the two-dimensional limit. For finite channel depth and fluid elasticity, flows initially have a single stagnation point and $\dot{\varepsilon}_{z,0} \geq 0$. As De increases, the flow field may undergo a steady bifurcation, and at approximately the same De, $\dot{\varepsilon}_{z,0}$ becomes negative and peripheral stagnation points emerge. These peripheral stagnation points move closer to the top/bottom walls for progressively higher De, eventually leading to the formation of two additional stagnation points, to a total of five, as illustrated in panel 6.8.j for $\mathrm{De} = 0.4$ and panel 6.9.i for $\mathrm{De} = 1.3$. Hypothetically, for very deep channels $\left(ARn > 0.9\right)$, it is possible that more stagnation points form, eventually merging into a stagnation axis, seen at the 2D limit. The second pair of peripheral stagnation points also triggers a change in the sign of $\dot{\varepsilon}_{z,0}$ in an already bifurcated flow, e.g. $\mathrm{De} = 1.3$ at $ARn = 0.8$ in Figure 6.7.b. Additionally, although usually the steady bifurcation and the emergence of peripheral stagnation points occur at the same De, in some instances there is a delay between phenomena. For instance, peripheral stagnation points start appearing prior to bifurcation for $\mathrm{De} = 0.4$ in panels 6.9.h, 6.9.i and 6.9.j, and bifurcation is seen to occur without the immediate formation of peripheral stagnation points for $\mathrm{De} = 0.3$ in panel 6.8.j and $\mathrm{De} = 1.0$ in panel 6.9.g. That such delays show no bias towards either phenomenon makes it difficult to establish a relation of cause and effect.

Work on viscoelastic creeping-flow around cylinders [12],[19],[20] has revealed the formation of steady-state, three-dimensional wake cellular structures above a critical Deborah number, shown in Ref. [12] to be a function of the cylinder blockage ratio. Furthermore, streamlines in the wake form bundles along the neutral axis of the cylinder (cf. Figure 26 in Ref. [12] and Figure 4 in Ref. [20]). Thus, the fluid selects a set of paths along which local, relative velocities become higher, as shown by the convergence of streamlines. Considering the steady bifurcation in planar cross-slots is accompanied by a

reduction in dissipated energy, as shown by the reduced extra pressure drop (Figure 6.6), the asymmetric flow field necessarily favors paths of least resistance, in a manner akin to the wake cells observed for creeping flow around cylinders. Hypothetically, the emergence of vertical flow upon steady bifurcation relates to the global decrease in energy dissipation seen in Figure 6.6.

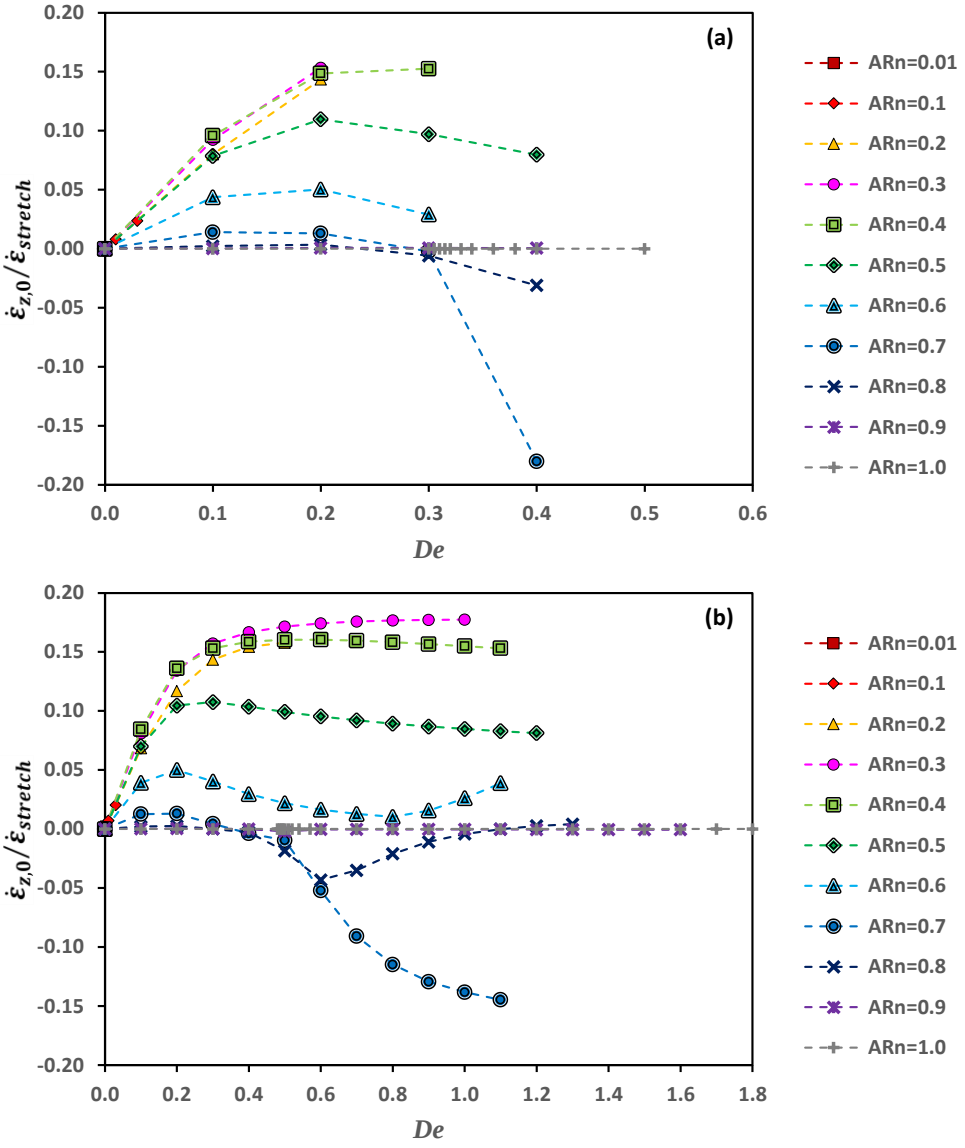

Figure 6.7 – Strain-rate along the z-direction at the central stagnation point, normalized by the stretch on the central XY plane, for the steady state flow of **(a)** the UCM fluid and **(b)** the sPTT fluid, with $\varepsilon = 0.02$ and $\beta = 1/9$. Positive values indicate local stretching and negative values represent local compression.

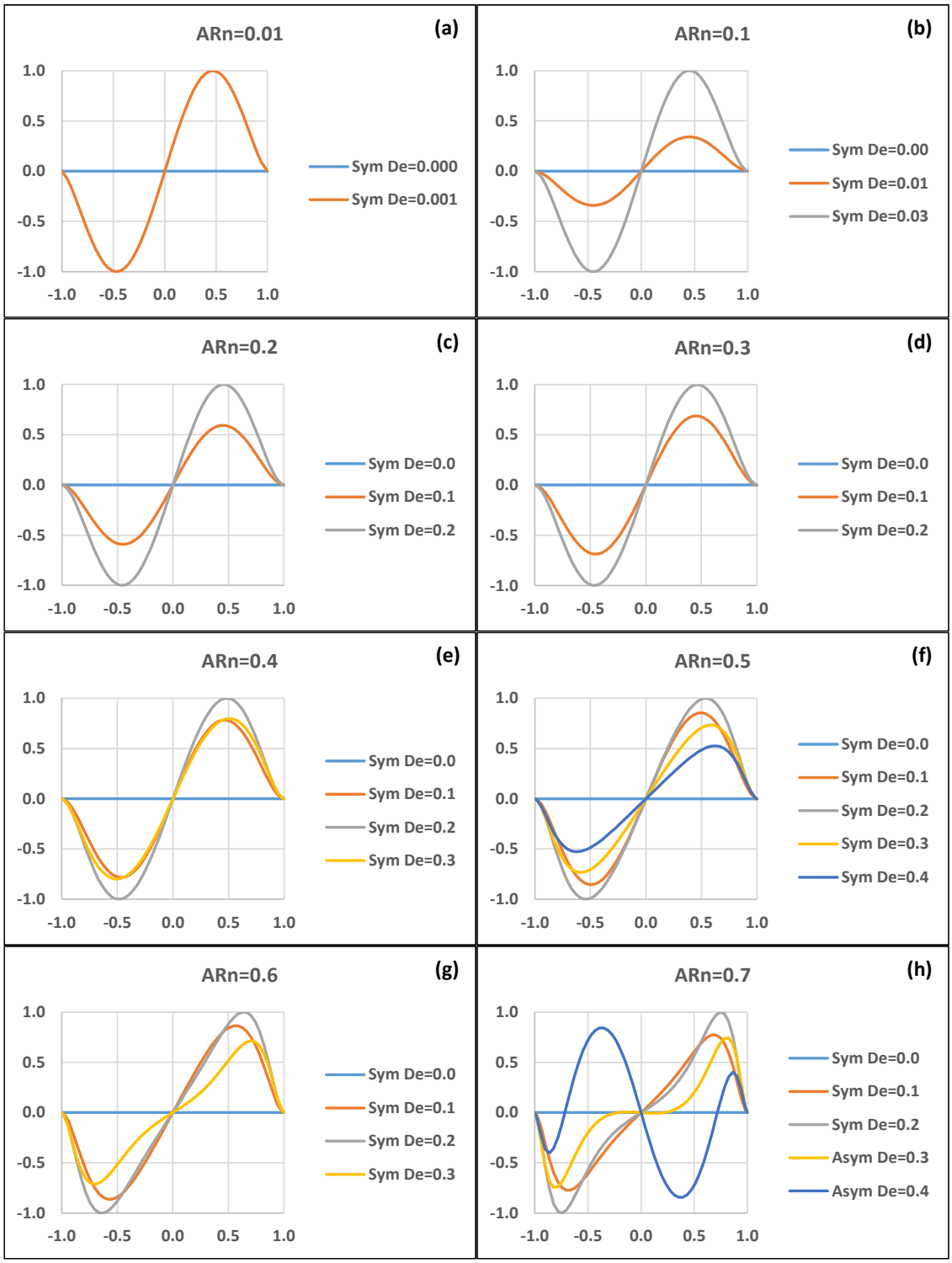

Figures 6.8 – (Continued on the next page) Velocity profiles along the vertical z-axis for the steady state flow of the UCM fluid. Newtonian flows are also shown at $\mathrm{De}=0.0$. Panels **(a)-(j)**: vertical axes represent the normalized velocity component $w_n = w/|w|_{max}$, and horizontal axes are the normalized position component $z_n = z/(H/2)$. Values of $|w|_{max}/U$ for each aspect ratio are given in panel **(k)**, with data point labels referring to the corresponding De; at $ARn=0.01$, the missing De label is 0.001.

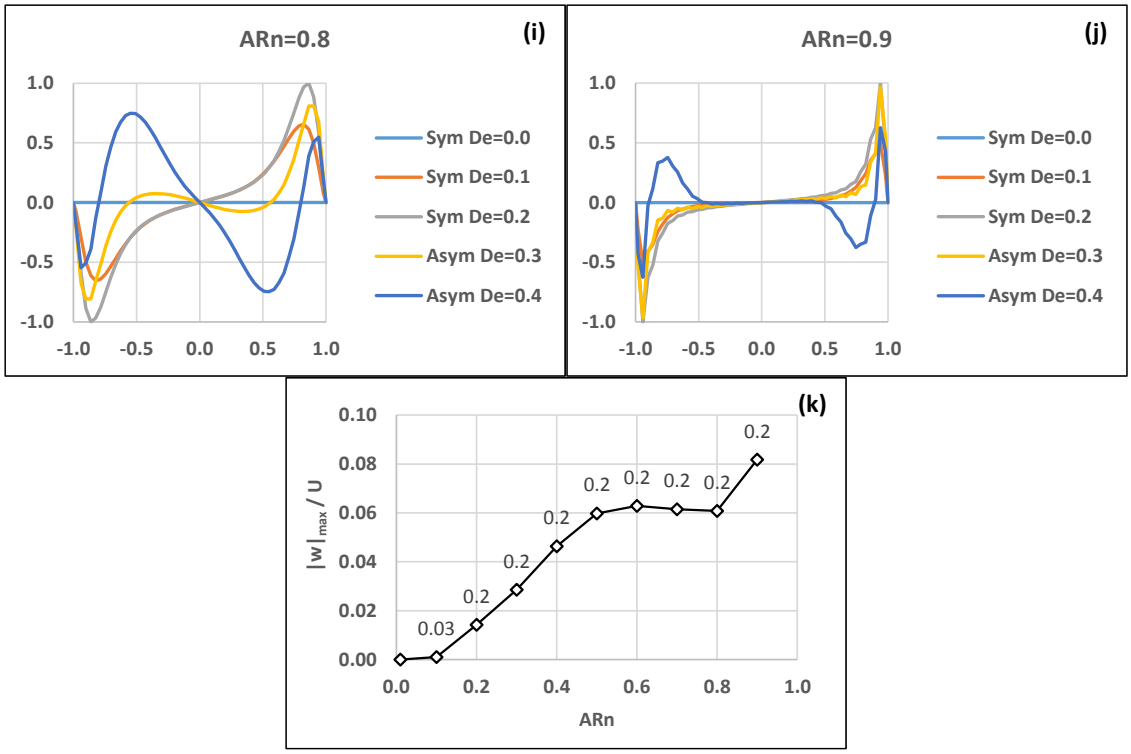

Figure 6.8 – (Conclusion).

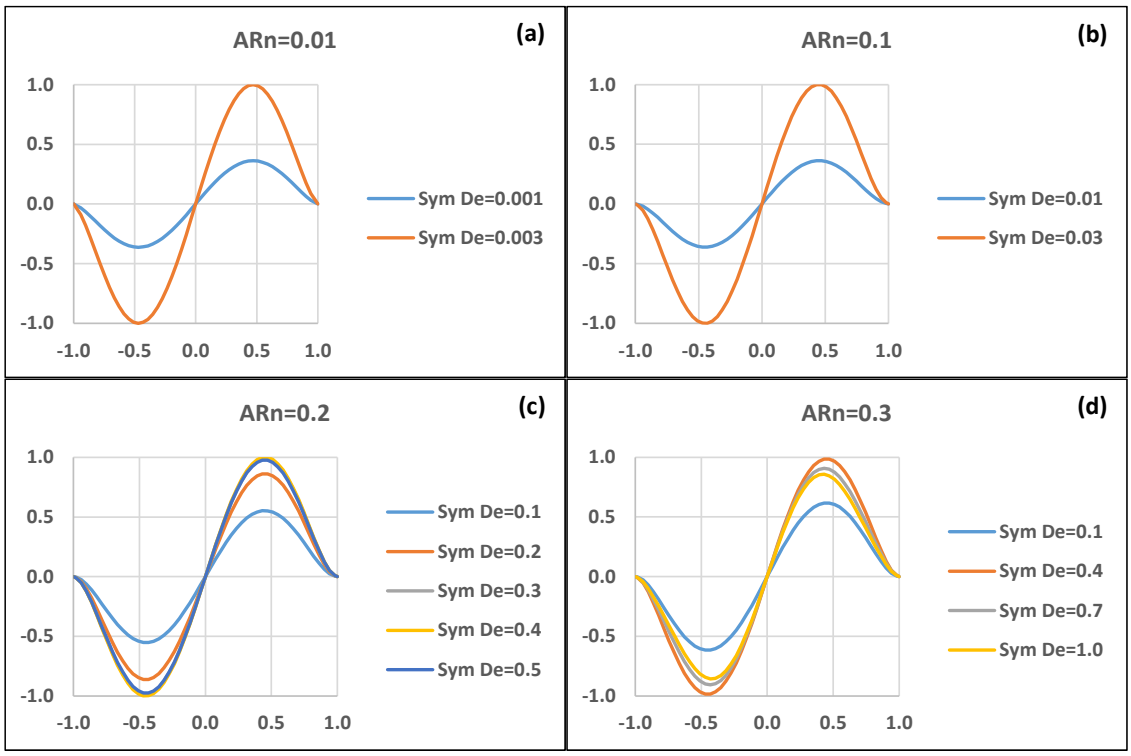

Figure 6.9 – (Continued on the next page).

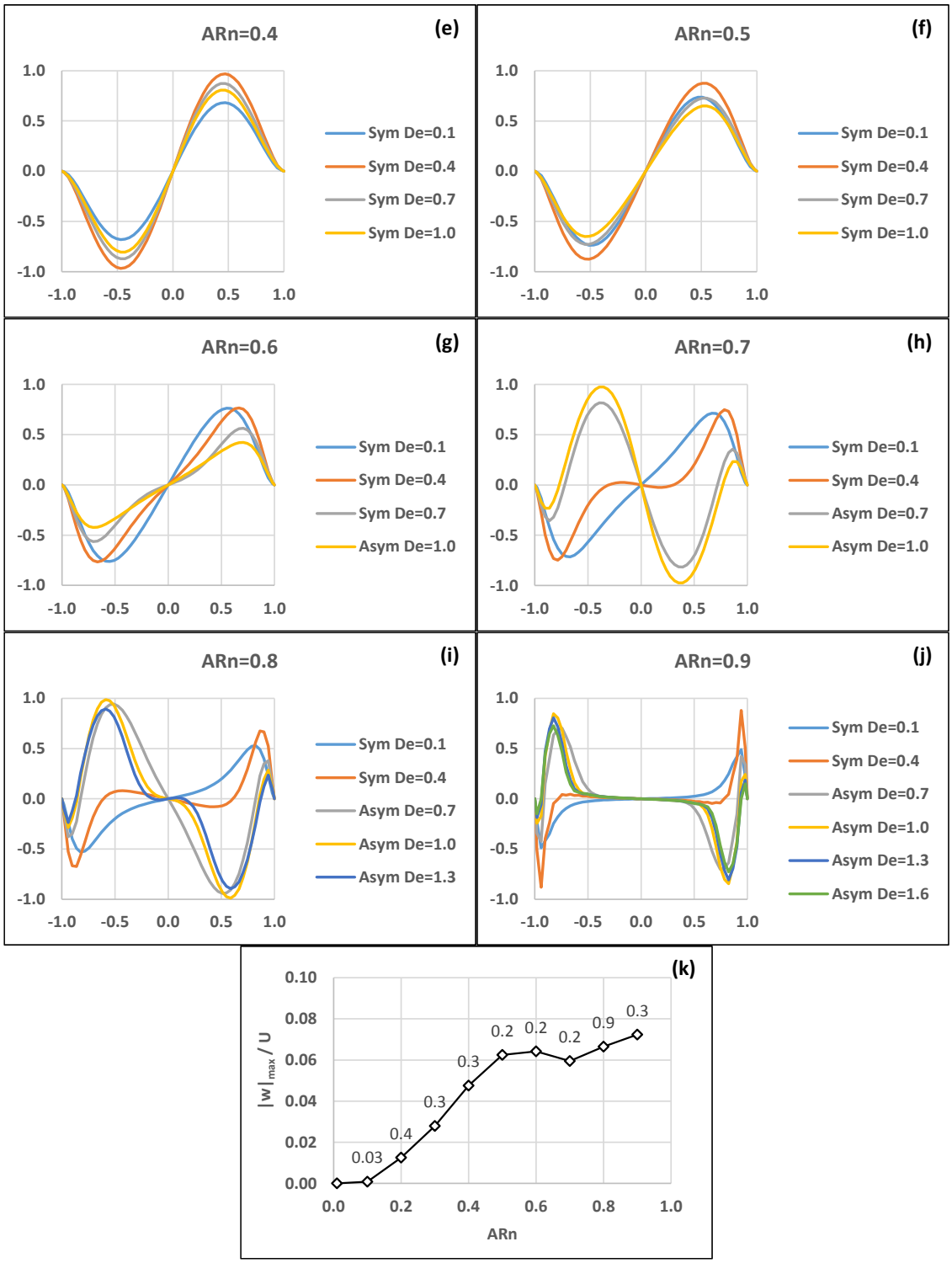

Figure 6.9 – (Conclusion) Velocity profiles along the vertical z-axis for the steady state flow of the sPTT fluid with $\varepsilon = 0.02$ and $\beta = 1/9$. For better visibility, only some De are shown. Panels **(a)-(j)**: vertical axes represent the normalized velocity component $w_n = w/|w|_{max}$, and horizontal axes are the normalized position component $z_n = z/(H/2)$. Values of $|w|_{max}/U$ for each aspect ratio are given in panel **(k)**, with data point labels referring to the corresponding De; at $ARn = 0.01$, the missing De label is 0.003.

Furthermore, as shown in Figure 6.10, gaps of low streamwise tensile stress $\tau_{ss} = \mathbf{u}^{\dagger}\boldsymbol{\tau}\mathbf{u}/\|\mathbf{u}\|^2$, computed as a projection of the stress tensor $\boldsymbol{\tau}$ onto the local velocity field streamline direction, $\mathbf{u}/\|\mathbf{u}\|$, are present along the central z-axis. Here $\|\mathbf{u}\|$ is the local velocity magnitude given by $\|\mathbf{u}\| = \sqrt{u^2 + v^2 + w^2}$. Since τ_{ss} may be construed as an indicator of resistance to flow, one might speculate that the emergent vertical flow upon bifurcation contributes, locally, to the observed global reduction in extra pressure drop.

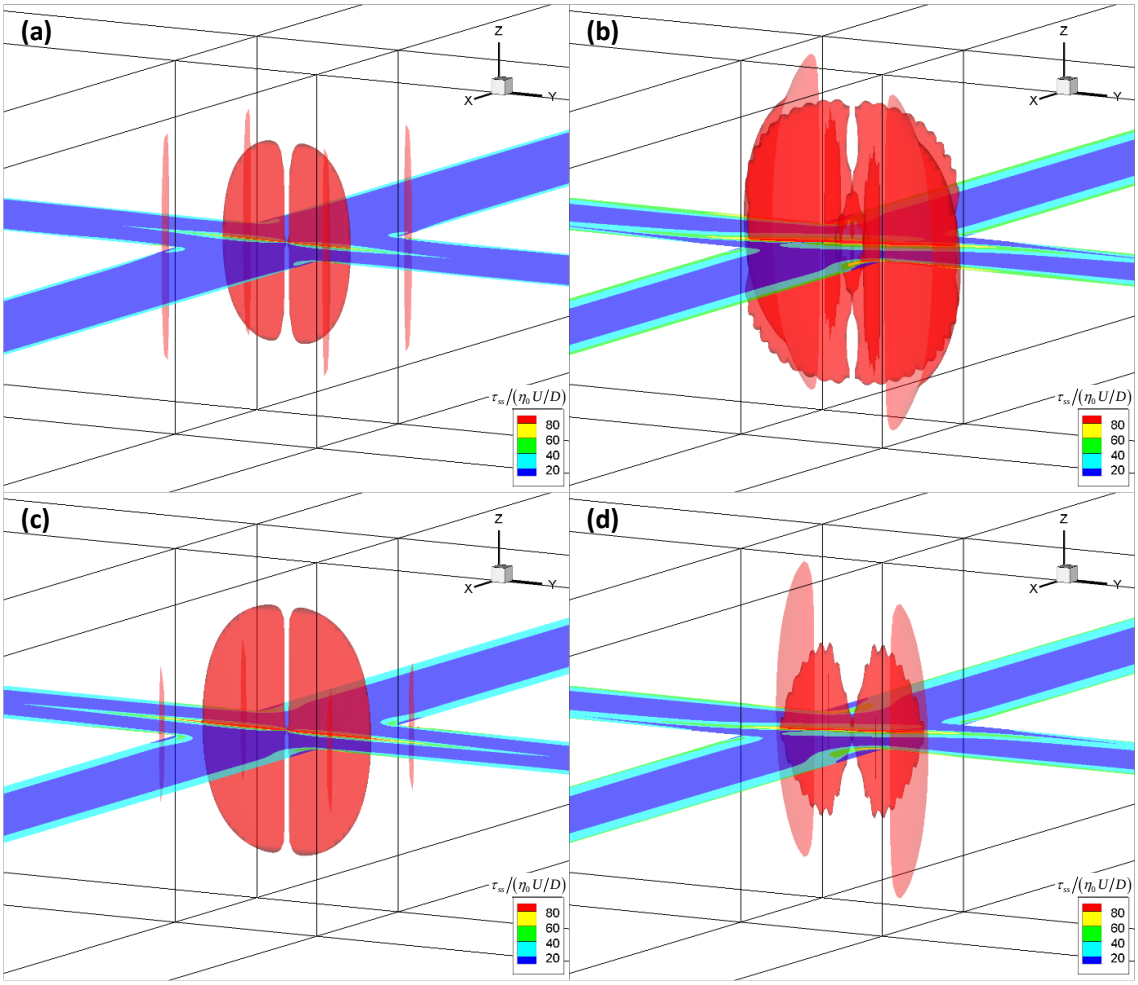

Figure 6.10 – Iso-surfaces and XY center plane of the normalized streamwise stress $\tau_{ss}/(\eta_0 U/D)$, for $ARn = 0.7$. **(a)** Symmetric UCM flow at $\mathrm{De} = 0.2$. **(b)** Asymmetric UCM flow at $\mathrm{De} = 0.4$. **(c)** Symmetric sPTT flow at $\mathrm{De} = 0.5$. **(d)** Asymmetric sPTT flow at $\mathrm{De} = 1.1$. Iso-surfaces are drawn at $\tau_{ss}/(\eta_0 U/D) = 80$. sPTT fluid with $\varepsilon = 0.02$ and $\beta = 1/9$.

6.3.4 Local evaluation of the Pakdel-McKinley criterion

The strong flow curvature near the four cross-slot corners is potentially responsible for the second transition, to an unsteady flow pattern, and therefore the ideas developed by McKinley and co-workers are applied in order to investigate this possibility. The Pakdel-McKinley criterion can be written as [14],

$$M = \sqrt{\frac{\lambda U}{R}\frac{\tau_{ss}}{\eta_0 \dot{\gamma}}}, \tag{6.8}$$

where $\lambda U = l$ is the characteristic length over which perturbations to the base stress and velocity fields relax, R is the radius of curvature, τ_{ss} is the streamwise tensile stress, η_0 is the zero-shear-rate shear viscosity and $\dot{\gamma}$ is the local shear rate. Conversion of this definition of the criterion to a form amenable to local evaluation in three-dimensional flows requires the substitution of characteristic values by local values. Considering the first non-dimensional group $\lambda U/R$, λ is substituted by its effective counterpart – which in this chapter is evaluated as $\lambda_{eff} = \lambda / g(\boldsymbol{\tau})$ – given that depending on flow conditions and fluid rheology, the local relaxation time may vary. Likewise the characteristic streamwise velocity U is substituted by the local velocity magnitude and the radius of curvature R is substituted by the local streamline radius of curvature r, yielding, via the parametric definition, $r = \|\mathbf{u}\|^3 / |\mathbf{u} \times \dot{\mathbf{u}}|$. Here, $\dot{\mathbf{u}}$ is the material derivative of the velocity vector, which reduces to $\mathbf{u} \cdot \nabla \mathbf{u}$ for steady-state flow. Regarding the second dimensionless group $\tau_{ss}/(\eta_0 \dot{\gamma})$, τ_{ss} is the streamwise tensile stress, as defined in the previous section. Concerning the shear viscosity, flow conditions and fluid rheology may result in local variations in viscosity, such that the effective shear viscosity η_{eff} is better suited for local evaluation. For the purposes of this study, $\eta_{eff} = \eta_s + \eta_p / g(\boldsymbol{\tau})$ for the sPTT fluid. Lastly, the local deformation rate may be expressed as the magnitude of the strain-rate tensor, $\dot{\gamma} = \|\dot{\boldsymbol{\gamma}}\| = \sqrt{\frac{1}{2}\dot{\boldsymbol{\gamma}} : \dot{\boldsymbol{\gamma}}^{\dagger}}$.

A further issue when considering the local evaluation of M is the rotational nature of flow in certain regions not too far from the corners of the cross-slot. In these locations, the magnitude of the strain-rate tensor approaches zero, leading to high values of M. However, the lack of shear in solid-like rotational flows invalidates the micromechanical model of purely elastic instabilities proposed by Larson et al. [21]. Thus, large values of M in rotational flow regions do not necessarily imply proneness to instability. The problem may be remedied by substitution of the term $\eta_{eff}\|\dot{\boldsymbol{\gamma}}\|$ by the magnitude of the stress tensor $\|\boldsymbol{\tau}\|_F$. Here the Frobenius norm is used, $\|\bullet\|_F$, so that the resulting dimensionless group $\tau_{ss}/\|\boldsymbol{\tau}\|_F$ will vary between zero, when normal stresses are weak, and one, when the tensile τ_{ss} normal stress dominates, as happens in highly elastic shear or extensional flows. Therefore in strongly extensional flows, M^* is approximately given by $\sqrt{\lambda_{eff}\|\mathbf{u}\|/r}$, such as in the optimized shape cross-slot extensional rheometer [22], where extensional flow is attained for finite values of r and therefore the criterion has a non-trivial value. To avoid confusion, we use here the notation M^* to represent the modified Pakdel-McKinley criterion,

$$M^* = \sqrt{\frac{\lambda_{eff}\|\mathbf{u}\|}{r}\frac{\tau_{ss}}{\|\boldsymbol{\tau}\|_F}}\,. \tag{6.9}$$

With the standard Pakdel-McKinley criterion the instability due to the coupling of tensile stresses along curved streamlines and the base shear flow sets in when M is larger than a critical value, which depends on the flow geometry. Here, since M^* is evaluated locally, the critical condition defining a flow transition is given by the maximum of the M^* scalar field over the flow domain. Hence, for each constitutive model-geometry pair, the maximum value of M^* at the highest De immediately prior to each flow transition was assessed and is given in Table 6.2. Critical values of the modified Pakdel-McKinley criterion are consistent with available literature, in which the characteristic range of M_{crit} is approximately $1-10$ for various flow geometries [14],[23],[24],[25],[26],[27]. The steady bifurcation occurs at consistently lower M^*_{crit} than the onset of time-dependent flow, regardless of whether the flow field is in a symmetric or asymmetric configuration

prior to the latter transition. Furthermore, values of M_{crit}^{*} pertaining specifically to the UCM fluid are somewhat insensitive to the aspect ratio of the channel. The small variability of M_{crit}^{*} indicates the usefulness of this modified criterion in the prediction of critical flow transitions.

Table 6.2 – Critical values of the modified, locally evaluated Pakdel-McKinley criterion M_{crit}^{*} for all observed flow transitions. *Types of transitions:* Sym-Unst, transition from a steady symmetric state to a time-dependent flow; Sym-Asym, flow remains steady, but bifurcates from a symmetric to an asymmetric configuration; Asym-Unst, transition from a steady asymmetric state to unsteady flow. Values are given for the last stable simulation prior to transition. STD: standard-deviation.

Model	Transition	ARn	De_{crit}	M_{crit}^{*}	$\overline{M_{crit}^{*}} \pm \mathrm{STD}$
UCM	Sym-Unst	0.01	0.001	1.2	1.7±0.3
		0.1	0.03	2.2	
		0.2	0.2	2.1	
		0.3	0.2	1.6	
		0.4	0.3	1.7	
		0.5	0.4	1.9	
		0.6	0.3	1.5	
	Sym-Asym	0.7	0.2	1.2	1.2±0.2
		0.8	0.2	1.1	
		0.9	0.2	1.1	
		1.0	0.3	1.5	
	Asym-Unst	0.7	0.4	1.9	1.8±0.1
		0.8	0.4	1.8	
		0.9	0.4	1.8	
		1.0	0.5	1.9	
Model	Transition	ARn	De_{crit}	M_{crit}^{*}	$\overline{M_{crit}^{*}} \pm \mathrm{STD}$
sPTT $\beta = 1/9$ $\varepsilon = 0.02$	Sym-Unst	0.01	0.003	2.4	2.6±0.3
		0.1	0.3	2.7	
		0.2	0.5	3.1	
		0.3	1.0	2.7	
		0.4	1.1	2.3	
		0.5	1.2	2.2	
	Sym-Asym	0.6	0.8	1.9	1.8±0.3
		0.7	0.5	2.2	
		0.8	0.4	1.6	
		0.9	0.4	1.5	
		1.0	0.5	1.8	
	Asym-Unst	0.6	1.1	3.1	2.7±0.5
		0.7	1.1	2.4	
		0.8	1.3	2.4	
		0.9	1.6	2.4	
		1.0	3.7	3.4	

Figure 6.11 shows the progression of the highest value of M^* for each geometry and constitutive model. For the UCM model, the values of M^*_{max} increase monotonically, up to the transition to time-dependent flow, seemingly ignoring the steady flow bifurcation. A similar scenario is observed for the sPTT model in panel 6.11.b, although a momentary decrease in M^*_{max} occurs between $\mathrm{De}=0.6$ and $\mathrm{De}=0.8$, regardless of aspect ratio – so long as the flow is still steady – or whether the flow field is in a symmetric or asymmetric configuration.

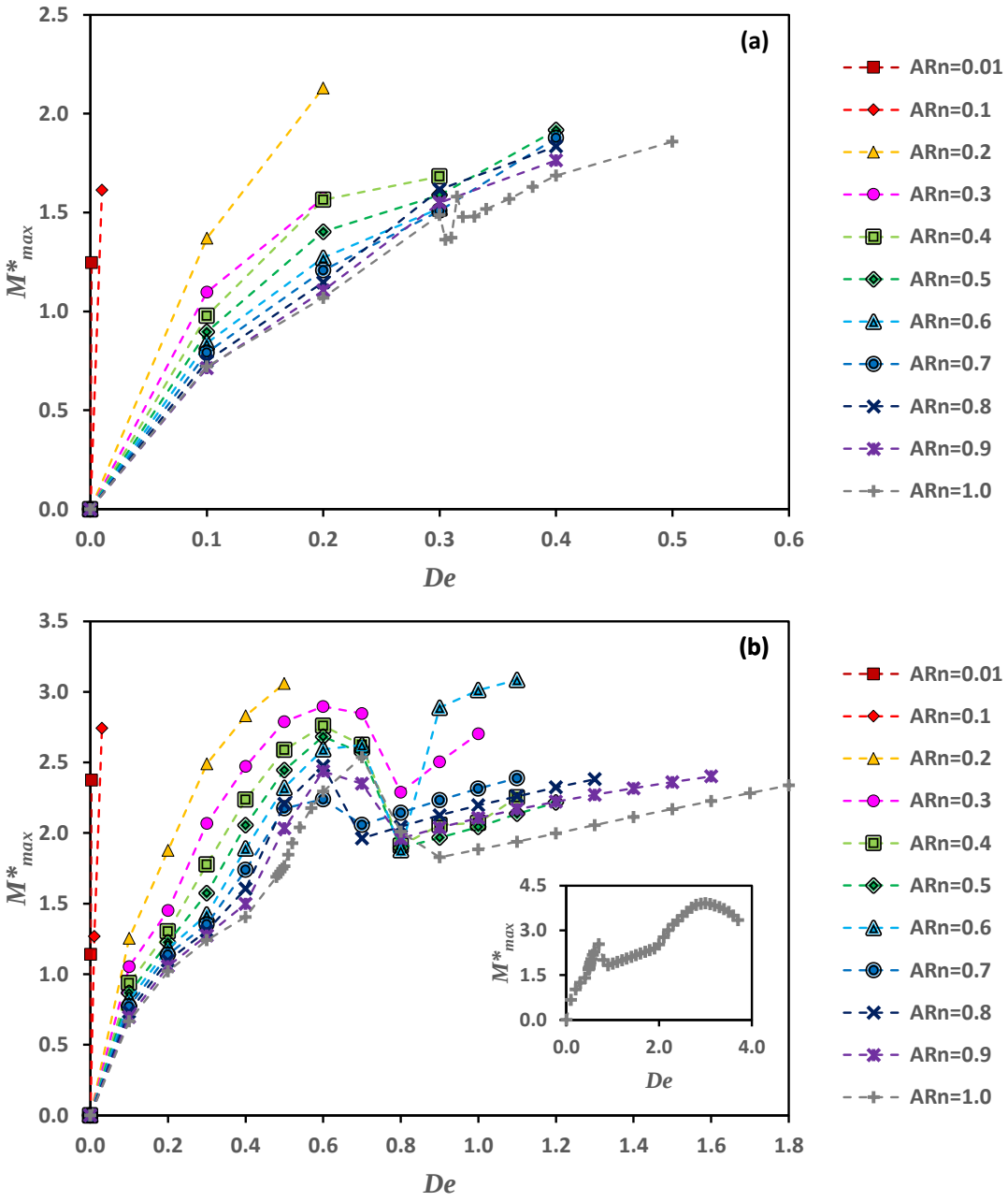

Figure 6.11 – Maximum value of the modified Pakdel-McKinley criterion M^*_{max}, for the **(a)** UCM and **(b)** sPTT models, the latter with $\varepsilon=0.02$ and $\beta=1/9$.

The local evaluation of M^* allows the construction of scalar stability maps, illustrated in Figures 6.12 and 6.13, thus facilitating the location of instability-driving regions within the flow field. The highest value of M^* is always located at the center plane $(z=0)$, approximately along the diagonals of the slot, closer to the corners than to the stagnation point, but not adjacent to the former.

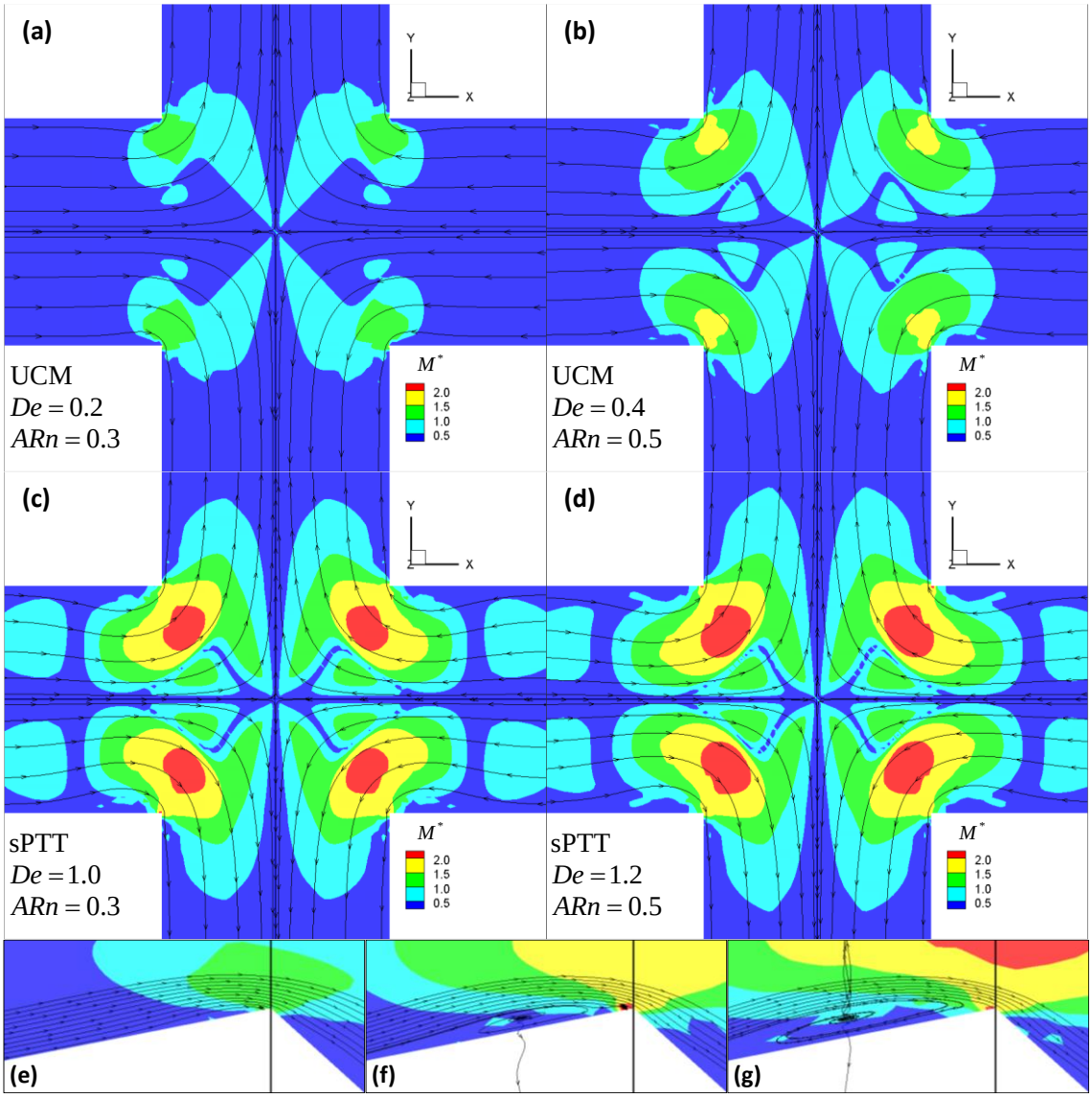

Figure 6.12 – Illustrative contour plots of the modified Pakdel-McKinley criterion M^* with superimposed streamlines, for the transition from steady symmetric to unsteady flow. Plots are given for the XY center plane, at $z=0$, for the highest simulated De prior to each transition. The constitutive model, Deborah number and normalized aspect ratio are indicated in each of the four main panels. Sub-panels **(e)**, **(f)** and **(g)**: slanted, 6x zoomed-in view of the southeast corner of the XY center plane. **(g)** corresponds to main panel **(c)**, while **(e)** and **(f)** are given for $\mathrm{De}=0.2$ and $\mathrm{De}=0.6$, for the same fluid and geometry.

Concerning the dip in the value of M^*_{max} between $\mathrm{De}=0.6$ and $\mathrm{De}=0.8$, seen in Figure 6.11.b, the formation of three-dimensional structures analogous to 2D lip vortices is visible in panels 6.12.e, 6.12.f and 6.12.g. These structures cause an increase in the radius of curvature of flow in the regions where M^* is highest, lowering its maximum value, and are also responsible for shifting matter vertically near the corners. However, since their emergence is consistently at approximately $\mathrm{De}=0.6$ they do not appear to directly influence the critical flow transitions studied elsewhere in this chapter. In Figure 6.13, the M^* field is shown at the same height as emerging peripheral stagnation points. Upon steady bifurcation, in the $z=0$ plane, the relative size of high M^* regions is enhanced on the concave side of the asymmetry and suppressed on the convex side. Maximum values of M^* near convex side corners are shifted vertically, and appear in the same planes as peripheral stagnation points (compare northwest or southeast cross-slot corners in panels 6.13.b→6.13.c and 6.13.e→6.13.f). Thus it seems a secondary effect of bifurcation is the spreading of instability prone regions along the z-direction.

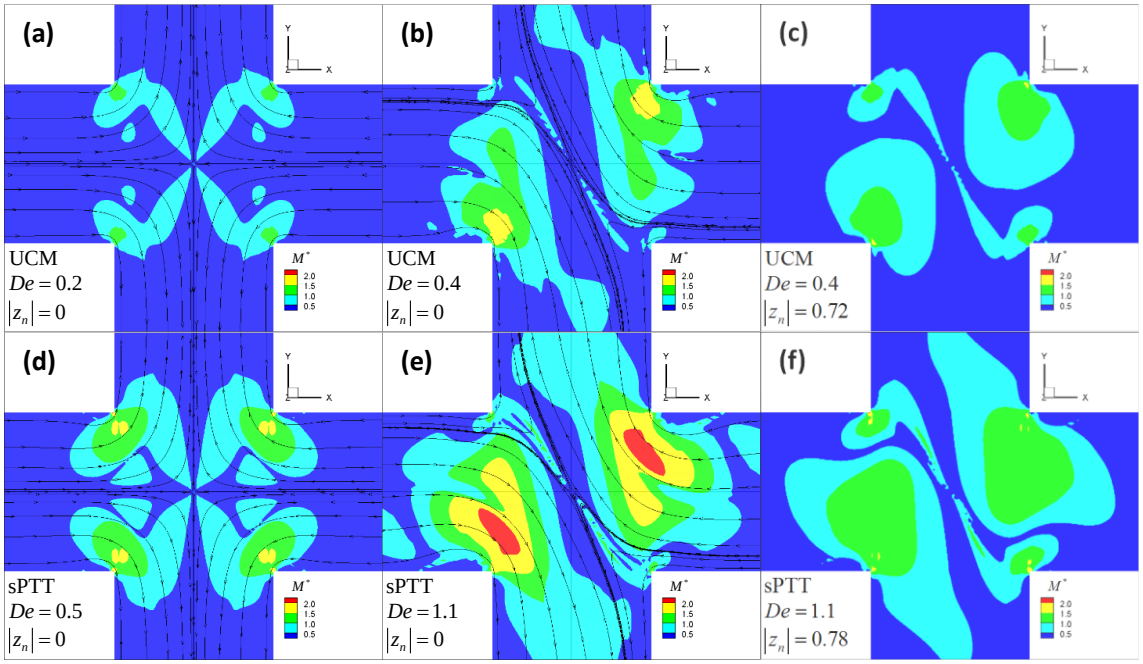

Figure 6.13 – Contour maps of the modified Pakdel-McKinley criterion M^* for $ARn=0.7$, at the highest simulated De prior to each flow transition. The constitutive model, Deborah number and normalized height coordinate of each horizontal map, defined as $z_n = z/(H/2)$, are given in each panel. Maps are shown **(a**,**d)** prior to the steady bifurcation and **(b**,**e)-(c**,**f)** prior to the onset of time-dependent flow. Maps drawn in **(c**,**f)** are centered at the location of a peripheral stagnation point; no streamlines are represented due to the three-dimensional nature of the flow in these planes.

6.4 References

[1] F.A. Cruz, R.J. Poole, A.M. Afonso, F.T. Pinho, P.J. Oliveira, M.A. Alves, Influence of channel aspect ratio on the onset of purely-elastic flow instabilities in three-dimensional planar cross-slots, J. Non-Newt. Fluid Mech. 227 (2016) 65–79. doi:10.1016/j.jnnfm.2015.11.008.

[2] N.P. Thien, R.I. Tanner, A new constitutive equation derived from network theory, J. Non-Newt. Fluid Mech. 2 (1977) 353–365. doi:10.1016/0377-0257(77)80021-9.

[3] N. Phan- Thien, A Nonlinear Network Viscoelastic Model, J. Rheol. 22 (1978) 259–283. doi:10.1122/1.549481.

[4] J.G. Oldroyd, On the Formulation of Rheological Equations of State, Proc. R. Soc. A Math. Phys. Eng. Sci. 200 (1950) 523–541. doi:10.1098/rspa.1950.0035.

[5] M.A. Alves, P.J. Oliveira, F.T. Pinho, A convergent and universally bounded interpolation scheme for the treatment of advection, Int. J. Numer. Meth. Fluids. 41 (2003) 47–75. doi:10.1002/fld.428.

[6] A.M. Afonso, P.J. Oliveira, F.T. Pinho, M.A. Alves, The log-conformation tensor approach in the finite-volume method framework, J. Non-Newt. Fluid Mech. 157 (2009) 55–65. doi:10.1016/j.jnnfm.2008.09.007.

[7] P.J. Oliveira, F.T. Pinho, G.A. Pinto, Numerical simulation of non-linear elastic flows with a general collocated finite-volume method, J. Non-Newt. Fluid Mech. 79 (1998) 1–43. doi:10.1016/S0377-0257(98)00082-2.

[8] R. Fattal, R. Kupferman, Constitutive laws for the matrix-logarithm of the conformation tensor, J. Non-Newt. Fluid Mech. 123 (2004) 281–285. doi:10.1016/j.jnnfm.2004.08.008.

[9] F.A. Cruz, R.J. Poole, A.M. Afonso, F.T. Pinho, P.J. Oliveira, M.A. Alves, A new viscoelastic benchmark flow: Stationary bifurcation in a cross-slot, J. Non-Newt. Fluid Mech. 214 (2014) 57–68. doi:10.1016/j.jnnfm.2014.09.015.

[10] D.V. Boger, A highly elastic constant-viscosity fluid, J. Non-Newt. Fluid Mech. 3 (1977) 87–91. doi:10.1016/0377-0257(77)80014-1.

[11] H.S. Hele-Shaw, The Flow of Water, Nature. 58 (1898) 34–36. doi:10.1038/058034a0.

[12] G.H. McKinley, R.C. Armstrong, R.A. Brown, The Wake Instability in Viscoelastic Flow past Confined Circular Cylinders, Philos. Trans. R. Soc. A Math. Phys. Eng. Sci. 344 (1993) 265–304. doi:10.1098/rsta.1993.0091.

[13] L.M. Quinzani, G.H. McKinley, R.A. Brown, R.C. Armstrong, Modeling the rheology of polyisobutylene solutions, J. Rheol. 34 (1990) 705. doi:10.1122/1.550148.

[14] G.H. McKinley, P. Pakdel, A. Öztekin, Rheological and geometric scaling of purely elastic flow instabilities, J. Non-Newt. Fluid Mech. 67 (1996) 19–47. doi:10.1016/S0377-0257(96)01453-X.

[15] F.J. Galindo-Rosales, L. Campo-Deaño, P.C. Sousa, V.M. Ribeiro, M.S.N. Oliveira, M.A. Alves, et al., Viscoelastic instabilities in micro-scale flows, Exp. Therm. Fluid Sci. 59 (2014) 128–139. doi:10.1016/j.expthermflusci.2014.03.004.

[16] R.J. Poole, M.A. Alves, P.J. Oliveira, Purely Elastic Flow Asymmetries, Phys. Rev. Lett. 99 (2007) 164503. doi:10.1103/PhysRevLett.99.164503.

[17] H.J. Wilson, Open mathematical problems regarding non-Newtonian fluids, Nonlinearity. 25 (2012) R45–R51. doi:10.1088/0951-7715/25/3/R45.

[18] G.N. Rocha, R.J. Poole, M.A. Alves, P.J. Oliveira, On extensibility effects in the cross-slot flow bifurcation, J. Non-Newt. Fluid Mech. 156 (2009) 58–69. doi:10.1016/j.jnnfm.2008.06.008.

[19] A.H. Shiang, A. Özkekin, J.-C. Lin, D. Rockwell, Hydroelastic instabilities in viscoelastic flow past a cylinder confined in a channel, Exp. Fluids. 28 (2000) 128–142. doi:10.1007/s003480050017.

[20] M. Sahin, Parallel large-scale numerical simulations of purely-elastic instabilities behind a confined circular cylinder in a rectangular channel, J. Non-Newt. Fluid Mech. 195 (2013) 46–56. doi:10.1016/j.jnnfm.2012.11.011.

[21] R.G. Larson, E.S.G. Shaqfeh, S.J. Muller, A purely elastic instability in Taylor–Couette flow, J. Fluid Mech. 218 (1990) 573–600. doi:10.1017/S0022112090001124.

[22] S.J. Haward, M.S.N. Oliveira, M.A. Alves, G.H. McKinley, Optimized cross-slot flow geometry for microfluidic extensional rheometry, Phys. Rev. Lett. 109 (2012) 128301. doi:10.1103/PhysRevLett.109.128301.

[23] P. Pakdel, G.H. McKinley, Elastic Instability and Curved Streamlines, Phys. Rev. Lett. 77 (1996) 2459–2462. doi:10.1103/PhysRevLett.77.2459.

[24] A. Öztekin, B. Alakus, G.H. McKinley, Stability of planar stagnation flow of a highly viscoelastic fluid, J. Non-Newt. Fluid Mech. 72 (1997) 1–29. doi:10.1016/S0377-0257(97)00021-9.

[25] R.J. Poole, F.T. Pinho, M.A. Alves, P.J. Oliveira, The effect of expansion ratio for creeping expansion flows of UCM fluids, J. Non-Newt. Fluid Mech. 163 (2009) 35–44. doi:10.1016/j.jnnfm.2009.06.004.

[26] J. Zilz, R.J. Poole, M.A. Alves, D. Bartolo, B. Levaché, A. Lindner, Geometric scaling of a purely elastic flow instability in serpentine channels, J. Fluid Mech. 712 (2012) 203–218. doi:10.1017/jfm.2012.411.

[27] A.M. Afonso, F.T. Pinho, M.A. Alves, Electro-osmosis of viscoelastic fluids and prediction of electro-elastic flow instabilities in a cross slot using a finite-volume method, J. Non-Newt. Fluid Mech. 179–180 (2012) 55–68. doi:10.1016/j.jnnfm.2012.05.004.

7 Time-Dependent Instabilities in an Optimized Cross-Slot Device

7.1 Summary

The time-dependent flow of Boger fluids is simulated in the Optimized Shape Cross-slot Extensional Rheometer, or OSCER device, using the FENE-CR constitutive model. A family of predominantly elastic instabilities is uncovered, resulting from the interaction of stationary asymmetric and time-dependent flow transitions. The superposition of pitchfork and Hopf bifurcations, with varying degrees of relative amplitude, produces five distinct flow regimes which are classified by their elasticity, suggesting that the dynamic system is situated in the vicinity of a codimension-2 point in the inertia-elasticity-viscosity parameter space. A detailed characterization of this codimension-2 bifurcation is provided, including the various associated modes of instability. Spectral analysis of the first component of the velocity vector suggests that the flow regimes featuring loss of birefringence strand integrity become chaotic and locally turbulent near the center of the cross-slot, above a certain flow rate threshold.

7.2 Numerical Methods

The isothermal, incompressible, time-dependent flow of monodisperse, dilute, long-chained polymer solutions is simulated, using a Finitely Extensible Nonlinear Elastic (FENE) constitutive model [1] with the Chilcott-Rallison (-CR) closure [2]. The relevant rheological properties of the model fluids are given in Table 7.1, and are based on real Boger fluids of the kind developed by Odell and Carrington [3].

Table 7.1 – Properties of the model fluids. Solvent shear viscosity for all fluids is η_s=0.059 Pa.s and density is ρ=981 kg.m^{-3}. The nominal Elasticity number El$_{nom}$ was calculated using zero shear-rate properties. Additional data was kindly provided by the authors of Ref. [4].

Fluid	**Flow Regime**	λ_0 **/s**	η_p **/Pa.s**	$\beta=\eta_s/\eta_0$	L^2	**El$_{nom}$**
aPS7-350ppm	Very Low Elasticity	0.010	0.005	0.92	6821	1.6
aPS7-700ppm	Very Low Elasticity	0.013	0.011	0.84	6821	2.3
aPS7-1400ppm	Low Elasticity	0.016	0.020	0.75	6821	3.2
aPS10-350ppm	Low Elasticity	0.025	0.006	0.91	10082	4.1
aPS10-700ppm	Intermediate Elasticity	0.030	0.014	0.81	10082	5.6
aPS10-1400ppm	High Elasticity	0.036	0.029	0.67	10082	8.1
aPS16-350ppm	Very High Elasticity	0.080	0.008	0.88	15951	13.7
aPS16-700ppm	Very High Elasticity	0.090	0.023	0.72	15951	18.8
aPS16-1400ppm	Very High Elasticity	0.120	0.046	0.56	15951	32.2

The governing equations are respectively the continuity and momentum equations,

$$\nabla \cdot \mathbf{u} = 0, \tag{7.1}$$

$$\rho \frac{\mathrm{D}\mathbf{u}}{\mathrm{D}t} = -\nabla p + \eta_s \nabla^2 \mathbf{u} + \nabla \cdot \boldsymbol{\tau}, \tag{7.2}$$

and the constitutive equations of the FENE-CR model,

$$\left[1 + \lambda_0 \frac{\mathrm{D}}{\mathrm{D}t}\left(\frac{1}{g}\right)\right]\boldsymbol{\tau} + \frac{\lambda_0}{g}\frac{\mathrm{D}\boldsymbol{\tau}}{\mathrm{D}t} = \eta_p\left(\nabla\mathbf{u} + \nabla\mathbf{u}^{\dagger}\right) + \frac{\lambda_0}{g}\left(\boldsymbol{\tau}\cdot\nabla\mathbf{u} + \nabla\mathbf{u}^{\dagger}\cdot\boldsymbol{\tau}\right), \tag{7.3}$$

$$g = \frac{L^2 + \left(\lambda_0/\eta_p\right)\mathrm{Tr}(\boldsymbol{\tau})}{L^2 - 3}. \tag{7.4}$$

In the above equations, η_s is the solvent viscosity, η_p is the polymer shear viscosity contribution, $\boldsymbol{\tau}$ is the polymeric extra stress tensor, L^2 is the extensibility of polymer chains, λ_0 is the zero shear-rate relaxation time, and g is an auxiliary function related to the decrease in effective relaxation time $\lambda_{eff} = \lambda_0/g$. Since the FENE-CR model is a constant shear viscosity approximation, it is only applicable to the simulation of at most weakly shear-thinning fluids. As mentioned in Table 7.1, some of the rheological data used in this chapter was kindly provided by the authors of Ref. [4] for other fluids tested but not reported in Ref. [4]. A cursory power law fit of the slopped portion of their shear-viscosity curves (cf. Figure 4 in Ref. [4]) indicates that the flow behavior index *n* varies between 0.95 and 1, confirming a very weak shear-thinning character. The FENE-CR model is more commonly formulated using the conformation tensor **A** as follows,

$$\frac{\mathrm{D}\mathbf{A}}{\mathrm{D}t} - \mathbf{A}\cdot\nabla\mathbf{u} - \nabla\mathbf{u}^{\dagger}\cdot\mathbf{A} = -\frac{g}{\lambda_0}\left(\mathbf{A} - \mathbf{I}\right), \tag{7.5}$$

$$g = \frac{L^2}{L^2 - Tr(\mathbf{A})}, \tag{7.6}$$

with the following relation between $\boldsymbol{\tau}$ and **A**,

$$\boldsymbol{\tau} = \frac{\eta_p g}{\lambda_0}\left(\mathbf{A} - \mathbf{I}\right). \tag{7.7}$$

The governing equations are solved using an implicit, second-order, finite volume numerical method using a collocated mesh arrangement, which is described in detail elsewhere [5], adapted from the SIMPLEC algorithm [6]. The method includes the CUBISTA high-resolution scheme for the treatment of advective terms [7] in the

momentum and constitutive equations, and the log-conformation technique for the transformation of the constitutive equation [8], following the methodology originally developed by Fattal and Kupferman [9], in order to increase the numerical stability. Furthermore, to increase the accuracy, the second-order backward differencing scheme [10] is used for time integration. At the walls, no-slip boundary conditions are assumed for the velocity components and the extra-stress components are linearly extrapolated from the first two adjacent cells along the wall-normal direction, as described elsewhere [11]. Uniform velocity profiles and null extra-stress profiles are assumed at the inlets. Neumann boundary conditions of the form $\mathbf{n}\cdot\nabla\phi = 0$ are assumed at the outlets, except for pressure which is linearly extrapolated from the first two upstream cells. Accumulation of round-off error at machine level precision suffices to generate flow instabilities, so no disturbances are artificially introduced. The numerical method is implemented in double precision Fortran.

The block structured mesh, depicted in Figure 7.1, is comprised of a total of 94233 cells, split over five blocks, one block with 21008 cells for each of the inlet and outlet channels and a fifth central block with 10201 cells. For each of the inlet and outlet blocks, the cell length along the streamwise direction is progressively larger towards the inlets and outlets. The center of the device is occupied by a square cell, with side length of 0.0616*H*.

Three nominal dimensionless numbers are defined, respectively the Weissenberg, Reynolds and Elasticity numbers,

$$\mathrm{Wi}_{nom} = \lambda_0 \dot{\varepsilon} = \lambda_0 \frac{1.5U_0}{15H}, \tag{7.8}$$

$$\mathrm{Re}_{nom} = \frac{\rho U_0 d_h}{\eta_0} = \frac{4\rho U_0 H}{\eta_s + \eta_p}, \tag{7.9}$$

$$\mathrm{El}_{nom} = \frac{\mathrm{Wi}_{nom}}{\mathrm{Re}_{nom}} = \frac{\lambda_0 \left(\eta_s + \eta_p\right)}{40\rho H^2}, \tag{7.10}$$

where U_0 is both the uniform inlet velocity and the characteristic velocity of the flow, $\eta_0 = \eta_s + \eta_p$ is the solution shear viscosity and d_h is the hydraulic diameter. Given that the flow is simulated on a two-dimensional geometry with bottom-top symmetry, the experimental equivalent would be a very deep channel, therefore the hydraulic diameter is twice the channel width, or in this case four times the half-width H which is defined as the characteristic length scale. These dimensionless quantities are designated as nominal since, for time-dependent flow, the effective relaxation time and strain-rate at the center of the device are variable.

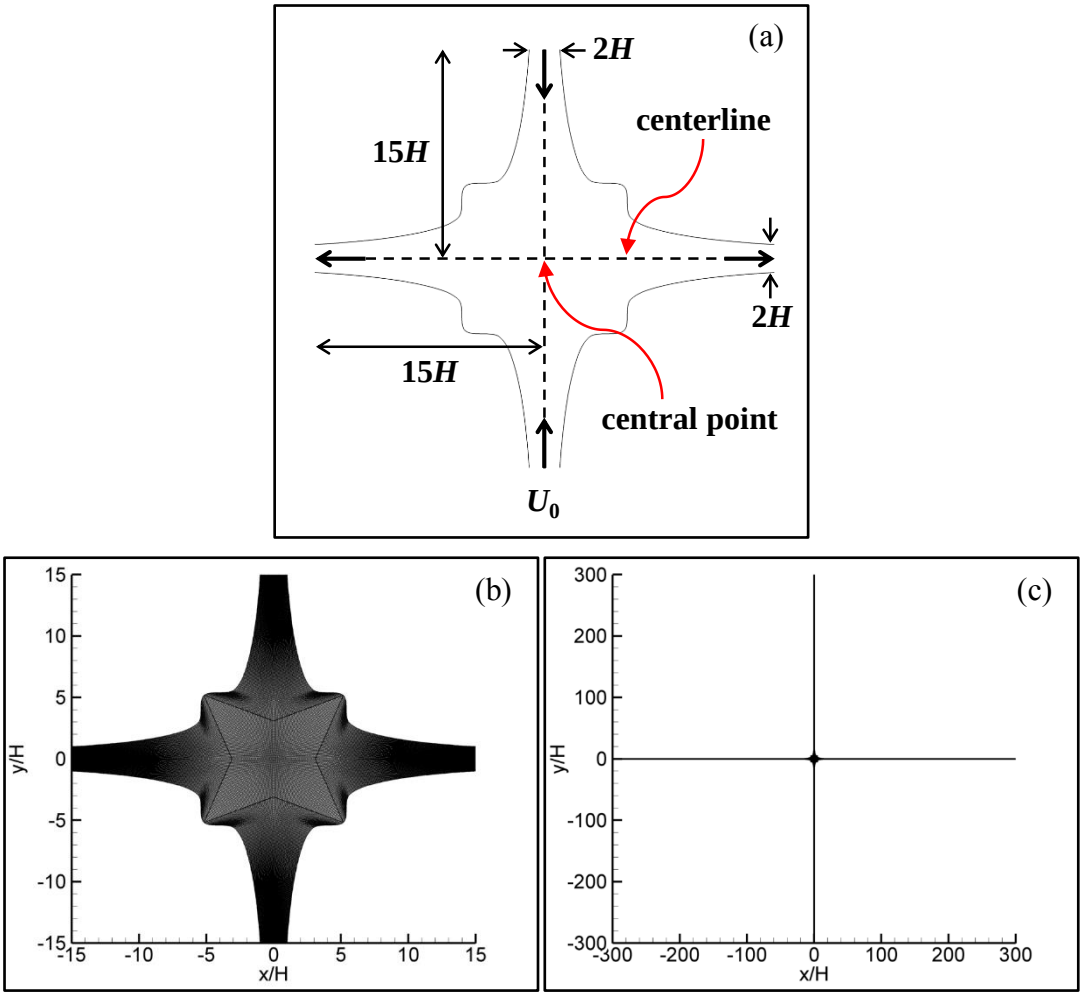

Figure 7.1 – (a) Geometry of the Optimized Shape Cross-slot Extensional Rheometer, or OSCER device. The half-width H is used as the characteristic length scale. (b) Detail of the computational mesh. The deformation of computational cells is the result of the application of an optimization algorithm to the mesh of a planar cross-slot, described in Ref. [12]. (c) Zoomed-out view of the mesh, showing the inlet and outlet channels. Cells in these channels are progressively larger in the streamwise direction towards the inlets and outlets.

For each model fluid, simulations are performed at progressively higher flow rates until the flow is clearly time-dependent. Due to the emergence of very large spatial and temporal gradients, in both velocity and stress fields, error propagation and eventual numerical divergence of simulations was common. Thus, computations were carried out using very small time-steps, usually $\Delta t/\lambda_0$=0.0001-0.0005, and were iterated five to fifteen times per time-step, specifically to allow the pressure-correction algorithm a higher degree of convergence and to reduce the explicitness of the method. Simulations were performed on an Intel Xeon E5-2643 CPU running at 3.30GHz. Using a sequential implementation of the numerical method and depending on the time-step and number of iterations per time-step, the CPU computed $5\lambda_0$-$75\lambda_0$ of real time per simulation, per month. Time elapsed between flow start-up and the development of periodic or quasi-periodic flow varies substantially, between $10\lambda_0$-$50\lambda_0$.

7.3 Numerical Results and Discussion

7.3.1 Classification of instability regimes

Based on the qualitative behavior of flow instabilities, the nominal elasticity number El_{nom} is used to divide the parameter space into five flow regimes.

Very low elasticity, El_{nom}={1.6, 2.3}

Figure 7.2 depicts an illustrative example of flow dynamics near the lower end of the elasticity spectrum, at Wi_{nom}=10.4. The stagnation point oscillates periodically along the horizontal centerline, with average position at the geometric center, $(x, y) = (0, 0)$. The amplitude of these fluctuations is small, with peak velocities measured at the center not larger than $u_x/U_0 \approx \pm 0.05$. The values of the normalized first normal stress difference $N_1/(\eta_0 U_0/2H)$ also oscillate in a similar manner, with no loss of birefringence strand integrity. Experimentally, such a strand would appear to brighten and dim periodically, albeit slightly. The periodic character of this flow is further reinforced by the converging phase-plane plot in Figure 7.2.d, suggesting that the flow underwent a supercritical Hopf bifurcation, as reported elsewhere for standard planar cross-slots [13]. Inertia is low yet not negligible, with $2.2<Re_{nom}<6.4$ for all reported time-dependent flows in this regime.

In Figure 7.2, and in the remaining figures, t=0 corresponds to the onset of periodic or quasi-periodic behavior, and not the initial simulation time, which can correspond to either the start-up of flow or the previous result of a simulation at a lower flow rate, used as the initial state of the flow field for the new simulation, in order to shorten start-up times.

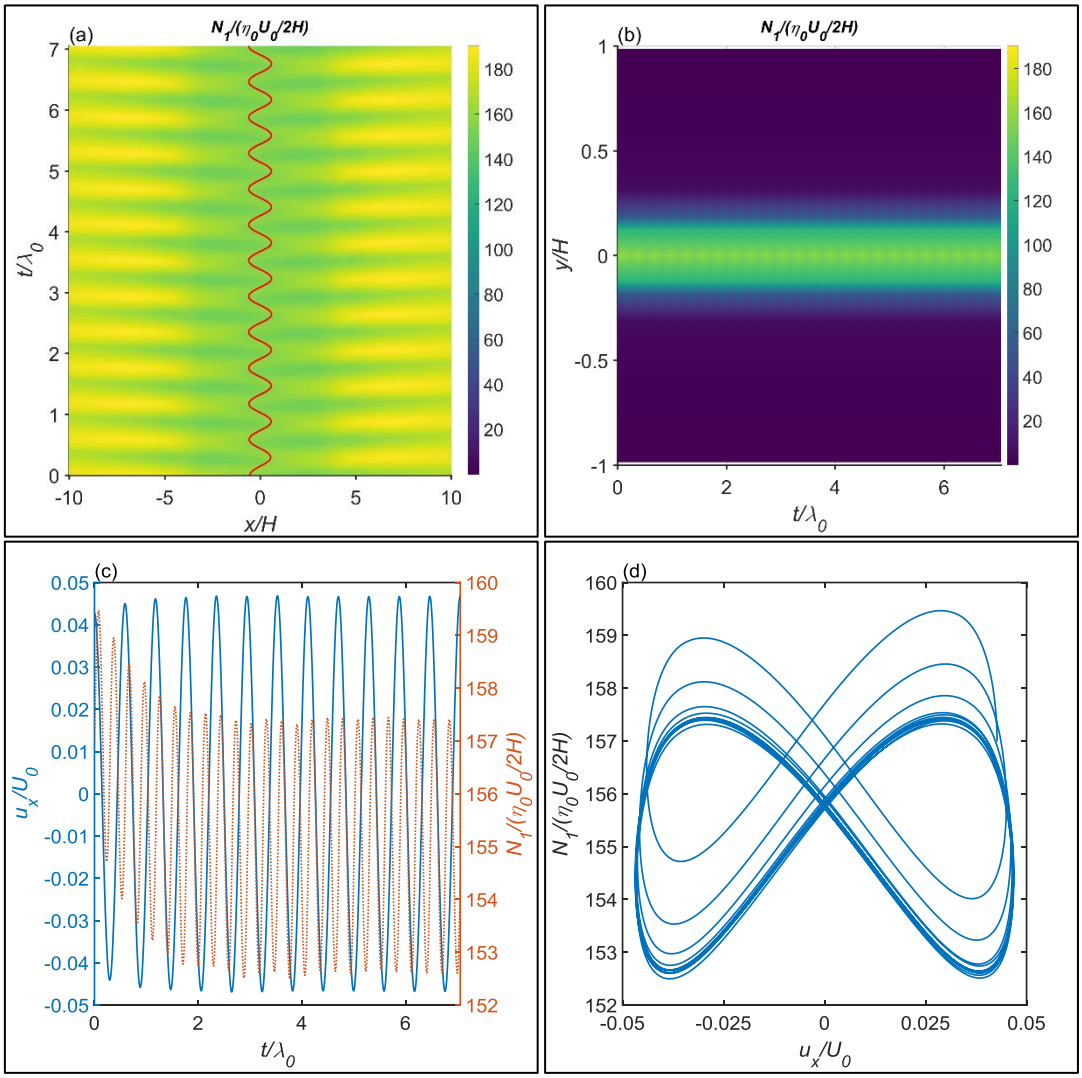

Figure 7.2 – Illustrative results for the **very low elasticity** regime. The example given is the fluid aPS7-350ppm at Wi_{nom}=10.4 and El_{nom}=1.6. The initial, transient segment of the simulation was discarded and time was reset to zero. (a,b) Space-time diagrams of the normalized first normal stress difference, respectively along the horizontal and vertical centerlines, with the evolving position of the stagnation point overlaid on the former. (c) Continuous line: time-series of the first velocity component u_x at the center of OSCER device, normalized by the characteristic velocity U_0; dotted line: time-series of the normalized first normal stress difference sampled at the same location. (d) Phase-plane plot constructed with the time-series shown in the previous panel.

Low elasticity, El_{nom}={3.2, 4.1}

An example of flow behavior in the low elasticity regime is depicted in Figure 7.3 for Wi_{nom}=3.4.

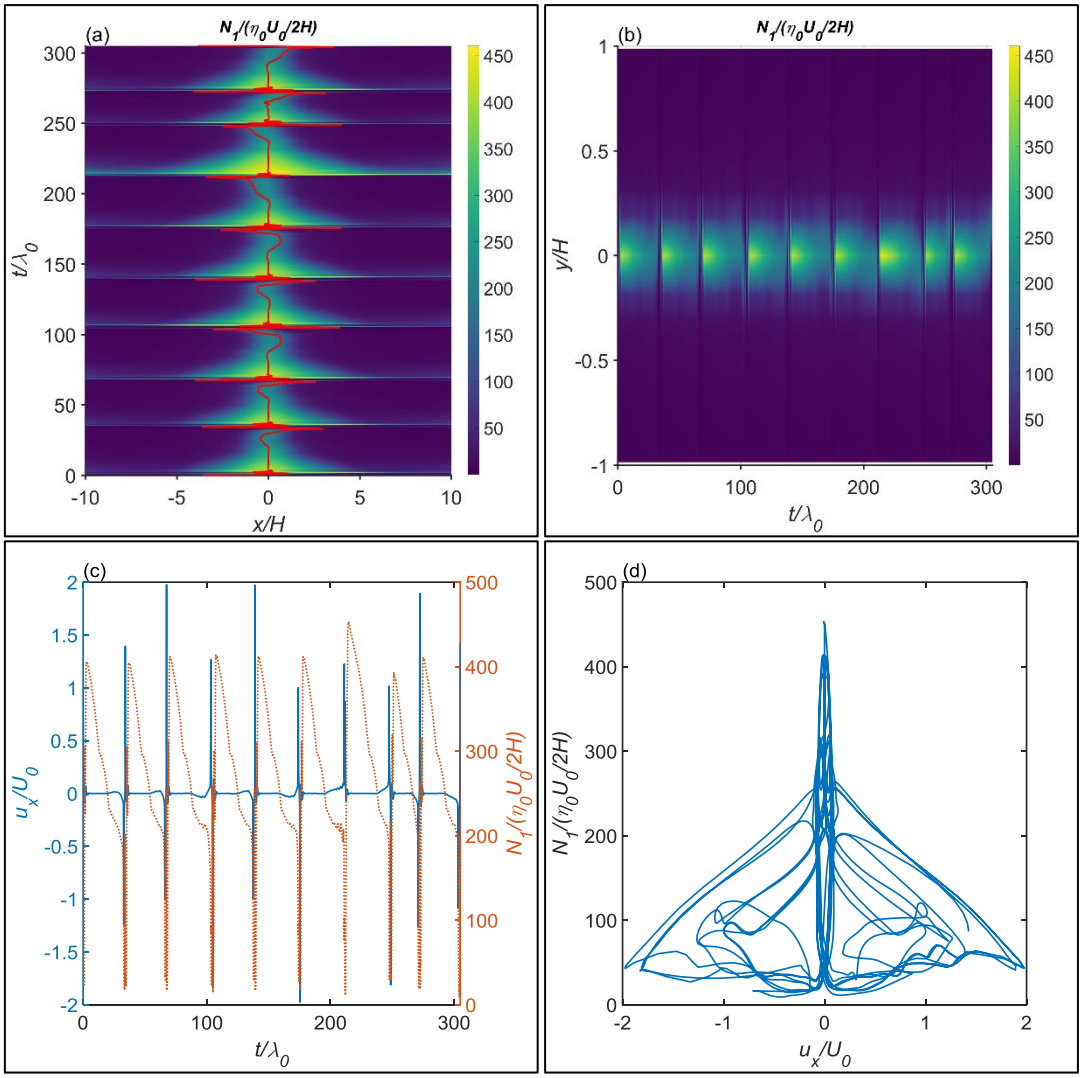

Figure 7.3 – Illustrative results for the **low elasticity** regime. The example given is the fluid aPS7-1400ppm at Wi_{nom}=3.4 and El_{nom}=3.2. The initial, transient segment of the simulation was discarded and time was reset to zero. (a,b) Space-time diagrams of the normalized first normal stress difference, respectively along the horizontal and vertical centerlines, with the evolving position of the stagnation point overlaid on the former. (c) Continuous line: time-series of the first velocity component u_x at the center of OSCER device, normalized by the characteristic velocity U_0; dotted line: time-series of the normalized first normal stress difference sampled at the same location. (d) Phase-plane plot constructed with the time-series shown in the previous panel.

An initially horizontal birefringence strand undergoes a loss of symmetry and begins rotating, either clockwise or anti-clockwise. The flow field becomes progressively more asymmetric as time evolves, until eventually the degree of asymmetry reaches a critical level and the birefringence strand breaks, followed by the downstream advection of what remains of the formerly contiguous strand. The breaking process is accompanied by the brief appearance of a secondary flow near the center of the geometry. The flow field then returns to a symmetric configuration, and a new birefringence strand forms, resetting the cycle. The amplitude of fluctuations is significant, with normalized velocity at the geometric center peaking at $u_x/U_0 \approx \pm 2$ and the normalized first normal stress difference $N_1/(\eta_0 U_0/2H)$ periodically approaching values near zero. The sequence of events culminating in this loss of strand integrity strongly resembles the start-up of stationary asymmetric cross-slot flows, which are thought to be the result of a supercritical pitchfork bifurcation [14]. However, the breaking process suggests the superposition of a different type of instability.

Intermediate elasticity, $\mathrm{El}_{nom}=5.6$

Figure 7.4 illustrates the typical flow behavior in the intermediate elasticity regime for $\mathrm{Wi}_{nom}=7.6$. Oscillations in velocity and normal stresses at the center of the OSCER device are quasi-periodic, albeit with very low amplitude, such that the normalized velocity is mostly contained within the range $u_x/U_0 \approx \pm 0.005$. Therefore the position of the stagnation point is nearly constant and consequently the aforementioned oscillations may be thought of as residual. However, as shown in Figure 7.5.b, the flow assumes a locally asymmetric configuration near the center of the OSCER device. Although small, this asymmetry is distinguishable from a similar snapshot of the flow field for the very low elasticity regime, shown in Figure 7.5.a. Thus the intermediate elasticity regime is characterized by a quasi-stationary, locally asymmetric flow field, which again indicates the presence of a secondary instability interfering with the expected behavior of a pitchfork bifurcation. Figure 7.4.d suggests a converging limit-cycle. Attempts to study higher flow rates, namely $\mathrm{Wi}_{nom}=\{8.2, 8.8, 9.4, 10.0\}$, resulted in the systematic numerical divergence of simulations, both with the method used in this thesis and with an alternative method using, in lieu of the CUBISTA scheme [7], a WENO-M

implementation [15] for the treatment of advective terms in the momentum and constitutive equations.

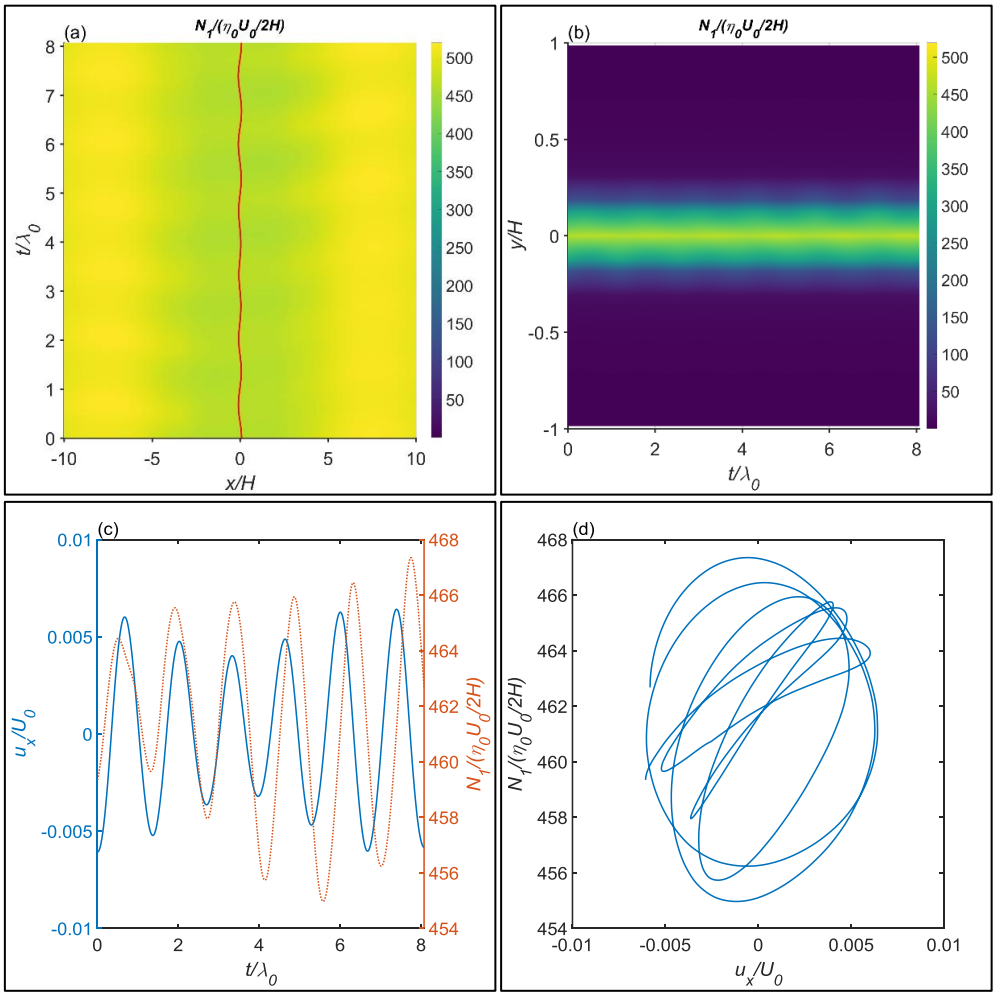

Figure 7.4 – Illustrative results for the **intermediate** elasticity regime. The example given is the fluid aPS10-700ppm at Wi_{nom}=7.6 and El_{nom}=5.6. The initial, transient segment of the simulation was discarded and time was reset to zero. (a,b) Space-time diagrams of the normalized first normal stress difference, respectively along the horizontal and vertical centerlines, with the evolving position of the stagnation point overlaid on the former. (c) Continuous line: time-series of the first velocity component u_x at the center of OSCER device, normalized by the characteristic velocity U_0; dotted line: time-series of the normalized first normal stress difference sampled at the same location. (d) Phase-plane plot constructed with the time-series shown in the previous panel.

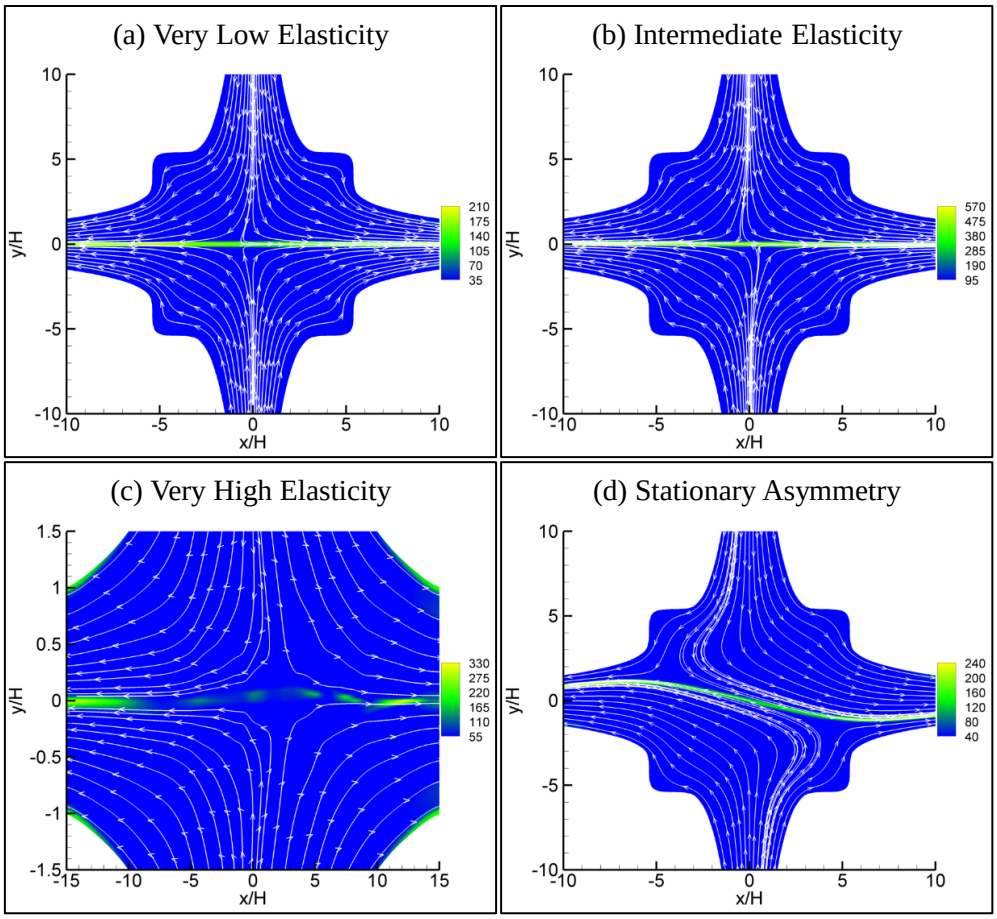

Figure 7.5 – Depictions of the flow field at specific points in time, represented as contour plots of the normalized first normal stress difference $N_1^* = N_1/(\eta_0 U_0/2H)$ with superimposed streamlines. (a) Snapshot depicting the flow of aPS7-350ppm, at Wi_{nom}=10.4 and El_{nom}=1.6, taken at t/λ_0≈7.1 of the corresponding time-series in Figure 7.2. (b) Snapshot depicting the flow of aPS10-700ppm, at Wi_{nom}=7.6 and El_{nom}=5.6, taken at t/λ_0≈6.8 of the corresponding time-series in Figure 7.4. (c) Snapshot depicting the flow of aPS16-1400ppm, at Wi_{nom}=2.0 and El_{nom}=32.2, zoomed-in along the *y*-axis direction, taken at t/λ_0≈22.4 of the corresponding time-series in Figure 7.7. (d) Stationary asymmetric flow field, aPS16-350ppm, Wi_{nom}=3.4, El_{nom}=13.7.

High elasticity, El_{nom}=8.1

The characteristic behavior in the high elasticity regime is illustrated in Figure 7.6 for Wi_{nom}=3.6. The periodic oscillations in this regime appear to be a combination of dynamics from the very low elasticity and low elasticity regimes. The time-series of normalized velocity is a periodic wave, punctuated by narrow peaks at its maxima and minima, which indicate the breaking of the birefringence strand. However, whereas in previous examples the position of the stagnation point remained near or at the center of

the geometry, except during loss of strand integrity, in this regime the horizontal location of the stagnation point oscillates significantly, in the range $x/H=\pm5$. Qualitatively, the motion of the birefringence strand is perhaps best described as analogous to the propagation of a wave in a finite elastic string, or rather a finite elastic sheet since the simulated geometry is equivalent to a deep channel, with the important distinction that the strand periodically breaks and reforms whenever the wave would be reflected by the fixed ends of the sheet. This string/sheet analogy has been previously used to describe the experimental behavior of birefringence strands in the OSCER device [16], albeit referring to the flow of a shear-thinning, 3000ppm poly(ethylene oxide) solution in water, with rheological properties which are significantly different from those typical of the high elasticity regime, namely $L^2=3360$, $\beta=0.26$, $\lambda_0=0.004$s, $\eta_0=0.0038$Pa.s, tested at a flow rate corresponding to Re=64.4, whereas the example in Figure 7.6 was simulated at $\mathrm{Re}_{nom}=0.45$.

Very high elasticity, $\mathrm{El}_{nom}=\{13.7, 18.8, 32.2\}$

Figure 7.7 illustrates the typical behavior near the higher end of the elasticity spectrum assessed in this chapter, at $\mathrm{Wi}_{nom}=2.0$. The flow may still be described as periodic, albeit with significant contamination by aperiodic modes of oscillation. At regular intervals, jets of fluid pierce the birefringence strand. Consequently, as seen in Figure 7.5.c, the strand is fragmented into segments, which upon downstream advection generate an apparent rippling pattern in Figure 7.7.a. While the instabilities in lower elasticity regimes are to some extent similar to previous observations in planar cross-slot flows, either individually or as a superposition of known phenomena, the very high elasticity regime is to the best of our knowledge a new observation. Although Haward *et al*. [4] studied the experimental counterpart of the simulation depicted in Figure 7.7, they were unable to describe the instantaneous dynamics of flow in detail. Considering the time-step of simulations, $\Delta t/\lambda_0=0.0001$, it is estimated that a data acquisition rate in the range of 10-100 kHz may be required for the detailed experimental characterization of a fluid with the same properties as aPS16-1400ppm, specifically the relaxation time.

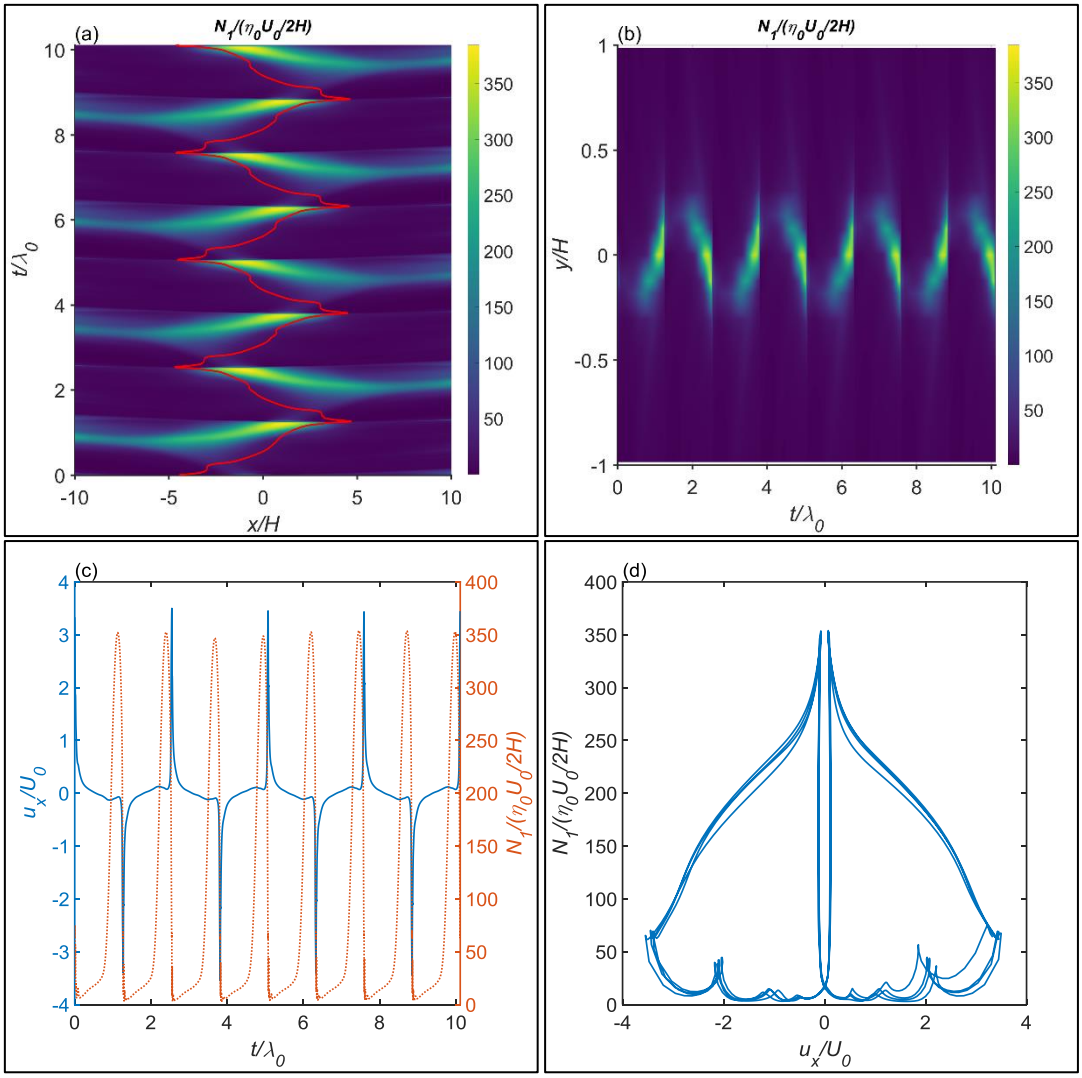

Figure 7.6 – Illustrative results for the **high elasticity** regime. The example given is the fluid aPS10-1400ppm at Wi_{nom}=3.6 and El_{nom}=8.1. The initial, transient segment of the simulation was discarded and time was reset to zero. (a,b) Space-time diagrams of the normalized first normal stress difference, respectively along the horizontal and vertical centerlines, with the evolving position of the stagnation point overlaid on the former. (c) Continuous line: time-series of the first velocity component u_x at the center of OSCER device, normalized by the characteristic velocity U_0; dotted line: time-series of the normalized first normal stress difference sampled at the same location. (d) Phase-plane plot constructed with the time-series shown in the previous panel.

Stationary asymmetric flow

In addition to the various time-dependent instabilities, a few stationary asymmetric flows were also observed, of which the most prominent example is shown in Figure 7.5.d. This was unexpected, since all model fluids have a high solvent viscosity ratio, β>0.5, and as shown elsewhere [17] for various solutions of poly(acrylamide) in

glycerol/water, fluids with β>0.05 undergo a direct transition to unsteady flow without an intermediary steady asymmetric state. Since the dynamics of cross-slot flows are the result of the relative contributions of extension and shear effects, a geometry such as the OSCER device, optimized to maximize the former, is able to generate the strong compressive/extensional normal stresses which are thought to be the cause of the stationary asymmetric instability in planar cross-slots [18], despite the dilute character of the fluids modelled in this investigation.

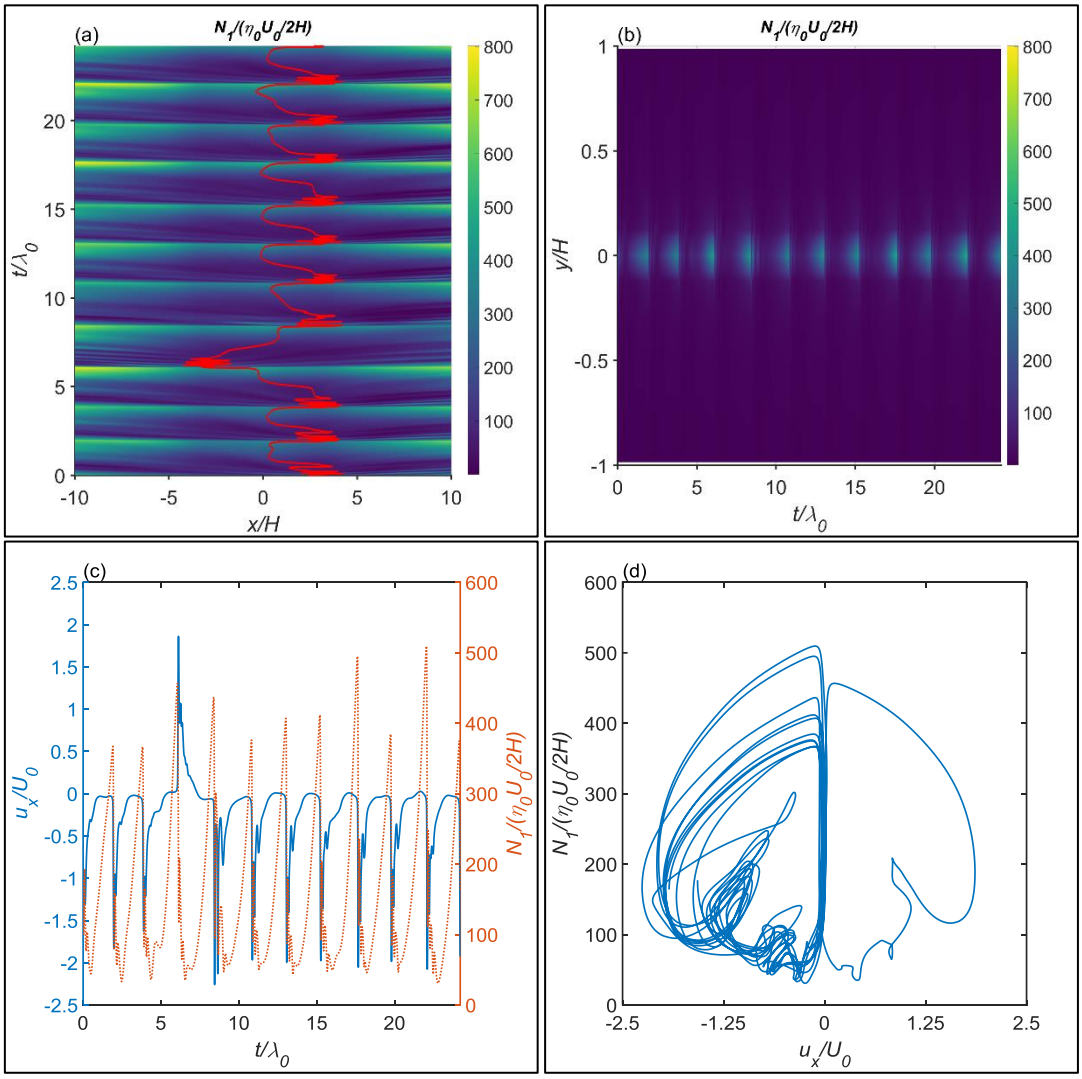

Figure 7.7 – Illustrative results for the **very high elasticity** regime. The example given is the fluid aPS16-1400ppm at Wi_{nom}=2.0 and El_{nom}=32.2. The initial, transient segment of the simulation was discarded and time was reset to zero. (a,b) Space-time diagrams of the normalized first normal stress difference, respectively along the horizontal and vertical centerlines, with the evolving position of the stagnation point overlaid on the former. (c) Continuous line: time-series of the first velocity component u_x at the center of OSCER device, normalized by the characteristic velocity U_0; dotted line: time-series of the normalized first normal stress difference sampled at the same location. (d) Phase-plane plot constructed with the time-series shown in the previous panel.

A stability map including all the fluids and flow rates discussed in this work is shown in Figure 7.8. As discussed by Haward *et al*. [4],[16], the nominal elasticity number represents the trajectory through the Wi–Re parameter space for a given fluid. Since the solvent viscosity contributes to the shear stress but not the elastic stresses, the Weissenberg number is more accurately estimated as $(1-\beta)\mathrm{Wi}_{nom}$, where $(1-\beta)$ is the polymer viscosity ratio, highlighting an underlying pattern to the various time-dependent instability transitions, all of which occur in the range $0.33<(1-\beta)\mathrm{Wi}_{nom}<1.06$, which is substantially narrower than the corresponding Wi_{nom} range, $1.2<\mathrm{Wi}_{nom}<6.4$.

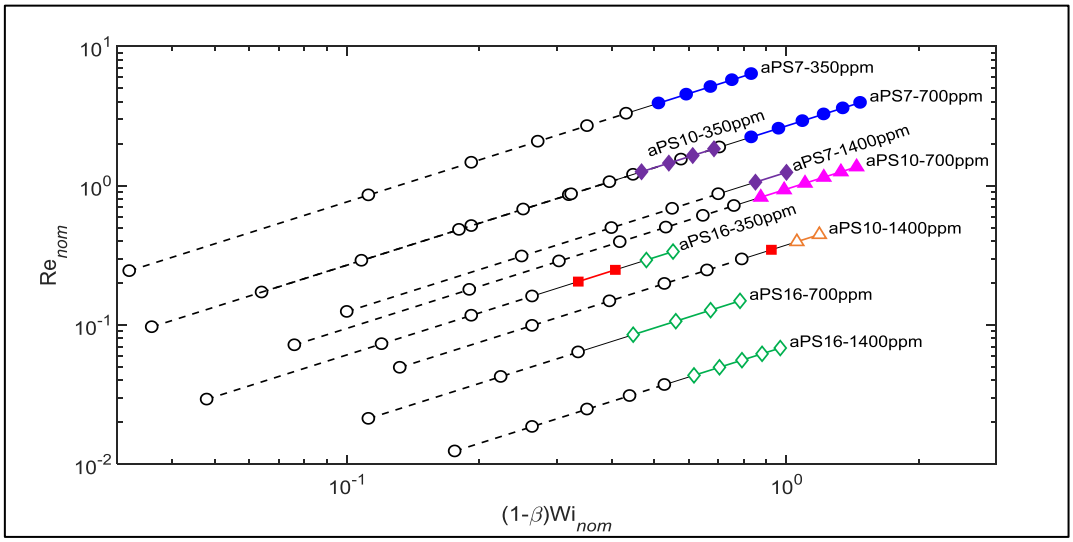

Figure 7.8 – Stability diagram showing the evolution of each fluid in the Wi–Re parameter space. Empty circles represent stationary symmetric flow, whereas filled squares indicate a stationary asymmetric flow field configuration. Each of the five time-dependent regimes identified in this work is represented as follows: filled circles – **very low elasticity** regime; filled diamonds – **low elasticity** regime; filled triangles – **intermediate elasticity** regime; empty triangles – **high elasticity** regime; empty diamonds – **very high elasticity** regime.

7.3.2 Distribution of normal stress at the center

Figure 7.9 shows the probability distribution of the normalized first normal stress difference, $N_1^* = N_1/(\eta_0 U_0/2H)$, at the center of the OSCER device, constructed from data cropped to an integer number of periods, for the flows used to describe the various elasticity regimes in the previous section. Each of these flows is compared to a steady state case obtained at a lower flow rate. The evolution of the distribution of N_1^* with Wi_{nom} provides information concerning the overall state of the flow field. For instance,

low amplitude instabilities, such as those seen for the very low elasticity regime, lead to a narrow distribution of N_1^*, depicted in Figure 7.9.a. Furthermore, whenever the birefringence strand assumes an asymmetric configuration, the values of N_1^* decrease concomitantly. For instance, as shown in Figure 7.5.d, the fluid aPS16-350ppm develops a stationary asymmetry at Wi_{nom}=3.4, leading to a threefold decrease in the N_1^* values due to this asymmetry, as shown in Figure 7.9.f.

Another important observation concerns the relation between N_1^* and time-dependent instabilities. At the onset of time-dependent flow, the average of the newly formed distribution of N_1^* tends to be smaller than the value of N_1^* for the formerly stationary flow, and the extent of this reduction varies considerably. For instance, in Figure 7.9.d there is an eightfold decrease in the average N_1^* at the onset of time-dependent instabilities. On the other hand, for example in Figure 7.9.e, the onset of time-dependent flow is accompanied by a twofold decrease in the average value of N_1^*. Individually, both the degree of asymmetry and the amplitude of time-dependent fluctuations contribute to the decrease in the average of N_1^*. However, the superimposed effect of both types of instabilities is not trivial, and the interpretation of N_1^* distributions may require complementary information. Supplementary information is provided at the end of this chapter, in the form of space-time diagrams of N_1^* along the horizontal centerline of the OSCER geometry. Some of the weakly time-dependent flows may appear stationary upon inspection of these space-time plots, owing to the very low amplitude of the N_1^* fluctuations.

Concerning the very low elasticity regime, depicted in Figure 7.9.a, besides the aforementioned narrow distribution of N_1^*, there is a slight decrease in the time averaged value of N_1^* at the onset of time-dependent flow. The intermediate elasticity regime is depicted in Figure 7.9.c. This regime is grouped with the very low elasticity flows due to various similarities, namely the persistent integrity of the birefringence strand, which correlates with the low amplitude of velocity fluctuations. However, these velocity fluctuations are one order of magnitude lower than in the flows underlying Figure 7.9.a, therefore the decrease of the modal N_1^* bin in Figure 7.9.c is an indicator of increased asymmetry, which nevertheless remains mild, as shown in Figure 7.5.b.

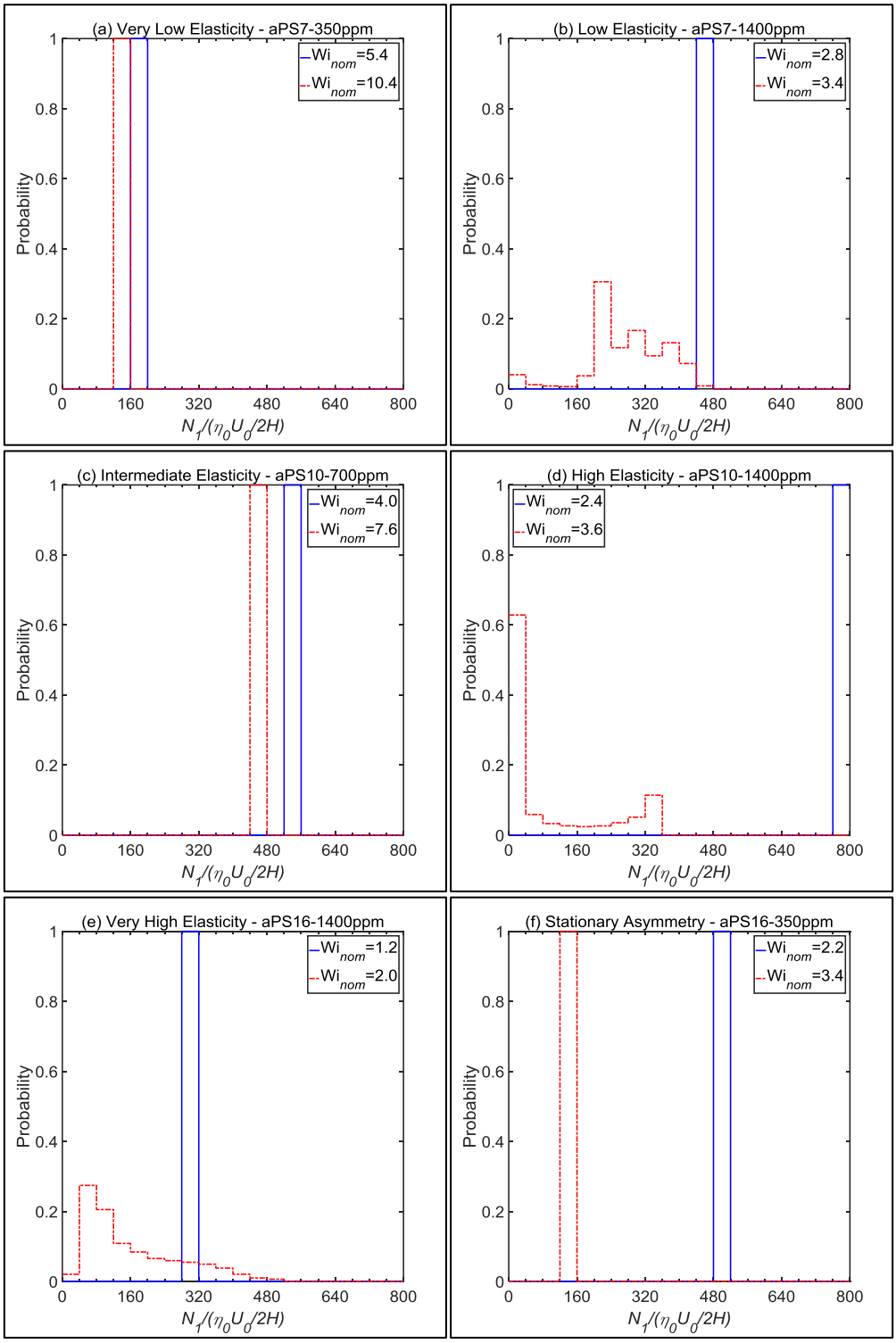

Figure 7.9 – Histograms showing the probability distribution of the normalized first normal stress difference, $N_1^* = N_1/(\eta_0 U_0/2H)$, at the center of the OSCER device. For each regime, represented by one of the fluids, results are shown for the highest stable flow rate (blue) and a relevant unstable flow (red). Data is organized into twenty equally spaced bins of N_1^* between 0 and 800.

The low elasticity regime is depicted in Figure 7.9.b. Two primary local maxima are identifiable, the N_1^* bins [0, 40] and [200, 240], separated by a valley of low probability. The latter bin is part of a larger cluster which itself has two additional secondary maxima, [280, 320] and [360, 400]. These four N_1^* bins correlate to different stages in the formation, rotation and breakup of the birefringence strand. The [360, 400] bin is the most probable range for N_1^* when the strand reforms after a breaking event, and as may be inferred from Figure 7.3.a, there is a slight delay before the strand starts rotating. The [280, 320] N_1^* bin corresponds to a momentary arrest in the rotation of the strand, also visible in Figure 7.3.a when the width of the brighter, central region starts decreasing at a lower rate. The [200, 240] bin is the most probable range for N_1^* when the strand reaches maximum tilt, and finally the [0, 40] bin corresponds to the temporary absence of the strand immediately following a breaking event. The cycle deducible from the N_1^* distribution, namely the absence, *de novo* formation, rotation and maximum tilt preceding the momentary loss of the birefringence strand, illustrates the superposition of a limit-cycle with an asymmetry.

The high elasticity regime is depicted in Figure 7.9.d. This regime is notable since, in addition to the rotation of the birefringence strand, the position of the stagnation point also changes substantially in a continuous fashion, as shown in Figure 7.6.a. Therefore, most of the time, the tilted strand does not intersect the center of the OSCER device, leading to a distribution of N_1^* that is dominated by a probability maximum in the range [0, 40] and a second, significantly less probable local maximum in the bin [320, 360], corresponding to the translation of the strand across the geometric center. The intermediate and high elasticity regimes exemplify how the superposition of two modes of instability can lead to different results depending on the corresponding amplitudes. Consulting Table 7.1, the high amplitude limit-cycle underlying Figure 7.9.d emerges with only small changes in the relaxation time and solvent viscosity ratio relative to Figure 7.9.c. The high elasticity regime is also, by a wide margin, the regime wherein the accumulation of N_1^* is largest during stationary symmetric flow, followed by the intermediate regime, occupied by the single fluid aPS10-700ppm, and closely by the fluid aPS16-350ppm, shown in Figure 7.9.f. Not coincidentally, these two fluids border the high elasticity regime in the El_{nom} parameter space. The emergence of the birefringence

strand fragmentation mechanism in the very high elasticity regime precludes the rotation of the strand, characteristic of various other preceding regimes, further illustrating the competition between different types of instability seen throughout this chapter.

The very high elasticity regime is depicted in Figure 7.9.e. The N_1^* histogram resembles the characteristic shape of a Poisson distribution, with a maximum in the bin [40, 80], followed by a series of trailing bins with progressively lower probability. After the fragmentation of the birefringence strand, the accumulation of normal stresses in the newly formed strand proceeds at an accelerating pace, as may be inferred from Figure 7.7.c, leading to a decrease of the probability of the various progressively higher N_1^* bins. Furthermore, the N_1^* bin [0, 40] has lower probability than the [40, 80], suggesting that the strand does not completely disintegrate.

7.3.3 Spectral analysis of velocity fluctuations

Power density spectra of the normalized first component of the velocity vector, u_x/U_0, sampled at coordinates $(x, y) = (H, 0)$, are depicted in Figures 7.10–7.14. Sampling at these coordinates instead of at the centre, $(x, y) = (0, 0)$, has the advantage of facilitating comparisons with experiments, since it is at the center of cross-slots that the noise-to-signal ratio in experimental measurements of the velocity is highest. The mean of each time-series was subtracted from the signal prior to transformation, and no windowing of the signal was used other than cropping the sample to an integer number of periods, since most time-series have a discernible dominant frequency. Frequency f was multiplied by the zero shear-rate relaxation time λ_0 and accordingly the dimensionless sampling frequency $\lambda_0 f_s$ was used in the presentation of power density plots. In order to assess the possibility of aliasing caused by the finite cell size of computational meshes, we estimated the residence time in the sampled cell as $t_{res} = \Delta x_{cell} / u_{x,rms}$. The characteristic local velocity is calculated as the root mean square of u_x instead of the arithmetic mean because u_x may often change sign, leading to unreasonably high values of t_{res}. From the Sampling Theorem, a discrete sequence of samples can perfectly reconstruct a continuous signal if the sampling frequency is at least twice the highest frequency component of the signal. In other words, the cutoff frequency f_c above which frequencies are poorly resolved due

to the finite cell size of the mesh is estimated as $2f_c \approx 1/t_{res}$, and is shown in dimensionless form in Table 7.2 for relevant flows. The estimated frequency cutoff, $\lambda_0 f_c$, was borne in mind in the evaluation of the spectral decay of velocity fluctuations, as an upper limit on the fitted data range.

Table 7.2 – Summary of findings concerning the power spectra of velocity fluctuations in the OSCER device, for the first normalized velocity component u_x/U_0 sampled at coordinates $(x,y)=(H,0)$. The power-law decay α was estimated via a linear fit, $\log_{10}(\mathrm{PSD}) = \alpha \log_{10}(\lambda_0 f) + c$, of the spectral data within the range $\left[\lambda_0 f_{low}, \lambda_0 f_{high}\right]$, and $\pm\varepsilon_\alpha$ is the corresponding 95% confidence interval, rounded up to the nearest decimal place. $\lambda_0 f_c$ is the estimated cutoff above which frequency components of the signal cannot be accurately resolved due to the finite cell size of computational meshes. The values of $\alpha \pm \varepsilon_\alpha$ are accurate for the specific fit range and method, however some uncertainty exists concerning the exact boundaries of the decay range.

Regime	**Fluid**	**Wi$_{nom}$**	**α**	**$\pm\varepsilon_\alpha$**	**$\lambda_0 f_{low}$**	**$\lambda_0 f_{high}$**	**$\lambda_0 f_c$**
Low elasticity	aPS7 -1400ppm	3.4	-4.7	0.1	10	40	40
		4.0	-5.2	0.1	20	70	70
High elasticity	aPS10 -1400ppm	3.2	-4.2	0.2	10	70	140
		3.6	-4.3	0.2	10	80	160
Very high elasticity	aPS16 -350ppm	4.0	-6.9	0.2	20	85	170
		4.6	-5.7	0.2	20	85	170
	aPS16 -700ppm	1.6	-4.7	0.3	5	25	50
		2.0	-4.7	0.3	5	35	70
		2.4	-5.2	0.1	10	90	90
		2.8	-6.7	0.1	10	110	110
	aPS16 -1400ppm	1.4	-6.8	0.2	5	50	50
		1.6	-6.7	0.2	5	50	50
		1.8	-5.8	0.3	10	60	60
		2.0	-6.1	0.3	10	40	80
		2.2	-6.1	0.2	20	90	90

The very low elasticity regime, depicted in Figure 7.10, is characterized by a principal frequency component, which is often the fundamental unit of a harmonic series and, specifically in Figure 7.10.b, may be contaminated by a variable amount of weakly non-periodic fluctuations. These fluctuations appear to increase in relative magnitude with the flow rate, up to a certain limit, above which a regularization of the flow occurs. This regularization is most visible in Figure 7.10.a when the flow rate increases from Wi$_{nom}$=8.4 to Wi$_{nom}$=9.4 and in Figure 7.10.b a similar transition is seen between Wi$_{nom}$=7.6 and Wi$_{nom}$=8.4.

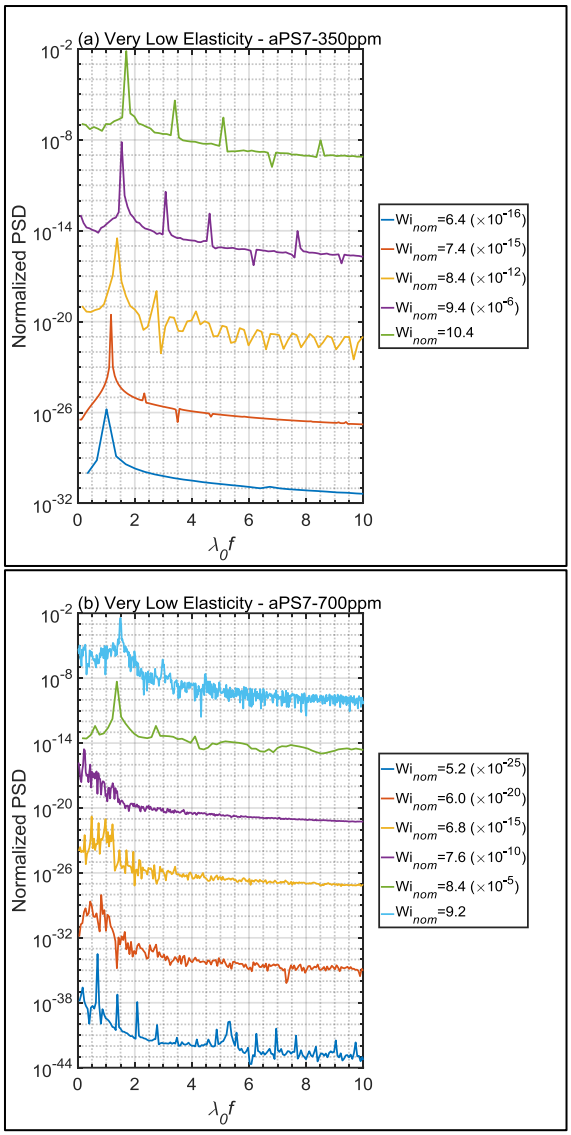

Figure 7.10 – Power spectra obtained from time-series of the normalized first velocity component u_x/U_0 sampled at coordinates $(x,y)=(H,0)$, for the **very low elasticity** regime. The degree of vertical shifting of the normalized PSD is indicated in the legend of each panel. The frequency axis is linear and the power density axis is logarithmic.

A similar regularization is also seen for the intermediate elasticity regime, depicted in Figure 7.11, when the flow rate increases from Wi_{nom}=5.8 to Wi_{nom}=6.4, although the latter spectra are primarily composed of broadband peaks instead of a well-defined harmonic series. The two regimes share other features, such as the trivial decay of the power spectra and more broadly the low amplitude of velocity oscillations and the persistent integrity of the birefringence strand. Qualitatively, emerging aperiodic components of motion appear to be suppressed by their periodic counterparts, thus the very low and intermediate regimes do not display the sudden instabilities seen in other regions of the inertia-elasticity-viscosity parameter space.

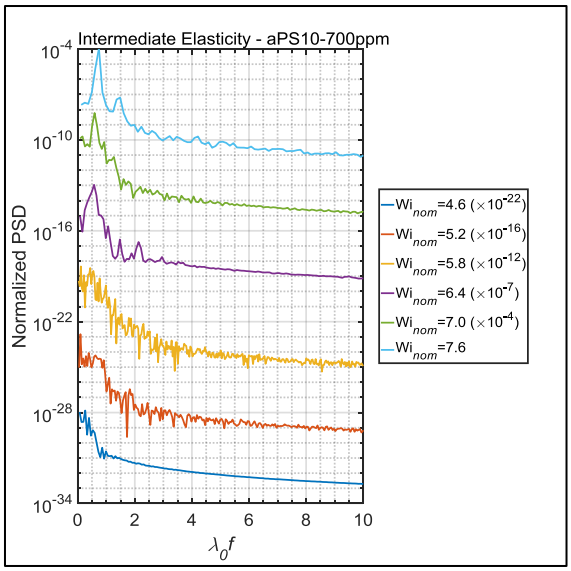

Figure 7.11 – Power spectra obtained from time-series of the normalized first velocity component u_x/U_0 sampled at coordinates $(x,y)=(H,0)$, for the **intermediate elasticity** regime. The degree of vertical shifting of the normalized PSD is indicated in the legend. The frequency axis is linear and the power density axis is logarithmic.

The low elasticity regime is depicted in Figure 7.12. The overall periodicity of the flow is visible in the initial portion of the spectra, such as the peak at $\mathrm{Wi}_{nom}=3.4$. However, the relative power density of the aperiodic modes of oscillation is now much larger and the power law decay range has an exponent, α, estimated as the slope in log-log coordinates, of approximately $\alpha \approx -4.9$, on average.

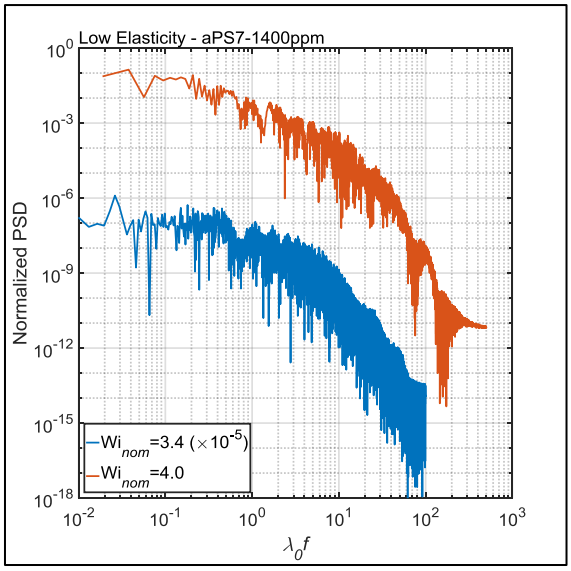

Figure 7.12 – Power spectra obtained from time-series of the normalized first velocity component u_x/U_0 sampled at coordinates $(x,y)=(H,0)$, for the **low elasticity** regime. The degree of vertical shifting of the normalized PSD is indicated in the legend. Both the frequency and power density axes are logarithmic.

The fluid aPS10-350ppm is the only instance in this work where the length of the time domain signal was deemed insufficient for the calculation of power spectra, essentially due to the inconsistent amplitude and, to a lesser extent, periodicity of u_x. Nevertheless, the inconsistent amplitude of the cycles underlying the aPS10-350ppm flows effectively serves as a secondary indicator of greater instability.

The high elasticity regime is depicted in Figure 7.13. The low frequency range is dominated by a harmonic series comprised of the odd multiples of the fundamental frequency. This frequency composition is characteristic of certain regular waveforms, such as the square wave or triangle wave, and indeed the limit-cycle in Figure 7.6.d confirms the well-defined periodicity of this regime. The decay range has a power law exponent of about $\alpha \approx -4.3$. In the very high elasticity regime, depicted in Figure 7.14, as the flow rate increases, the formerly predominantly harmonic spectra become increasingly irregular in the low frequency range, without significant changes in the power law decay rate, $\alpha \approx -5.9$. Note that there are no harmonic series in Figure 7.14.a possibly because we increased the flow rate in steps corresponding to ΔWi_{nom}=0.6 and may have skipped this regime. Concerning the specific spectral decay estimates for each flow, given in Table 7.2, even though the values shown are accurate for the specific fit range and method, some uncertainty exists on the correct boundaries of the decay range.

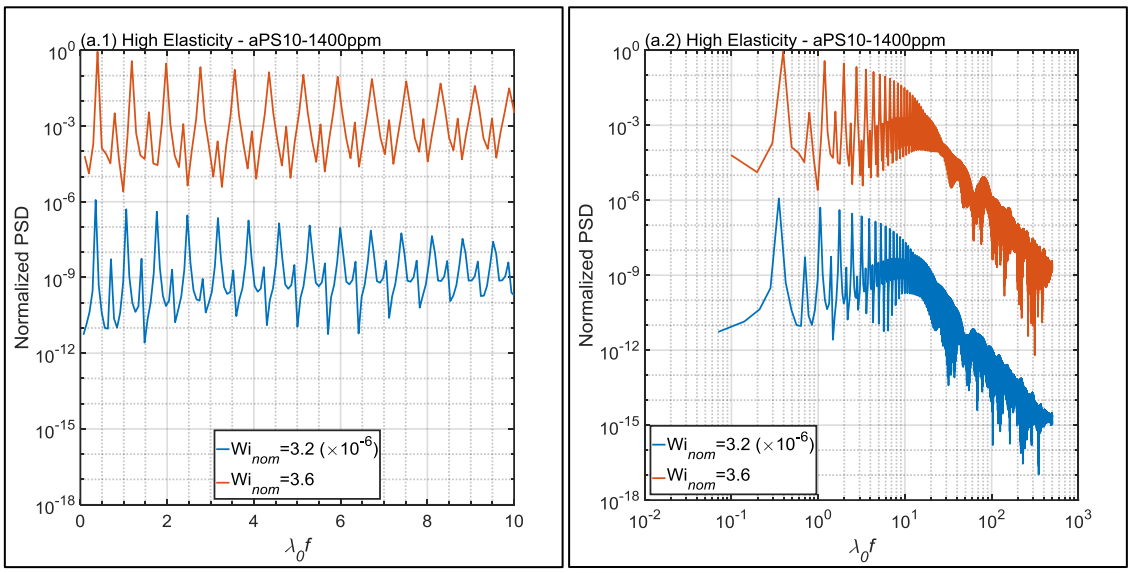

Figure 7.13 – Power spectra obtained from time-series of the normalized first velocity component u_x/U_0 sampled at coordinates $(x,y)=(H,0)$, for the **high elasticity** regime. The degree of vertical shifting of the normalized PSD is indicated in the legend. In panel (a.1) the frequency axis is linear and the power density axis is logarithmic, whereas in panel (a.2) both axes are logarithmic.

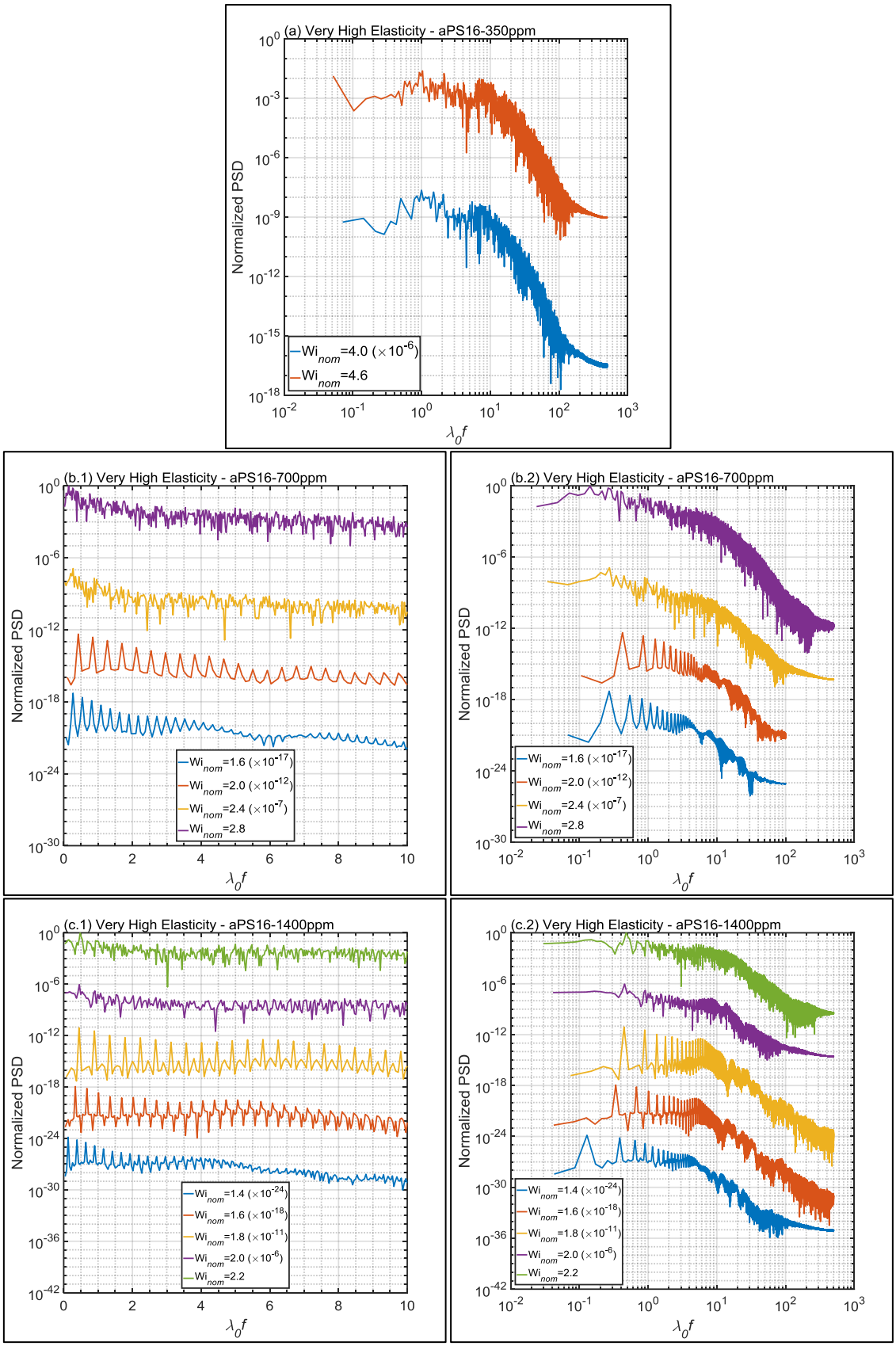

Figure 7.14 – Power spectra obtained from time-series of the normalized first velocity component u_x/U_0 sampled at coordinates $(x,y)=(H,0)$, for the **very high elasticity** regime. The degree of vertical shifting of the normalized PSD is indicated in the legend of each panel. In panels (x.1) the frequency axis is linear and the power density axis is logarithmic, whereas in panels (a) and (x.2) both axes are logarithmic.

For elastic turbulence, the velocity power spectrum decay rate is predicted to be faster than $\alpha = -3$ for unbounded flows [19], and early experimental observations point to a decay rate between $\alpha = -3$ and $\alpha = -3.5$ [20],[21]. Given the lack of a universal definition of turbulence, one of the parameters used to quantify the phenomenon is employed, the turbulence intensity, *T*, calculated along the downstream centerline of the OSCER device, here defined as,

$$T = \frac{\left\langle \left(\|\mathbf{u}\| - \langle \|\mathbf{u}\| \rangle \right)^2 \right\rangle^{1/2}}{U_0}, \tag{7.11}$$

where the operators $\|\cdot\|$ and $\langle \cdot \rangle$ denote, respectively, the magnitude and the average over time. Note that periodic flows may also generate a high value of *T*, therefore a separate method is necessary to evaluate if a given flow qualifies as chaotic. From the preceding spectral analysis, the very low and intermediate elasticity regimes are characterized by regular, low amplitude fluctuations and also lack a broad range of excited frequencies, one of the commonly cited characteristics of turbulence. On the other hand, the high elasticity regime is unequivocally periodic, and in particular is defined by a very well resolved harmonic series. For the low and very high elasticity regimes, only the highest flow rates seem to qualify as chaotic, mildly for the former regime and strongly for the latter. The corresponding turbulence intensity plots are shown in Figure 7.15. As expected, the results for each regime differ, with the low elasticity regime having mild values of *T* near the center of the OSCER device, and the very high elasticity regime exhibiting 2.4 fold higher values of *T* along the same region. However, for all examples, *T* decays to a residual value near the outlet of the geometry, indicating an ephemeral character of the unstable flow near the center, induced by the high normal stresses therein.

An additional observation concerns the relation between the principal frequency component and the characteristic flow rate, depicted in dimensionless form in Figure 7.16. It is unsurprising that fluids with higher elasticity develop instabilities at lower flow rates and consequently with lower thresholds for excitable frequencies, as shown in Figure 7.16.a. The nominal effective relaxation time, $\lambda_{eff,nom}$, is defined as the theoretical effective relaxation time, $\lambda_{eff} = \lambda_0 / g$, with g given by eq. 7.6, calculated at the

characteristic deformation rate $\dot{\varepsilon} = 1.5U_0/(15H)$ of the corresponding simulation. Multiplication of the principal frequency f_{max} by $\lambda_{eff,nom}$ yields a narrow distribution of values, shown in Figure 7.16.b, with $\overline{\lambda_{eff,nom} f_{max}} = 0.075$. This value is a reasonable approximation of the principal frequency component nearly up to the onset of chaotic flow, above which the identification of a characteristic frequency is no longer possible and a power law spectral decay over a wide range of frequencies is observed.

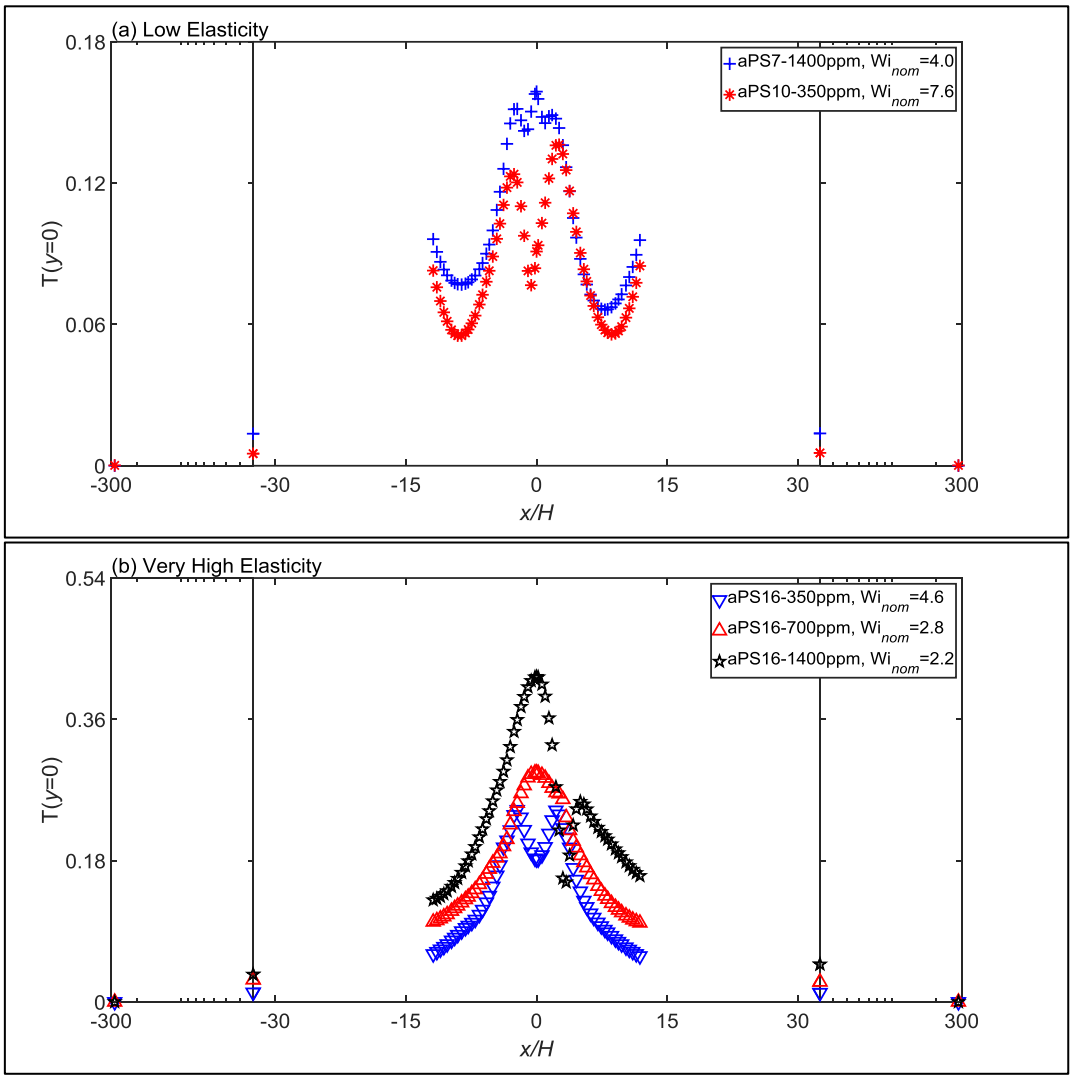

Figure 7.15 – Turbulence intensity along the downstream centerlines of the OSCER device for the highest simulated flow rate for each of the test fluids. (a) **Low elasticity** regime and (b) **very high elasticity** regime. A mixed linear/log scale is used in the *x*/*H* axis.

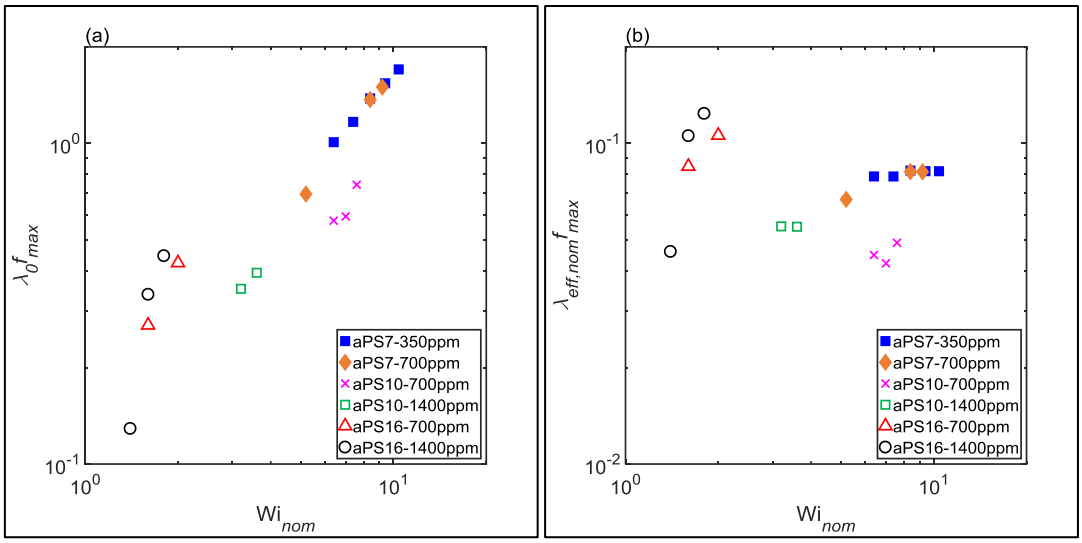

Figure 7.16 – Principal frequency f_{max} (a) multiplied by the zero shear-rate relaxation time λ_0 or (b) multiplied by the nominal effective relaxation time $\lambda_{eff,nom}$, plotted against the dimensionless flow rate expressed as the nominal Weissenberg number Wi_{nom}. $\lambda_{eff,nom}$ is calculated at the center of the OSCER device for a hypothetical stationary symmetric flow with characteristic strain rate $\dot{\varepsilon} = 1.5U_0/(15H)$. Only the flows with a clearly defined maximum power density peak are represented, usually in the form of the principal component of a harmonic series.

7.3.4 Other considerations

Central to the phenomenology described in this chapter is the idea that different types of instability co-exist in a superimposed state. Moreover, the two primary types of bifurcation discussed, Hopf and pitchfork, often compete in order to determine the dynamics of flow. This behavior is characteristic of a codimension-2 bifurcation [22], and is common in many other nonequilibrium systems [23]. In the field of fluid dynamics, two recent studies are of particular interest to this discussion.

Wen *et al.* [24] studied the flow of a shear-thinning, 0.15% (w/w) aqueous solution of xanthan gum in a cylindrical pipe. The authors measured streamwise velocity profiles for Reynolds numbers corresponding to laminar, transition and turbulent flows. In the transition regime a loss of symmetry occurs and the location of peak velocity shifts away from the center of the pipe. Symmetry is then restored in the turbulent regime. This flow rate dependent restoration of symmetry is also seen at least partially in several of the flows discussed throughout this chapter, most notably concerning fluid aPS16-350ppm in the very high elasticity regime. Figure 7.5.d and the accompanying changes in the

distribution of the normalized N_1 values at the center of the OSCER device shown in Figure 7.9.f demonstrate a loss of symmetry. With the onset of time-dependent instabilities characteristic of the very high elasticity regime, the birefringence strand is no longer able to rotate and thus a restoration of symmetry occurs. In Ref. [24], the restoration of symmetry is shown to be a consequence of the onset of turbulence. By analogy, it may be inferred that the restoration of symmetry induced by the onset of time-dependent instabilities for the fluid aPS16-350ppm constitutes indirect evidence of the onset of chaotic-like flow.

Varshney and Steinberg [25] studied the flow of a 100 ppm, 18MDa polyacrylamide aqueous solution in 62% (w/w) sucrose and 1% (w/w) NaCl, past two widely spaced cylindrical obstacles, with normalized spacing E=3.3. The creeping viscoelastic flow generates a sequence of two elastic instabilities, a loss of time-reversal symmetry and at higher flow rates a superimposed loss of mirror symmetry. The authors then speculate on why the second instability was not reported in previous studies, such as in Refs. [26],[27]. Below a critical normalized cylinder spacing E=1.25, only the Hopf bifurcation is present, leading to the conclusion that a codimension-2 point probably occurs in the range $1.25<E<3.3$. Previous experimental [17] and computational [28] work on creeping viscoelastic flows in standard planar cross-slots with variable aspect ratio indicates a reverse sequence of transitions. An initial loss of symmetry is followed by the onset of time-dependent flow at higher flow rates. However, for sufficiently shallow channels, the flow transitions directly to an unsteady state. Based on the results presented in this chapter, it is possible that a collapse of instabilities into a codimension-2 bifurcation also occurs in shallow, standard planar cross-slots.

7.4 References

[1] H.R. Warner, Kinetic Theory and Rheology of Dilute Suspensions of Finitely Extendible Dumbbells, Ind. Eng. Chem. Fundam. 11 (1972) 379–387. doi:10.1021/i160043a017.

[2] M. Chilcott, J. Rallison, Creeping flow of dilute polymer solutions past cylinders and spheres, J. Non-Newt. Fluid Mech. 29 (1988) 381–432. doi:10.1016/0377-0257(88)85062-6.

[3] J.A. Odell, S.P. Carrington, Extensional flow oscillatory rheometry, J. Non-Newt. Fluid Mech. 137 (2006) 110–120. doi:10.1016/j.jnnfm.2006.03.010.

[4] S.J. Haward, G.H. McKinley, A.Q. Shen, Elastic instabilities in planar elongational flow of monodisperse polymer solutions, Sci. Rep. 6 (2016) 33029. doi:10.1038/srep33029.

[5] P.J. Oliveira, F.T. Pinho, G.A. Pinto, Numerical simulation of non-linear elastic flows with a general collocated finite-volume method, J. Non-Newt. Fluid Mech. 79 (1998) 1–43. doi:10.1016/S0377-0257(98)00082-2.

[6] J.P. van Doormaal, G.D. Raithby, Enhancements of the simple method for predicting incompressible fluid flows, Numer. Heat Transf. 7 (1984) 147–163. doi:10.1080/01495728408961817.

[7] M.A. Alves, P.J. Oliveira, F.T. Pinho, A convergent and universally bounded interpolation scheme for the treatment of advection, Int. J. Numer. Meth. Fluids. 41 (2003) 47–75. doi:10.1002/fld.428.

[8] A.M. Afonso, P.J. Oliveira, F.T. Pinho, M.A. Alves, The log-conformation tensor approach in the finite-volume method framework, J. Non-Newt. Fluid Mech. 157 (2009) 55–65. doi:10.1016/j.jnnfm.2008.09.007.

[9] R. Fattal, R. Kupferman, Constitutive laws for the matrix-logarithm of the conformation tensor, J. Non-Newt. Fluid Mech. 123 (2004) 281–285. doi:10.1016/j.jnnfm.2004.08.008.

[10] P.J. Oliveira, Method for time-dependent simulations of viscoelastic flows: vortex shedding behind cylinder, J. Non-Newt. Fluid Mech. 101 (2001) 113–137. doi:10.1016/S0377-0257(01)00146-X.

[11] F. Pimenta, M.A. Alves, Stabilization of an open-source finite-volume solver for viscoelastic fluid flows, J. Non-Newt. Fluid Mech. 239 (2017) 85–104. doi:10.1016/j.jnnfm.2016.12.002.

[12] M.A. Alves, Design of a Cross-Slot Flow Channel for Extensional Viscosity Measurements, in: AIP Conf. Proc., AIP, 2008: pp. 240–242. doi:10.1063/1.2964648.

[13] L. Xi, M.D. Graham, A mechanism for oscillatory instability in viscoelastic cross-slot flow, J. Fluid Mech. 622 (2009) 145. doi:10.1017/S0022112008005119.

[14] F.A. Cruz, R.J. Poole, A.M. Afonso, F.T. Pinho, P.J. Oliveira, M.A. Alves, A new viscoelastic benchmark flow: Stationary bifurcation in a cross-slot, J. Non-Newt. Fluid Mech. 214 (2014) 57–68. doi:10.1016/j.jnnfm.2014.09.015.

[15] A.K. Henrick, T.D. Aslam, J.M. Powers, Mapped weighted essentially non-oscillatory schemes: Achieving optimal order near critical points, J. Comput. Phys. 207 (2005) 542–567. doi:10.1016/j.jcp.2005.01.023.

[16] S.J. Haward, G.H. McKinley, Instabilities in stagnation point flows of polymer solutions, Phys. Fluids. 25 (2013) 083104. doi:10.1063/1.4818151.

[17] P.C. Sousa, F.T. Pinho, M.S.N. Oliveira, M.A. Alves, Purely elastic flow instabilities in microscale cross-slot devices, Soft Matter. 11 (2015) 8856–8862. doi:10.1039/C5SM01298H.

[18] R.J. Poole, M.A. Alves, P.J. Oliveira, Purely Elastic Flow Asymmetries, Phys. Rev. Lett. 99 (2007) 164503. doi:10.1103/PhysRevLett.99.164503.

[19] A. Fouxon, V. Lebedev, Spectra of turbulence in dilute polymer solutions, Phys. Fluids. 15 (2003) 2060–2072. doi:10.1063/1.1577563.

[20] A. Groisman, V. Steinberg, Elastic turbulence in a polymer solution flow, Nature. 405 (2000) 53–55. doi:10.1038/35011019.

[21] A. Groisman, V. Steinberg, Efficient mixing at low Reynolds numbers using polymer additives., Nature. 410 (2001) 905–908. doi:10.1038/35073524.

[22] H.R. Brand, P.C. Hohenberg, V. Steinberg, Codimension-2 bifurcations for convection in binary fluid mixtures, Phys. Rev. A. 30 (1984) 2548–2561. doi:10.1103/PhysRevA.30.2548.

[23] M.C. Cross, P.C. Hohenberg, Pattern formation outside of equilibrium, Rev. Mod. Phys. 65 (1993) 851–1112. doi:10.1103/RevModPhys.65.851.

[24] C. Wen, R.J. Poole, A.P. Willis, D.J.C. Dennis, Experimental evidence of symmetry-breaking supercritical transition in pipe flow of shear-thinning fluids, Phys. Rev. Fluids. 2 (2017) 031901. doi:10.1103/PhysRevFluids.2.031901.

[25] A. Varshney, V. Steinberg, Elastic wake instabilities in a creeping flow between two obstacles, Phys. Rev. Fluids. 2 (2017) 051301. doi:10.1103/PhysRevFluids.2.051301.

[26] K. Arora, R. Sureshkumar, B. Khomami, Experimental investigation of purely elastic instabilities in periodic flows, J. Non-Newt. Fluid Mech. 108 (2002) 209–226. doi:10.1016/S0377-0257(02)00131-3.

[27] M. Grilli, A. Vázquez-Quesada, M. Ellero, Transition to Turbulence and Mixing in a Viscoelastic Fluid Flowing Inside a Channel with a Periodic Array of Cylindrical Obstacles, Phys. Rev. Lett. 110 (2013) 174501. doi:10.1103/PhysRevLett.110.174501.

[28] F.A. Cruz, R.J. Poole, A.M. Afonso, F.T. Pinho, P.J. Oliveira, M.A. Alves, Influence of channel aspect ratio on the onset of purely-elastic flow instabilities in three-dimensional planar cross-slots, J. Non-Newt. Fluid Mech. 227 (2016) 65–79. doi:10.1016/j.jnnfm.2015.11.008.

7.5 Appendix: Space-Time Diagrams of the First Normal Stress Difference

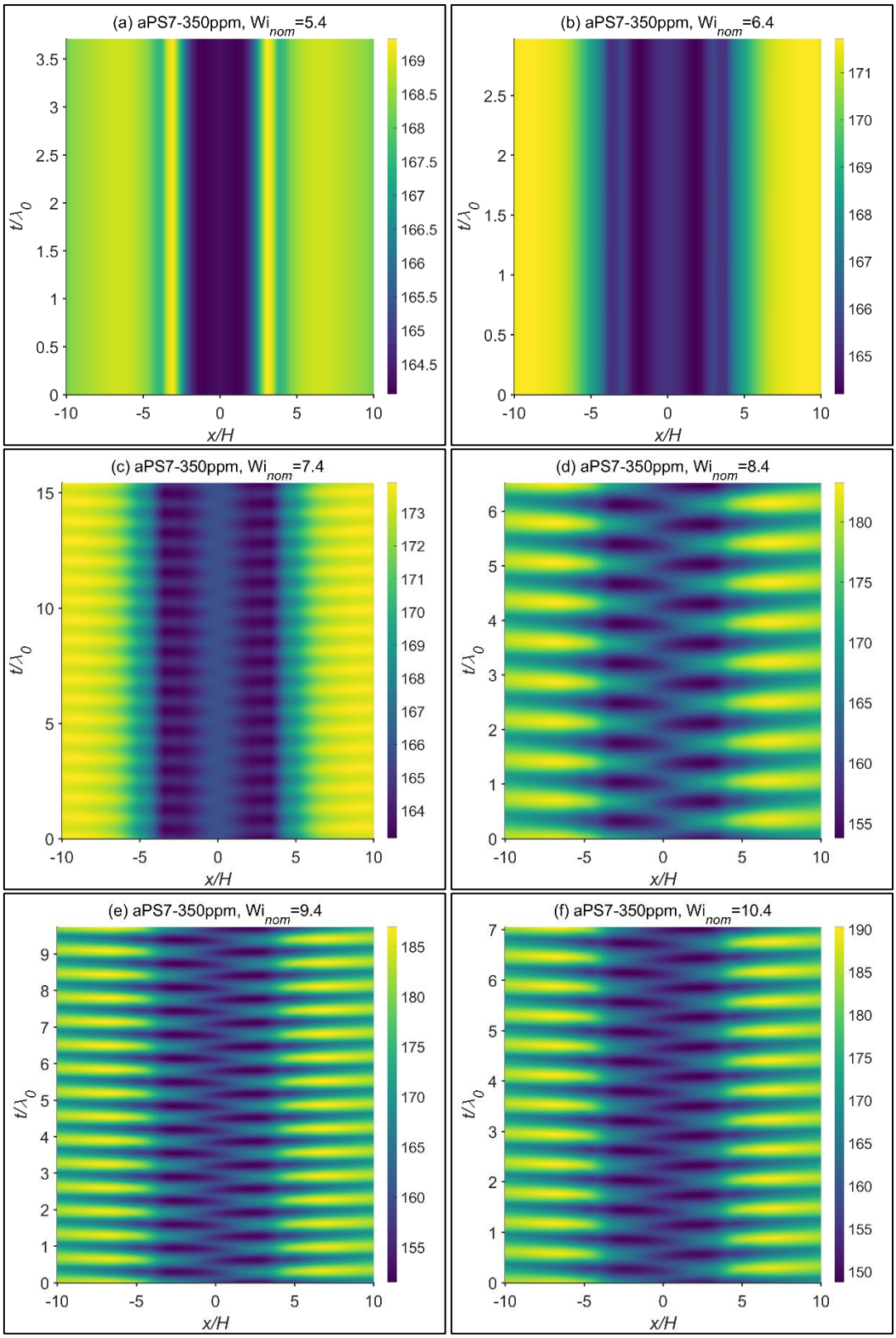

Figure 7.17 – Space-time diagrams of the normalized first normal stress difference $N_1/(\eta_0 U_0/2H)$ along the horizontal centerline of the OSCER device, for the fluid aPS7-350ppm. Behavior is characteristic of the **very low elasticity** regime, at El$_{nom}$=1.6.

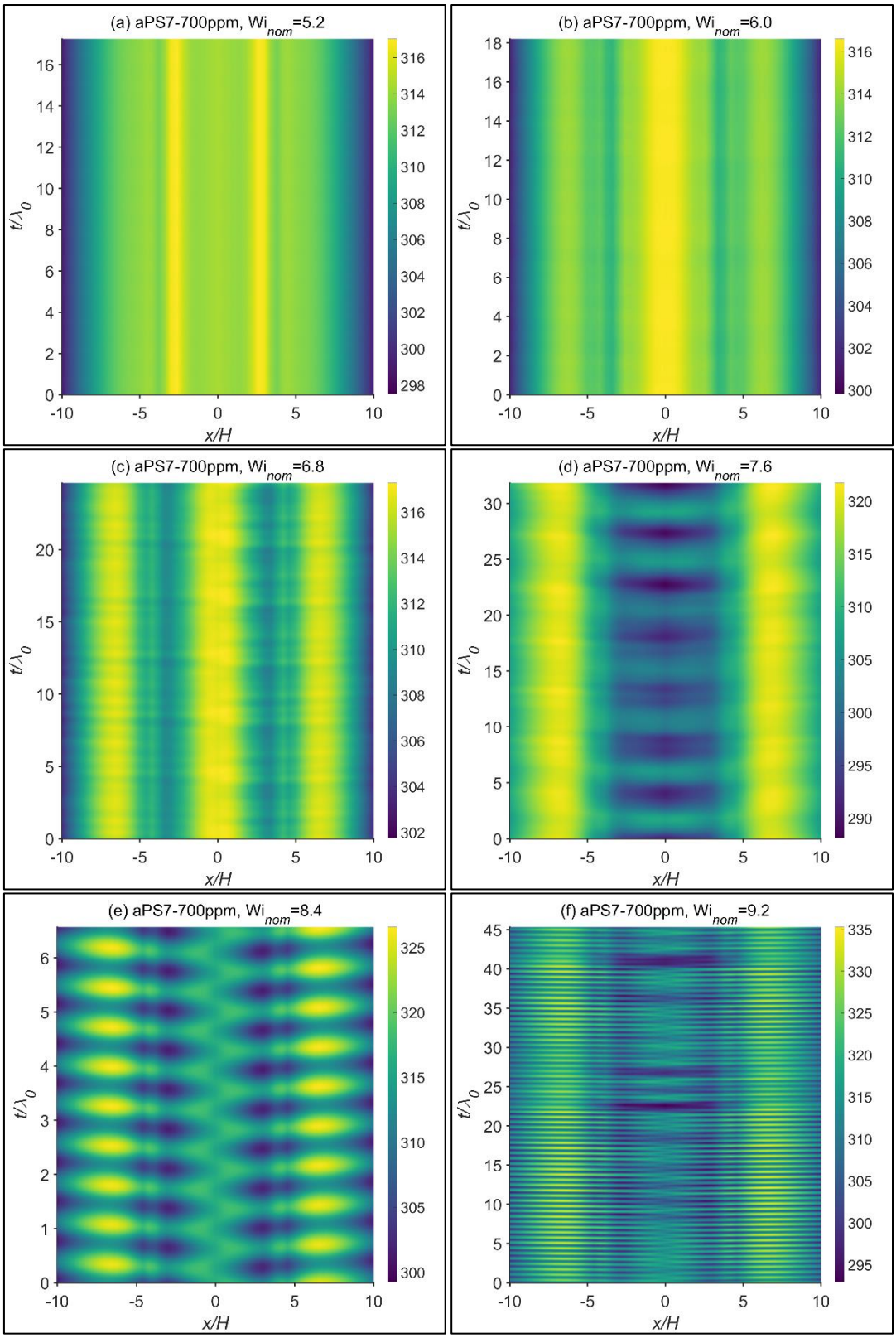

Figure 7.18 – Space-time diagrams of the normalized first normal stress difference $N_1/(\eta_0 U_0/2H)$ along the horizontal centerline of the OSCER device, for the fluid aPS7-700ppm. Behavior is characteristic of the **very low elasticity** regime, at El$_{nom}$=2.3.

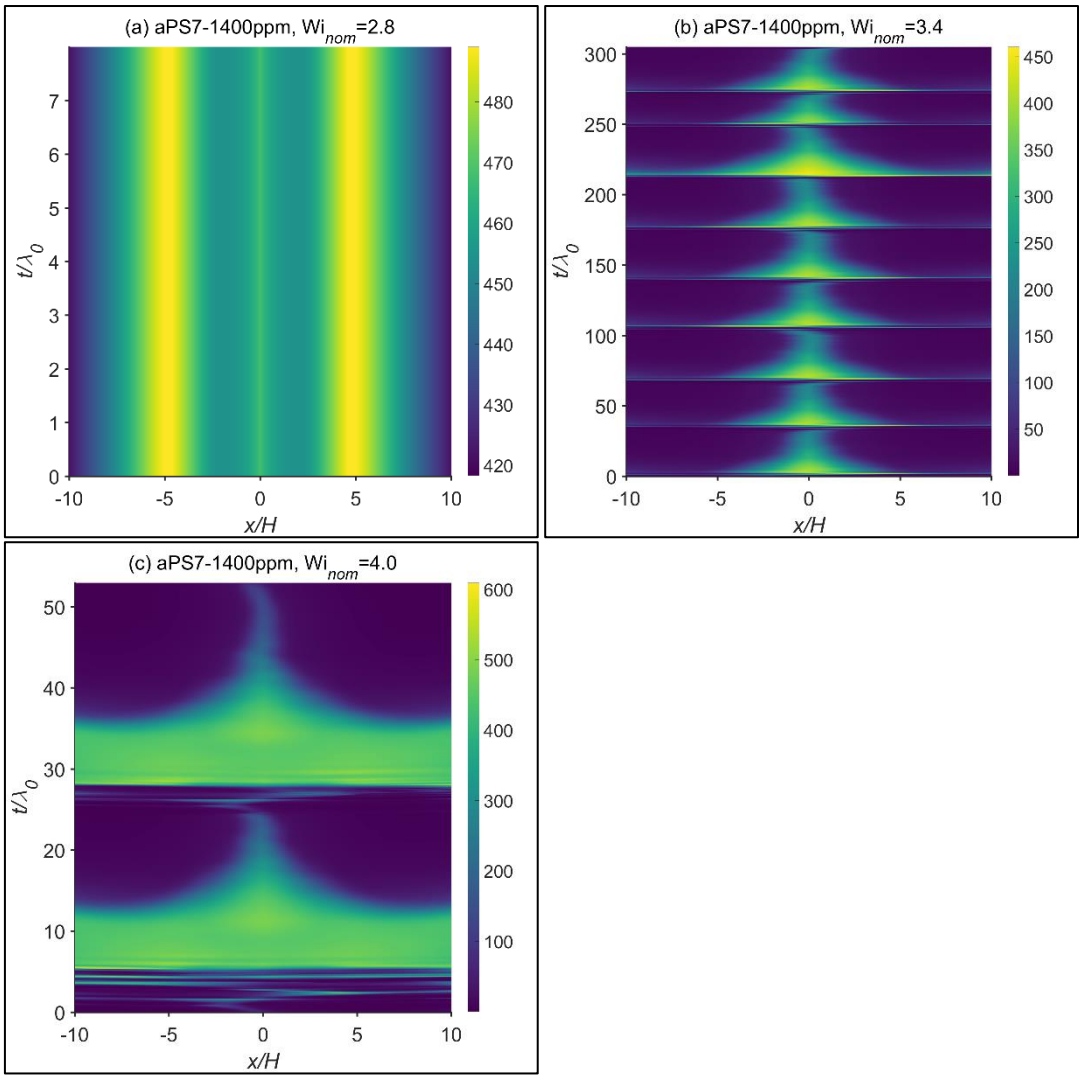

Figure 7.19 – Space-time diagrams of the normalized first normal stress difference $N_1/(\eta_0 U_0/2H)$ along the horizontal centerline of the OSCER device, for the fluid aPS7-1400ppm. Behavior is characteristic of the **low elasticity** regime, at El$_{nom}$=3.2.

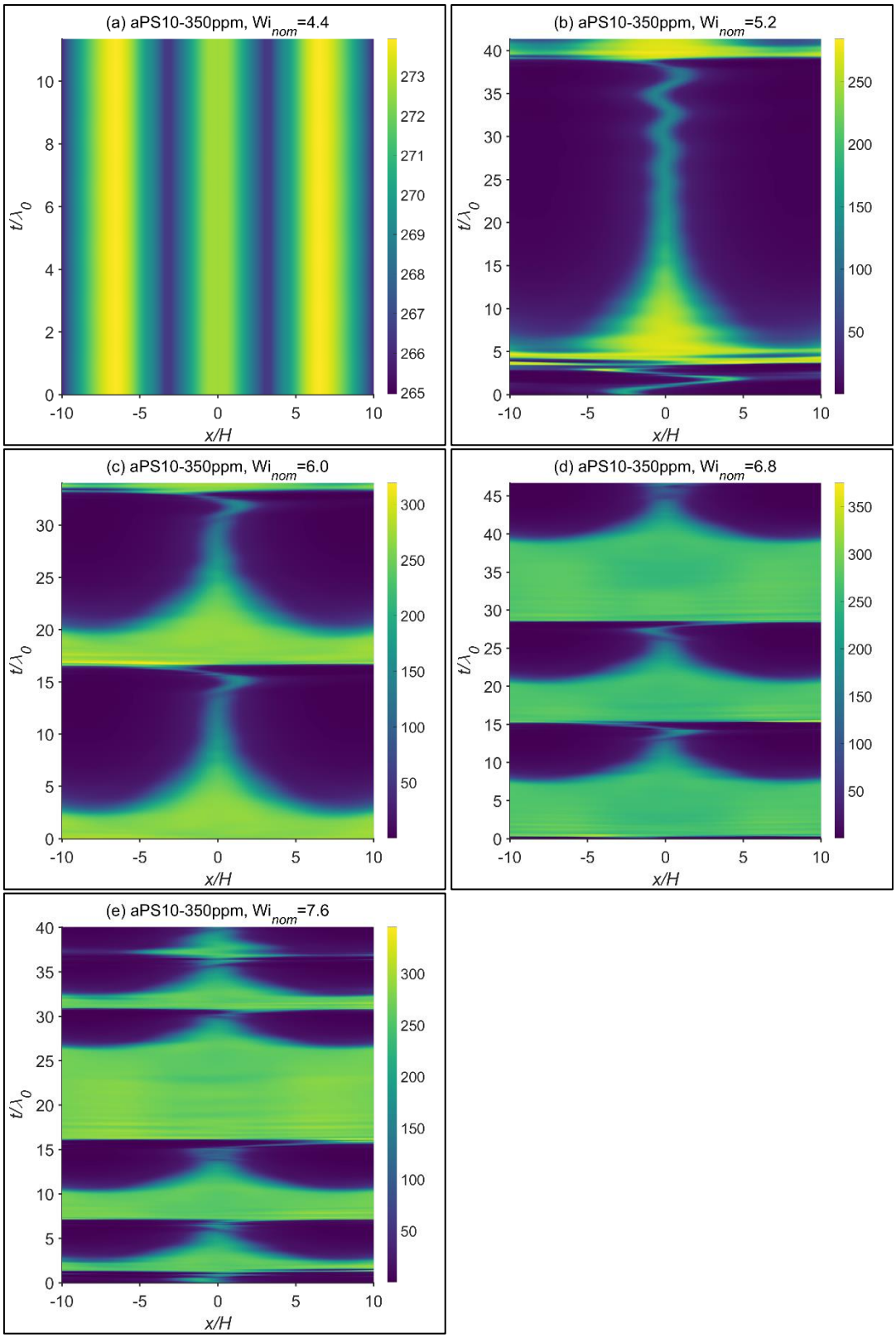

Figure 7.20 – Space-time diagrams of the normalized first normal stress difference $N_1/(\eta_0 U_0/2H)$ along the horizontal centerline of the OSCER device, for the fluid aPS10-350ppm. Behavior is characteristic of the **low elasticity** regime, at El$_{nom}$=4.1.

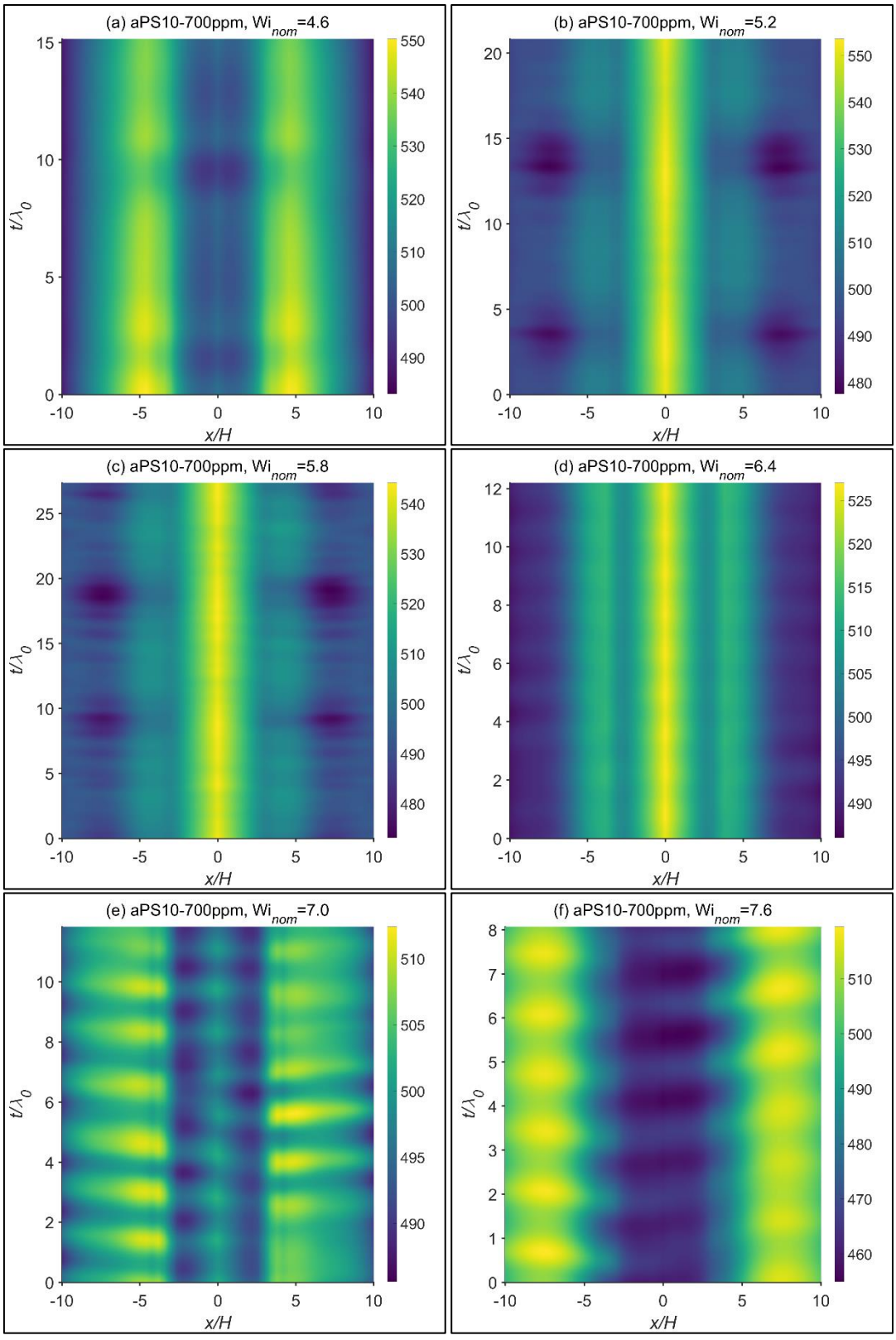

Figure 7.21 – Space-time diagrams of the normalized first normal stress difference $N_1/(\eta_0 U_0/2H)$ along the horizontal centerline of the OSCER device, for the fluid aPS10-700ppm. Behavior is characteristic of the **intermediate elasticity** regime, at El$_{nom}$=5.6.

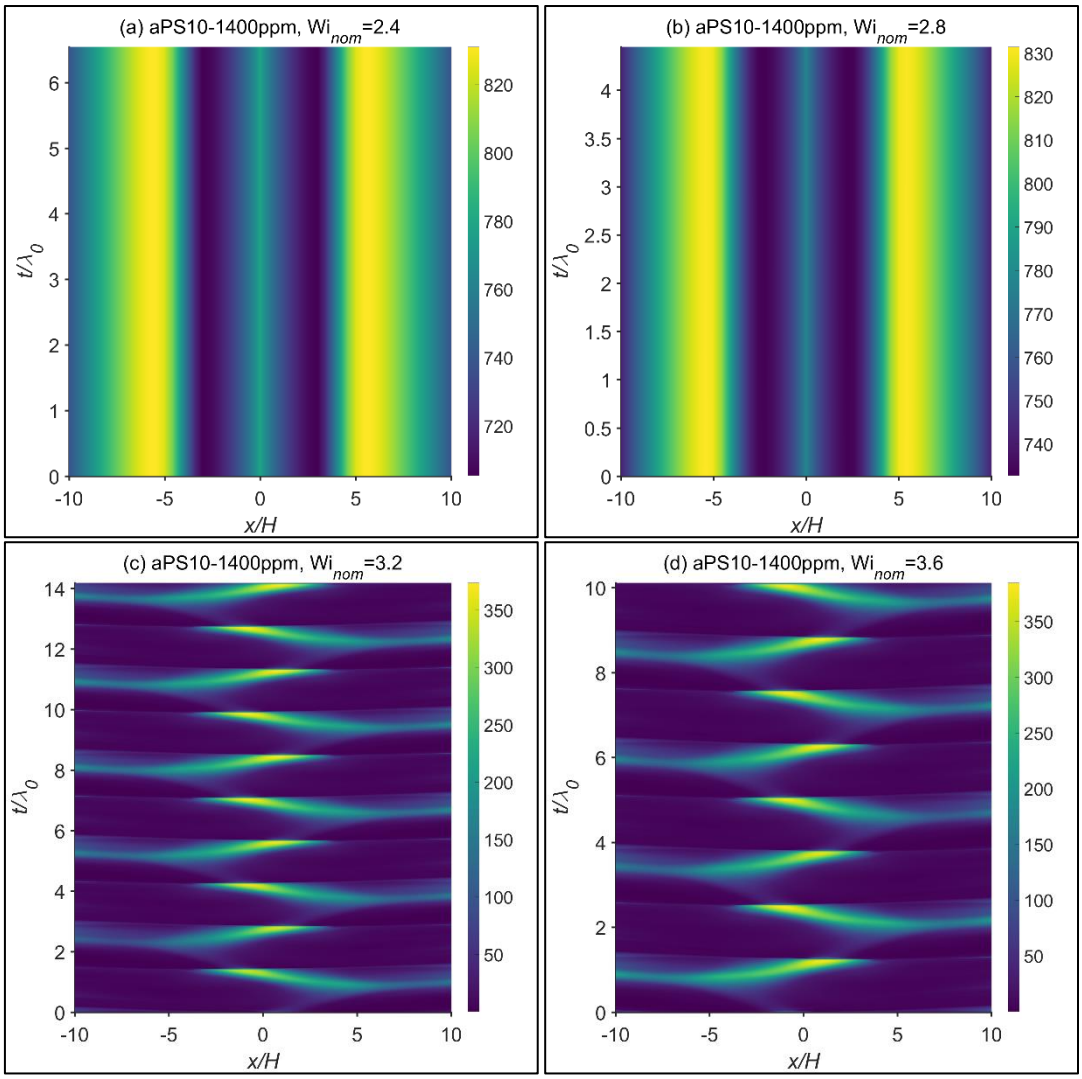

Figure 7.22 – Space-time diagrams of the normalized first normal stress difference $N_1/(\eta_0 U_0/2H)$ along the horizontal centerline of the OSCER device, for the fluid aPS10-1400ppm. Behavior is characteristic of the **high elasticity** regime, at El$_{nom}$=8.1.

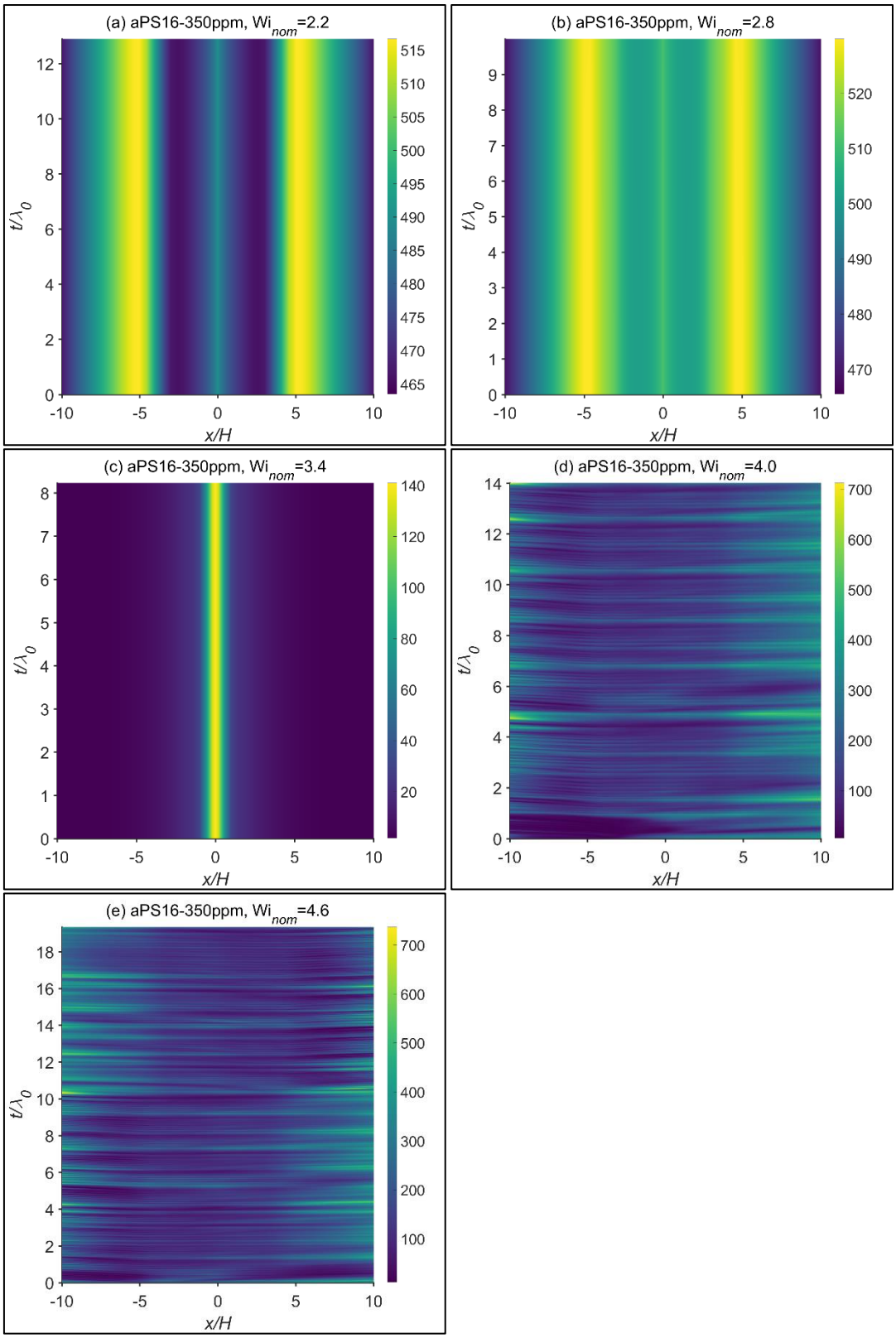

Figure 7.23 – Space-time diagrams of the normalized first normal stress difference $N_1/(\eta_0 U_0/2H)$ along the horizontal centerline of the OSCER device, for the fluid aPS16-350ppm. Behavior is characteristic of the **very high elasticity** regime, at El$_{nom}$=13.7.

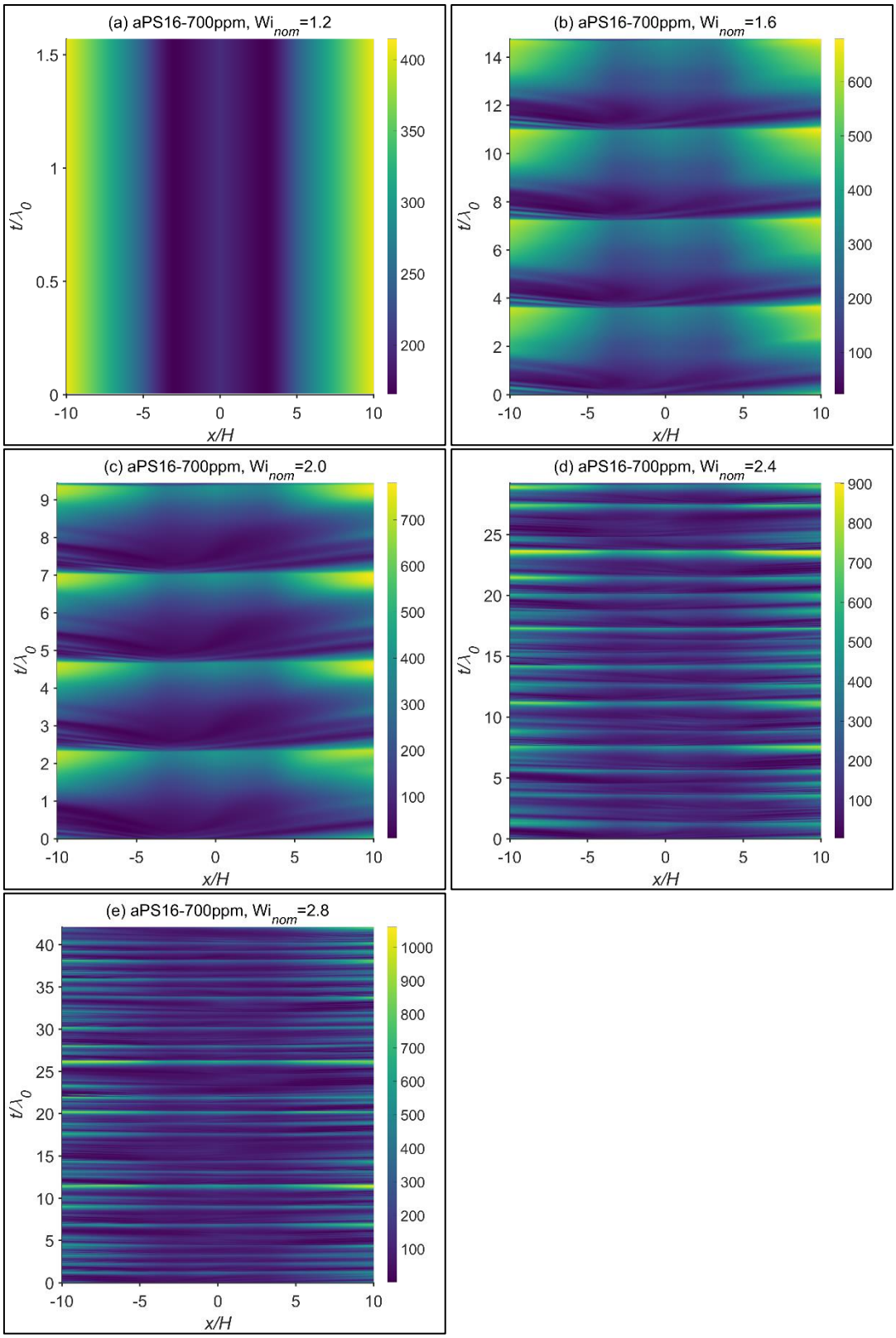

Figure 7.24 – Space-time diagrams of the normalized first normal stress difference $N_1/(\eta_0 U_0/2H)$ along the horizontal centerline of the OSCER device, for the fluid aPS16-700ppm. Behavior is characteristic of the **very high elasticity** regime, at El$_{nom}$=18.8.

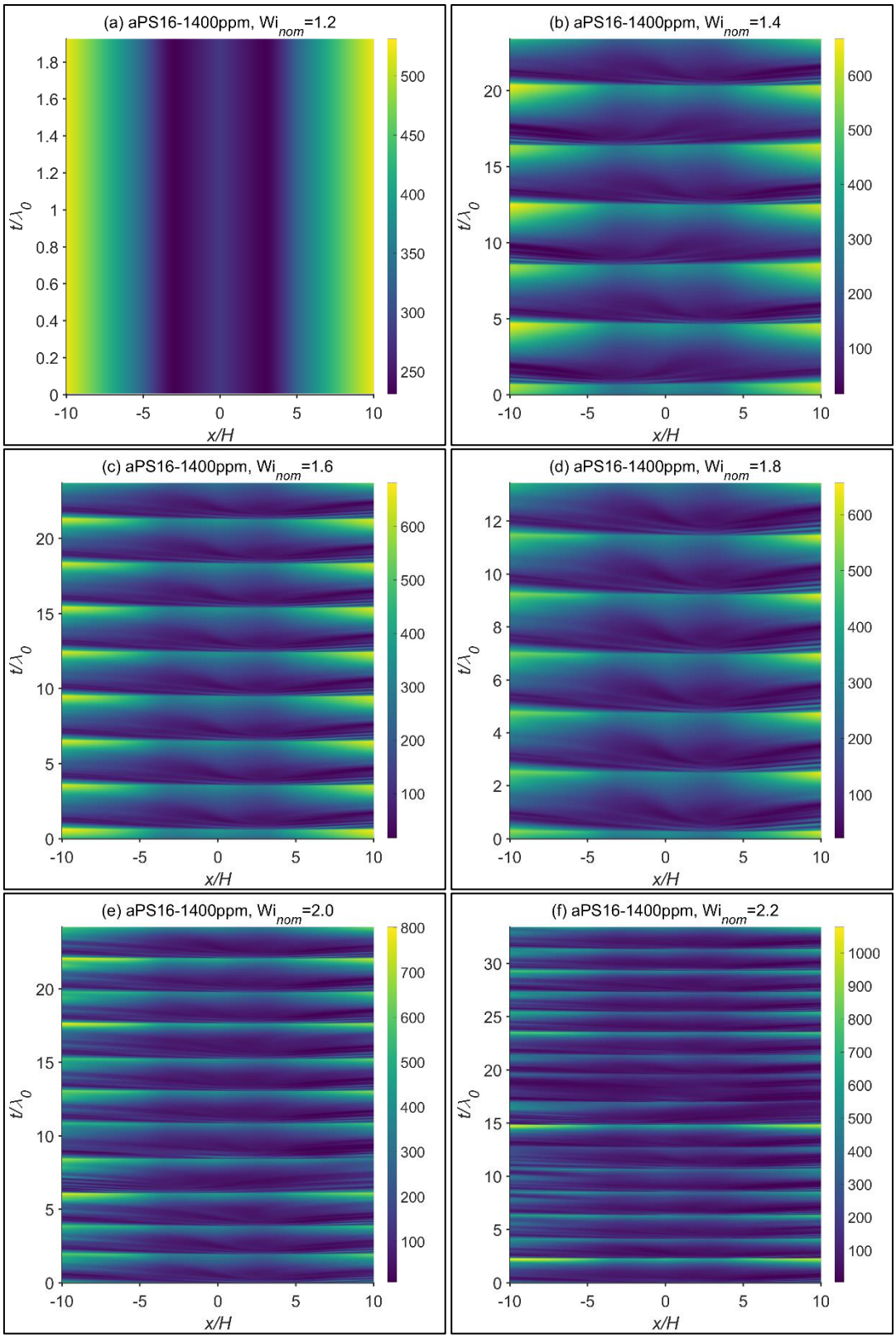

Figure 7.25 – Space-time diagrams of the normalized first normal stress difference $N_1/(\eta_0 U_0/2H)$ along the horizontal centerline of the OSCER device, for the fluid aPS16-1400ppm. Behavior is characteristic of the **very high elasticity** regime, at El$_{nom}$=32.2.

8 Time-Dependent Instabilities in a Standard Planar Cross-Slot

8.1 Summary

A preliminary investigation on the transition to elastic turbulence in a standard planar cross-slot is presented. The flow of an Oldroyd-B fluid, and of FENE-CR fluids with extensibilities $L^2 = 1000$ and $L^2 = 10000$, is simulated for two different characteristic Deborah and Elasticity numbers. Various stages of the transition to turbulence are discussed, up to and including fully-developed elastic turbulence, as demonstrated by several characteristic properties, including the spectral decay of velocity fluctuations and the ejection of excessive elastic stresses concentrated in the boundary layers along the walls of the outlet channels.

8.2 Numerical Methods

The isothermal, incompressible, time-dependent flow of monodisperse, dilute, long-chained polymer solutions is simulated using a Finitely Extensible Nonlinear Elastic (FENE) constitutive model [1] with the Chilcott-Rallison (-CR) closure [2], or alternatively the Oldroyd-B model [3]. The relevant parameters and flow conditions are given in Table 8.1. All of the fluids tested in this chapter have a solvent viscosity ratio $\beta = \eta_s / \eta_0 = 0.5$, where $\eta_0 = \eta_s + \eta_p$ is the solution shear viscosity and η_s and η_p are the corresponding solvent and polymer contributions, respectively.

The governing equations are the continuity, momentum and constitutive equations, respectively,

$$\nabla \cdot \mathbf{u} = 0, \tag{8.1}$$

$$\rho \frac{\mathrm{D}\mathbf{u}}{\mathrm{D}t} = -\nabla p + \eta_s \nabla^2 \mathbf{u} + \nabla \cdot \boldsymbol{\tau}, \tag{8.2}$$

$$\begin{cases} \boldsymbol{\tau} + \lambda_0 \dfrac{\mathrm{D}}{\mathrm{D}t}\left(\dfrac{\boldsymbol{\tau}}{g}\right) = \eta_p \left(\nabla \mathbf{u} + \nabla \mathbf{u}^{\dagger}\right) + \dfrac{\lambda_0}{g}\left(\boldsymbol{\tau} \cdot \nabla \mathbf{u} + \nabla \mathbf{u}^{\dagger} \cdot \boldsymbol{\tau}\right) \\ \text{Oldroyd-B}: g = 1 \\ \text{FENE-CR}: g = \dfrac{L^2 + \left(\lambda_0 / \eta_p\right) \mathrm{tr}(\boldsymbol{\tau})}{L^2 - 3} \end{cases}, \tag{8.3}$$

where ρ is the density of the fluid, $\boldsymbol{\tau}$ is the polymeric extra stress tensor, L^2 is the extensibility of polymer chains, λ_0 is the zero shear-rate relaxation time, and g is an auxiliary function related to the decrease of the effective relaxation time for the FENE-CR model, $\lambda_{eff} = \lambda_0 / g$. If g is set to one, which is equivalent to assuming $L^2 \to \infty$, then the Oldroyd-B model is recovered.

Table 8.1 – Model fluids and dimensionless flow parameters. The solvent viscosity ratio is the same for all simulations, $\beta = \eta_s / \eta_0 = 0.5$. De denotes the Deborah number, Re denotes the Reynolds number and El refers to the Elasticity number, defined as El=De/Re.

Model	L^2	**El**	**De**	**Re**
FENE-CR	1000	10	6	0.6
FENE-CR	1000	10	10	1
FENE-CR	1000	100	6	0.06
FENE-CR	1000	100	10	0.1
FENE-CR	10000	10	6	0.6
FENE-CR	10000	10	10	1
FENE-CR	10000	100	6	0.06
FENE-CR	10000	100	10	0.1
Oldroyd-B	-	10	6	0.6
Oldroyd-B	-	10	10	1
Oldroyd-B	-	100	6	0.06
Oldroyd-B	-	100	10	0.1

Three characteristic dimensionless numbers are defined, respectively the Deborah, Reynolds and Elasticity numbers,

$$\mathrm{De} = \lambda_0 \frac{U_0}{2H}, \tag{8.4}$$

$$\mathrm{Re} = \frac{\rho U_0 2H}{\eta_0}, \tag{8.5}$$

$$\mathrm{El} = \frac{\mathrm{De}}{\mathrm{Re}} = \frac{\lambda_0 \eta_0}{4\rho H^2}, \tag{8.6}$$

where U_0 is both the uniform inlet velocity and the characteristic velocity of the flow, and H denotes the half-width of the inlet and outlet channels, and is the characteristic length scale of the flow.

The governing equations are solved using an implicit, second-order, finite volume numerical method using a collocated mesh arrangement, which is described in detail elsewhere [4], adapted from the SIMPLEC algorithm [5]. The method includes the CUBISTA high-resolution scheme for the treatment of advective terms [6] in the momentum and constitutive equations, and the log-conformation technique for the transformation of the constitutive equation [7], following the methodology originally developed by Fattal and Kupferman [8], in order to increase the numerical stability. Furthermore, to increase the numerical accuracy, the second-order backward differencing scheme [9] is used for time integration. At the walls, no-slip boundary conditions are assumed for the velocity components and the polymeric extra stress components are linearly extrapolated from the first two adjacent cells along the wall-normal direction. Uniform velocity profiles and null extra-stress profiles are assumed at the inlets. Neumann boundary conditions of the form $\mathbf{n}\cdot\nabla\phi = 0$ are assumed at the outlets, except for pressure which is linearly extrapolated from the first two upstream cells. Round-off error at machine level precision suffices to generate flow instabilities, so no disturbances are artificially introduced. Computations were carried out using time-steps of the order of $\Delta t/\lambda_0 \approx 10^{-5}$ and the data corresponding to the start-up of flow, between $t/\lambda_0 = [0, 60]$ and $t/\lambda_0 = [0, 120]$ depending on the simulation, was excluded from the results presented in this chapter. The numerical method is implemented in double precision Fortran.

The block structured mesh, depicted in Figure 8.1, is comprised of a total of 19329 cells, split over five blocks, one block with 4182 cells for each of the inlet and outlet channels and a fifth central block with 2601 cells. For each of the inlet and outlet blocks, the cell length along the streamwise direction is progressively larger towards the inlets and outlets. The grid spacing is uniform in the central block, with $\Delta x = \Delta y \approx 0.0392H$.

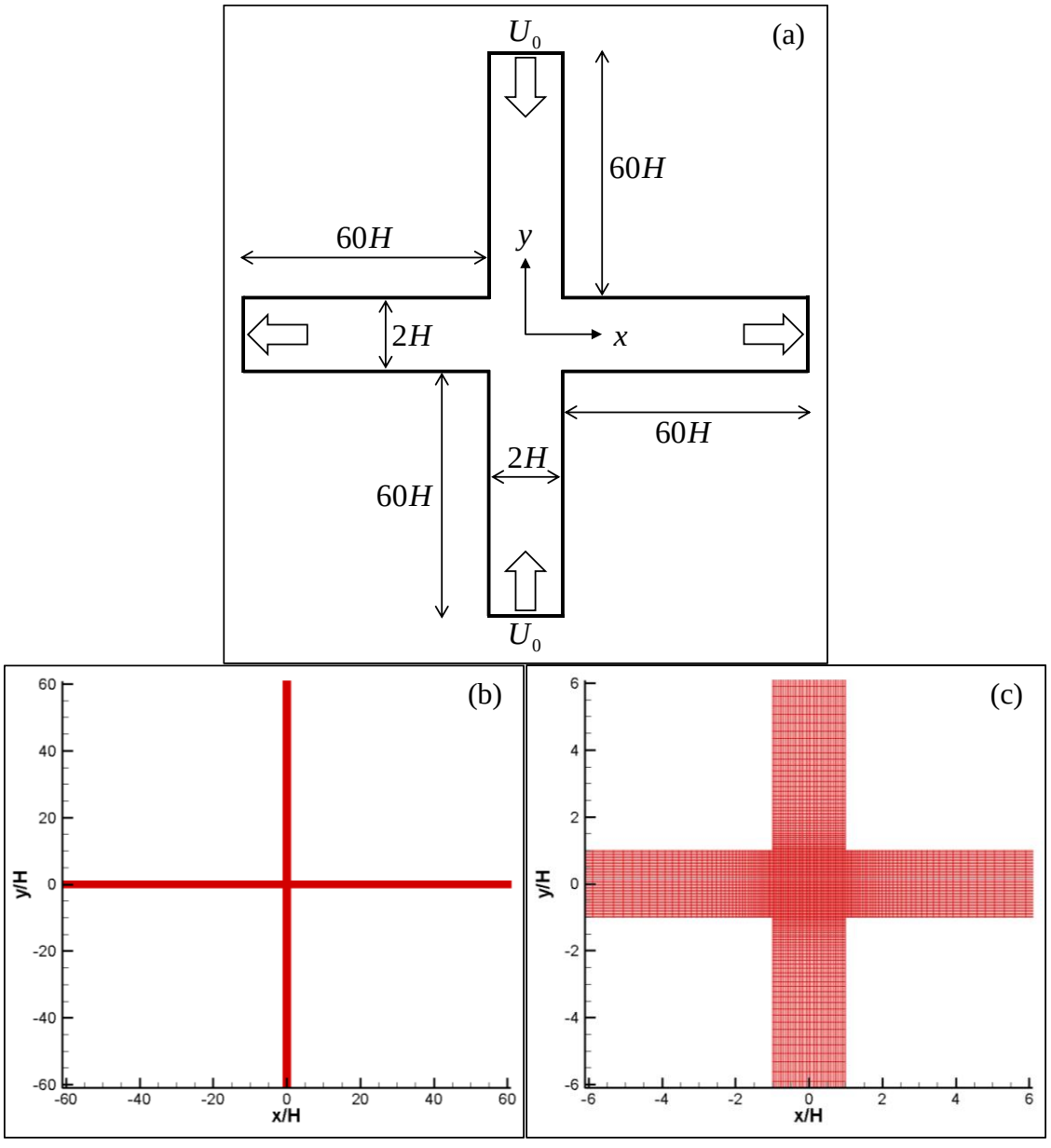

Figure 8.1 – (a) Geometry of the planar cross-slot. The half-width H is used as the characteristic length scale. The corresponding mesh is shown in panel (b), and the detailed structure near the central slot is shown in panel (c). Cells in the inlet and outlet channels are progressively larger away from the central slot.

8.3 Numerical Results and Discussion

8.3.1 Instability regimes

The character of the various flow instabilities discussed in this chapter is primarily determined by the extensibility of the model fluid. Space-time plots of the normalized first normal stress difference, $N_1^* = N_1/(\eta_0 U_0/2H)$, along the horizontal centerline of the slot are shown in Figure 8.2 for the FENE-CR fluid with extensibility $L^2 = 1000$.

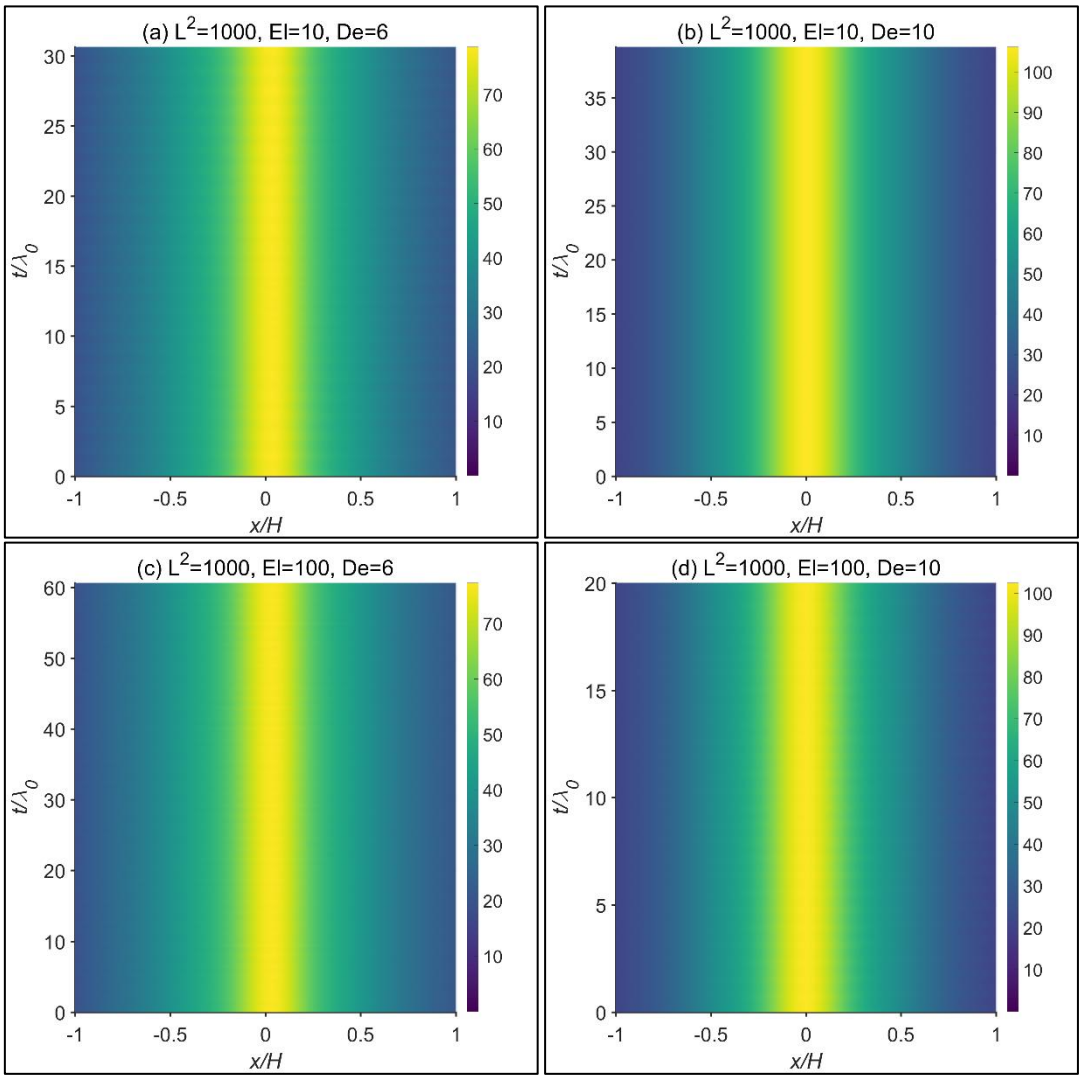

Figure 8.2 – Space-time diagrams of the normalized first normal stress difference $N_1^* = N_1/(\eta_0 U_0/2H)$ along the horizontal centerline of the slot, for the FENE-CR fluid with extensibility $L^2 = 1000$.

For all combinations of elasticity and flow-rate, i.e. El and De, the flow field is quasi-stationary and is only perturbed by a low amplitude periodic instability. A snapshot of the flow field for one of the simulations, corresponding to Figure 8.2.d, is shown in Figure 8.3. In addition to the asymmetric configuration of the birefringence strand, shared by all flows of the FENE-CR fluid with extensibility $L^2 = 1000$, lip vortices are also visible in Figure 8.3, similar to those mentioned in Chap. 6 of this thesis [10].

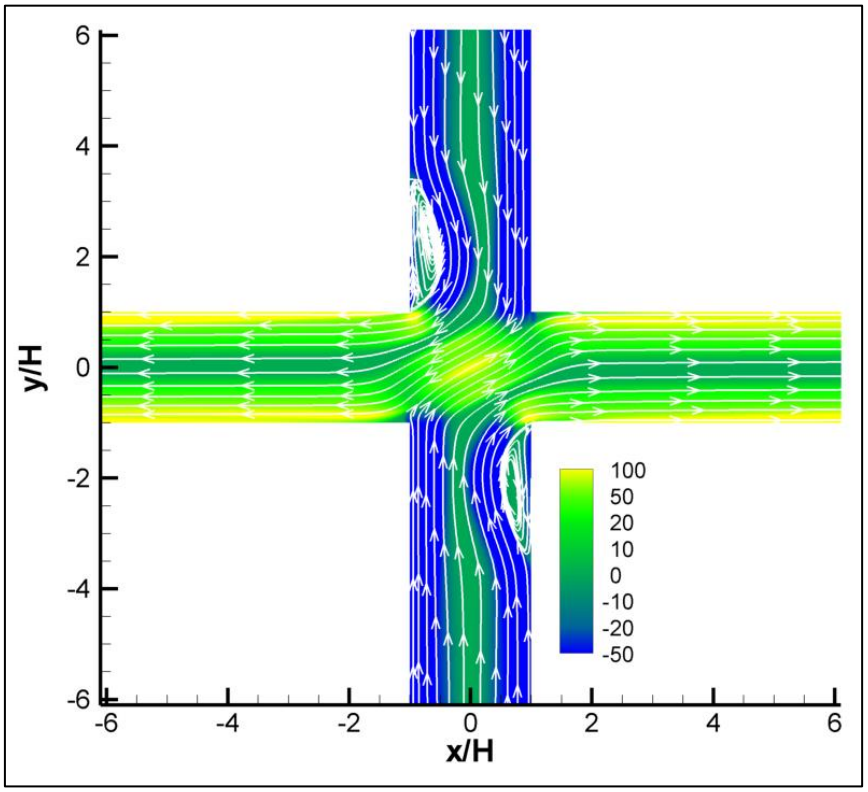

Figure 8.3 – Snapshot depicting the flow of the FENE-CR fluid with $L^2 = 1000$, at $\mathrm{El} = 100$ and $\mathrm{De} = 10$, taken at $t/\lambda_0 \approx 17.61$, represented as a contour plot of the normalized first normal stress difference $N_1^* = N_1 / (\eta_0 U_0 / 2H)$ with superimposed instantaneous streamlines.

Figure 8.4 shows the temporal evolution of N_1^* along the horizontal centerline of the slot for the FENE-CR fluid with extensibility $L^2 = 10000$. The behavior of the flow is controlled by the Deborah number. For $\mathrm{De} = 6$, and regardless of the Elasticity number, the flow is periodic, whereas for $\mathrm{De} = 10$ the underlying periodicity of the flow field is distorted by aperiodic modes of oscillation.

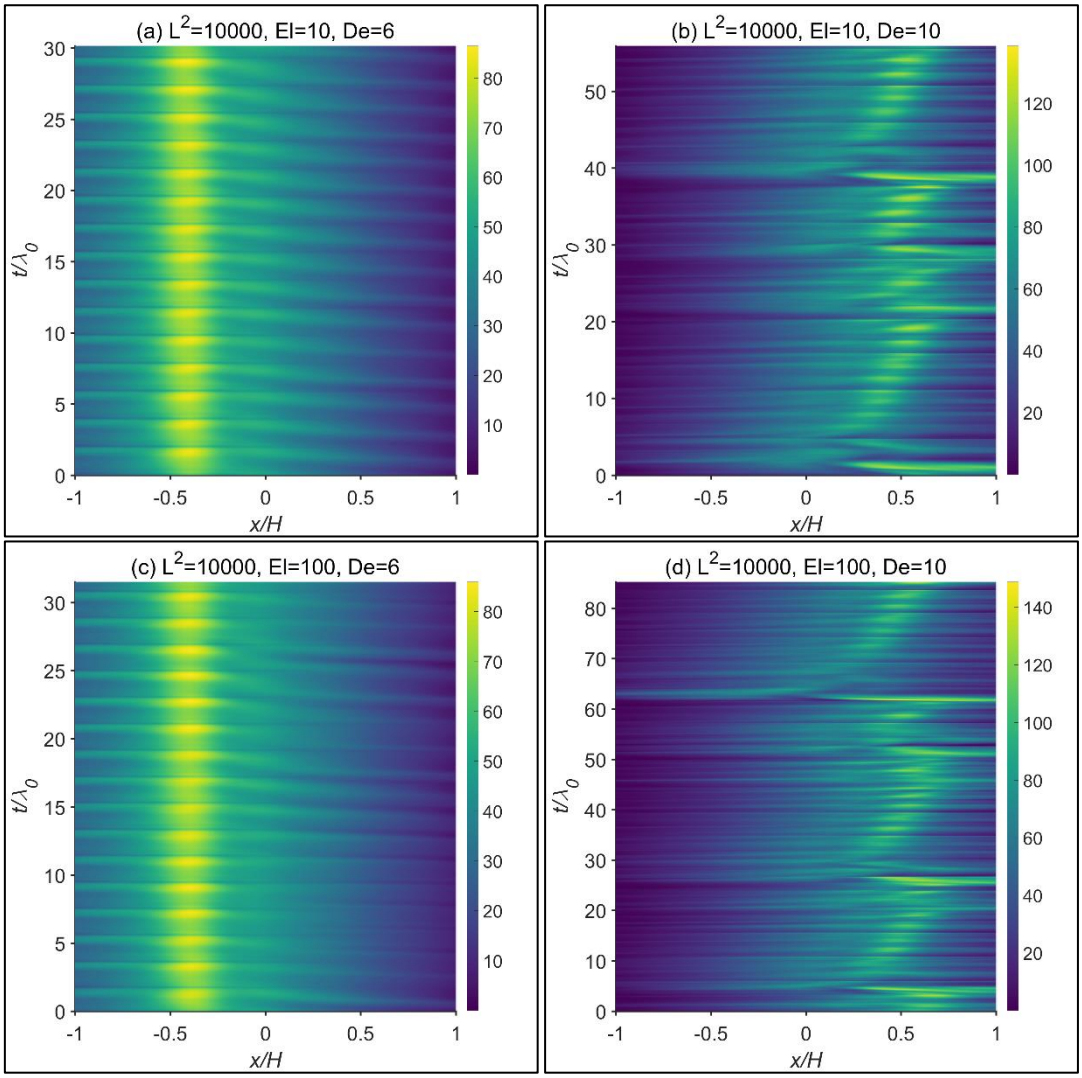

Figure 8.4 – Space-time diagrams of the normalized first normal stress difference $N_1^* = N_1/(\eta_0 U_0/2H)$ along the horizontal centerline of the slot, for the FENE-CR fluid with extensibility $L^2 = 10000$.

The lateral displacement of the stagnation point hinted at by the N_1^* space-time diagrams is further illustrated by the distorted velocity field shown in Figure 8.5. The tilted birefringence strand oscillates along the vertical axis for the flows at $\mathrm{De} = 6$, and also along the horizontal axis for the flows at $\mathrm{De} = 10$. Additionally, a careful examination of Figure 8.5 reveals the presence of two parallel birefringence strands, in a manner similar to the birefringence pipe observed in opposed-jets experiments, e.g. [11].

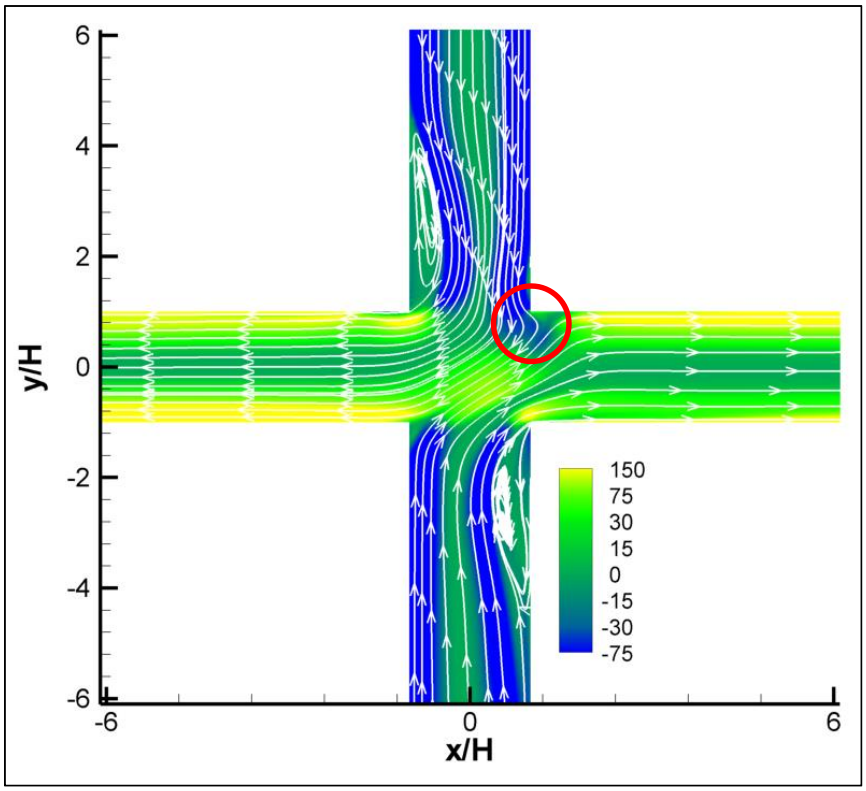

Figure 8.5 – Snapshot depicting the flow of the FENE-CR fluid with $L^2 = 10000$, at $\mathrm{El} = 100$ and $\mathrm{De} = 10$, taken at $t/\lambda_0 \approx 84.42$, represented as a contour plot of the normalized first normal stress difference $N_1^* = N_1 / (\eta_0 U_0 / 2H)$ with superimposed instantaneous streamlines.

Figure 8.6 shows the temporal evolution of N_1^* along the horizontal centerline of the slot for the Oldroyd-B fluid. At $\mathrm{El} = 10$ and $\mathrm{De} = 6$ the flow is similar to the $\mathrm{De} = 10$ cases shown earlier in Figure 8.4. However, further increases in either the Elasticity or Deborah numbers lead to a transition in the configuration of the flow field, with an apparent complete loss of periodicity. In Figures 8.6.b-d the brightness of the birefringence strand, or more accurately the amplitude of N_1^*, changes abruptly over time. Since the various modes of instability discussed in Chap. 7 of this thesis are associated with the presence of spatio-temporal gradients in the corresponding N_1^* plots, one may infer the absence of a deterministic cycle in Figures 8.6.b-d. Note that considering both the relaxation time of the fluid and the finite mesh size, the unbounded extensibility of the Oldroyd-B model is not by itself sufficient to explain the sudden appearance and disappearance of the birefringence strand.

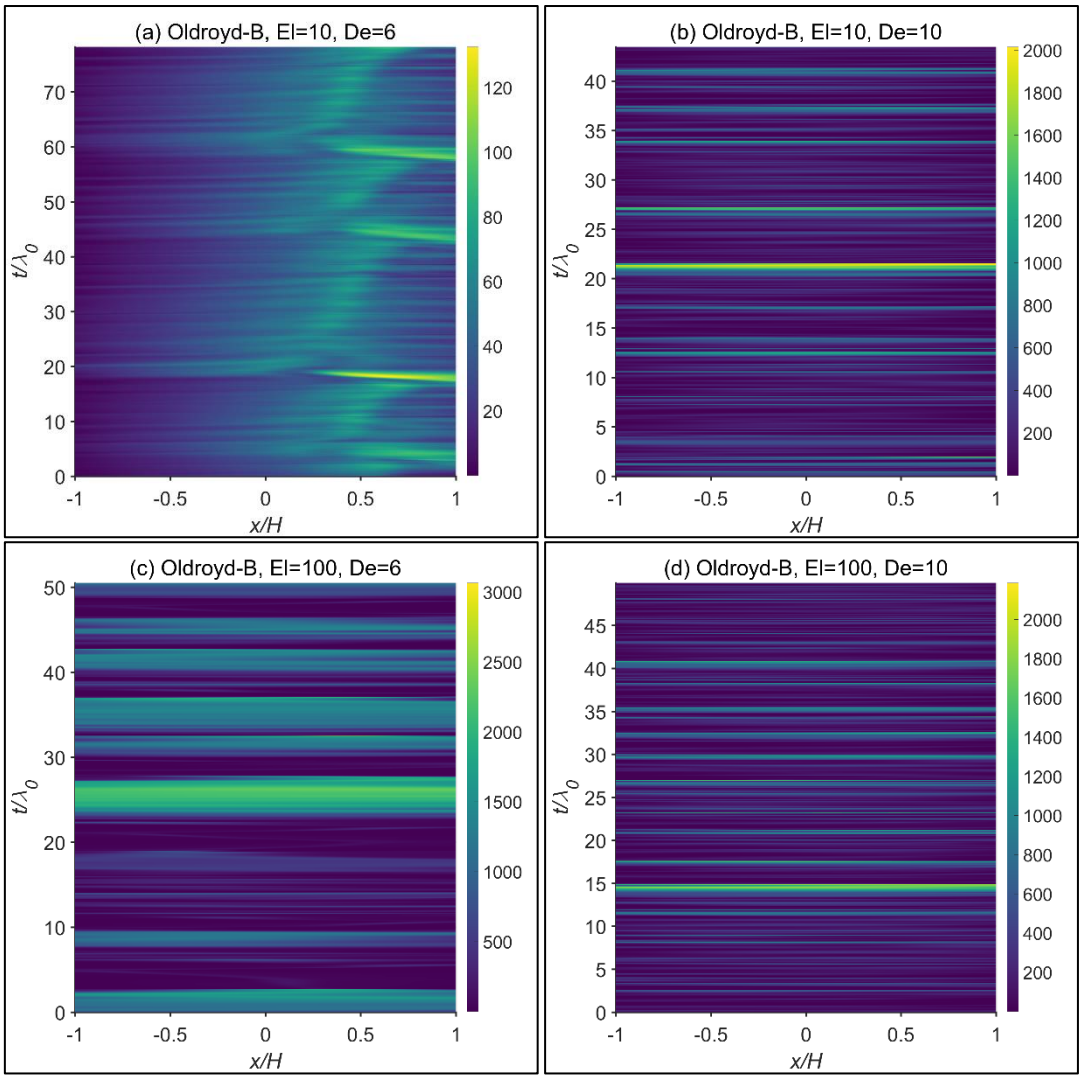

Figure 8.6 – Space-time diagrams of the normalized first normal stress difference $N_1^* = N_1/(\eta_0 U_0/2H)$ along the horizontal centerline of the slot, for the Oldroyd-B fluid.

Contour plots of N_1^* with superimposed streamlines are shown in Figure 8.7.a for the Oldroyd-B fluid at $\mathrm{El}=100$ and $\mathrm{De}=10$. For the flows corresponding to Figures 8.6.b-d, the lip vortices shown previously for the fluids with finite extensibilities now trail the four corners of the slot instead of just two diagonally opposite corners. Furthermore, one of the diagonally opposite pairs is comprised of two counter-rotating vortices. Figure 8.7.b shows an expanded view of the outlet channels, highlighting the detachment of the stress boundary layers from the walls. This process is consistent with the ejection of excessive elastic stresses concentrated in the boundary layer, as reported by Steinberg and co-workers, e.g. [12], for elastic turbulent flows. To a much lesser extent, this type of detachment also occurs for the FENE-CR flows with extensibility $L^2=10000$ and $\mathrm{De}=10$.

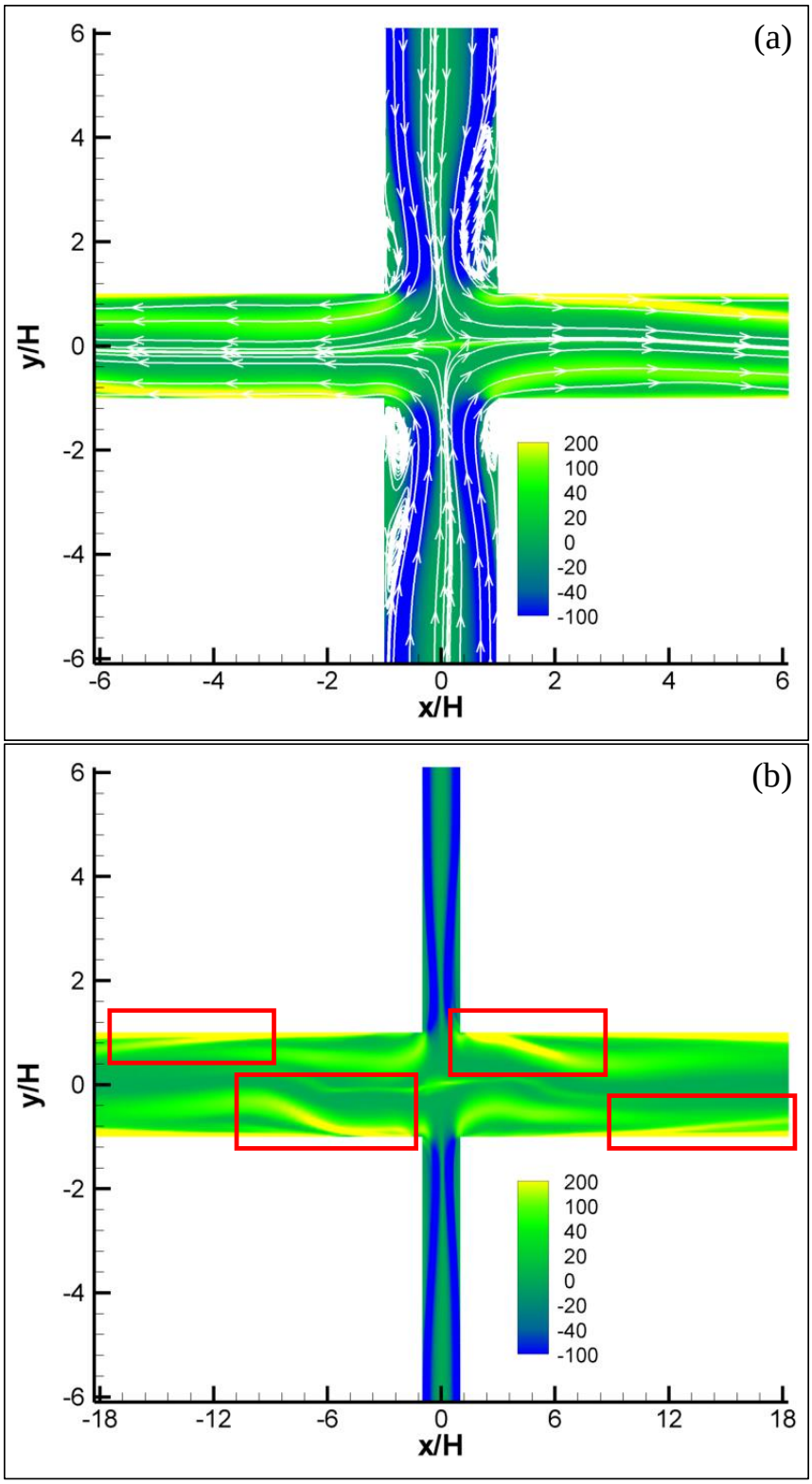

Figure 8.7 – (a) Snapshot depicting the flow of the Oldroyd-B fluid, at $\mathrm{El}=100$ and $\mathrm{De}=10$, taken at $t/\lambda_0 \approx 42.19$, represented as a contour plot of the normalized first normal stress difference $N_1^* = N_1/(\eta_0 U_0/2H)$ with superimposed streamlines. (b) Expanded view of the outlet channels, showing the detachment of the stress boundary layer from the walls (note that the $x-$ and $y-$axis are not to scale).

8.3.2 Spectral analysis

Power density spectra of the normalized first component of the velocity vector, u_x/U_0, sampled at coordinates $(x,y)=(-H,0)$ and $(x,y)=(H,0)$, are depicted in Figures 8.8–8.10. Sampling at these coordinates instead of at the center, $(x,y)=(0,0)$, has the advantage of facilitating comparisons with experiments, since it is at the center of cross-slots that the noise-to-signal ratio in experimental measurements is highest. The mean of each time-series was subtracted from the signal prior to transformation, and no windowing of the signal was used other than cropping the sample to an integer number of periods for the time-series with a discernible dominant frequency. Frequency f was multiplied by the zero shear-rate relaxation time λ_0 and accordingly the dimensionless sampling frequency $\lambda_0 f_s$ was used in the presentation of power density plots.

In order to assess the possibility of aliasing caused by the finite cell size of computational meshes, the residence time in the sampled cell was estimated, $t_{res}=\Delta x_{cell}/u_{x,rms}$, which for a locally uniform mesh is equivalent to the spatial sampling time of a signal as it travels downstream. The characteristic local velocity was calculated as the root-mean-square of u_x instead of the arithmetic mean because u_x may often change sign, leading to unreasonably high values of t_{res}. From the Sampling Theorem, a discrete sequence of samples can perfectly reconstruct a continuous signal if the sampling frequency is at least twice the highest frequency component of the signal. In other words, the cutoff frequency f_c above which frequencies are poorly resolved due to the finite cell size of the mesh was estimated as $2f_c=1/t_{res}$, and is shown in dimensionless form in Table 8.2 for the relevant flows. The estimated frequency cutoff, $\lambda_0 f_c$, was borne in mind in the evaluation of the spectral decay of velocity fluctuations, as an upper limit on the fitted data range.

The power spectra corresponding to the FENE-CR fluid with $L^2=1000$ are shown in Figure 8.8. The periodicity of the flows is generally evidenced by a single sinusoidal component, with consistent frequency regardless of the sampling position, either $x/H=-1$ or $x/H=1$, albeit with different amplitude as a result of the slight lateral

displacement of the stagnation point. Conversely, the low amplitude of oscillations is underlined by the low power density of the dominant frequency, generally of the order of 10^{-3}.

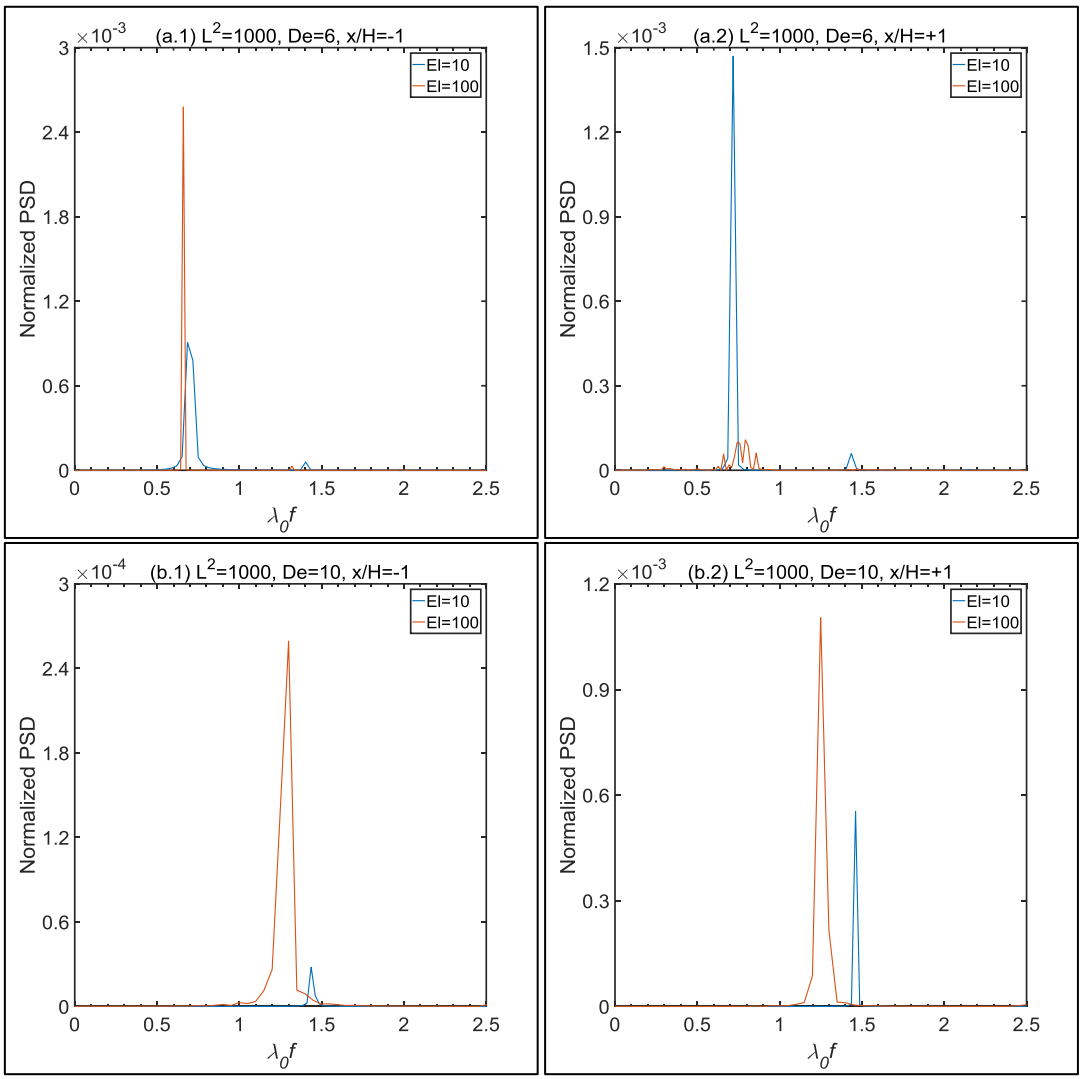

Figure 8.8 – Power spectra computed from time-series of the normalized first velocity component u_x/U_0 sampled at either $(x,y)=(-H,0)$ or $(x,y)=(H,0)$, as denoted by the title of each panel, for the FENE-CR fluid with extensibility $L^2=1000$.

Figure 8.9 shows the power spectra corresponding to the FENE-CR fluid with $L^2=10000$. The flows at $\mathrm{De}=6$ are periodic, however the spectral composition differs depending on the position where the time-series of u_x is sampled. To the right of the stagnation point, i.e. at $x/H=1$, the signal has a single frequency component, whereas to the left of the stagnation point, i.e. $x/H=-1$, multiple evenly spaced frequency

components are visible in Figure 8.9.a.1. These frequencies appear to be components of an harmonic series with fundamental frequency $\lambda_0 f_0 \approx 0.5$, albeit with a non-monotonic variation of the corresponding power density, and are associated with the type of velocity field protrusion highlighted earlier in Figure 8.5. Whereas in Figure 8.5 the protrusion occurs around the top-right corner of the slot, in the flows corresponding to Figure 8.9.a.1 the protrusion is present around the top-left corner, consequently inducing modifications in the velocity field along the left outlet of the central slot.

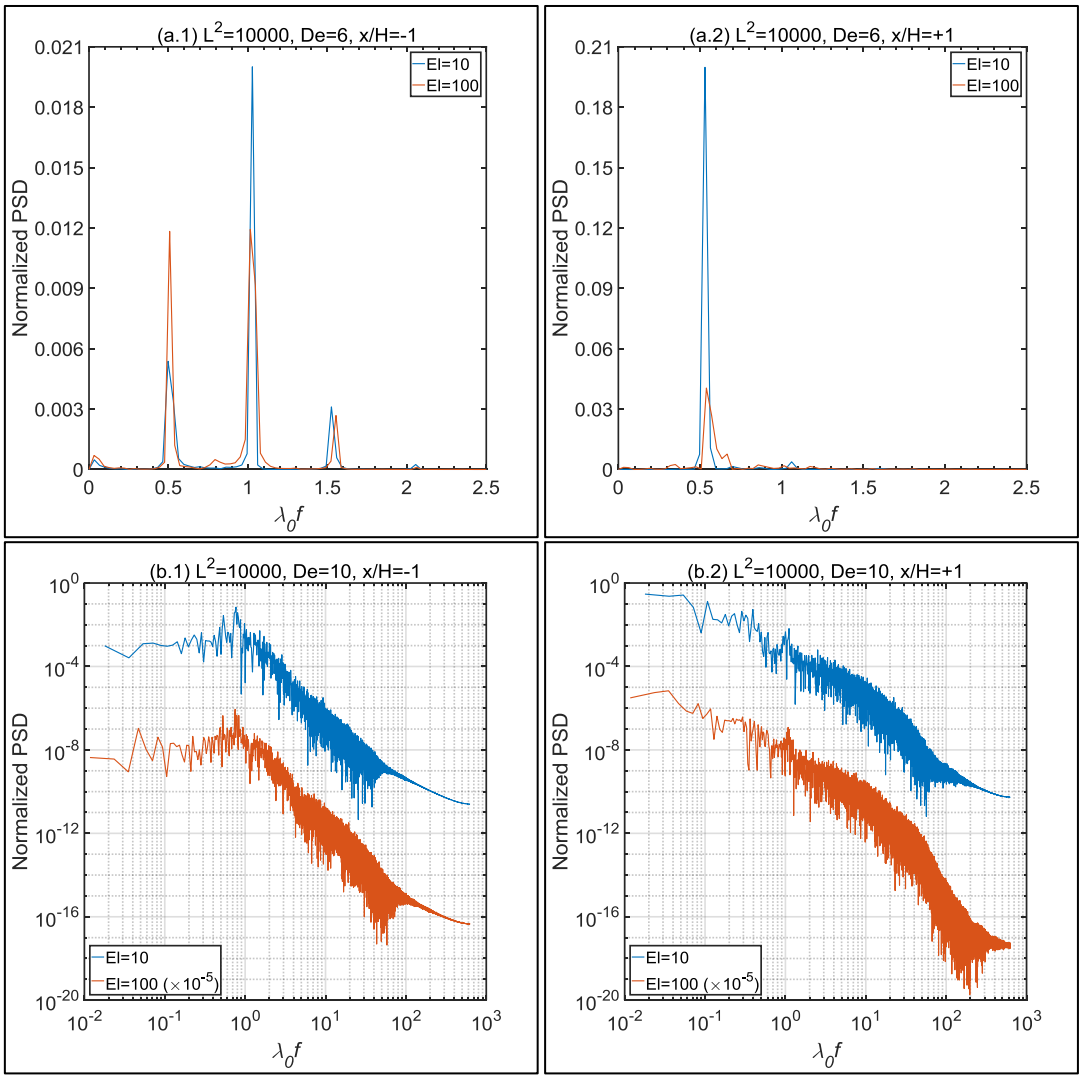

Figure 8.9 – Power spectra computed from time-series of the normalized first velocity component u_x/U_0 sampled at either $(x,y)=(-H,0)$ or $(x,y)=(H,0)$, as denoted by the title of each panel, for the FENE-CR fluid with extensibility $L^2 = 10000$.

This type of protrusion is also responsible for the differences between the spectra at $\mathrm{De} = 10$, shown in Figures 8.9.c-d. In these flows, such as in the aforementioned Figure

8.5, the protrusion occurs either around the top-right or bottom-right corner of the slot. Since the flows at $\mathrm{De}=10$ are aperiodic with a broad range of excited frequencies, the corresponding spectral decay slopes α, at either $(x,y)=(-H,0)$ or $(x,y)=(H,0)$, differ due to the influence of the protrusion, as shown in Table 8.2. Although the exact nature of the relation between the values of α and the emergence of the protrusion is currently difficult to scrutinize, the presence of a permanent flow field feature suggests that the flows of the FENE-CR fluid with $L^2=10000$ at $\mathrm{De}=10$ are not in the elastic turbulence regime.

Table 8.2 – Evaluation of the spectral decay of the first normalized velocity component u_x/U_0 sampled at either $(x,y)=(-H,0)$ or $(x,y)=(H,0)$, where H is the half-width of the channels. The power-law decay α was estimated via a linear fit, $\log_{10}(\mathrm{PSD})=\alpha\log_{10}(\lambda_0 f)+c$, of the spectral data within the range $\left[\lambda_0 f_{low},\lambda_0 f_{high}\right]$, and $\pm\varepsilon_\alpha$ is the corresponding 95% confidence interval, rounded up to the nearest decimal place. $\lambda_0 f_c$ is the estimated cutoff above which frequency components of the signal cannot be accurately resolved due to the finite cell size of computational meshes. The values of $\alpha\pm\varepsilon_\alpha$ are accurate for the specific fit range and method, however some uncertainty exists concerning the exact boundaries of the decay range.

$x/H=-1$							
L^2	El	De	α	$\pm\varepsilon_\alpha$	$\lambda_0 f_{low}$	$\lambda_0 f_{high}$	$\lambda_0 f_c$
10000	10	10	-3.1	0.1	5	50	380
10000	100	10	-4.4	0.1	10	50	380
Oldroyd-B	10	6	-6.1	0.2	15	55	220
Oldroyd-B	10	10	-4.9	0.3	160	250	250
Oldroyd-B	100	6	-1.6	0.1	10	65	130
Oldroyd-B	100	10	-3.6	0.2	160	250	250
$x/H=+1$							
L^2	El	De	α	$\pm\varepsilon_\alpha$	$\lambda_0 f_{low}$	$\lambda_0 f_{high}$	$\lambda_0 f_c$
10000	10	10	-3.9	0.2	10	50	210
10000	100	10	-3.7	0.2	10	50	210
Oldroyd-B	10	6	-4.9	0.2	15	50	140
Oldroyd-B	10	10	-4.9	0.3	160	250	250
Oldroyd-B	100	6	-1.7	0.1	10	70	140
Oldroyd-B	100	10	-3.3	0.3	160	250	250

Figure 8.10 shows the power spectra corresponding to the Oldroyd-B fluids. The flow at $\mathrm{El}=10$ and $\mathrm{De}=6$ has a similar spectral structure to the FENE-CR fluids with

$L^2 = 10000$ at $\mathrm{De} = 10$, including the different spectral decay rates on either side of the center of the slot, and the corresponding space-time plots of N_1^* shown respectively in Figures 8.6.a, 8.4.b and 8.4.d are also similar.

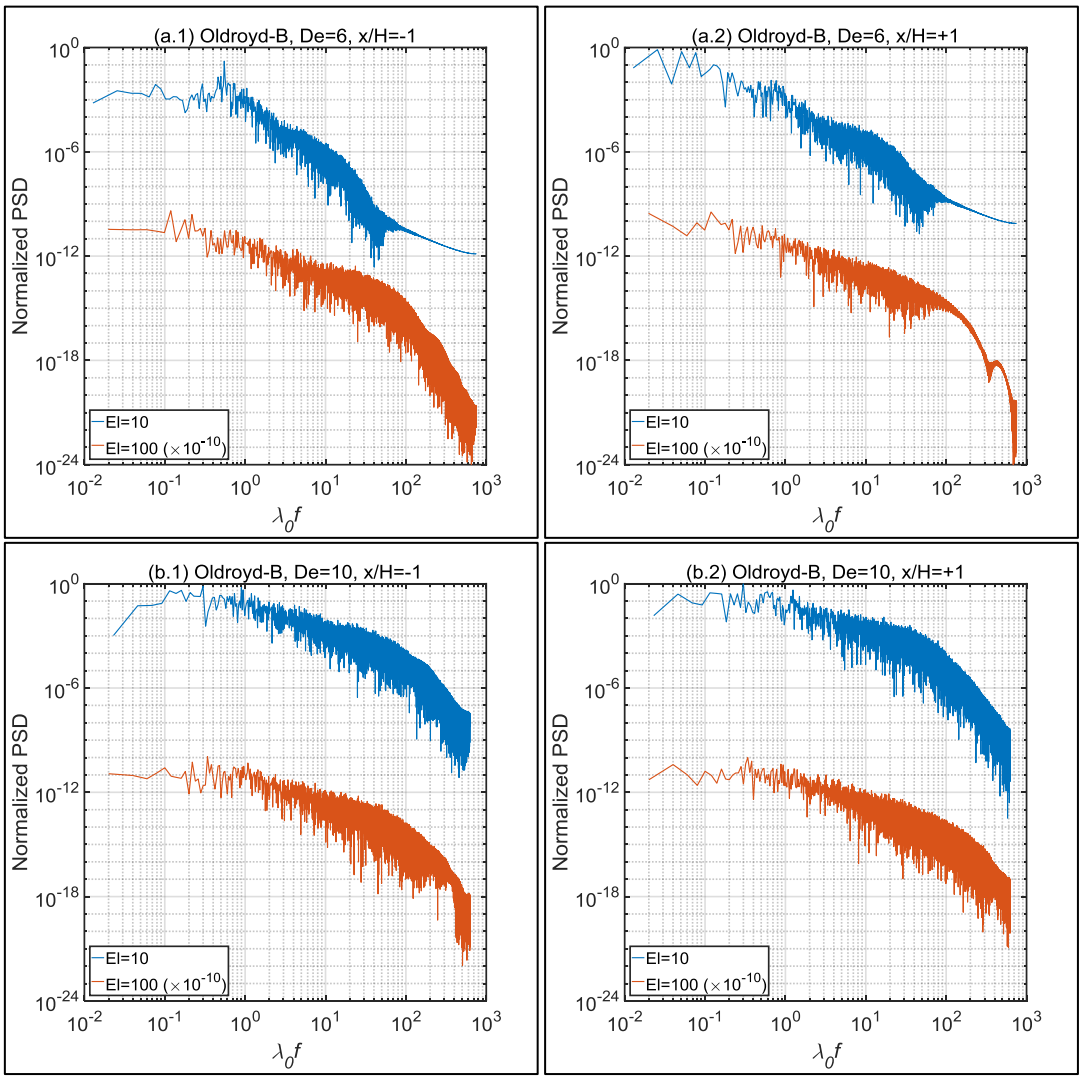

Figure 8.10 – Power spectra computed from time-series of the normalized first velocity component u_x/U_0 sampled at either $(x,y)=(-H,0)$ or $(x,y)=(H,0)$, as denoted by the title of each panel, for the Oldroyd-B fluid.

The spectra for $\mathrm{El} = 100$ and $\mathrm{De} = 6$ and also for $\mathrm{El} = 10$ and $\mathrm{De} = 10$ have a double slope, and the spectral structure within the second slope differs depending on the position where the velocity u_x is sampled. Time-series of the normalized first component of the velocity vector, u_x/U_0, are shown in Figure 8.11. An increase in either the Elasticity or Deborah numbers leads to the emergence of irregularly spaced, narrow, high amplitude peaks in u_x. Thus the double slopes are possibly a consequence of the superposition of

low frequency high amplitude velocity spikes with the high frequency low amplitude velocity baseline. For the Oldroyd-B fluid flow at $\mathrm{El}=100$ and $\mathrm{De}=10$, both the spectra and the corresponding time-series indicate the lack of a clear demarcation between the two components of the velocity signal, and the spectral decay is approximately $\alpha \approx -3.5$. This decay rate is consistent with the original reports on elastic turbulence by Groisman and Steinberg [13],[14], despite the shear dominated nature of their experiments, respectively, flow in a plate-and-plate rheometer and flow in a curvilinear channel, whereas cross-slot flows are extension dominated. Furthermore, the spectral decay $\alpha \approx -3.5$ is in good agreement with Fouxon and Lebedev's theoretical predictions [15], namely $|\alpha| > 3$, despite their assumption of isotropic, unbounded and homogeneous flow.

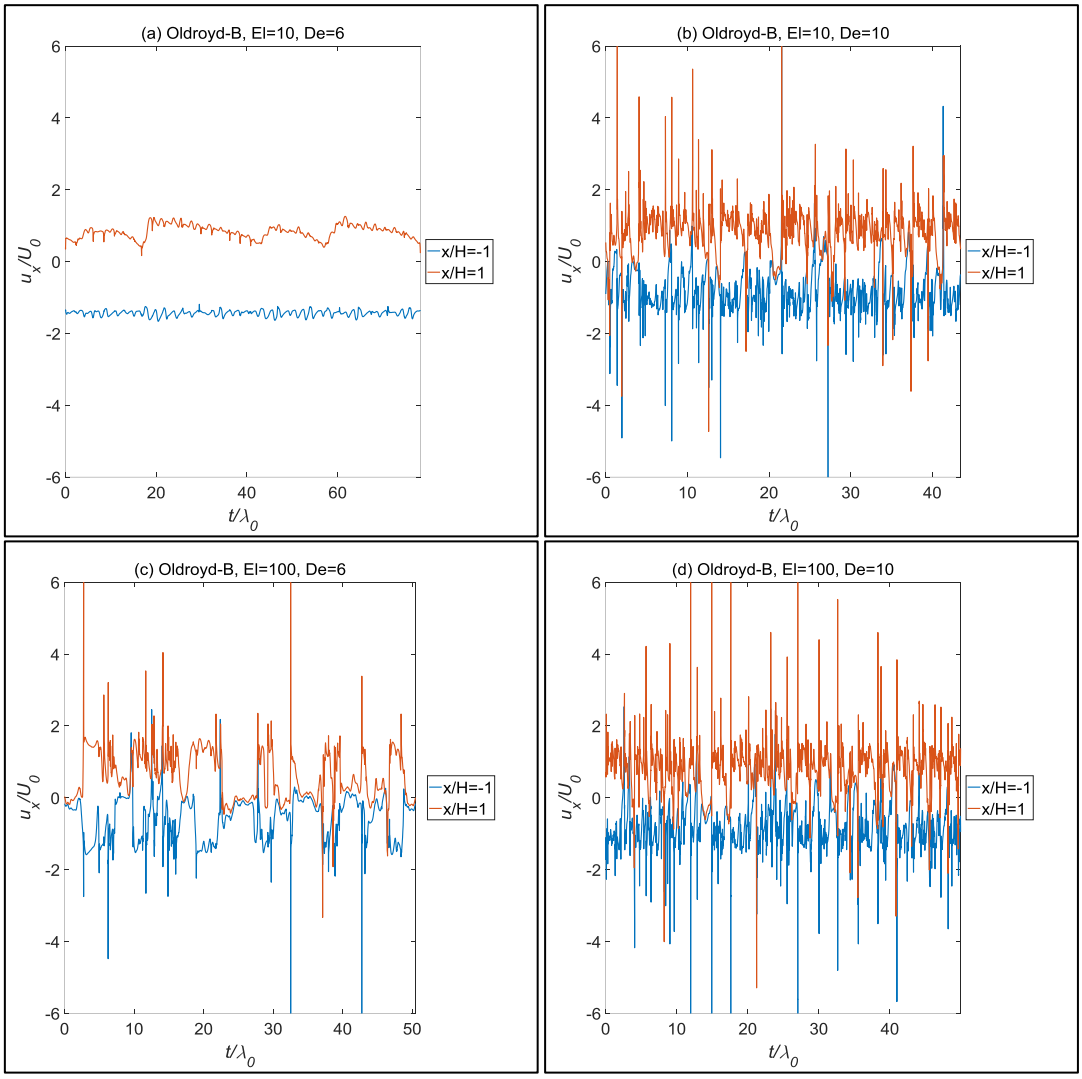

Figure 8.11 – Time-series of the normalized first component of the velocity vector, u_x/U_0, sampled at either $(x,y)=(-H,0)$ or $(x,y)=(H,0)$, for the Oldroyd-B fluid flows.

Various lines of evidence suggest that the Oldroyd-B fluid flow at $\mathrm{El}=100$ and $\mathrm{De}=10$ is turbulent. To assess if the elastic turbulence generated in the central slot is sustained far downstream, the additional velocity time-series shown in Figure 8.12 demonstrate that the fluctuations in u_x subside along the outlet channels. As discussed by Jun and Steinberg [12], the feedback (or back reaction) of the elastic stress field stabilizes the driving velocity field, and the ejection of the elastic stresses stored at boundary layers (cf. Figure 8.7.b) also leads to a decrease of the mixing efficiency within the bulk flow. Consequently, the turbulence generated in the central slot is dampened along the outlet channels.

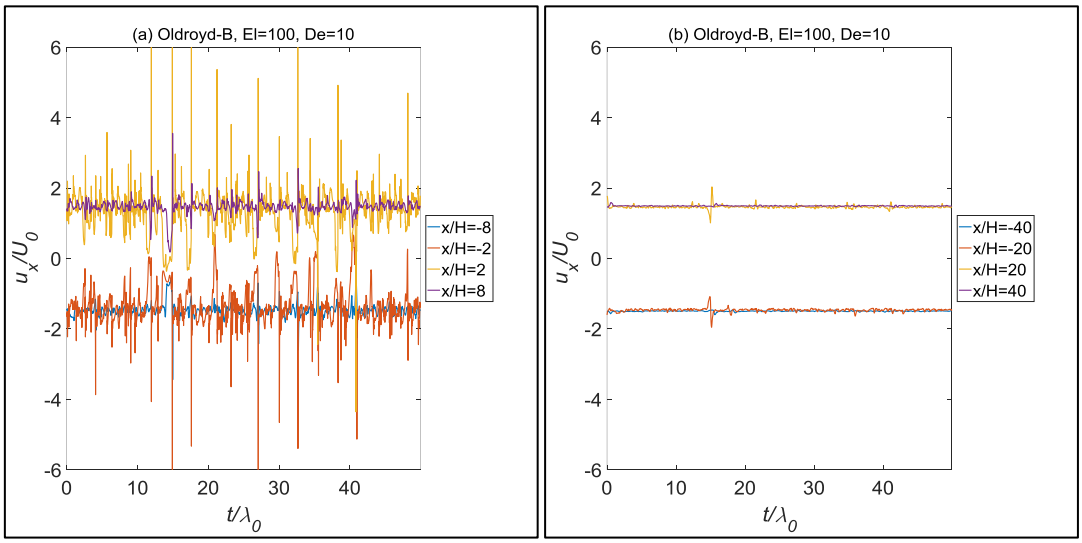

Figure 8.12 – Time-series of the normalized first component of the velocity vector, u_x/U_0, along the outlet centerline of the planar cross-slot, for the Oldroyd-B fluid flow with Elasticity number $\mathrm{El}=100$ and Deborah number $\mathrm{De}=10$.

8.4 References

[1] H.R. Warner, Kinetic Theory and Rheology of Dilute Suspensions of Finitely Extendible Dumbbells, Ind. Eng. Chem. Fundam. 11 (1972) 379–387. doi:10.1021/i160043a017.

[2] M. Chilcott, J. Rallison, Creeping flow of dilute polymer solutions past cylinders and spheres, J. Non-Newt. Fluid Mech. 29 (1988) 381–432. doi:10.1016/0377-0257(88)85062-6.

[3] J.G. Oldroyd, On the Formulation of Rheological Equations of State, Proc. R. Soc. A Math. Phys. Eng. Sci. 200 (1950) 523–541. doi:10.1098/rspa.1950.0035.

[4] P.J. Oliveira, F.T. Pinho, G.A. Pinto, Numerical simulation of non-linear elastic flows with a general collocated finite-volume method, J. Non-Newt. Fluid Mech. 79 (1998) 1–43. doi:10.1016/S0377-0257(98)00082-2.

[5] J.P. van Doormaal, G.D. Raithby, Enhancements of the simple method for predicting incompressible fluid flows, Numer. Heat Transf. 7 (1984) 147–163. doi:10.1080/01495728408961817.

[6] M.A. Alves, P.J. Oliveira, F.T. Pinho, A convergent and universally bounded interpolation scheme for the treatment of advection, Int. J. Numer. Meth. Fluids. 41 (2003) 47–75. doi:10.1002/fld.428.

[7] A.M. Afonso, P.J. Oliveira, F.T. Pinho, M.A. Alves, The log-conformation tensor approach in the finite-volume method framework, J. Non-Newt. Fluid Mech. 157 (2009) 55–65. doi:10.1016/j.jnnfm.2008.09.007.

[8] R. Fattal, R. Kupferman, Constitutive laws for the matrix-logarithm of the conformation tensor, J. Non-Newt. Fluid Mech. 123 (2004) 281–285. doi:10.1016/j.jnnfm.2004.08.008.

[9] P.J. Oliveira, Method for time-dependent simulations of viscoelastic flows: vortex shedding behind cylinder, J. Non-Newt. Fluid Mech. 101 (2001) 113–137. doi:10.1016/S0377-0257(01)00146-X.

[10] F.A. Cruz, R.J. Poole, A.M. Afonso, F.T. Pinho, P.J. Oliveira, M.A. Alves, Influence of channel aspect ratio on the onset of purely-elastic flow instabilities in three-dimensional planar cross-slots, J. Non-Newt. Fluid Mech. 227 (2016) 65–79. doi:10.1016/j.jnnfm.2015.11.008.

[11] A. Chow, A. Keller, A.J. Müller, J.A. Odell, Entanglements in polymer solutions under elongational flow: a combined study of chain stretching, flow velocimetry and elongational viscosity, Macromolecules. 21 (1988) 250–256. doi:10.1021/ma00179a048.

[12] Y. Jun, V. Steinberg, Elastic turbulence in a curvilinear channel flow, Phys. Rev. E. 84 (2011) 56325. doi:10.1103/PhysRevE.84.056325.

[13] A. Groisman, V. Steinberg, Elastic turbulence in a polymer solution flow, Nature.

405 (2000) 53–55. doi:10.1038/35011019.

[14] A. Groisman, V. Steinberg, Efficient mixing at low Reynolds numbers using polymer additives., Nature. 410 (2001) 905–908. doi:10.1038/35073524.

[15] A. Fouxon, V. Lebedev, Spectra of turbulence in dilute polymer solutions, Phys. Fluids. 15 (2003) 2060–2072. doi:10.1063/1.1577563.

9 Conclusions and Future Work

9.1 The Planar Cross-Slot as a Benchmark Problem

Detailed numerical data concerning flow quantities of interest for three different viscoelastic models in the cross-slot geometry was provided, with particular emphasis placed on the bifurcation to steady asymmetric flow which occurs at a critical Deborah number. The steady flow bifurcation – in such a conceptually simple geometry – is proposed as a useful test case against which to benchmark, and compare, different numerical schemes for the simulation of viscoelastic fluid flows. Accordingly the relevant numerical data is provided in Chap. 5, for both the standard sharp corner cross-slot and also for a slightly rounded geometry, such that benchmarking of spectral or other higher-order methods is not impeded by the existence of geometrical singularities due to sharp corners. Furthermore, the critical De for the onset of time-dependent flow is also estimated. The proposed benchmark variables – local Weissenberg number Wi_o at the stagnation point, asymmetry parameter *DQ*, Couette correction *C*, and the critical Deborah numbers De_{CR} – can also be measured experimentally, offering a standardized form of communicating results for the cross-slot flow. The occurrence of an interior stagnation point, away from any boundary conditions, where the stress field can become unbounded is also a noteworthy flow feature, useful for the benchmarking of simulations, given the difficulty in resolving accurately the sharp birefringence strand developed at high De.

9.2 Stationary Instabilities in Cross-Slots with Different Aspect Ratio

Based on the evidence presented in Chap. 6, the mechanism of three-dimensional planar cross-slot steady flow bifurcations is characterized by a buckling-type instability, by which the fluid is redirected via paths of least resistance, therefore reducing energy dissipation. Since the path of highest resistance is a direct approach to the central

stagnation point along the inlet axis, streamlines tend to curve around it along the XY plane when the normal compressive stresses increase concomitantly with the Deborah number, as a consequence of progressively larger elasticity. Consequently, the central stagnation point receives matter via newly formed, paired and symmetrically-located peripheral stagnation points along the central vertical axis. Additionally, based on the sequence of flow transitions, the creeping flow of viscoelastic fluids in three-dimensional cross-slots may be divided in two regimes: the shallow channel regime when the depth is smaller than the width, and the deep channel regime when the depth is larger than the width. In the shallow channel regime, flow transitions directly from a steady symmetric pattern to a time-dependent flow. On the other hand, in the deep channel regime, which ultimately encompasses the limiting two-dimensional case, the flow first bifurcates from a steady symmetric to a steady asymmetric configuration, and, at higher Deborah number, transitions to unsteady flow. Therefore, square section channels, being at the intersection of the two regimes, may exhibit an unclear sequence of transitions. Furthermore, an assessment of flow stability via the local computation of a modified Pakdel-McKinley criterion indicates the presence of potentially unstable flow regions approximately along the diagonals of the central XY plane. Peripheral stagnation points generated by the steady bifurcation may further contribute to the destabilization of the flow, as shown by the presence of secondary instability prone regions in the corresponding z -planes.

9.3 Time-Dependent Instabilities in an Optimized Cross-Slot Device

Based on simulations of the flow of Boger fluids in the Optimized Shape Cross-slot Extensional Rheometer, or OSCER device, documented in Chap. 7, a family of predominantly elastic, time-dependent instabilities has been identified. The different types of flow dynamics may be grouped by their nominal elasticity number, defined as $\mathrm{El}_{nom} = \lambda_0 \eta_0 / \left(40 \rho H^2\right)$, where λ_0, η_0 and ρ are, respectively, the relaxation time, zero-shear-rate viscosity and volumetric mass density of the fluid, and H is the half-width of the inlet and outlet channels in the OSCER geometry. For El_{nom}={1.6, 2.3}, the flow is characterized by low amplitude, periodic oscillations, with a high degree of flow field symmetry and no loss of birefringence strand integrity. For El_{nom}={3.2, 4.1}, the flow field gradually loses symmetry over time as the birefringence strand rotates either

clockwise or counterclockwise, eventually resulting in the breaking and subsequent reconstitution of the strand. For El_{nom}=5.6, the flow is locally asymmetric near the center of the OSCER device yet mostly stationary, only perturbed by a very low amplitude quasi-periodic limit-cycle, without loss of strand integrity. For El_{nom}=8.1, the birefringence strand simultaneously rotates and translates along the outflow axis, periodically breaking and reforming. For El_{nom}={13.7, 18.8, 32.2}, the birefringence strand no longer rotates in a continuous, smooth motion. Instead, it is periodically fragmented by jets of fluid that pierce it along the normal direction, causing the stagnation point to rapidly oscillate some distance downstream of the center of the OSCER device. Spectral analysis of the first velocity component u_x, normalized by the average inlet velocity U_0, suggests that the flow regimes featuring loss of strand integrity become chaotic and locally turbulent above a certain flow rate threshold. However, this localized turbulence intensity decays along the outlet channels of the cross-slot, and is undetectable at the exit of the geometry. This family of instabilities is interpreted as the result of close proximity to a codimension-2 point in the parameter space, such that relatively small changes in various rheological properties or flow rate may cause the flow field behavior to be primarily determined by a Hopf bifurcation, a pitchfork bifurcation, or a combination of the two with varying degrees of relative amplitude. To the best of my knowledge, this is currently the most thorough characterization of this codimension-2 bifurcation.

9.4 Time-Dependent Instabilities in a Standard Planar Cross-Slot

In Chap. 8, a preliminary investigation on the transition to elastic turbulence in a standard planar cross-slot was discussed. The flow of an Oldroyd-B fluid, and of FENE-CR fluids with extensibilities $L^2 = 1000$ and $L^2 = 10000$, was simulated for two different characteristic Deborah (De) and Elasticity (El) numbers. Depending on the combination of El, De and, most importantly, the extensibility of the model polymer, which for an Oldroyd-B fluid is infinite, the sequential development of progressively more chaotic time-dependent instabilities is observed. For $L^2 = 1000$, the flow field is only perturbed by low amplitude, periodic fluctuations. For $L^2 = 10000$, a lateral displacement of the stagnation point occurs, accompanied also by fluctuations along the inlet axis of the cross-slot at higher De. For the Oldroyd-B fluid, the flow field develops chaotic fluctuations

for sufficiently high De or El, and specifically for $De = 10$ and $El = 100$, the spectral decay of velocity fluctuations, $\alpha \approx -3.5$, suggests the emergence of elastic turbulence. Nevertheless, this turbulence remains localized in the central slot, since the back reaction of the elastic stress field, amplified by the ejection of elastic stresses stored in the boundary layers along the outlet channels, leads to a stabilization of the velocity field along the downstream direction.

9.5 Future Work

From the information presented throughout this thesis, several future avenues of research seem plausible. Concerning the potential relation between stagnation point extensional flows and elastic turbulence (ET), inferred from Chaps. 7 and 8, two matters should be addressed. The first is an investigation assessing the extent to which cross-slot flows can generate sustained turbulence, or in other words, how far downstream can the chaotic motion reported in Chaps. 7 and 8 propagate, and what is the required level of elasticity and/or flow-rate. The second topic would be the further characterization of the path towards elastic turbulence, an issue that hasn't receive much attention despite the now almost two decades since the original observations on the phenomenon. It seems plausible that some type of subcritical bifurcation would play a role, yet at the moment this hypothesis remains speculative. It is, however, interesting to note that the onset of chaotic motion, as seen in Chap. 7, has a negating effect on instabilities that emerge at lower flow-rates. This is particularly noticeable with the highest elasticity regime in Chap. 7, which initially evolves along the familiar path of stationary bifurcation, until the onset of a birefringence strand fragmentation mechanism completely negates the formation of asymmetries.

On the topic of asymmetries, and considering how much more enlightening the research presented in Chap. 6 is when compared with Chap. 5, an important long term goal of numerical investigations would be the simulation of extensionally driven chaotic motion in three-dimensional (3D) geometries. One of the more striking results in classical inertial turbulence is the way in which energy flows between length scales. In 3D flows, energy travels from the larger length scales to the smaller scales, and is eventually dissipated by viscous effects. However, the reverse occurs in two-dimensional (2D)

turbulence [1], with energy that is injected at the forcing scale transferring to larger scales, a phenomenon that ultimately occurs due to the conservation of vorticity in 2D flows. A comparison of 2D and 3D flows may ultimately prove difficult for extensionally driven chaotic flow in a cross-slot, since shallow slots tend to exacerbate the role of shearing in the destabilization of flow, consequently masking the role of elongation, as shown in Chap. 6. One possible way around this problem would be the numerical optimization of a 3D geometry capable of producing an extension dominated flow field. By analogy with the role of recirculation flows in the receded corners of the OSCER device, one may envision an equivalent 3D geometry with protruding top and bottom walls, forming a sort of "six sphere mill" that presses fluid from the inlets into the outlets. This kind of irregularly shaped geometry should pose significant experimental challenges.

The experimental investigation of cross-slot instabilities has in some respects lagged behind computational work. Part of the reason is the difficulty in imaging the flow in planes other than the XY center plane, i.e. the plane formed by the inlet and outlet axes, or planes parallel to it. A recent contribution has been made in the form of a flow field visualization technique using a long working distance lens [2], such that an elastomeric microfluidic cross-slot device may now lay vertically over a microscopy setup, allowing the visualization of the vertical inlet plane. Visualization of the equivalent outlet plane may pose additional problems since the focal length of the long working lens would effectively restrict the length of the inlet channels, perhaps impeding the full development of flow profiles, rendering the experiments difficult to reproduce.

On the numerical front as well, significant challenges are posed by the study of 3D elastic turbulence. This type of investigation inevitably requires a parallelized, scalable computational method. Recent progress has been made towards this goal by the same research group that hosted the work presented in this thesis [3], namely by porting some of the stabilizing elements of the in-house, Fortran based method into an existing OpenFOAM® viscoelastic solver, especially the log-conformation representation (LCR) and the high resolution schemes for the treatment of advection, such as the CUBISTA scheme. It should now be possible to investigative 3D elastic turbulence using this method, due to the availability of parallelized solvers in OpenFOAM®. Tentatively, I envision the rotation and rupture of the birefringence plane examined in Chap. 6, which may eventually evolve towards an asymmetry-denying fragmentation mechanism such as the one seen in Chap. 7, which in turn may generate elastic turbulence in the central slot

as seen in Chap. 8. This sort of analysis would prove invaluable in establishing whether 2D and 3D elastic turbulence differ substantially in any manner, which would then have repercussions on the standardization of methods for the study of ET.

9.6 References

[1] R.E. Ecke, From 2D to 3D in fluid turbulence: unexpected critical transitions, J. Fluid Mech. 828 (2017) 1–4. doi:10.1017/jfm.2017.507.

[2] N. Burshtein, K. Zografos, A.Q. Shen, R.J. Poole, S.J. Haward, Inertioelastic Flow Instability at a Stagnation Point, Phys. Rev. X. 7 (2017) 41039. doi:10.1103/PhysRevX.7.041039.

[3] F. Pimenta, M.A. Alves, Stabilization of an open-source finite-volume solver for viscoelastic fluid flows, J. Non-Newt. Fluid Mech. 239 (2017) 85–104. doi:10.1016/j.jnnfm.2016.12.002.

10 Appendix: A Higher Order Advection Scheme

10.1 Summary

The following appendix describes the implementation of a fifth order, mapped Weighted Essentially Non-Oscillatory (WENO) scheme for the treatment of the advective terms in the momentum and constitutive equations. The estimated face center value is then incorporated into the source term of the respective equation by deferred correction. Since no substantial benefits could be obtained from this method alone, and given the increase in computational time relative to the much simpler Convergent and Universally Bounded Interpolation Scheme for the Treatment of Advection (CUBISTA) scheme, the WENO method described in this appendix was not utilized elsewhere in the thesis.

10.2 Motivation

The motivation for the implementation of higher order methods stems from the possibility of obtaining accurate results in coarse meshes. This is particularly important for three-dimensional (3D) simulations. For example, if the cell size is decreased by a factor of two, then, roughly speaking, the computational load per time-step or time-marching iteration increases by a factor of four, 2^2, in a two-dimensional (2D) problem and by a factor of eight, 2^3, in a 3D problem. Furthermore, High Resolution schemes, including the CUBISTA scheme [1], used elsewhere in this thesis, reduce to first order accuracy in non-monotonic regions of the advected scalar profile, such as local extrema. This is particularly problematic in the simulation of turbulent flows, since variable profiles are essentially a sequence of local maxima and minima. One interesting higher order method for the treatment of advection is the bounded, upwind biased WENO scheme developed by Liu et al. [2], which is based on the essentially non-oscillatory scheme (ENO) originally proposed by Harten at al. [3],[4]. The method is fifth order accurate in monotonic regions of the advected scalar profile, and provided the mapping described by

Henrick et al. [5] is used, the WENO scheme is third order accurate in local extrema. Additionally, the original purpose of these methods was to improve the resolution of shockwave fronts in compressible flows, hence the ENO and WENO schemes are sometimes also referred to as shock capturing methods, and their properties may also be of use in improving the resolution of elastic wave fronts, which have been observed in the transition to elastic turbulence of a simulated two-dimensional viscoelastic Kolmogorov flow [6].

10.3 Introduction

This introduction outlines key concepts concerning the WENO methodology, and is adapted from the description given by Jiang and Shu [7]. For a one-dimensional (1D) mesh with uniformly spaced control volumes Δx, as shown in Figure 10.1, a polynomial reconstruction of the scalar function $\phi(x)$ is used to approximate the cell face value, $\phi(x_\mathrm{e}) \equiv \phi_\mathrm{e}$.

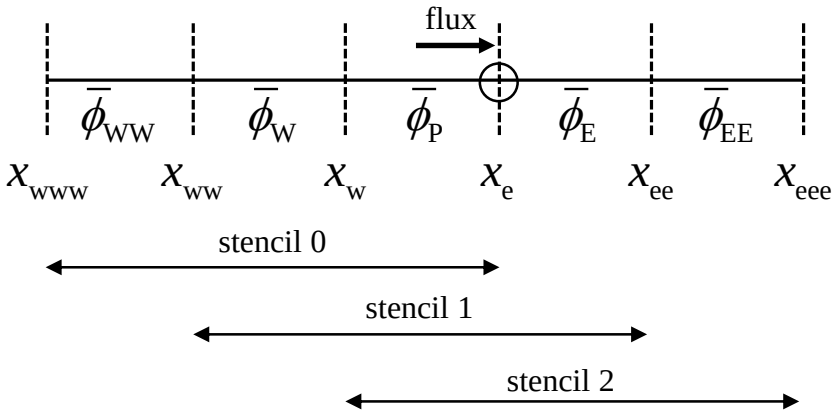

Figure 10.1 – Illustrative one-dimensional mesh. The flux is assumed positive for simplicity. $\overline{\phi}_\mathrm{C}$ is the average value of $\phi(x)$ within cell C, and x_f denotes the location of cell face f, which coincides with the location of the corresponding face center for a 1D mesh.

Defining the primitive function of $\phi(x)$ as,

$$\Phi(x) = \int_{x_{\mathrm{www}}}^{x} \phi(q)\,\mathrm{d}q, \tag{10.1}$$

where q is a dummy variable, $\Phi(x)$ can be calculated from the cell averages $\bar{\phi}_{\mathrm{C}}$. For instance,

$$\Phi(x_{\mathrm{e}}) = \int_{x_{\mathrm{www}}}^{x_{\mathrm{e}}} \phi(x)\,\mathrm{d}x = (x_{\mathrm{e}} - x_{\mathrm{w}})\bar{\phi}_{\mathrm{P}} + (x_{\mathrm{w}} - x_{\mathrm{ww}})\bar{\phi}_{\mathrm{W}} + (x_{\mathrm{ww}} - x_{\mathrm{www}})\bar{\phi}_{\mathrm{WW}}. \qquad (10.2)$$

Using the face values of the primitive function $\Phi(x)$, a polynomial interpolation $P(x)$ is constructed such that $\phi(x) = P'(x)$, i.e. $P'(x)$ is a polynomial reconstruction of $\phi(x)$.

The face values of $\Phi(x)$ may be grouped into a six point stencil S, which would result in a polynomial reconstruction $P'(x)$ of degree at most four, or instead the stencil may be sub-divided into smaller groups of r face values. In this example, $r = 4$ and the corresponding sub-stencils are shown in Figure 10.1, and are respectively,

$$\begin{aligned} S_0 &: \{x_{\mathrm{www}}, x_{\mathrm{ww}}, x_{\mathrm{w}}, x_{\mathrm{e}}\} \\ S_1 &: \{x_{\mathrm{ww}}, x_{\mathrm{w}}, x_{\mathrm{e}}, x_{\mathrm{ee}}\} \\ S_2 &: \{x_{\mathrm{w}}, x_{\mathrm{e}}, x_{\mathrm{ee}}, x_{\mathrm{eee}}\} \end{aligned} \quad . \qquad (10.3)$$

The polynomial of degree at most four, $P'(x)$, can be written as a convex combination, i.e. a linear combination where all coefficients are non-negative and sum to one, of the second degree polynomials $p_0'(x)$, $p_1'(x)$ and $p_2'(x)$, which reconstruct $\phi(x)$ in the stencils S_0, S_1 and S_2, respectively. For instance, if an approximation to the value of $\phi(x_{\mathrm{e}}) \equiv \phi_{\mathrm{e}}$ is desired, the values of the coefficients $C_k(x_{\mathrm{e}})$, also known as linear weights, where k refers to the number of the corresponding sub-stencil, are calculated according to the following restrictions,

$$0 \le C_k(x_e) \le 1, \tag{10.4}$$

$$\sum_{k=0}^{2} C_k(x_e) = 1, \tag{10.5}$$

$$P'(x_e) = \sum_{k=0}^{2} C_k(x_e)\, p_k'(x_e). \tag{10.6}$$

Note that the linear weights $C_k(x)$ are themselves second degree polynomials, and without additional restrictions their computation is an indeterminate problem, which is an issue that will be addressed later. Furthermore, WENO methods require an evaluation of the smoothness of each of the $p_k'(x)$ polynomials, via the corresponding smoothness indicators β_k, which for a uniform mesh are defined as,

$$\begin{aligned} &\beta_k = \sum_{l=1}^{2} \Delta x^{2l-1} \int_{x_w}^{x_e} \left(\frac{\mathrm{d}^l}{\mathrm{d}x^l} p_k'(x) \right)^2 \mathrm{d}x \\ &\Leftrightarrow \beta_k = \Delta x \int_{x_w}^{x_e} \left(p_k''(x) \right)^2 \mathrm{d}x + (\Delta x)^3 \int_{x_w}^{x_e} \left(p_k'''(x) \right)^2 \mathrm{d}x \end{aligned} . \tag{10.7}$$

This is a scaled sum of the L^2 norms of all the derivatives of $p_k'(x)$. For larger values of β_k the polynomial $p_k'(x)$ is less smooth in the central cell $[x_w, x_e]$. Normalized non-linear weights w_k can then be computed from the smoothness indicators,

$$\alpha_k = \frac{C_k(x_e)}{(\varepsilon + \beta_k)^p}, \tag{10.8}$$

$$w_k(x_e) = \frac{\alpha_k}{\sum_{k=0}^{2} \alpha_k}, \tag{10.9}$$

where α_k are auxiliary variables, ε is a small parameter that ensures α_k remain bounded, and p is chosen to accelerate the convergence of weights to zero as $\Delta x \to 0$, in regions where $\phi(x)$ is non-smooth, with usually $p = 2$. These non-linear weights can then be used to calculate a weighted approximation to $\phi(x_e) \equiv \phi_e$,

$$\phi_e = \sum_{k=0}^{2} w_k(x_e)\, p'_k(x_e). \tag{10.10}$$

Therefore, sub-stencils S_k wherein $\phi(x)$ is smooth will have a greater weight in the approximation, and sub-stencils containing discontinuities will have marginal weight. This approximation is formally fifth order accurate in smooth monotonic regions and, with suitable modifications to the values of the non-linear weights $w_k(x_e)$, to be discussed later, third order accurate in local extrema.

10.4 Implementation

A one-dimensional implementation is outlined along the West-East axis, shown schematically in Figure 10.2. The implementation for South-North and Bottom-Top axes is identical. The procedure is described for a scalar quantity convected according to the generic expression $\nabla \cdot (\mathbf{u}\varphi)$, which is equivalent to $\mathbf{u} \cdot \nabla \varphi$ for incompressible flows. φ is one of the velocity or stress components in the momentum or constitutive equations, respectively, or any other scalar quantity transported by advection, such as the concentration of a solute. The function to be reconstructed is designated as $\varphi(\xi)$, where ξ is the piece-wise linear distance between the point of interest and the center of cell P. The detailed implementation is described for positive flux through face e.

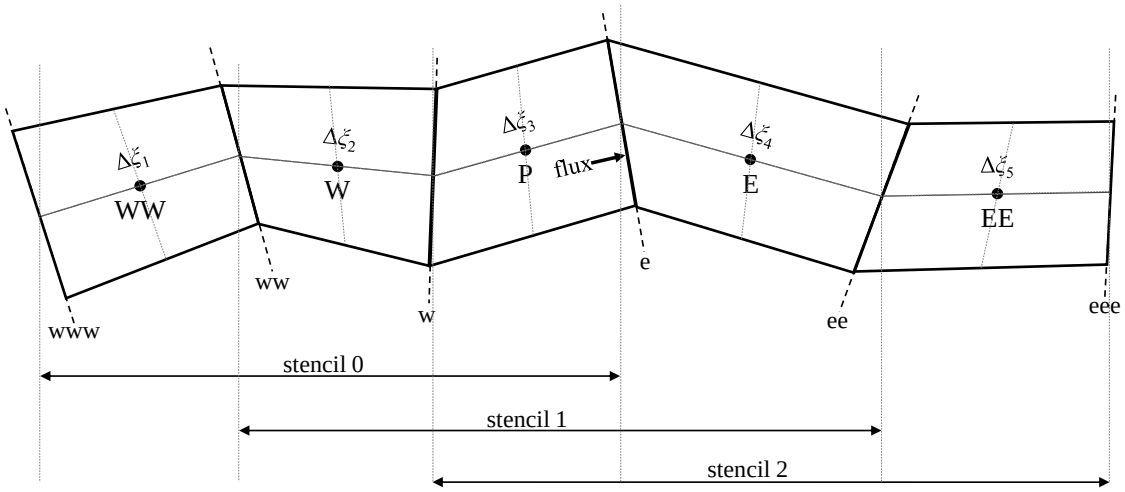

Figure 10.2 – Illustrative mesh segment for an implementation along the West-East axis. Positive flux is assumed.

First, the values of the piece-wise linear distance to the center of cell P, denoted by the variable ξ, are calculated for each face center, using the corresponding Cartesian coordinates.

$$\begin{cases} \Delta\xi_1 = \sqrt{\left(x_{\mathrm{ww}} - x_{\mathrm{www}}\right)^2 + \left(y_{\mathrm{ww}} - y_{\mathrm{www}}\right)^2 + \left(z_{\mathrm{ww}} - z_{\mathrm{www}}\right)^2} \\ \Delta\xi_2 = \sqrt{\left(x_{\mathrm{w}} - x_{\mathrm{ww}}\right)^2 + \left(y_{\mathrm{w}} - y_{\mathrm{ww}}\right)^2 + \left(z_{\mathrm{w}} - z_{\mathrm{ww}}\right)^2} \\ \Delta\xi_3 = \sqrt{\left(x_{\mathrm{e}} - x_{\mathrm{w}}\right)^2 + \left(y_{\mathrm{e}} - y_{\mathrm{w}}\right)^2 + \left(z_{\mathrm{e}} - z_{\mathrm{w}}\right)^2} \\ \Delta\xi_4 = \sqrt{\left(x_{\mathrm{ee}} - x_{\mathrm{e}}\right)^2 + \left(y_{\mathrm{ee}} - y_{\mathrm{e}}\right)^2 + \left(z_{\mathrm{ee}} - z_{\mathrm{e}}\right)^2} \\ \Delta\xi_5 = \sqrt{\left(x_{\mathrm{eee}} - x_{\mathrm{ee}}\right)^2 + \left(y_{\mathrm{eee}} - y_{\mathrm{ee}}\right)^2 + \left(z_{\mathrm{eee}} - z_{\mathrm{ee}}\right)^2} \end{cases} \tag{10.11}$$

$$\begin{cases} \xi_{\mathrm{www}} = -\left(\Delta\xi_1 + \Delta\xi_2 + \Delta\xi_3/2\right) \\ \xi_{\mathrm{ww}} = -\left(\Delta\xi_2 + \Delta\xi_3/2\right) \\ \xi_{\mathrm{w}} = -\Delta\xi_3/2 \\ \xi_{\mathrm{P}} = 0 \\ \xi_{\mathrm{e}} = +\Delta\xi_3/2 \\ \xi_{\mathrm{ee}} = +\left(\Delta\xi_3/2 + \Delta\xi_4\right) \\ \xi_{\mathrm{eee}} = +\left(\Delta\xi_3/2 + \Delta\xi_4 + \Delta\xi_5\right) \end{cases} \tag{10.12}$$

Second, the scalar function $\varphi(\xi)$ is reconstructed with the aid of Lagrange polynomials. For a generic set of $k+1$ data points, $\{(x_0, y_0),...,(x_j, y_j),...,(x_k, y_k)\}$, the interpolating Lagrange polynomial $L(x)$ is a linear combination of the basis polynomials $l_j(x)$, defined as follows,

$$l_j(x) = \prod_{\substack{0 \le m \le k \\ m \ne j}} \frac{x - x_m}{x_j - x_m}, \tag{10.13}$$

$$L(x) = \sum_{j=0}^{k} y_j l_j(x). \tag{10.14}$$

The reconstruction of $\varphi(\xi)$ is obtained by differentiating the polynomial which interpolates the corresponding primitive function $\Phi(\xi)$. From eq. 10.2,

$$\begin{cases} \Phi(\xi_{\mathrm{www}}) = 0 \\ \Phi(\xi_{\mathrm{ww}}) = \Delta\xi_1 \bar{\varphi}_{\mathrm{WW}} \\ \Phi(\xi_{\mathrm{w}}) = \Delta\xi_1 \bar{\varphi}_{\mathrm{WW}} + \Delta\xi_2 \bar{\varphi}_{\mathrm{W}} \\ \Phi(\xi_{\mathrm{e}}) = \Delta\xi_1 \bar{\varphi}_{\mathrm{WW}} + \Delta\xi_2 \bar{\varphi}_{\mathrm{W}} + \Delta\xi_3 \bar{\varphi}_{\mathrm{P}} \\ \Phi(\xi_{\mathrm{ee}}) = \Delta\xi_1 \bar{\varphi}_{\mathrm{WW}} + \Delta\xi_2 \bar{\varphi}_{\mathrm{W}} + \Delta\xi_3 \bar{\varphi}_{\mathrm{P}} + \Delta\xi_4 \bar{\varphi}_{\mathrm{E}} \\ \Phi(\xi_{\mathrm{eee}}) = \Delta\xi_1 \bar{\varphi}_{\mathrm{WW}} + \Delta\xi_2 \bar{\varphi}_{\mathrm{W}} + \Delta\xi_3 \bar{\varphi}_{\mathrm{P}} + \Delta\xi_4 \bar{\varphi}_{\mathrm{E}} + \Delta\xi_5 \bar{\varphi}_{\mathrm{EE}} \end{cases}. \tag{10.15}$$

The data points $\{\xi_{\mathrm{f}}, \Phi(\xi_{\mathrm{f}})\}$ are then used to construct three interpolating Lagrange polynomials, one per each sub-stencil in Figure 10.2, which are then differentiated, yielding the following polynomial reconstructions of $\varphi(\xi)$.

$$
\begin{aligned}
p_0'(\xi) = {} & \frac{(\xi-\xi_{\mathrm{w}})(\xi-\xi_{\mathrm{e}})+(\xi-\xi_{\mathrm{www}})(\xi-\xi_{\mathrm{e}})+(\xi-\xi_{\mathrm{www}})(\xi-\xi_{\mathrm{w}})}{(\xi_{\mathrm{ww}}-\xi_{\mathrm{www}})(\xi_{\mathrm{ww}}-\xi_{\mathrm{w}})(\xi_{\mathrm{ww}}-\xi_{\mathrm{e}})}\left[\Delta\xi_1\bar{\varphi}_{\mathrm{WW}}\right] \\
& + \frac{(\xi-\xi_{\mathrm{ww}})(\xi-\xi_{\mathrm{e}})+(\xi-\xi_{\mathrm{www}})(\xi-\xi_{\mathrm{e}})+(\xi-\xi_{\mathrm{www}})(\xi-\xi_{\mathrm{ww}})}{(\xi_{\mathrm{w}}-\xi_{\mathrm{www}})(\xi_{\mathrm{w}}-\xi_{\mathrm{ww}})(\xi_{\mathrm{w}}-\xi_{\mathrm{e}})}\begin{bmatrix}\Delta\xi_1\bar{\varphi}_{\mathrm{WW}} \\ +\Delta\xi_2\bar{\varphi}_{\mathrm{W}}\end{bmatrix} \\
& + \frac{(\xi-\xi_{\mathrm{ww}})(\xi-\xi_{\mathrm{w}})+(\xi-\xi_{\mathrm{www}})(\xi-\xi_{\mathrm{w}})+(\xi-\xi_{\mathrm{www}})(\xi-\xi_{\mathrm{ww}})}{(\xi_{\mathrm{e}}-\xi_{\mathrm{www}})(\xi_{\mathrm{e}}-\xi_{\mathrm{ww}})(\xi_{\mathrm{e}}-\xi_{\mathrm{w}})}\begin{bmatrix}\Delta\xi_1\bar{\varphi}_{\mathrm{WW}} \\ +\Delta\xi_2\bar{\varphi}_{\mathrm{W}} \\ +\Delta\xi_3\bar{\varphi}_{\mathrm{P}}\end{bmatrix}
\end{aligned}
\tag{10.16}
$$

$$
\begin{aligned}
p_1'(\xi) = {} & \frac{(\xi-\xi_{\mathrm{e}})(\xi-\xi_{\mathrm{ee}})+(\xi-\xi_{\mathrm{ww}})(\xi-\xi_{\mathrm{ee}})+(\xi-\xi_{\mathrm{ww}})(\xi-\xi_{\mathrm{e}})}{(\xi_{\mathrm{w}}-\xi_{\mathrm{ww}})(\xi_{\mathrm{w}}-\xi_{\mathrm{e}})(\xi_{\mathrm{w}}-\xi_{\mathrm{ee}})}\left[\Delta\xi_2\bar{\varphi}_{\mathrm{W}}\right] \\
& + \frac{(\xi-\xi_{\mathrm{w}})(\xi-\xi_{\mathrm{ee}})+(\xi-\xi_{\mathrm{ww}})(\xi-\xi_{\mathrm{ee}})+(\xi-\xi_{\mathrm{ww}})(\xi-\xi_{\mathrm{w}})}{(\xi_{\mathrm{e}}-\xi_{\mathrm{ww}})(\xi_{\mathrm{e}}-\xi_{\mathrm{w}})(\xi_{\mathrm{e}}-\xi_{\mathrm{ee}})}\begin{bmatrix}\Delta\xi_2\bar{\varphi}_{\mathrm{W}} \\ +\Delta\xi_3\bar{\varphi}_{\mathrm{P}}\end{bmatrix} \\
& + \frac{(\xi-\xi_{\mathrm{w}})(\xi-\xi_{\mathrm{e}})+(\xi-\xi_{\mathrm{ww}})(\xi-\xi_{\mathrm{e}})+(\xi-\xi_{\mathrm{ww}})(\xi-\xi_{\mathrm{w}})}{(\xi_{\mathrm{ee}}-\xi_{\mathrm{ww}})(\xi_{\mathrm{ee}}-\xi_{\mathrm{w}})(\xi_{\mathrm{ee}}-\xi_{\mathrm{e}})}\begin{bmatrix}\Delta\xi_2\bar{\varphi}_{\mathrm{W}} \\ +\Delta\xi_3\bar{\varphi}_{\mathrm{P}} \\ +\Delta\xi_4\bar{\varphi}_{\mathrm{E}}\end{bmatrix}
\end{aligned}
\tag{10.17}
$$

$$
\begin{aligned}
p_2'(\xi) = {} & \frac{(\xi-\xi_{\mathrm{ee}})(\xi-\xi_{\mathrm{eee}})+(\xi-\xi_{\mathrm{w}})(\xi-\xi_{\mathrm{eee}})+(\xi-\xi_{\mathrm{w}})(\xi-\xi_{\mathrm{ee}})}{(\xi_{\mathrm{e}}-\xi_{\mathrm{w}})(\xi_{\mathrm{e}}-\xi_{\mathrm{ee}})(\xi_{\mathrm{e}}-\xi_{\mathrm{eee}})}\left[\Delta\xi_3\bar{\varphi}_{\mathrm{P}}\right] \\
& + \frac{(\xi-\xi_{\mathrm{e}})(\xi-\xi_{\mathrm{eee}})+(\xi-\xi_{\mathrm{w}})(\xi-\xi_{\mathrm{eee}})+(\xi-\xi_{\mathrm{w}})(\xi-\xi_{\mathrm{e}})}{(\xi_{\mathrm{ee}}-\xi_{\mathrm{w}})(\xi_{\mathrm{ee}}-\xi_{\mathrm{e}})(\xi_{\mathrm{ee}}-\xi_{\mathrm{eee}})}\begin{bmatrix}\Delta\xi_3\bar{\varphi}_{\mathrm{P}} \\ +\Delta\xi_4\bar{\varphi}_{\mathrm{E}}\end{bmatrix} \\
& + \frac{(\xi-\xi_{\mathrm{e}})(\xi-\xi_{\mathrm{ee}})+(\xi-\xi_{\mathrm{w}})(\xi-\xi_{\mathrm{ee}})+(\xi-\xi_{\mathrm{w}})(\xi-\xi_{\mathrm{e}})}{(\xi_{\mathrm{eee}}-\xi_{\mathrm{w}})(\xi_{\mathrm{eee}}-\xi_{\mathrm{e}})(\xi_{\mathrm{eee}}-\xi_{\mathrm{ee}})}\begin{bmatrix}\Delta\xi_3\bar{\varphi}_{\mathrm{P}} \\ +\Delta\xi_4\bar{\varphi}_{\mathrm{E}} \\ +\Delta\xi_5\bar{\varphi}_{\mathrm{EE}}\end{bmatrix}
\end{aligned}
\tag{10.18}
$$

Therefore, the reconstructed values of $\varphi(\xi)$ at the face center e are $p_0'(\xi_{\mathrm{e}})$, $p_1'(\xi_{\mathrm{e}})$ and $p_2'(\xi_{\mathrm{e}})$.

Third, the linear weights are calculated according to the procedure outlined in Ref. [8]. In addition to the restrictions specified in eqs. 10.4-10.6, explicit computation of the linear weights $C_k(\xi)$ requires the assumption that the polynomial $p_k'(\xi)$ does not contribute to the approximation of the function $\varphi(\xi)$ outside the range of the

corresponding sub-stencil S_k, i.e. $C_k\left(\xi_l\right)=0$ when $\xi_l \notin S_k$. Since the full WENO stencil has six data points, i.e. six face centers, and each sub-stencil S_k is comprised of four face centers, the remaining two face centers can therefore be used as roots in the construction of the second degree polynomials $C_k\left(\xi\right)$,

$$C_k(\xi)=\gamma_k \prod_{\xi_l \in S \setminus S_k}\left(\xi-\xi_l\right), \tag{10.19}$$

where γ_k are coefficients, calculated recursively as follows,

$$\begin{aligned} &C_1(\xi_{\mathrm{www}})=C_2(\xi_{\mathrm{www}})=0 \Rightarrow C_0(\xi_{\mathrm{www}})=1 \\ &\Rightarrow \gamma_0=\frac{1}{\left(\xi_{\mathrm{www}}-\xi_{\mathrm{ee}}\right)\left(\xi_{\mathrm{www}}-\xi_{\mathrm{eee}}\right)} \end{aligned}, \tag{10.20}$$

$$\begin{aligned} &C_0(\xi_{\mathrm{eee}})=C_1(\xi_{\mathrm{eee}})=0 \Rightarrow C_2(\xi_{\mathrm{eee}})=1 \\ &\Rightarrow \gamma_2=\frac{1}{\left(\xi_{\mathrm{eee}}-\xi_{\mathrm{www}}\right)\left(\xi_{\mathrm{eee}}-\xi_{\mathrm{ww}}\right)} \end{aligned}, \tag{10.21}$$

$$\begin{aligned} &C_0(\xi_{\mathrm{P}})+C_1(\xi_{\mathrm{P}})+C_2(\xi_{\mathrm{P}})=1 \\ &\Rightarrow \gamma_1=\frac{1-\gamma_0\left(\xi_{\mathrm{P}}-\xi_{\mathrm{ee}}\right)\left(\xi_{\mathrm{P}}-\xi_{\mathrm{eee}}\right)-\gamma_2\left(\xi_{\mathrm{P}}-\xi_{\mathrm{www}}\right)\left(\xi_{\mathrm{P}}-\xi_{\mathrm{ww}}\right)}{\left(\xi_{\mathrm{P}}-\xi_{\mathrm{www}}\right)\left(\xi_{\mathrm{P}}-\xi_{\mathrm{eee}}\right)}. \end{aligned} \tag{10.22}$$

Finally the values of the linear weights at the face center e can be calculated,

$$\begin{cases} C_0\left(\xi_{\mathrm{e}}\right)=\gamma_0\left(\xi_{\mathrm{e}}-\xi_{\mathrm{ee}}\right)\left(\xi_{\mathrm{e}}-\xi_{\mathrm{eee}}\right) \\ C_1\left(\xi_{\mathrm{e}}\right)=\gamma_1\left(\xi_{\mathrm{e}}-\xi_{\mathrm{www}}\right)\left(\xi_{\mathrm{e}}-\xi_{\mathrm{eee}}\right) \\ C_2\left(\xi_{\mathrm{e}}\right)=\gamma_2\left(\xi_{\mathrm{e}}-\xi_{\mathrm{www}}\right)\left(\xi_{\mathrm{e}}-\xi_{\mathrm{ww}}\right) \end{cases}. \tag{10.23}$$

Fourth, the smoothness indicators are calculated as described in Ref. [7]. The reconstructing polynomials $p_k'(\xi)$ are differentiated analytically to prevent loss of accuracy. These derivatives are then integrated using Simpson's rule,

$$\int_a^b f(x)\,\mathrm{d}x \approx \frac{b-a}{6}\left[f(a)+4f\left(\frac{a+b}{2}\right)+f(b)\right], \tag{10.24}$$

yielding the smoothness indicators β_k,

$$\begin{cases} \beta_0 = \dfrac{1}{6}(\xi_\mathrm{e}-\xi_\mathrm{w})^2\left[\left(p_0''(\xi_\mathrm{e})\right)^2+4\left(p_0''(\xi_\mathrm{P})\right)^2+\left(p_0''(\xi_\mathrm{w})\right)^2\right]+(\xi_\mathrm{e}-\xi_\mathrm{w})^4\left(p_0'''\right)^2 \\ \beta_1 = \dfrac{1}{6}(\xi_\mathrm{e}-\xi_\mathrm{w})^2\left[\left(p_1''(\xi_\mathrm{e})\right)^2+4\left(p_1''(\xi_\mathrm{P})\right)^2+\left(p_1''(\xi_\mathrm{w})\right)^2\right]+(\xi_\mathrm{e}-\xi_\mathrm{w})^4\left(p_1'''\right)^2 \\ \beta_2 = \dfrac{1}{6}(\xi_\mathrm{e}-\xi_\mathrm{w})^2\left[\left(p_2''(\xi_\mathrm{e})\right)^2+4\left(p_2''(\xi_\mathrm{P})\right)^2+\left(p_2''(\xi_\mathrm{w})\right)^2\right]+(\xi_\mathrm{e}-\xi_\mathrm{w})^4\left(p_2'''\right)^2 \end{cases} . \tag{10.25}$$

Note that the third derivative, $p_k'''(\xi)\equiv p_k'''$, is constant.

Fifth, the non-linear weights $w_k(\xi_\mathrm{e})$ are calculated as described in Ref. [7], and adjusted as proposed in Ref. [5]. Using the linear weights $C_k(\xi_\mathrm{e})$ and the smoothness indicators β_k,

$$\begin{cases} \alpha_0 = \dfrac{C_0(\xi_\mathrm{e})}{(\varepsilon+\beta_0)^p} \Rightarrow w_0(\xi_\mathrm{e}) = \dfrac{\alpha_0}{\sum_{k=0}^{2}\alpha_k} \\ \alpha_1 = \dfrac{C_1(\xi_\mathrm{e})}{(\varepsilon+\beta_1)^p} \Rightarrow w_1(\xi_\mathrm{e}) = \dfrac{\alpha_1}{\sum_{k=0}^{2}\alpha_k} \\ \alpha_2 = \dfrac{C_2(\xi_\mathrm{e})}{(\varepsilon+\beta_2)^p} \Rightarrow w_2(\xi_\mathrm{e}) = \dfrac{\alpha_2}{\sum_{k=0}^{2}\alpha_k} \end{cases}, \tag{10.26}$$

where $p=2$ and $\varepsilon=10^{-40}$, as suggested by Henrick et al. [5]. To ensure at least third order accuracy at local extrema, specifically where $\varphi'(\xi)=0$ and $\varphi'''(\xi)\neq 0$, the non-linear weights are mapped according to Ref. [5],

$$\alpha_{k,map}=\frac{w_k(\xi_e)\left[C_k(\xi_e)+\left(C_k(\xi_e)\right)^2-3C_k(\xi_e)w_k(\xi_e)+\left(w_k(\xi_e)\right)^2\right]}{\left(C_k(\xi_e)\right)^2+w_k(\xi_e)\left[1-2C_k(\xi_e)\right]}, \quad (10.27)$$

$$w_{k,map}(\xi_e)=\frac{\alpha_{k,map}}{\sum_{k=0}^{2}\alpha_{k,map}}. \quad (10.28)$$

Finally, using the mapped non-linear weights, $\varphi(\xi_e)$ is estimated as follows,

$$\varphi(\xi_e)=w_{0,map}(\xi_e)\,p_0'(\xi_e)+w_{1,map}(\xi_e)\,p_1'(\xi_e)+w_{2,map}(\xi_e)\,p_2'(\xi_e), \quad (10.29)$$

and is then incorporated into the source term of the respective equation by deferred correction. This completes the implementation for positive flux. For negative flux, all steps are identical, except the WENO stencil is now centered in cell E (cf. Figure 10.2), and all the subscripts change accordingly. Namely, for negative flux, the range of the sub-stencils is as follows,

$$\begin{aligned} S_0&:\{\xi_{ww},\xi_w,\xi_e,\xi_{ee}\}\\ S_1&:\{\xi_w,\xi_e,\xi_{ee},\xi_{eee}\}\\ S_2&:\{\xi_e,\xi_{ee},\xi_{eee},\xi_{eeee}\} \end{aligned}. \quad (10.30)$$

10.4.1 Boundary Conditions

With the exception of axes with symmetry boundary conditions, it is assumed that meshes have at least five cells in any given generalized coordinate axis, i.e. the full WENO stencil never intersects more than one boundary. Given this restriction, there are eight boundary cases, four each for positive and negative flux, which are handled according to the diagrams shown in Figure 10.3. The total number of boundary conditions in a practical implementation is smaller, since cases such as Case 1 and Case 2 can be handled jointly.

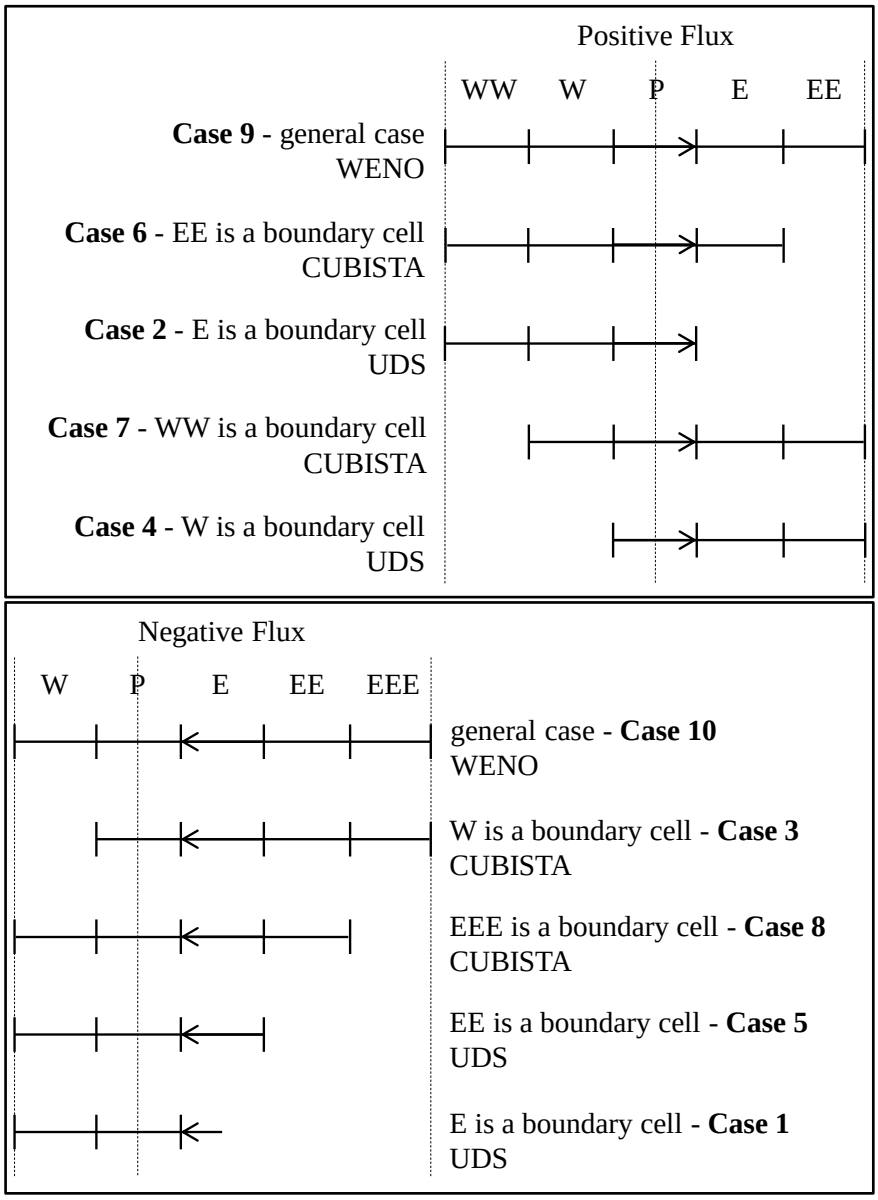

Figure 10.3 – Diagrams illustrating the implementation of boundary conditions. If the full WENO stencil (i.e. five cells) cannot be constructed due to proximity to a boundary, the CUBISTA scheme is used instead. If the CUBISTA stencil (i.e. three cells) cannot be constructed, then the deferred correction is not calculated.

10.5 Validation

10.5.1 Simplified Advection Problem

In order to assess if the WENO scheme is correctly implemented, the performance of the method is tested for a simplified advection problem,

$$u\frac{\partial \varphi}{\partial x}+v\frac{\partial \varphi}{\partial y}=0, \tag{10.31}$$

simulated in the two-dimensional geometry shown in Figure 10.4. Four systematically refined uniform meshes are used, with the following number of cells: 9^2, 17^2, 33^2 and 65^2.

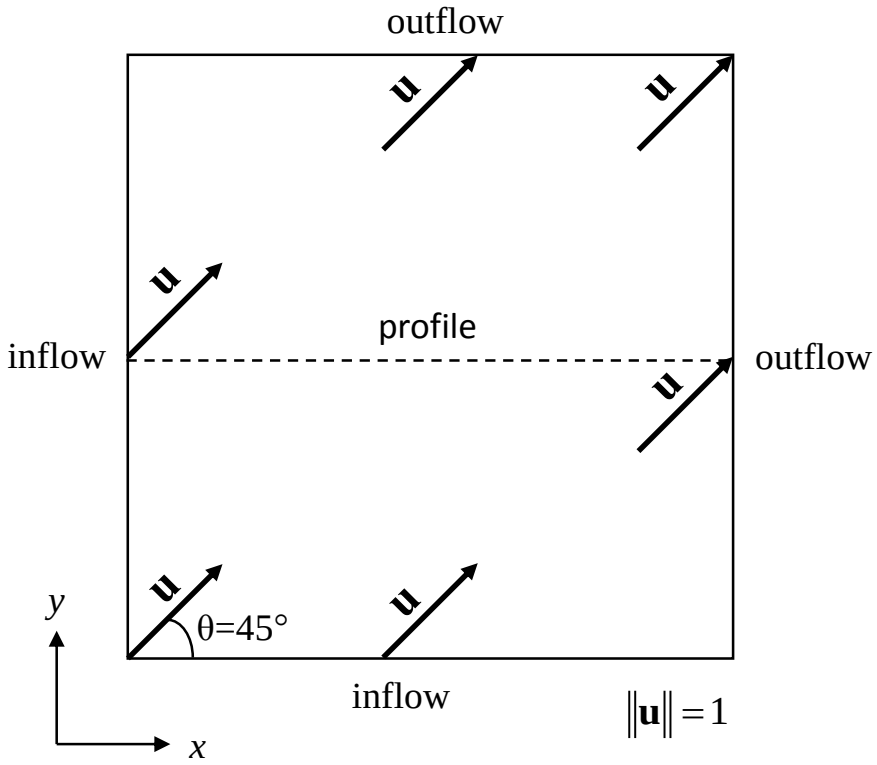

Figure 10.4 – Geometry used for the simplified assessment of the WENO implementation. Values of φ are assigned at the inflow boundaries, and the resulting centerline profile of φ is compared with the expected analytical result.

The WENO and CUBISTA schemes are compared. For reference, results for the upwind differencing scheme (UDS) and linear upwind differencing scheme (LUDS) are also shown. Figure 10.5 shows the performance of each method for a step profile. Qualitatively, the WENO and CUBISTA schemes produce similar results. Both methods are bounded, and their performance is identical near discontinuities. However, the WENO scheme improves the resolution of the maximum depicted in Figure 10.6. The CUBISTA scheme, and other High Resolution schemes in general, tend to flatten local extrema, due to the aforementioned first order accuracy in regions where the scalar profile in non-monotonic. This phenomenon is accentuated for narrower extrema, i.e. peaks or valleys with higher local curvature, as depicted in Figure 10.7.

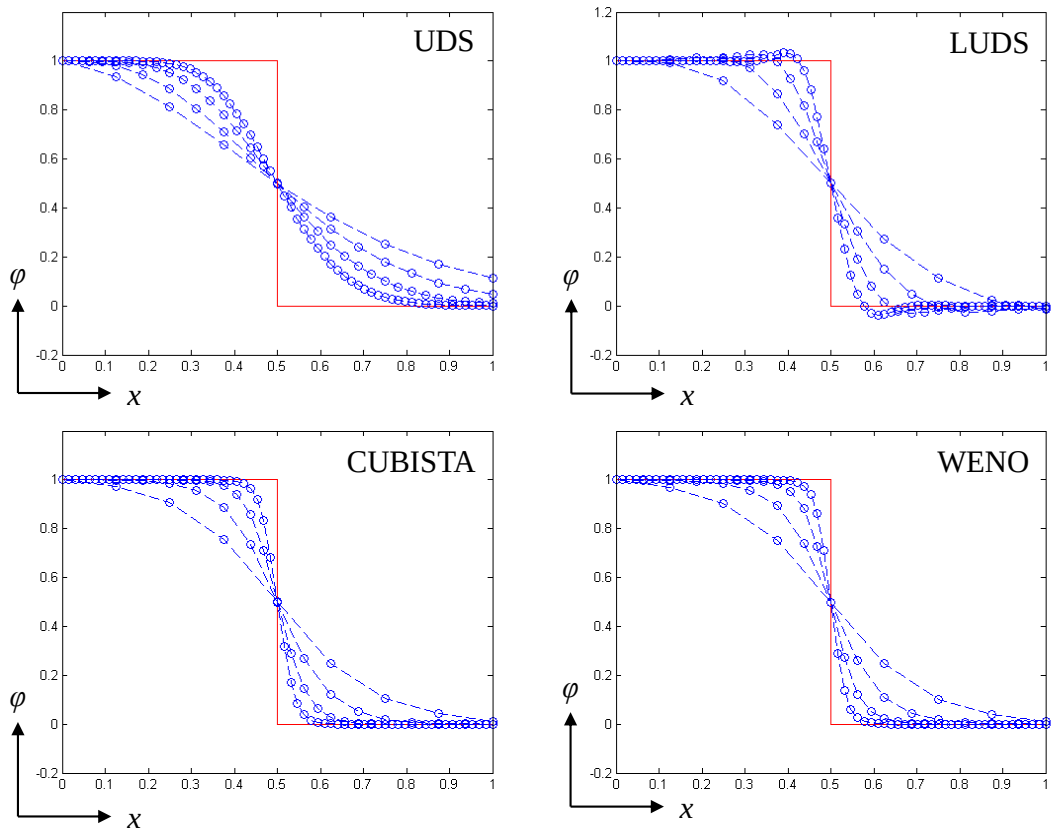

Figure 10.5 – Comparison of schemes for the treatment of advection, evaluated using the simplified advection problem defined by eq. 10.31 and Figure 10.4. The analytical centerline profile is shown as a solid line, and is a step function defined as $\varphi(x) = H(-x+1/2)$, where $H(x)$ is the Heaviside function. Numerical results are shown for four systematically refined uniform meshes, with 9^2, 17^2, 33^2 and 65^2 cells.

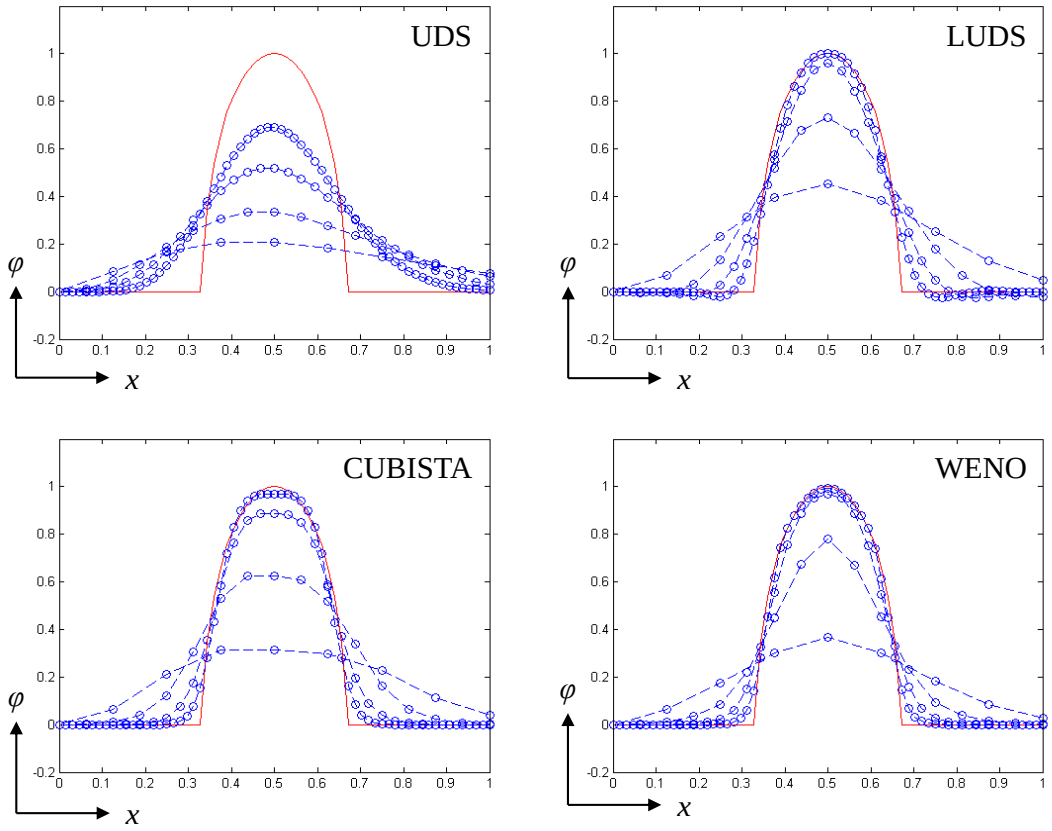

Figure 10.6 – Comparison of schemes for the treatment of advection, evaluated using the simplified advection problem defined by eq. 10.31 and Figure 10.4. The analytical centerline profile is shown as a solid line, and is a semi-ellipse defined as $\varphi(x)=\sqrt{1-\left[(x-1/2)/(1/6)\right]^2}$ for $x\in[1/3,2/3]$, and $\varphi(x)=0$ elsewhere. Numerical results are shown for four systematically refined uniform meshes, with 9^2, 17^2, 33^2 and 65^2 cells.

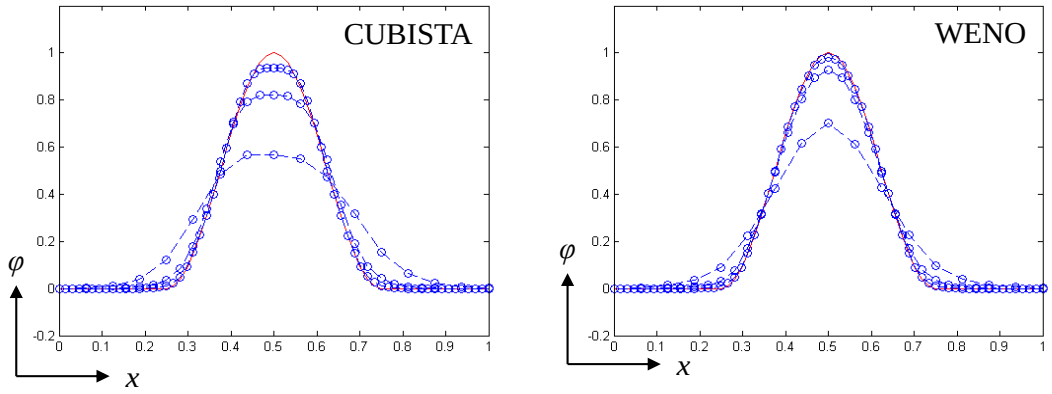

Figure 10.7 – Comparison of schemes for the treatment of advection, evaluated using the simplified advection problem defined by eq. 10.31 and Figure 10.4. The analytical centerline profile is shown as a solid line, and is a half-sine defined as $\varphi(x)=1/2\sin\left(4\pi\left[x-7/8\right]\right)+1/2$ for $x\in[1/4,3/4]$, and $\varphi(x)=0$ elsewhere. Numerical results are shown for three systematically refined uniform meshes, with 17^2, 33^2 and 65^2 cells.

10.5.2 Viscoelastic Flows

The performance of the WENO implementation is tested by incorporating the scheme into the viscoelastic flow solver used elsewhere in this thesis, where it replaces the CUBISTA scheme for the treatment of the advective terms in the momentum and constitutive equations. The performance of both schemes is compared in two reference flow problems, the planar cross-slot and the 4:1 sudden contraction. Inertialess, isothermal, incompressible two-dimensional flow is assumed. The governing equations are the continuity equation,

$$\nabla \cdot \mathbf{u} = 0, \tag{10.32}$$

the momentum equation,

$$-\nabla p + \nabla \cdot \boldsymbol{\tau} + \eta_s \nabla^2 \mathbf{u} = \mathbf{0}, \tag{10.33}$$

and the constitutive equation for the Oldroyd-B model,

$$\boldsymbol{\tau} + \lambda \left[\frac{\partial \boldsymbol{\tau}}{\partial t} + \mathbf{u} \cdot \nabla \boldsymbol{\tau} \right] = \eta_p \left[\nabla \mathbf{u} + (\nabla \mathbf{u})^{\dagger} \right] + \lambda \left[\boldsymbol{\tau} \cdot \nabla \mathbf{u} + (\nabla \mathbf{u})^{\dagger} \cdot \boldsymbol{\tau} \right]. \tag{10.34}$$

In these equations, $\mathbf{u}$ is the velocity vector, $\boldsymbol{\tau}$ is the polymeric extra stress tensor, p is the pressure, λ is the relaxation time of the fluid, η_s is the solvent shear viscosity and η_p is the polymeric shear viscosity. The solvent viscosity ratio for the Oldroyd-B model was kept constant at $\beta = \eta_s / \eta_0 = 1/9$, where $\eta_0 = \eta_s + \eta_p$ is the solution shear viscosity. The governing equations are solved using an implicit, second-order, finite volume numerical method using a collocated mesh arrangement, which is described in detail elsewhere [9], and was adapted from the SIMPLEC algorithm [10]. The method uses the log-conformation representation for the transformation of the constitutive equation [11],

following the methodology originally developed by Fattal and Kupferman [12]. At the walls, no-slip boundary conditions are assumed for the velocity components and the extra stress components are linearly extrapolated from the first two adjacent cells along the wall-normal direction, as described elsewhere [13]. Uniform velocity profiles and null extra stress profiles are assumed at the inlets. Neumann boundary conditions of the form $\mathbf{n}\cdot\nabla\phi = 0$ are assumed at the outlets, except for pressure which is linearly extrapolated from the first two upstream cells. Round-off error at machine level precision suffices to generate flow instabilities, so no disturbances are artificially introduced. The numerical method is implemented using double precision in Fortran. Since creeping flow is assumed, the performance of the WENO scheme is here assessed solely by the resolution of polymeric extra stress profiles, specifically concerning the advective term in eq. 10.34, namely $\lambda\mathbf{u}\cdot\nabla\boldsymbol{\tau}$. Furthermore, only steady state flows are considered. The properties of the systematically refined computational meshes are described in Table 10.1 and illustrated in Figures 10.8 and 10.9.

Table 10.1 – Properties of the computational meshes used in the validation of the WENO implementation. The characteristic length scale of the cross-slot geometry is the channel width D [14], whereas the equivalent conventional length scale for the 4:1 contraction is the half-width of the smaller channel H [15]. The location of the smallest cell also differs. In the cross-slot, $\Delta x_{\min}$ and $\Delta y_{\min}$ indicate the size of cells in the central slot, wherein the mesh is uniform. In the 4:1 contraction, the smallest cell is located at the reentrant corner.

	Cross-slot		4:1 contraction	
Mesh	NC	$\Delta x_{\min}/D = \Delta y_{\min}/D$	NC	$\Delta x_{\min}/H = \Delta y_{\min}/H$
M0	4375	0.04	–	–
M1	17901	0.02	17972	0.02
M2	70801	0.01	72232	0.01
M3	–	–	289616	0.005

For each geometry, the Deborah number is defined as,

$$\begin{cases} \text{Cross-slot}: \ \mathrm{De} = \lambda\dfrac{U}{D} \\ 4:1 \text{ contraction}: \ \mathrm{De} = \lambda\dfrac{4U}{H} \end{cases} \tag{10.35}$$

where U is the uniform inlet velocity, D is the channel width in the cross-slot and H is the half-width of the smaller channel in the 4:1 contraction. The different definitions of De stem from the conventional characteristic velocities and length scales of each benchmark flow geometry, taken from Ref. [14] for the cross-slot and Ref. [15] for the 4:1 contraction. To avoid confusion, the first normal stress difference is normalized using the Deborah number, $N_1/(\eta_0 \mathrm{De}/\lambda)$.

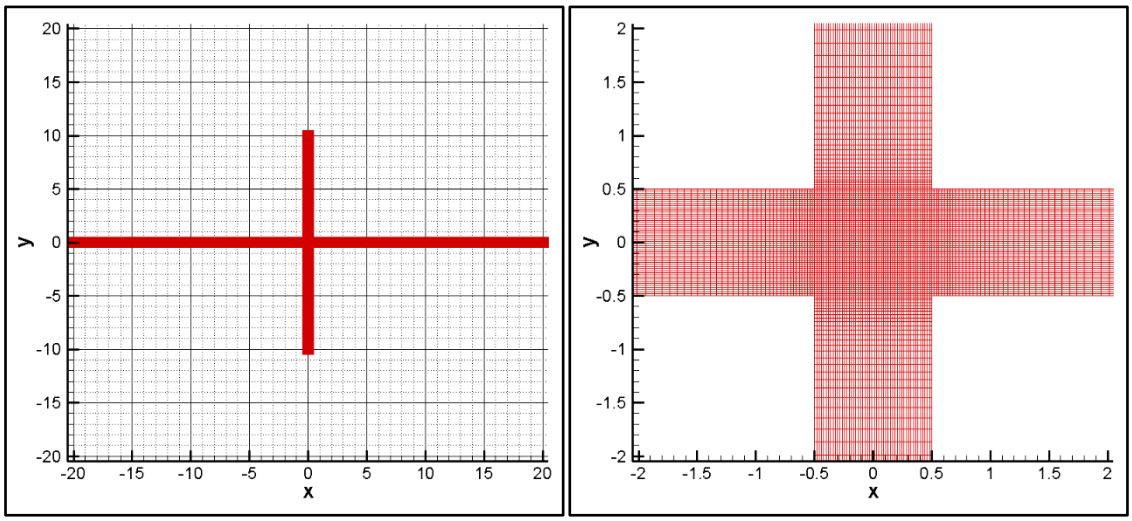

Figure 10.8 – Mesh used for the assessment of the WENO scheme in a cross-slot flow. The longer inlet channels along the *y*-centerline permit the full development of velocity and stress profiles, which are uniform at the inlets. The detailed structure of the grid in the central slot is shown for mesh M1 (cf. Table 10.1).

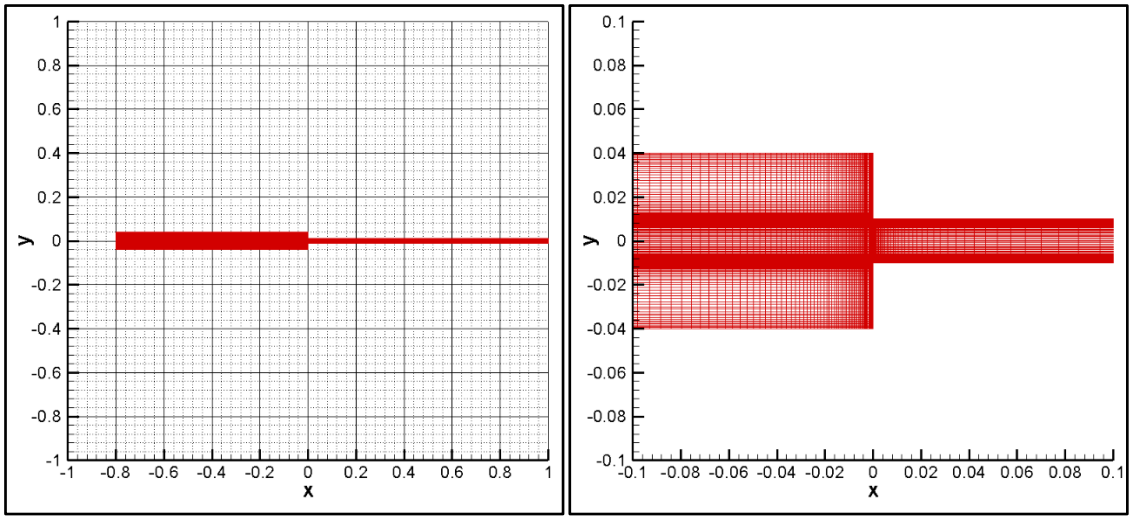

Figure 10.9 – Mesh used for the assessment of the WENO scheme in a 4:1 contraction flow. The larger channel is longer than in Ref. [15] to ensure the full development of the velocity and stress profiles, which are uniform at the inlet. The detailed structure of the grid near the contraction is shown for mesh M1 (cf. Table 10.1).

Contour plots of the normalized first normal stress difference, with superimposed streamlines, are shown in Figure 10.10 for the planar cross-slot and in Figure 10.11 for the 4:1 sudden contraction. The range of Deborah numbers for the cross-slot simulations allows for the development of stationary asymmetries [14], extensively discussed elsewhere in this thesis. Alternatively, the values of De for the 4:1 contraction flows are such that a direct comparison with published benchmark data is feasible [15]. Other than the random rotation of the birefringence strand in asymmetric cross-slot flows, either clockwise or counterclockwise, the results are qualitatively indistinguishable for the CUBISTA and WENO schemes. A more rigorous evaluation is therefore conducted using established benchmark parameters, namely the asymmetry parameter DQ for cross-slot flows [14], shown in Table 10.2, or the normalized size of the recirculating corner vortex X_{R} for the 4:1 sudden contraction [15], shown in Table 10.3. In both instances, the Richardson extrapolation is used to evaluate the order of convergence and the value of the benchmark parameters in the limit of infinite mesh refinement. For both flow problems, and across the range of simulated De, the order of convergence of DQ or X_{R} is at most two, and the corresponding extrapolated values are similar to the published benchmark data. Since the CUBISTA scheme is third order accurate and the WENO scheme is fifth order accurate, the limitations on the order of convergence stem from other components of the viscoelastic flow solver. Besides the treatment of advection, all other elements of the spatial discretization described in Ref. [9] are second order accurate. Hence it is unsurprising that the convergence of the method is globally unaffected by further improvements in the treatment of advection. However, the desire to improve the resolution of advected scalar profiles stems from localized deficiencies attributable to the first order accuracy of High Resolution schemes at local extrema. Therefore, profiles of the normalized first normal stress difference are shown in Figure 10.12, along the outlet centerline of the planar cross-slot, and in Figure 10.13 along the centerline of the sudden contraction. Concerning the cross-slot flows, whenever the flow field is in an asymmetric configuration, the WENO scheme slightly improves the resolution of N_1 profiles along the outlet centerline, and the additional sharpness of N_1 peaks is more pronounced in finer meshes. Alternatively, no visible improvements are seen for the N_1 profiles along the centerline of the 4:1 contraction.

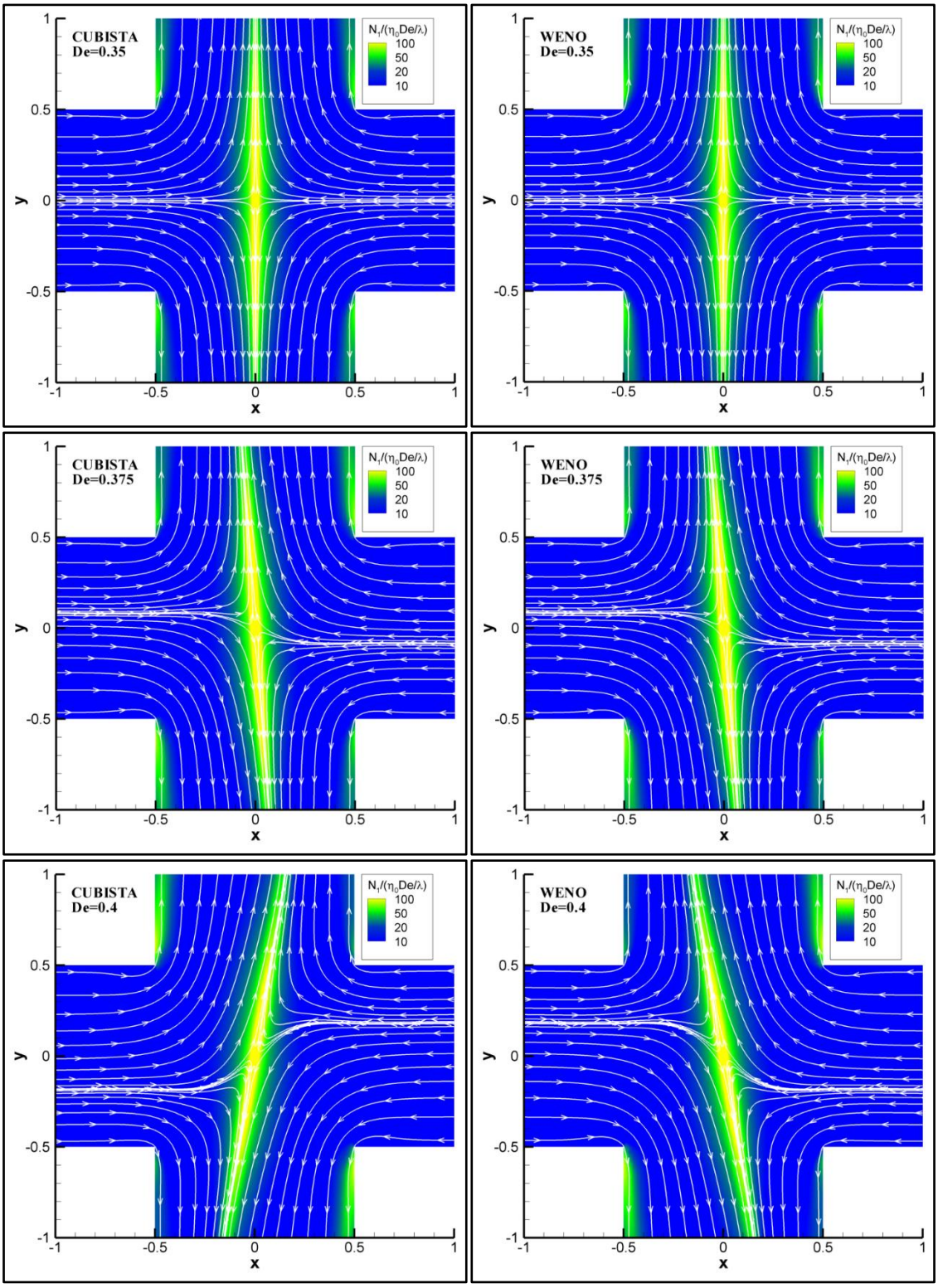

Figure 10.10 – Contour plots of the normalized first normal stress difference with superimposed streamlines. Results are shown for the CUBISTA and WENO schemes in the creeping flow of an Oldroyd-B fluid, with $\beta = 1/9$, through a planar cross-slot. Data was obtained for mesh M1 (cf. Table 10.1).

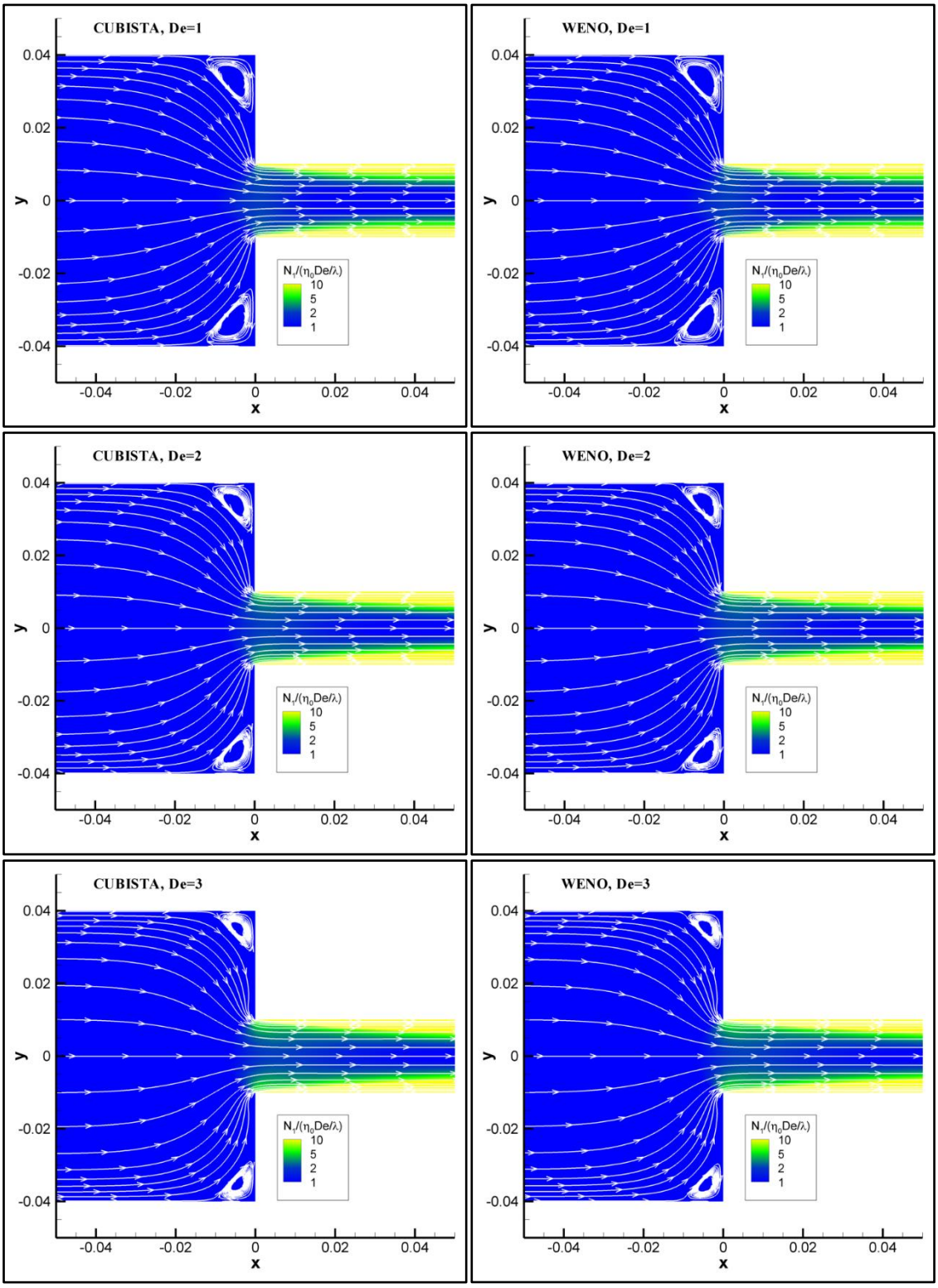

Figure 10.11 – Contour plots of the normalized first normal stress difference with superimposed streamlines. Results are shown for the CUBISTA and WENO schemes in the creeping flow of an Oldroyd-B fluid, with $\beta = 1/9$, through a planar 4:1 contraction. Data was obtained for mesh M1 (cf. Table 10.1).

Table 10.2 – Convergence and extrapolation of the asymmetry parameter DQ, defined as one of the benchmark parameters for planar cross-slot flows. Reference values, $DQ_{\mathrm{Ref.}}$, were taken from Ref. [14]. p denotes the order of convergence.

CUBISTA						
De	DQ_{M0}	DQ_{M1}	DQ_{M2}	p	$DQ_{\mathrm{extrap.}}$	$DQ_{\mathrm{Ref.}}$
0.350	0	0	0	–	–	0
0.375	0.001	0.244	0.318	1.712	0.351	0.338
0.400	0.406	0.523	0.551	2.053	0.560	0.562
WENO						
De	DQ_{M0}	DQ_{M1}	DQ_{M2}	p	$DQ_{\mathrm{extrap.}}$	$DQ_{\mathrm{Ref.}}$
0.350	0	0	0	–	–	0
0.375	0.049	0.250	0.311	1.716	0.338	0.338
0.400	0.409	0.521	0.549	2.026	0.558	0.562

Table 10.3 – Convergence and extrapolation of the size of the recirculating corner vortex X_{R}, normalized by the half-width of the smaller channel H, defined as one of the benchmark parameters for planar 4:1 contraction flows. Reference values, $X_{\mathrm{R,Ref.}}$, were taken from Ref. [15]. p denotes the order of convergence.

CUBISTA						
De	$X_{\mathrm{R,M1}}$	$X_{\mathrm{R,M2}}$	$X_{\mathrm{R,M3}}$	p	$X_{\mathrm{R,extrap.}}$	$X_{\mathrm{R,Ref.}}$
1	1.385	1.376	1.372	1.217	1.369	1.373
2	1.217	1.189	1.180	1.712	1.176	1.181
3	1.045	0.989	0.976	2.059	0.971	0.973
WENO						
De	$X_{\mathrm{R,M1}}$	$X_{\mathrm{R,M2}}$	$X_{\mathrm{R,M3}}$	p	$X_{\mathrm{R,extrap.}}$	$X_{\mathrm{R,Ref.}}$
1	1.380	1.374	1.371	1.316	1.370	1.373
2	1.204	1.185	1.179	1.726	1.177	1.181
3	1.024	0.986	0.976	1.860	0.972	0.973

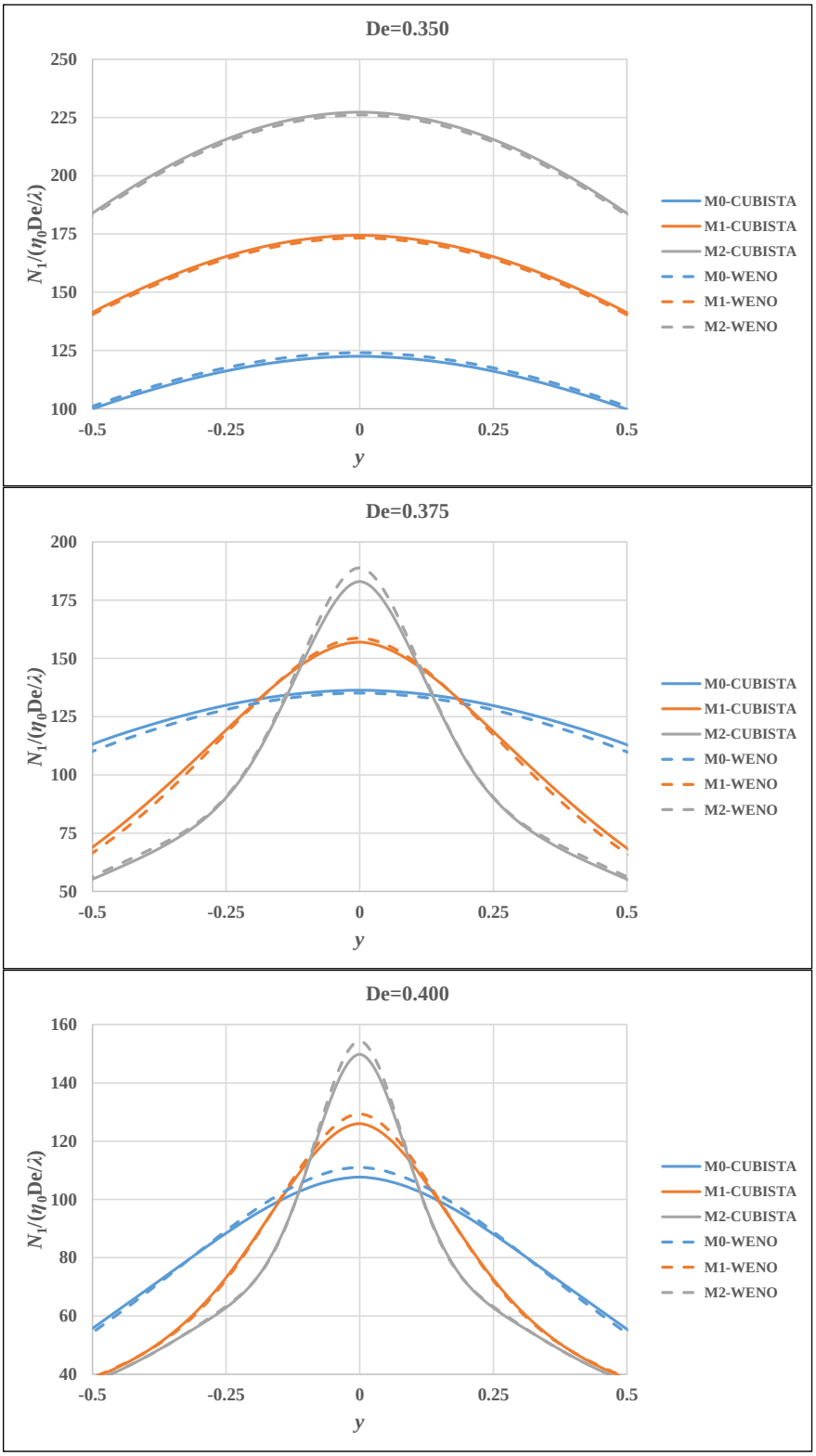

Figure 10.12 – Profiles of the normalized first normal stress difference along the outlet centerline of the planar cross-slot. For each mesh and Deborah number, the profiles obtained using the CUBISTA and WENO schemes are compared.

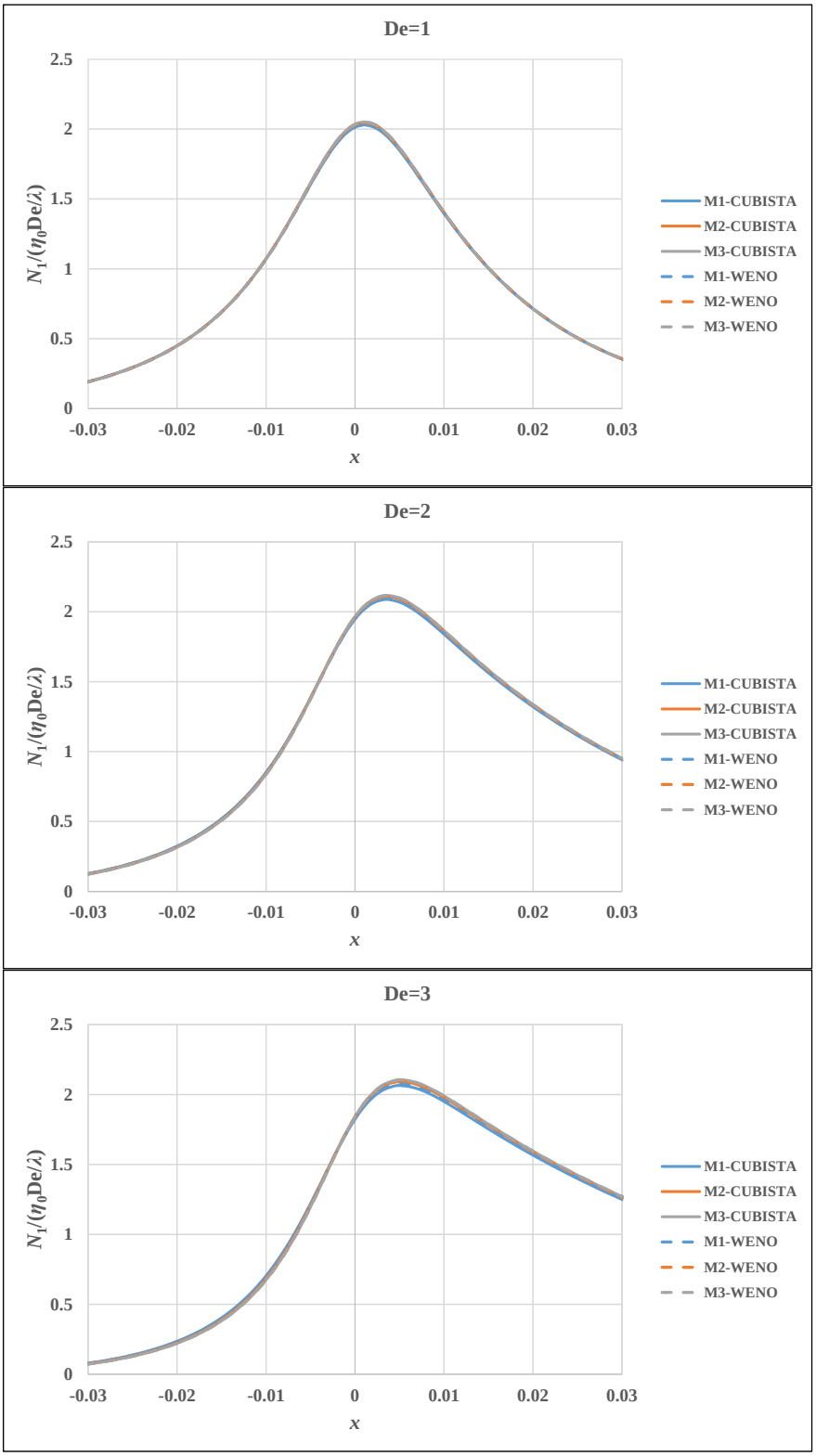

Figure 10.13 – Profiles of the normalized first normal stress difference along the centerline of the planar 4:1 contraction. For each mesh and Deborah number, the profiles obtained using the CUBISTA and WENO schemes are compared.

Concerning the computational efficiency of the WENO implementation, i.e. the time required for the calculations in both the WENO subroutine itself and the viscoelastic flow solver as a whole, a comparison with the CUBISTA subroutine is shown in Table 10.4. Measurements of the computational time were conducted in an Intel Xeon E5-2643 CPU running at 3.30GHz, for a Fortran based implementation.

Table 10.4 – Efficiency of the WENO scheme in the simulation of the flow of an Oldroyd-B fluid, with $\beta = 1/9$, in either a planar cross-slot or a 4:1 sudden contraction. For a Fortran based implementation, calls to the subroutines containing either the CUBISTA or the WENO schemes were timed, as well as the overall computational time per global iteration of the viscoelastic flow solver. Times are shown in milliseconds, and each time is the average of ten samples, gathered upon the full development of the flow.

Cross-slot							
Subroutine CUBISTA only				Full iteration with CUBISTA			
De	t_{M0}	t_{M1}	t_{M2}	De	t_{M0}	t_{M1}	t_{M2}
0.350	3	16	57	0.350	37	131	640
0.375	3	14	56	0.375	32	142	651
0.400	3	15	58	0.400	36	139	828
Subroutine WENO only				Full iteration with WENO			
De	t_{M0}	t_{M1}	t_{M2}	De	t_{M0}	t_{M1}	t_{M2}
0.350	9	46	182	0.350	49	224	923
0.375	9	40	196	0.375	43	187	830
0.400	9	43	172	0.400	46	227	904
4:1 contraction							
Subroutine CUBISTA only				Full iteration with CUBISTA			
De	t_{M1}	t_{M2}	t_{M3}	De	t_{M1}	t_{M2}	t_{M3}
1	14	58	269	1	176	1018	4621
2	16	57	275	2	163	1076	4503
3	14	58	264	3	209	1051	4518
Subroutine WENO only				Full iteration with WENO			
De	t_{M1}	t_{M2}	t_{M3}	De	t_{M1}	t_{M2}	t_{M3}
1	43	179	674	1	253	927	3273
2	40	190	666	2	249	586	3749
3	44	166	751	3	248	897	3356

The additional floating point operations required by the WENO scheme imply a threefold increase in the computational time of the corresponding subroutine, relative to the CUBISTA scheme. However, the effects on the computational time of global

iterations are less noticeable, with an average 1.2 fold increase. The bottleneck in the performance of the viscoelastic flow solver is the numerical solution of the pressure correction equation, hence even a treatment of advection as demanding as the WENO scheme has a relatively minor impact on the overall computational cost. Interestingly, for the finer meshes of the sudden contraction problem, the WENO implementation decreases the overall computational load, presumably because of an improved conditioning of the input values to the pressure correction solver, which subsequently converges in fewer internal iterations. However, for the cross-slot flows, where the WENO scheme was shown to improve the resolution of advected polymeric extra stress profiles along the outlet centerline, the computational time per global iteration increases regardless of the specific mesh.

10.6 Conclusions

A fifth order accurate WENO scheme for the treatment of advection was implemented and validated in the in-house viscoelastic flow solver, where it replaces the third order accurate CUBISTA scheme. Marginal improvements in the resolution of polymeric extra stress profiles were obtained for a planar cross-slot flow. The overall order of convergence of the viscoelastic flow solver was unaffected, and the additional floating point operations required by the WENO scheme imply, on average, a 1.2 fold increase in the computational time per global iteration. However, for a 4:1 sudden contraction flow, the WENO scheme led to a decrease of the computational time per global iteration in relatively fine meshes. Overall, the accuracy of the in-house solver is similar with either the CUBISTA or WENO schemes, therefore I conclude that further improvements of the treatment of advection will not, on their own, produce substantial benefits in the solution of viscoelastic flow problems.

10.7 References

[1] M.A. Alves, P.J. Oliveira, F.T. Pinho, A convergent and universally bounded interpolation scheme for the treatment of advection, Int. J. Numer. Meth. Fluids.

41 (2003) 47–75. doi:10.1002/fld.428.

[2] X.-D. Liu, S. Osher, T. Chan, Weighted Essentially Non-oscillatory Schemes, J. Comput. Phys. 115 (1994) 200–212. doi:10.1006/jcph.1994.1187.

[3] A. Harten, S. Osher, Uniformly High-Order Accurate Nonoscillatory Schemes. I, SIAM J. Numer. Anal. 24 (1987) 279–309. doi:10.1137/0724022.

[4] A. Harten, B. Engquist, S. Osher, S.R. Chakravarthy, Uniformly high order accurate essentially non-oscillatory schemes, III, J. Comput. Phys. 71 (1987) 231–303. doi:10.1016/0021-9991(87)90031-3.

[5] A.K. Henrick, T.D. Aslam, J.M. Powers, Mapped weighted essentially non-oscillatory schemes: Achieving optimal order near critical points, J. Comput. Phys. 207 (2005) 542–567. doi:10.1016/j.jcp.2005.01.023.

[6] S. Berti, G. Boffetta, Elastic waves and transition to elastic turbulence in a two-dimensional viscoelastic Kolmogorov flow, Phys. Rev. E. 82 (2010) 36314. doi:10.1103/PhysRevE.82.036314.

[7] G.-S. Jiang, C.-W. Shu, Efficient Implementation of Weighted ENO Schemes, J. Comput. Phys. 126 (1996) 202–228. doi:10.1006/jcph.1996.0130.

[8] E. Carlini, R. Ferretti, G. Russo, A Weighted Essentially Nonoscillatory, Large Time-Step Scheme for Hamilton–Jacobi Equations, SIAM J. Sci. Comput. 27 (2005) 1071–1091. doi:10.1137/040608787.

[9] P.J. Oliveira, F.T. Pinho, G.A. Pinto, Numerical simulation of non-linear elastic flows with a general collocated finite-volume method, J. Non-Newt. Fluid Mech. 79 (1998) 1–43. doi:10.1016/S0377-0257(98)00082-2.

[10] J.P. van Doormaal, G.D. Raithby, Enhancements of the simple method for predicting incompressible fluid flows, Numer. Heat Transf. 7 (1984) 147–163. doi:10.1080/01495728408961817.

[11] A.M. Afonso, P.J. Oliveira, F.T. Pinho, M.A. Alves, The log-conformation tensor approach in the finite-volume method framework, J. Non-Newt. Fluid Mech. 157 (2009) 55–65. doi:10.1016/j.jnnfm.2008.09.007.

[12] R. Fattal, R. Kupferman, Constitutive laws for the matrix-logarithm of the conformation tensor, J. Non-Newt. Fluid Mech. 123 (2004) 281–285.

doi:10.1016/j.jnnfm.2004.08.008.

[13] F. Pimenta, M.A. Alves, Stabilization of an open-source finite-volume solver for viscoelastic fluid flows, J. Non-Newt. Fluid Mech. 239 (2017) 85–104. doi:10.1016/j.jnnfm.2016.12.002.

[14] F.A. Cruz, R.J. Poole, A.M. Afonso, F.T. Pinho, P.J. Oliveira, M.A. Alves, A new viscoelastic benchmark flow: Stationary bifurcation in a cross-slot, J. Non-Newt. Fluid Mech. 214 (2014) 57–68. doi:10.1016/j.jnnfm.2014.09.015.

[15] M.A. Alves, P.J. Oliveira, F.T. Pinho, Benchmark solutions for the flow of Oldroyd-B and PTT fluids in planar contractions, J. Non-Newt. Fluid Mech. 110 (2003) 45–75. doi:10.1016/S0377-0257(02)00191-X.